

MASOUD RAMUZ

DEVELOPING HIGH-THROUGHPUT TOOLS FOR
STUDY OF CYCLIC NUCLEOTIDE SIGNALLING IN
AGING HIPSC-CM

IMPERIAL COLLEGE LONDON
NATIONAL HEART AND LUNG INSTITUTE

A THESIS SUBMITTED FOR THE DEGREE OF DOCTOR OF
PHILOSOPHY
15-02-2023

Declaration of Originality

I declare that this thesis and the research it depicts are the product of my own labour and that any ideas or works of other people, published or otherwise, are fully acknowledged and provided with references.

Copyright Declaration

'The copyright of this thesis rests with the author. Unless otherwise indicated, its contents are licensed under a Creative Commons Attribution-Non Commercial 4.0 International Licence (CC BY-NC). Under this licence, you may copy and redistribute the material in any medium or format. You may also create and distribute modified versions of the work. This is on the condition that: you credit the author and do not use it, or any derivative works, for a commercial purpose. When reusing or sharing this work, ensure you make the licence terms clear to others by naming the licence and linking to the licence text. Where a work has been adapted, you should indicate that the work has been changed and describe those changes. Please seek permission from the copyright holder for uses of this work that are not included in this licence or permitted under UK Copyright Law.'

Abstract

There is potential in the use of HiPSC-CMs (human induced pluripotent stem cell derived cardiomyocytes) in drug testing, genetic studies, and cell replacement therapy. However, current methods of differentiation produce cells that structurally and physiologically differ from adult human cardiomyocytes. Adult cardiomyocytes regulate the signalling molecules cAMP and cGMP that control contraction and relaxation into strict nano-domains through structural elements such as caveolae, t-tubules, and the SR, then further regulate them through a hydrolysing protein family of phosphodiesterases (PDEs). Of these signalling molecules, cGMP is relatively lacking in descriptive studies. In our study we first produce tools and methods needed for experiments studying cGMP signalling in HiPSC-CM. Then, using our novel tools and methods as well as existing ones, we examine the maturation of cGMP signalling between D30 and D90 HiPSC-CM by characterising pathways that produce cGMP, the PDEs that can hydrolyse cGMP pools produced through each of these pathways, and the effect of structural compartmentation through caveolae on these pools.

MultiFRET is a novel and highly flexible high-throughput real-time FRET measurement and analysis tool, which was developed in Java for use with the Icy Bioimaging suite. With MultiFRET we increase the number of cells measured in an experiment 50 times what was possible before under the same circumstances. Though it is technically possible to obtain even more cells, provided the computer has enough RAM and the dish contains enough cells, this was not tested in our experiments. MultiFRET further exhibits functionality for enhanced real-time and post-experiment analysis, as well as for the simultaneous measurement of multiple FRET sensors.

We test several cGMP-detecting FRET sensors for appropriate sensitivity and find that ScGi performs the best for our needs. We then lay the groundwork for the generation of a transgenic HiPSC-CM line that expresses ScGi and one that expresses a cAMP sensor with compatible fluorophores for multiplexed FRET measurements with ScGi.

Experiments using the ScGi FRET sensor to measure the effects of stimulating three different cGMP producing pathways; the NO-pathway (nitric oxide), the NP-pathway (natriuretic peptide), and the β_3 -pathway. After this stimulation, we inhibit one of the following PDEs relevant to cGMP: PDE1, PDE3, PDE5, or PDE9. Our results show that the NO-pathway produces less cGMP in D90 versus D30, that PDE3 regulation of NO-cGMP decreases with this maturation, that NP-cGMP regulation by PDE3 and PDE5 decrease after maturation, and that PDE2 and PDE3 regulation of β_3 -cGMP decreases in D90.

We then examine the effects of lipid depletion to remove caveolae on our previous experimental conditions and find that removal of caveolae results in a decrease in NO-cGMP response in D30 and D90 and an increased regulation by PDE2 and PDE9 in D30, that caveolae removal increases NP-cGMP production in both D30 and D90, and that caveolae removal enhances β_3 -cGMP production in D90.

Supporting our FRET studies, we examine the change in expression of relevant genes and proteins and find increases in PDE5A and ADRB3 as well as a decrease in PDE9A gene

expression from D30 to D90. Protein expression however only showed a decrease in PDE1C and PDE2A as well as an increase in PDE4B. Finally, we compare contraction and calcium handling dynamics between the experimental conditions of some of our FRET experiments using a new CytoCypher device, but surprisingly find no significant effect of our drugs.

In conclusion we provide a comprehensive characterisation of the regulation of cGMP and its change between D30 and D90 HiPSC-CM, as well as the tools and methods to dive deeper.

Acknowledgements

I am grateful to my three supervisors and would like to thank them for their continuous support and guidance. Firstly, Professor Julia Gorelik for her everlasting passion and fierce way of keeping me challenged. My second supervisor Professor Sian Harding for her impressive insights and thoughtful suggestions. And my third supervisor Doctor Chris Dunsby for his compassionate support, exceptional assistance with my writing and refreshing points of view. Finally, I want to thank Doctor Ivan Diakonov for his continual day-to-day mentorship and inexhaustive support wherever it was needed.

I want to express my deepest appreciation to the members of both Julia Gorelik's and Sian Harding's groups, who have made my time here into the most fun educational experience of my academic career and whose friendship has become indispensable to me.

Special thanks to all external collaborators, advisors, and providers of consumables, including but not limited to: N. Viacheslav, KW. Andressen, K. Jalink, A. Dufour, H. Kitaguchi.

Publications

A Software Tool for High-Throughput Real-Time Measurement of Intensity-Based Ratio-Metric FRET

*Authors: **Masoud Ramuz**, Alveera Hasan, Lena Gruscheski, Ivan Diakonov, Nikoleta*

Pavlaki, Viacheslav O. Nikolaev, Sian Harding, Chris Dunsby and Julia Gorelik

Cells. 2019 Nov 29;8(12):1541. doi: 10.3390/cells8121541. PMID: 31795419; PMCID: PMC6952787.

MultiFRET: A Detailed Protocol for High-Throughput Multiplexed Ratiometric FRET

*Authors: **Masoud Ramuz**, Ivan Diakonov, Chris Dunsby, Julia Gorelik*

Zaccolo M. (eds) cAMP Signaling. Methods in Molecular Biology 2022, vol 2483. Humana, New York, NY. https://doi.org/10.1007/978-1-0716-2245-2_3

Exploring the cGMP production pathways and their compartmentalisation within

HiPSC-derived cardiomyocytes

*Authors: Maria Faleeva, Ivan Diakonov, **Masoud Ramuz**, Xiaoli Lin, Thusharika Kodagoda, Nadja Bork, Prashant Srivastava, Kjetil Wessel Andressen, Viacheslav O Nikolaev, Sian E. Harding, Julia Gorelik.*

Paper in preparation.

Conferences and Scholarships

16-09-2019 London, UK | Nanodomains in cyclic nucleotide signalling: from mechanisms to therapeutic approaches

Contribution: Poster presentation titled “Development of a high-throughput multiplexed FRET system for study of cAMP/cGMP interplay in HiPSC-CM”

09-07-2019 London, UK | NHLI Postgraduate research day

Contribution: Poster presentation titled “Development of a high-throughput multiplexed FRET system for study of cAMP/cGMP interplay in HiPSC-CM”

7-06-2019 Tokyo, Japan | Research Visit Tokyo Tech-Imperial - Global Fellows Programme

A 3-week research visit to the Kitaguchi laboratory under Tokyo tech to exchange knowledge of FRET sensors creation and measurement. Bursary of £1200 paid by the Imperial International Relations office.

Contents

Declaration of Originality	2
Copyright Declaration	2
Abstract.....	3
Acknowledgements.....	4
Publications.....	4
Conferences and Scholarships	5
List of Tables	9
List of Figures	9
Glossary.....	11
Chapter 1: General Introduction.....	13
1.1. Human Stem Cell Derived Cardiomyocytes	14
1.1.1. HiPSC-CM Maturity	15
1.1.2. HiPSC-CM Maturation Techniques.....	27
1.2. Cyclic Nucleotide Proteins in Cardiomyocytes.....	46
1.2.1. cAMP in Cardiomyocytes	49
1.2.2. cGMP in Cardiomyocytes	50
1.2.3. Phosphodiesterases and Compartmentation	52
1.2.4. FRET Investigations of the cGMP Pathways.....	60
1.3. Tools and Techniques Used in cGMP Studies	62
1.3.1. Non-FRET Methods	63
1.3.2. FRET Tools and Methods.....	63
1.3.3. Other relevant tools and techniques	68
1.4. Hypotheses and Aims.....	69
Chapter 2: General Methods.....	72
2.1. Adult Mouse Cardiomyocytes isolation	73
2.2. Neonatal Mouse and Rat Cardiomyocyte isolation	73
2.3. Generating HiPSC-derived Cardiomyocytes.....	74
2.4. Sensors used	75
2.4.1. Sensors used: Validation experiments.....	75
2.4.2. Sensors used: cGMP studies	77
2.5. Transfection.....	78
2.6. FRET Experimental protocol.....	80
2.7. FRET calculations.....	80
2.8. FRET statistical analysis.....	81
Chapter 3: MultiFRET Development	83

3.1. Introduction	84
3.2. Methods.....	93
3.2.1. Multiplexed FRET System Design	93
3.2.2. Software development	93
3.2.3. QuadView-Based Microscopy System.....	94
3.2.5. Corrections and Analyses.....	96
3.2.6. Software Validation Through FRET	99
3.3. Results.....	99
3.3.1. MultiFRET Protocol	99
3.3.2. Software validation	128
3.4. Discussion.....	129
3.5. Limitations and Future Work	130
Chapter 4: Sensor Selection and Transgenic Line Development	132
4.1. Introduction	133
4.2. Methods.....	141
4.3. Results.....	145
4.4. Discussion.....	152
4.5. Limitations and future work	154
Chapter 5: Age-Dependent Compartmentation of cGMP signalling in HiPSC-CMs -role of PDEs ...	156
5.1. Introduction	157
5.2. Methods.....	160
5.3. Results.....	161
5.3.1. PDEi dose-response results.....	161
5.3.2. FRET PDEi D30 vs D90 in IMR-90 HiPSC-CM.....	166
5.3.3. FRET PDEi Untreated vs Caveolae Disruption through Cyclodextrin in IMR-90 HiPSC-CM	167
5.4. Discussion.....	176
5.5. Limitations and future work	180
Chapter 6: Analysis of Gene and Protein expression, Contractility, and Calcium Dynamics in D30 and D90 HiPSC-CM in relation to cGMP Pathways	182
6.1. Introduction	183
6.2. Methods.....	185
6.3. Results.....	188
6.5. Limitations and Future Work	197
Chapter 7: Final Discussion	199
7.1. Discussion and Conclusions	200

7.2. Limitations and Future Work	204
References	205

List of Tables

Table 1. HiPSC-CM electrophysiological phenotypes.	26
Table 2 FRET sensors used in this project.....	79
Table 3. cGMP sensors compared in this chapter	137
Table 4. Primers used in this work.....	142
Table 5. RT-qPCR primers.....	185

List of Figures

Figure 1 Brightfield and fluorescence imaging of D30 early stage hESC-CM	20
Figure 2 Proliferation rate, ANP expression, and action potential compared between early HiPSC-CM, late HiPSC-CM, and adult human CM	27
Figure 3 Transplantation of HiPSC-CM into neonatal rat hearts and subsequent extraction 3 months later results in partially matured HiPSC-CM.....	31
Figure 4. PDE families 1 to 9, showing structure, selectivity, and affinity.....	53
Figure 5. Schematic overview of PDE localised functions	54
Figure 6 Protocol for the differentiation of IMR-90 HiPSCs to cardiomyocytes, and replating for FRET experiments.....	76
Figure 7 ScGi plasmid with highlighted in orange the transcribed sensor and a schematic representation of the effect of cGMP binding to the FRET sensor.	78
Figure 8. Active Contours used with default settings save for the Export ROI and Type of ROI	90
Figure 9. Default automated Excel output from MultiFRET	90
Figure 10. Old method of single cell analysis vs new software.	92
Figure 11. Nikon TE2000 microscope hardware.....	94
Figure 12. A system of fluorophores, mirrors and filters that will work in conjunction while minimizing overlap between signals.....	96
Figure 13. Beamsplitter correction	98
Figure 14. Uniformly lit channels	104
Figure 15. An example of Active Contours pane with typical settings	105
Figure 16. Example of an Excel output workbook	107
Figure 17. Example MDA set-up.	112
Figure 18. An example of MultiFRET workspace	121
Figure 19. A possible error in cell-detection when using the automatic cell contouring function.....	127
Figure 20. Comparison of MultiFRET to the previously standard macro	128
Figure 21. Schematic representation of sensors used in this project	136
Figure 22. Schematic representation of the CRISPR/Cas9 method.....	140
Figure 23. Comparisons of FRET responses to cGMP production stimulants in HiPSC-CM ..	147
Figure 24. Comparisons of FRET responses to cGMP production stimulants in NRVM	148
Figure 25. Comparison between ScGi and CGES-DE5 sensors for cGMP	149

Figure 26. CRISPR-ready aavsCAGdest-TEV plasmid containing our TEV sensor for cAMP	Error! Bookmark not defined.
Figure 27 Test-cuts of aavsCAGdest-TEV using Xho-I	152
Figure 28. IMR-90 cell 2-days post transfection with aavsCAGtev and pXAT2	152
Figure 29. Dose-response of PDEs in FRET-sensor transfected HiPSC-CM cells with CNP stimulant	164
Figure 30. Dose-response of PDEs in FRET-sensor transfected HiPSC-CM cells with GSNO stimulant	165
Figure 31. D30 vs D90 PDE responses in FRET-sensor transfected IMR90 HiPSC-CM after stimulation with CNP	170
Figure 32. D30 vs D90 PDE responses in FRET-sensor transfected IMR90 HiPSC-CM after stimulation with GSNO	171
Figure 33. D30 vs D90 PDE responses in FRET-sensor transfected IMR90 HiPSC-CM after stimulation with ISO.....	172
Figure 34. D90 untreated vs D90 cyclodextrin PDE responses in FRET-sensor transfected IMR90 HiPSC-CM after stimulation with CNP	173
Figure 35. D90 untreated vs D90 cyclodextrin PDE responses in FRET-sensor transfected IMR90 HiPSC-CM after stimulation with GSNO	175
Figure 37. Successful and failed experiments for each age of HiPSC-CM	178
Figure 38. Expression of genes of interest measured in triplicates through RT-qPCR.....	191
Figure 39. D30 vs D90 Western blot protein expression	192
Figure 40. Representative trace of D30 HiPSC-CM PC and RMC baseline data.....	193
Figure 41. Representative trace of D90 HiPSC-CM PC and RMC baseline data.....	194
Figure 1. CytoCypher contraction (PC) and ratiometric calcium-handling (RMC) data measured from D90 HiPSC-CM	194

Glossary

%S	Percentage shortening
AC	Adenylyl cyclase
Ach	Acetylcholine
AKAP	A-kinase-anchoring protein
AKT	Protein kinase B
ANP	Atrial natriuretic peptide
ARVM	Adult rat ventricular myocyte
API	Application programming interface
BNP	Brain/B-type natriuretic peptide
CaMKII	Calmodulin kinase II
cAMP	Cyclic adenosine monophosphate
CAV3	Caveolin 3
CFL	Actin depolymerizing factor cofilin
cGMP	Cyclic guanosine monophosphate
CGP	CGP 12388
cGKI α	cGMP-dependent protein kinase isozyme α
CM	Cardiomyocyte
CNP	C-type natriuretic peptide
cTnI	Cardiac troponin-I
CUTie	Cyclic nucleotide Universal Tag for imaging experiments
ECM	Extracellular matrix
EHNA	erythro-9-(2-hydroxy-3-nonyl)-adenine
eNOS	Endothelial nitric oxide synthase
EPAC	The exchange protein directly activated by cAMP
ER	Endoplasmic reticulum
ESC	Embryonic stem cell
FORSK	Forskolin
FRET	Förster resonance energy transfer
GPCR	G-protein coupled receptor
HEK	Human embryonic kidney
hESC	Human embryonic stem cell
HFpEF	Heart failure with preserved ejection fraction
HiPSC	Human induced pluripotent stem cell
IBMX	3-isobutyl-1-methylxanthine
ICI	ICI 118,551
IGF-1	Insulin-like growth factor 1
ISO	Isoproterenol
LTCC	L-type calcium channels
MHC	Myosin heavy chain
MiR	MicroRNA
nNOS	Neuronal nitric oxide synthase
NO	Nitric oxide
NP	Natriuretic peptide

NPR	Natriuretic peptide receptor
NRVM	Neonatal rat ventricular myocytes
P/B	Peak divided by baseline
PC	Pixel correlation
PDE	Phosphodiesterase
PDMS	Polydimethylsiloxane
pGC	Particulate guanylyl cyclases
PKA	Protein kinase A
PKG	Protein kinase G
PLB	Phospholamban
RMC	Ratiometric calcium
ROCK	Rho-associated protein kinase
RT-QPCR	Real-time quantitative reverse transcription pcr
RV	Return velocity
RyR	Ryanodine receptor
sGC	Soluble guanylyl cyclase
SICM	Scanning ion conductance microscopy
SR	Sarcoplasmic reticulum
SRF	Serum response factor
SSH1	Slingshot protein phosphatase
TGF- β 1	Transforming growth factor-beta1
TnI	Troponin-I
TTP	Time to peak
T-tubule	Transverse tubule
VCL	Cytoskeletal protein vinculin
VTK	Visualisation toolkit
β -AR	β -adrenergic receptors

Chapter 1: General Introduction

1.1. Human Stem Cell Derived Cardiomyocytes

Study of human cardiomyocyte development and disease requires a suitable and easily ethically obtainable model. Near the end of the last millennium researchers made progress differentiating mouse fetal tissue through transplantation into infarcted tissue where the fetal-derived cardiomyocytes would survive and possibly improve cardiac performance (Soonpaa et al. 1994; Leor et al. 1996). Since human fetal tissue cannot ethically be obtained in adequate quantities for most purposes, clinical or scientific, researchers looked to ESCs as a sustainable model. ESCs are continuously growing pluripotent cells that are isolated from the inner cell mass of blastocysts and cultured on an embryonic fibroblast feeder layer. When isolated ESCs grow in absence of an embryonic fibroblast feeder layer, they spontaneously differentiate into cystic embryoid bodies (Evans & Kaufman, 1981; Martin, 1981; Robertson et al. 1983). These embryoid bodies, found to be polarized into two parts and appeared to be similar to the egg-cylinder stage of the 5-day embryo, can under the right conditions differentiate into beating muscle cells resembling those of the heart (Doetschman, Eistetter, and Katz 1985). They quickly develop responses to the effectors of the sympathetic and parasympathetic nervous system. ESC derived cardiomyocytes display structural and functional similarity to early-staged cardiomyocytes, with β -agonist ISO, FORSK and the phosphodiesterase inhibitor IBMX invoking positive chronotropic responses and the muscarinic agonist carbamylcholine invoking negative chronotropic responses (Kehat et al. 2001).

Despite successes in ESC driven research, the use of hESC has yet remained ethically controversial as well as logistically challenging to supply. Fortunately, in 2007 a landmark discovery showed that hiPSC could be derived from human somatic cells (Yu et al. 2007) and

human fibroblasts (Takahashi et al. 2007), and that these cells show remarkable similarity to hESC in terms of morphology and physiology (Narsinh, Plews, and Wu 2011). Soon thereafter an optimised protocol was developed for the differentiation of HiPSC into cardiomyocytes using modulation Wnt/ β -catenin signalling pathways (Lian et al. 2013).

1.1.1. HiPSC-CM Maturity

In this work I investigate a new method of assessing cardiomyocyte maturity through live cGMP measurements and set the groundwork for improving HiPSC-CM. Improving the creation of HiPSC-CM can open up a constant source of cardiac cells and their availability could drive a wide variety of drug testing, disease modelling, cell therapy and tissue transplantation methods. To this purpose I discuss here characteristics and existing methods of assessing maturation such as measurements of changes in gene expression, protein isoform switching, cardiomyocyte morphology, sarcomere development, changes in cell-membrane structural elements called t-tubules and caveolae, changes in calcium handling dynamics, mitochondrial development, and changes in electrophysiology.

1.1.1.1. *Gene Expression Changes During Cardiomyocyte Maturation*

Gene expression is often measured through RNA and protein assays, these studies have shown that HiPSC-CM compared to adult cardiomyocytes have a lower expression of calcium handling, ion transport and sarcomere associated genes (Lopaschuk and Jaswal 2010; Schaper, Meiser, and Stammler 1985). Systematic analysis of expression levels of cardiac proteins important for generation of action potentials and muscle contraction showed great differences between HiPSC-CM and the cardiomyocytes from the adult heart, with HiPSC-CM resembling immature stem-like cells more than mature cardiomyocytes (Kodama et al. 2019). RNA-seq studies provide that the cAMP pathway shows genetic

enrichment during maturation of HiPSC-CM with upregulation of ADRB1, ADRB2, the cardiomyocyte-specific adenylyl cyclase isoform ACY5. Furthermore, the sGC isoform GUCY1A3 was also found to be upregulated. Primary endothelial cells express NOS3, an endothelial cell specific nitric oxide synthase. Nitric oxide is known to be of importance to HiPSC-CM maturation and can activate the cGMP pathway through activation of the sGC (Giacomelli et al. 2020). Data regarding expression of the cGMP pathways between different stages of HiPSC-CM maturation are unfortunately lacking, in chapter 6 we perform qPCR and Western Blot on D30 and D90 HiPSC-CM to investigate these pathways as well as their compartmentation by PDEs in more detail.

Recently, a key regulator of cardiomyocyte regulation has been identified in serum response factor (SRF), depletion of which disrupts transcriptional regulation of sarcomere expansion, mitochondria biogenesis, T-Tubule formation, hypertrophy, lipid metabolism, and oxidative respiration. Furthermore, switches of key electrophysiological and Ca^{2+} handling genes to mature regulatory states were reversed, this includes the upregulation of Hcn4 and the downregulation of Kcnj2, Serca2a, and Ryr2 (Guo et al. 2018). Similarly, disruption of another gene important for sarcomere assembly, ACTN2, showed very similar maturational deficiencies and transcriptional changes (Guo et al. 2021). These findings allude to a conclusion on the hierarchy of the importance of aspects of cardiomyocyte maturation, wherein proper sarcomere maturation is required above most other aspects. SRF is regulated by three myocardin-family transcriptional regulators: MYOCD, MRTFA, and MRTFB (Posern and Treisman 2006). It has been suggested that a synergistic role of these three regulators is involved in SRF activation and subsequent cardiomyocyte maturation (Huang et al. 2009). Through this signalling axis, it has been suggested that physical stimuli such as mechanical stretch and ECM stiffness may be translated into stimulation of maturation

(Mendez and Janmey 2012). Another SRF-binding transcription factor, HOPX, is a newly found activator of cardiomyocyte maturation with strong roles in myofibrillar isoform switching and hypertrophy (Friedman et al. 2018). Knock-out of this gene is lethal for a portion of the transgenic mice, with survivors showing normal contractile function (Shin et al. 2002; Chen et al. 2002). One study found that overexpression of HOPX results in severe cardiac hypertrophy, fibrosis, and death. It was reported that an impairment of hypertrophic signalling caused by monolayer-based cardiac differentiation prevented HOPX expression, thereby preventing the activation of down-stream genes governing cardiomyocyte maturation (Friedman et al. 2018). This provides an interesting dilemma for established differentiation protocols and shows that work is required in the investigation of HOPX as a possible target for the maturation of hiPSC-CM.

1.1.1.2. Protein Isoforms Switching During Cardiomyocyte Maturation

It is further shown that during development several proteins important to the maintenance and function of the sarcomere change isoforms. For instance, Titin which is involved in integrity and elasticity of sarcomeres shifts from N2BA to a shorter and stiffer N2B isoform. In the post-natal left ventricle, N2B is the dominant isoform (Warren et al. 2004). Troponin-I, another myofibrillar protein family important in cardiac and skeletal muscle, binds to actin in thin myofilaments, preventing a myosin-actin connection from forming in relaxed muscle. Troponin-I has been shown to switch from predominantly being in the slow skeletal isoform (ssTnI) to cardiac Troponin-I (cTnI) in development from embryonic adult cardiomyocytes (Saggin et al. 1989). cTnI contains an extra pair of serine residues in its extended N-terminal sequence which are phosphorylated in response to adrenergic stimulation, mediated by cAMP-dependent PKA, and this results in altered contractile properties of the myocardium (Bhavsar et al. 1991). The troponin complexes with cTnI have been shown to be less

Ca²⁺ sensitive for tension production compared to ssTnI containing complexes, revealing a functional relevance to the transition during maturation (Siedner et al. 2003). MHC- α and MHC- β are proteins that are predominantly expressed in human cardiac atria, with minor expression in cardiac ventricles, and in the motor protein of muscle thick filaments (Wells, Edwards, and Bernstein 1996). MHC proteins are another example of proteins that switch from a MHC- β to an MHC- α from rodent fetal to adult hearts, paired with a post-natal increase in heart rate (Mahdavi et al. 1984). In human hearts however, there is more MHC- β than MHC- α throughout development but an overall larger amount of MHC- α in fetal hearts than in adults, correlating with a post-natal increase in heart rate (Xiu et al. 2009).

1.1.1.3. Changes in Cardiomyocyte Morphology During Cardiomyocyte Maturation

While hiPSC-CM are routinely obtainable, there are many discrepancies of characteristics important to cardiomyocyte function between those of adult and hiPSC-derived. One of the most widely studied characteristics of cardiomyocytes is the cell morphology. The volume, length and cross-sectional area measurements of healthy human adult cardiomyocytes were first reported in 1992 and compared to ischemic cardiomyocytes. This study found that left ventricular human cardiomyocytes have a length/width ratio of 7:1 (Gerdes et al. 1992), a ratio that is observed in rats, hamsters, guinea pigs, cats and ferrets (Campbell, Gerdes, and Smith 1987; Kozlovskis et al. 1991; Smith and Bishop 1985). They also found that in the adult hypertrophic ischemic patient derived cardiomyocytes show a 49% higher length/width ratio.

The size of cardiomyocytes is also of importance to their function, as the cell capacitance that drives the action potential behind the contraction of a cardiomyocyte increases with its size from 17.5 ± 7.6 pF in hESC-CM (Zhu et al. 2010) to roughly 150 pF in healthy adult

ventricular cardiomyocytes (Drouin et al. 1995). Indeed the morphology of cardiomyocytes strongly influences maximal rate of action potential depolarisation, but also impulse propagation and total contractile force (Spach et al. 2004). While adult and even neonatal cardiomyocytes retain their rod shaped morphology (Louch, Sheehan, and Wolska 2011), truly immature cells such as those derived from stem cells flatten and spread in all directions, and thus have irregular shapes (Mummery et al. 2003; Mummery et al. 2012).

1.1.1.4. Sarcomere Characteristics and Changes During Cardiomyocyte Maturation

An important element of a cardiomyocyte's internal structures is the sarcomere, the fundamental unit for contraction of cardiomyocytes in striated muscle, it provides an angle for the assessment of functional maturity. The contractile apparatus of the sarcomere lies in the longitudinally repeated cytoskeletal structures called myofibrils (Henderson et al. 2017; Gautel and Djinović-Carugo 2016). In mature sarcomere the myofibrils are comprised of thin filaments, thick filaments, titin filaments, Z-lines composed of actinin and M-lines composed of myomesin. When activated through ATP hydrolysis, M-lines enable thin filaments to pull thick filaments towards the Z-lines, resulting in a contraction (Agarkova and Perriard 2005). Sarcomere assembly begins after cardiomyocyte differentiation and markers include α -actinin, cardiac troponin-T, cardiac troponin-I, and MHC (Bird et al. 2003). Although the presence of sarcomeres and expression level of sarcomeric proteins such as alpha-actinin, beta-myosin heavy chain, cardiac troponin T and cardiac troponin I can be used as a basic assessment of specialisation of HiPSC-CM, these proteins can be found quite early on and should not be used as the only measurement of HiPSC-CM maturity (Zhang et al. 2009). Electron microscopy (Gherghiceanu et al. 2011) as well as alpha-actinin staining (Yang, Pabon, and Murry 2014) show that the sarcomere is disorganised in HiPSC-CM, but aligned along the length of the cell in adult cardiomyocytes. The sarcomere organisation and length

of approximately 2.2 μm in a relaxed adult cardiomyocyte facilitates force-generation and supports the cardiomyocyte structure (Bird et al. 2003). In HiPSC-CM the sarcomere is only around $1.65 \pm 0.02 \mu\text{m}$ in length at 30 days past the start of differentiation, but has been shown to grow towards the adult phenotype in both a length of 1.81 ± 0.01 and organisation that follows the larger and more rod-shaped day 100 HiPSC-CM (Figure 2). Furthermore, the day 100 HiPSC-CM show other characteristics similar to adult cardiomyocytes such as a greater myofibril density, Z-disks, multinucleation, A- and I- bands as well as H-zones in the sarcomere but no clear M-zone (Lundy et al. 2013).

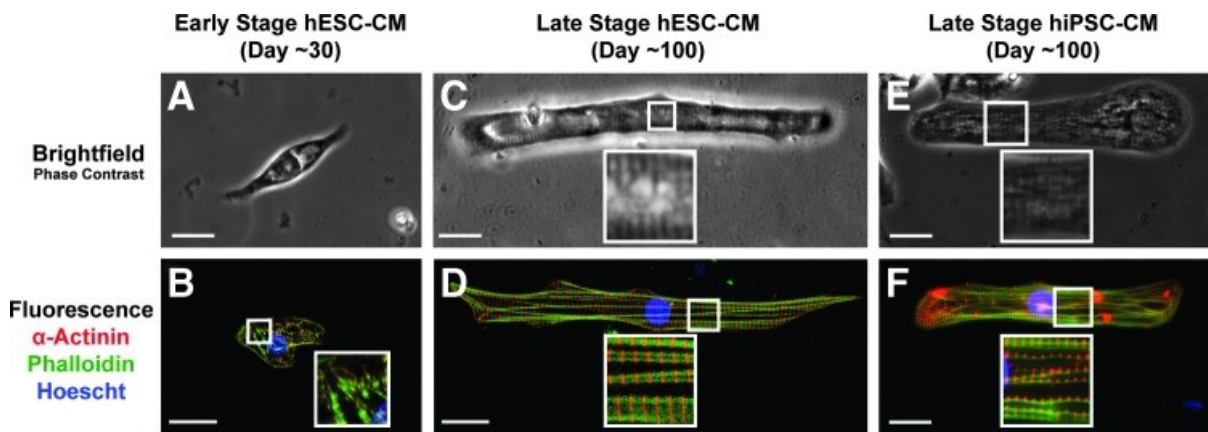


Figure 2 Brightfield and fluorescence imaging of D30 early stage hESC-CM (A, B), D100 late stage hESC-CM (C, D), and D100 late stage HiPSC-CM (E,F) modified from (Lundy et al. 2013).

1.1.1.5. Transverse Tubule and Caveolae Structure Changes During Cardiomyocyte Maturation

Proper contractility stems from the T-tubules, which form as ion channel rich membrane invaginations along the Z-line regions and allow the cardiomyocyte to develop rapid electric excitation and synchronous triggering of the SR calcium release. The T-tubules are spaced regularly at 2 microns along the longitudinal axis of adult mammalian ventricular cardiomyocytes as a hallmark of cardiomyocyte development, and key representative of

excitation-contraction coupling (Ziman et al. 2010; Robertson, Tran, and George 2013). Responsible for the excitation-contraction coupling are LTCCs, which are long lasting voltage activated calcium channels passing inward Ca^{2+} current which then triggers calcium release from the SR by activating the RyRs for what is known as calcium-induced-calcium-release. LTCCs can further increase contractility of cardiomyocytes after phosphorylation induces enhanced permeability (Yamakage and Namiki 2002). It was recently shown that failing cardiomyocytes incur a relocalisation of LTCC to the crest, an enhanced LTCC open-probability, and an enhancement of CaMKII activity. It was theorised that disruption of T-tubules in HF leads to LTCC redistribution to the crest where they are susceptible to phosphorylation by CaMKII, dramatically increasing their open-probability resulting in development of arrhythmogenic early afterdepolarisations. A CaMKII inhibitor experiment had shown that LTCC in control cells or localised to T-tubules were not affected by the inhibitor, indicating that the increase in CaMKII activity only had an effect on the LTCC in the failing myocyte crest (Sanchez-Alonso et al. 2016). Importantly, redistributed LTCCs are no longer co-localised with RyRs and stop contributing to ECC.

T-tubule-like structures first appear in neonatal rat cardiomyocytes 6 to 9 days after birth, at 12 to 14 days these cardiomyocytes will contain T-tubules extending to the cell interior and one month after birth the T-tubule system will resemble adult cardiomyocyte patterning. In hESC-CMs however, very few to no t-tubules are found 40 days post initial beating and these cardiomyocytes display unsynchronised Ca^{2+} transients as well as non-uniform calcium dynamics (Satin et al. 2008; Lieu et al. 2009). Another form of membrane invaginations is the caveola, relatively small 50-80 nm cup-shaped invagination of the plasma membrane, which resembles the t-tubule in its variety of surface receptors. Both T-tubules and caveolae are thought to be regulated by various caveolin scaffolding proteins, most

notable of which is CAV3 thought to regulate plasma membrane invagination (Parton et al. 1997). However, T-tubules still form in *Cav3*-knockout mice (Bryant et al. 2018). It is theorised that Cav3 works in conjunction with other proteins notably Cav1, which can generate caveolae when expressed without other accessory proteins, and Cavin1 which is deemed essential for caveolae formation (Parton, McMahon, and Wu 2020). Additionally, T-tubules and caveolae in healthy adult cardiomyocytes contain β_2 -adrenoceptors which upon stimulation increase contractility through a cAMP second messenger cascade. In heart failure, these β_2 -ARs redistribute to the inter-groove or membrane crest, resulting in a delocalised cAMP signal (Nikolaev et al. 2010; Lyon et al. 2012). T-tubules and caveolae have been found to be absent from both stem cells and neonatal cardiomyocytes, though maturation can induce the formation of these structures (Ibrahim et al. 2011). CAV3 has been shown to have a crucial role in controlling cAMP signalling nano-domains in ventricular cardiomyocytes (Loucks, O'Hara, and Trayanova 2018). The effect of caveolae on cAMP compartmentation in HiPSC-CMs of different ages was investigated as part of a study investigating the use of cAMP pathways for assessment of HiPSC-CM maturity. It was found that aging of HiPSC-CMs from D30 to D90 specifically increases the caveolae content, and the removal of caveolae in D90 had a positive effect on the detectable cytosolic cAMP produced through β_2 -AR but not β_1 -AR stimulation (Hasan et al. 2020). This illustrates the advanced structural compartmentation of cAMP in D90 HiPSC-CMs in comparison to D30 HiPSC-CMs, and reveals that β_2 -AR are only redistributed to these structural elements after aging. In chapter 5 we investigate the role of caveolae in the compartmentation of cGMP by applying the same experimental methods.

1.1.1.6. Calcium Handling Dynamics Change During Cardiomyocyte Maturation

Calcium handling is one of the most important and widely characterised functional parameters in assessing maturity of both natural and hiPSC-CMs. It has been shown that hiPSC-CMs express proteins important in Ca^{2+} handling as well as showing Ca^{2+} transients (Liu et al. 2007; Satin et al. 2008; Germanguz et al. 2011; Itzhaki et al. 2011; Zhu, Santana, and Laflamme 2009). Another study however, using ESC derived cardiomyocytes, indicated that the transients and contraction were insensitive to drugs that modulate Ca^{2+} release and re-uptake by the SR (Dolnikov et al. 2006). A protein expression analysis in the same study had further shown that calsequestrin and phospholamban, key SR regulatory proteins, could not be detected in either hiPSC-CMs nor hESC-CMs, suggesting that the rise in Ca^{2+} transients comes mainly from trans-sarcolemmal entry and not so much from the internal Ca^{2+} stores. However, there are studies that support the notion that hiPSC-CMs have functional SR Ca^{2+} stores and that in an early stage of hiPSC-CM maturation a tightly localised control of excitation-contraction coupling is established (Satin et al. 2008; Zhu, Santana, and Laflamme 2009). More recent studies show support that hiPSC-CMs have functional SR-dependent handling of Ca^{2+} by identifying expression of key regulatory proteins such as calsequestrin (Germanguz et al. 2011; Itzhaki et al. 2011).

1.1.1.7. Mitochondrial Activity Changes During Maturation

The mitochondrial presence undergoes a significant transformation from immature to mature cardiomyocytes. In early stages mitochondria are distributed in the cytoplasm as a reticular network that accounts for a fraction of the cell volume. Early stage mitochondria have an inner membrane without well-formed cristae (Shepard, Muffley, and Smith 1998), have a low oxidative capacity and use glycolysis as their main source of energy (Lopaschuk and Jaswal 2010). As the cardiomyocytes mature the permeability transition pore, which

leads to cell death in adults but lies open in embryonic mice cardiomyocytes (Crompton, Ellinger, and Costi 1988), closes and leads to increased mitochondrial length, membrane potential and decreased reactive oxygen species production (Hom et al. 2011). Thereafter development proceeds with the formation of mature and regularly distributed lamellar cristae, increase in mitochondrial volume to match 20-40% of the adult cardiomyocyte, distribution of mitochondria throughout the cell in a crystal-like lattice pattern, and a switch to fatty acid β -oxidation as the energy source (Lopaschuk and Jaswal 2010; Schaper, Meiser, and Stammler 1985). Conversely, HiPSC-CMs have long, slender, glycolysis dependent mitochondria that are clustered next to the nucleus or cell periphery (Lopaschuk and Jaswal 2010; Schaper, Meiser, and Stammler 1985). The development of mitochondria throughout aging-dependent maturation of HiPSC-CMs has been characterised in terms of increased mitochondrial relative abundance, enhanced membrane potential, and increased activity of several mitochondrial respiratory complexes. Comparisons of day 25 and day 40 with day 100 HiPSC-CMs revealed that mitochondria improve maturity along-side other cellular components. However, 100 days of aging did not allow mitochondria to reach the same characteristics as those from fetal heart cells (Dai et al. 2017).

1.1.1.8. Electrophysiological Changes During Cardiomyocyte Maturation

Two fundamental measurements to determine cardiomyocyte maturity are the electrophysiology and ion channel function. The action potential that is the direct cause for contraction in cardiomyocytes is generated out of the orchestrated activity of several types of ionic channels on the cell surface. These functions change over development, while the resting membrane potential sits around -90 mV in adult cardiomyocytes, immature cells show a membrane potential of 60 mV as well as lower levels of sodium channel Nav1.5 and the LTCC leading to slower upstroke velocity and shorter plateau phase respectively (Drouin

et al. 1995; Kléber and Rudy 2004; Blazeski et al. 2012). Sarcomere contraction and membrane depolarisation are linked through T-tubules transferring the signal to the SR, which results in Ca^{2+} release. This Ca^{2+} binds to troponin and changes its conformation, removing the blocking action of tropomyosin, and allowing myosin and actin to interact with each other, resulting in sarcomere contraction. During diastole, Ca^{2+} is removed from the SR via SERCA2, and from the cell via an Na^+ - Ca^{2+} exchanger. Action potentials of single cardiomyocytes derived from HiPSC have been recorded and found to fit three phenotypes: nodal-, atrial-, or ventricular-like (Table 1). Action potentials in immature HiPSC-CMs which have ventricular-like action potentials have a maximum diastolic potential values close to -60 mV (Haase et al. 2009; Fujiwara et al. 2011), though blasticidin-enriched cardiomyocytes go down to -75 mV (Ma et al. 2011), which is closer to the resting potential of adult ventricular cardiomyocytes at -87 mV (Drouin et al. 1995). This resting potential is maintained by the inward rectifying current I_{K1} (Guo and Pu 2020). Action potential amplitude in HiPSC-CM ranges from 85 to 105 mV (-90 mV in adult), maximum upstroke velocity (dV/dt_{max}) in HiPSC-CM ranges from 10 to 40 V/s (120 to 160 V/s in adult), and HiPSC-CM action potential duration at 90% repolarisation ranges from 300 to 400 ms (400 ms in adult)(Zhang et al. 2009; Spach et al. 2004; Karbassi et al. 2020). The slower upstroke velocity measured in HiPSC-CMs is a result of lower expression of SCN5A and other sodium channels (Haufe et al. 2005; Yu et al. 2011), while the longer action potential is partly due to higher expression of cav1.2 (Qu and Boutjdir 2001). Overall, as cardiomyocytes grow out of early developmental stages there is a shift from a cellular physiology in which there are high proliferation rates and a characteristically immature action potential (Figure 3). Structurally, in immature cardiomyocytes where the sarcomeres are closely located to the plasma membrane, the Ca^{2+} released there is enough to trigger sarcomere contraction. As

cardiomyocytes mature, the distance increases along with their size and the development of t-tubules is required to trigger contraction in the now more distant sarcomeres (Robertson, Tran, and George 2013).

Table 1. HiPSC-CM electrophysiological phenotypes. These percentages are similar to those in hESC-CMs, and to optical mapping measurements from our labs that found predominantly ventricular-like potentials for both hESC-CMs and HiPSC-CM (Burrige et al., 2011).

Table 1

Proportion of principal cellular electrophysiological phenotypes in hiPSC-CM cultures

N	Cell Line(s) (all from fibroblasts)	% Nodal- like	% Atrial- like	% Vent- like	Quantitative criteria ^a	Reference
23	fetal IMR90 C4	13	13	74	No	(Zhang et al., 2009)
20	newborn foreskin C1	20	10	70	No	(Zhang et al., 2009)
29	fetal IMR90 and adult dermal KS1	45	17	38	No	(Lee et al., 2011)
59	reprogrammed human fibroblast line	22	24	54	Yes	(Ma et al., 2011)

Notes:

^aQuantitative criteria are those using numerical values of AP parameters to distinguish different phenotypes.

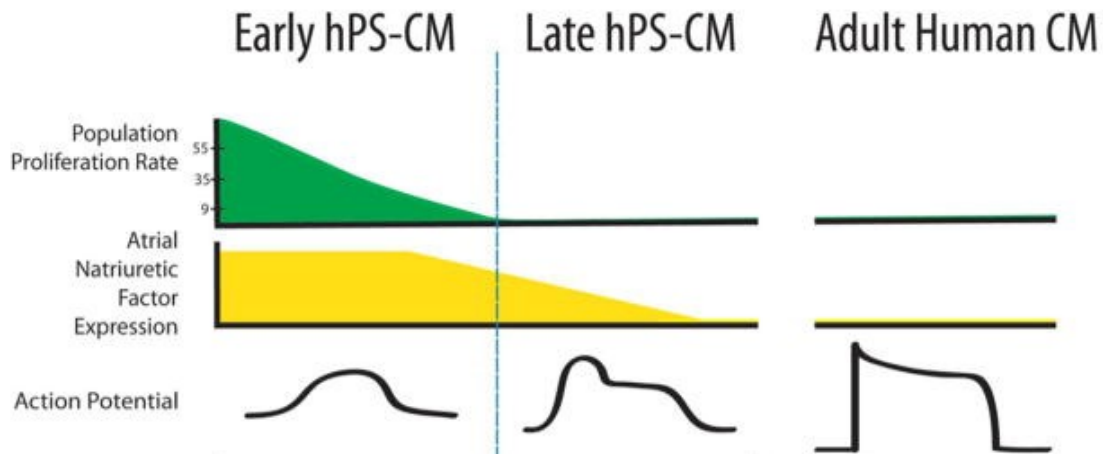


Figure 3 Proliferation rate, ANP expression, and action potential compared between early HiPSC-CM, late HiPSC-CM, and adult human CM. Image modified from Robertson, Tran, and George 2013.

1.1.2. HiPSC-CM Maturation Techniques

There have been a wide variety of studies targeting the many inadequacies of HiPSC-CMs and though no single or combination of techniques has yet yielded HiPSC-CM that match the structure and function of mature cardiomyocytes, there are many recent and promising advancements in the field which will be discussed in this section. The most commonly used method is the long-term culture, which we also apply in our aging experiments. We further discuss the use of co-culture with non-cardiomyocyte cells, in-vivo maturation, plating HiPSC-CM on altered substrates, patterning, tissue engineering, mechanical loading, biochemical stimulation, metabolic maturation, and electrical stimulation.

1.1.2.1. Long-Term Culture of HiPSC-CM

The generation of beating cardiomyocytes from HiPSC takes less than 15 days (Laflamme and Murry 2011), a fraction of the 6 to 10 years human neonatal cardiomyocytes take to reach adult phenotype in vivo (Peters et al. 1994). Over time in serum-free medium the cells undergo processes of ultrastructural maturation, cell-cycle and withdrawal, which results in

autonomous hypertrophy over a 35 day culture period (Snir et al. 2003; Földes et al. 2011). Phenotypical changes over a 120-day incubation include cell size, sarcomere length, anisotropy, and frequency of multinucleation. Paired with these developments came functional changes such as an increased shortening magnitude of a slower contraction, and increased calcium uptake and release (Lundy et al. 2013). Changes in electrophysiological characteristics found during incubation up to 90 days include developmental maturation of the transient outward and inward rectifier potassium currents, the calcium current, the pace-making current (Sartiani et al. 2007), hyperpolarized maximum diastolic potentials, increased action potential amplitudes, and faster upstroke velocities (Lundy et al. 2013). Over this incubation period spontaneous beating rate has either increased or decreased depending on culture conditions (Hazeltine et al. 2012; Földes et al. 2011), conduction velocity was significantly upregulated (Kadota et al. 2013), but there was no increase in generation of contraction stress (Kita-Matsuo et al. 2009). Finally, the M-band, an important characteristic of structurally maturing sarcomeres, was seen after 1 year of incubation (Kamakura et al. 2013). These changes brought on by long-term culture imply the existence of time-dependent developmental mechanisms. While maturity is improved on a functional level, the prolonged experimental time is an issue that has led scientists to study other solutions.

1.1.2.2. Co-Culture with Non-Cardiomyocyte Cells Enhances hiPSC-CM Maturity

While cardiomyocytes take up over 70% of the volume of cardiac tissue, numerically they are at most 30% of the cells (Bergmann et al. 2015; Pinto et al. 2016; Zhou and Pu 2016). Non-cardiomyocytes in cardiac tissue consists of 64% endothelial cells, 27% cardiac fibroblasts, and 9% leukocytes (Bergmann et al. 2015). Development of cells in vivo is guided by many factors, including interactions with the surrounding cells. The use of co-culture has been

studied for the differentiation into and maturation of cardiomyocytes as well, using endothelial and stromal cells to increase the proliferation and development of cardiomyocytes and vascular structures (Tulloch et al. 2011; Kim et al. 2010). The effects of non-cardiomyocytes on cardiomyocyte maturation are caused by paracrine stimulation, physical adhesion, fibroblast construction of coronary vasculature, and the secretion of extra-cellular matrix (Yoshida et al. 2018; D. S. Lee et al. 2015; Kim et al. 2010). One study found that hESC-CMs co-cultured with non-contractile slices of neonatal rat ventricle resulted in spontaneously beating clusters that respond to extracellular Ca^{2+} with increased beating rates (Pillekamp et al. 2012). Similarly, another study adding human fibroblasts and mesenchymal stem cells to hESC-CM at a rate of 3% of total cell number found increased twitch force, sarcomeric alignment, regularly dispersed N-Cadherin and Cx43, and an upregulation of maturation-associated genes (Zhang et al. 2017).

1.1.2.3. In-Vivo Maturation by grafting hiPSC-CM into living tissues

We have already discussed the importance of co-culture with non-cardiomyocyte cells in maturation, alluding to the environment of developing cardiomyocytes in vivo. Halbach et al. 2007 grafted GFP-transgenic murine fetal cardiomyocytes (D12.5 – D15.5) into healthy and cryoinjured areas of adult murine hearts, then used glass micro-electrodes to measure electrophysiological properties at stimulation frequencies up to 10 Hz. Cells transplanted into cryo-injured areas showed spontaneous electrical and contractile activity, asynchronous to host tissue. Meanwhile 82% of fetal cardiomyocytes transplanted into healthy regions were electrically integrated, showing electrical and contractile activity synchronous to that of the host tissue (Halbach et al. 2007).

More recently, a similar study was performed with transplantation HiPSC-CM into neonatal and adult rat hearts for 3 months, hypothesising that the developing neonatal heart would grow the HiPSC-CM as it develops into an adult heart (Kadota et al. 2017). Partially matured myofibrils, increased cell size and sarcomere length were found in the neonatally grafted cells. An infarction of adult heart only further increased cardiomyocyte hypertrophy and cardiac troponin I expression. Interestingly, at the end of the 3 months, transplanted neonatal rat cardiomyocytes had reached an adult size and structure, while the HiPSC-CM were still significantly smaller and underdeveloped (Figure 4). This indicates an environmental mismatch brought on by disparities between the species and may hint towards more successful results if the HiPSC-CM were matured within a human heart, though a more likely solution will lie in the perfection of biomimetic environments. A further consideration is that HiPSC-CM matured in rat hearts exhibit more binucleation (80% vs 25-57% in humans) than adult human cardiomyocytes (Ruan et al. 2015; Olivetti et al. 1996), raising the question of whether the matured cells are becoming more rat-like (Cho et al. 2017).

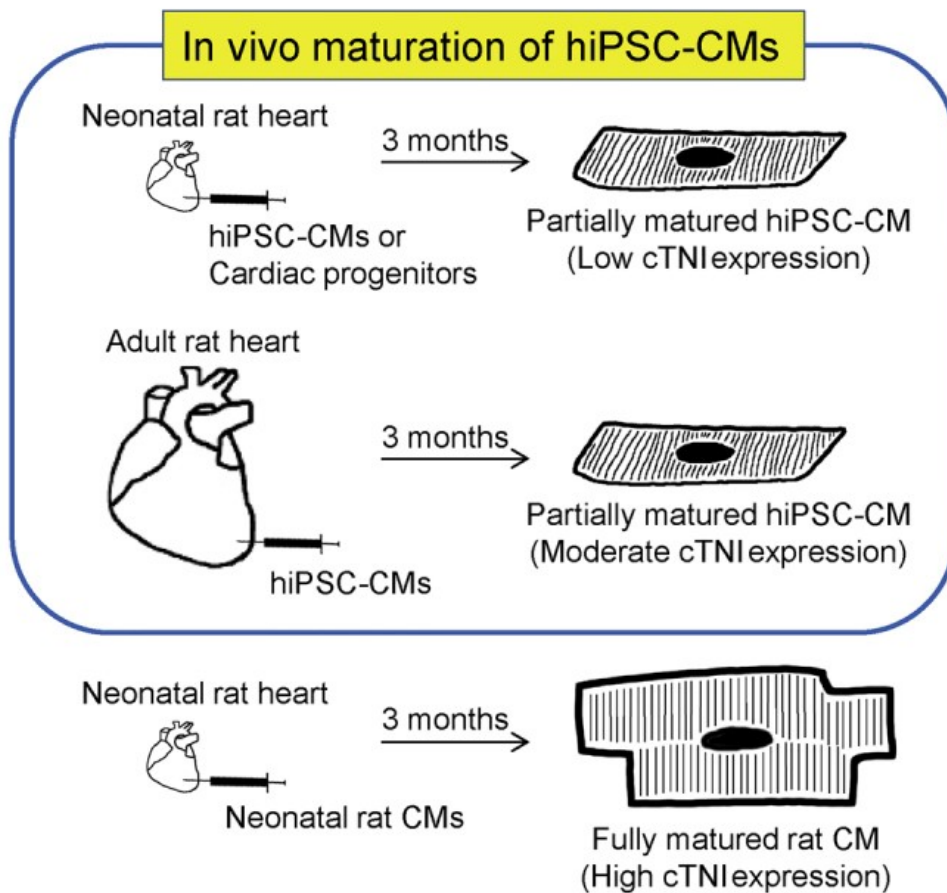


Figure 4 Transplantation of HiPSC-CM into neonatal rat hearts and subsequent extraction 3 months later results in partially matured HiPSC-CM. Image modified from Kadota et al. 2017.

1.1.2.4. Altering Substrate Stiffness and Composition to Enhance HiPSC-CM Maturity

An important factor which is partly regulated by non-cardiomyocyte cells in vivo is the environment of the cardiomyocyte, namely the ECM. The stiffness of myocardial ECM increases starting from the embryonic development stage and until several weeks after birth, with accumulation of collagen and other changes inducing a 3-fold increase in elasticity modulus in neonatal mice ECM (Jacot, Martin, and Hunt 2010) and 2-fold in neonatal rat ECM (Prakash et al. 1999). The stiffening of the myocardium coincides with

increases in blood pressure and pumping capability. Studies investigating the use of artificial ECM in the maturation of cardiomyocytes plate cells on various surfaces. Studies using NRVMs or hESC-CMs on a collagen-coated polyacrylamide gel with varying elastic moduli found significantly enhanced maturation reflected by increased sarcomere alignment, mechanical force, calcium transients, and calcium-ATPase 2a found in the sarco- or endoplasmic reticulum (Jacot et al. 2010; Jacot, McCulloch, and Omens 2008). The increased contractile force was attributed to activation of the RhoA/RhoA-kinase (ROCK) pathway (Jacot, McCulloch, and Omens 2008). Rodriguez et al. developed a method growing NRVMs on flexible posts of varying stiffness, and measuring the contractile force of these cells through high-speed line scanning (Rodriguez et al. 2011). With this method it was found that NRVMs had an up to 6-fold greater twitch force paired with a slower twitch velocity when cultured on stiffer substrates, this was reflected by more mature myofibril structures boasting greater sarcomere length and Z-band width. Furthermore, cells performing a twitch on stiffer substrates showed higher intracellular calcium levels compared to those on softer substrates. While a positive correlation between post stiffness and contractile force was found, there was also a negative correlation between the post stiffness and degree of alignment. The effects of substrate stiffness were corroborated by studies tracking fluorescent beads embedded in two-dimensional polyacrylamide hydrogels of 4.4 to 99.7 kPa stiffness. NRVMs (Bhana et al. 2010) as well as HiPSC-CMs (Hazeltine et al. 2012) cultured on these gels generated greater force with greater stiffness. For unclear reasons however, contrastingly one study by Hazeltine et al. found mature myofibril structures at all levels of stiffness. A more recent study used fetal chicken cardiomyocytes on a time-dependent thiolated hyaluronic acid hydrogel, which crosslinked with poly ethylene glycol diacrylate became stiffer from 1.9 to 8.2 kPa (Young and Engler 2011). Compared to static

polyacrylamide gels, cells grown on the hyaluronic acid gels which stiffen over time showed a downregulation of early cardiac marker NKX2.5. Additionally, these cells showed a 3-fold increase in troponin-T, a late cardiac marker.

1.1.2.5. Patterning of hiPSC-CM in Culture to Enhance Maturity

In vivo cardiomyocytes grow in an environment of physical stimuli including topographical cues such as striated tissue containing myofibrils, Z-bands and sarcomeres. These surface structures keep the cardiomyocytes elongated and rod-shaped. A study by Bray et al. 2008 has used polydimethylsiloxane (PDMS) polymer stamps designed for microcontact printing to create patterned and un-patterned ECM islands (Bray, Sheehy, and Parker 2008). Cells seeded on these ECM islands would take on shapes corresponding to the pattern of the stamp. NRVMs cultured on rectangular patterned ECM islands with 7:1 aspect ratio would take to a rod shape, their sarcomeres similarly were directed into a longitudinal pattern more similar to those of in vivo cardiomyocytes, their myofibril filaments aligned parallel to the longitudinal axis of the cell, with increasing density of filaments closer to the edges of the gel, and Z lines perpendicular to the longitudinal axis. It has been shown that cells grown on patterned substrates have significantly enhanced cell alignment (Heidi Au et al. 2009; Wang et al. 2011). It has been found that NRVMs seeded to microprinted lanes exhibit a bipolar localisation of N-cadherin and Cx43 resembling intercalated disk (McDevitt et al. 2002). Several studies have used an anisotropically nanofabricated substratum with polyethylene, the polyethylene layer was glycol-patterned with ridges and grooves simulating the structure of myocardial ECM (Heidi Au et al. 2009). While a single plated cardiomyocyte would cover at least 10 of these nano-ridges, the cells still aligned in the same orientation as these structures. Aligned cells would exhibit conduction velocities, Cx43 expression and cell geometry closer to that of the adult heart. Additionally, a study testing

varying depths and widths used 8-100 μm in width and 5-1000 nm in depth of the grooves. It was found with increasing depth (8-30 μm wide and 850-1000 nm deep) hiPSC-CMs would increase in alignment, elongation, and contractile function, with a maturation indicative average sarcomere length of 1.8 μm (Huethorst et al. 2016). Studying these effects further it was found that grooves with a width of 600-900 nm produce the greatest maturation of hiPSC-CMs, reflected by increased cell size, elongation, and anisotropic structure (Carson et al. 2016). Combining the topographical orientation of NRVMs with varying substrate stiffness showed that while orientation was mainly influenced by nano-grooved gels, contraction was regulated by both surface topography and a softer substrate (Wang et al. 2011). More recent studies have compared gels stamped with anisotropic, isotropic and line surface topographies (Feinberg et al. 2007, 2012). Isotropic patterning leads to unaligned sarcomeres with lower peak sarcomere generated stress, slower Ca^{2+} cycling, and a shortening of conduction velocities. Contrastingly, gels with line and anisotropic surface topography show a more mature phenotype with aligned sarcomeres, uniaxial myofibrillar alignment, contractile cytosolic stresses over 10kPa, faster Ca^{2+} cycling, and larger transients. Other recent approaches investigated the effect of cardiomyocyte shape on contractility and sarcomere alignment. One study used polyacrylamide gels with aspect ratios ranging from 1:1 to 11:1, finding that contractility is optimised at the 7:1 ratio found in vivo and decreases with cell morphologies associated with failing hearts (Kuo et al. 2012). Interestingly, higher ratios were found to affect calcium metabolism, prolonging calcium transient durations in a similar manner to diastole prolongation in rodent models of congestive heart failure. These findings show a link between the maturation of morphology and physiology of cardiomyocytes, in that cardiomyocyte shape alters both myofibrillar structure and calcium handling. Another approach employs use of a micro-electrode array

coated with fibronectin and gelatin (Pijnappels et al. 2008). This coating is then micro-abraded parallel or perpendicular to the flow of the current. NVRMs showed the highest conduction velocity in the perpendicularly scraped dish, while the dish with parallel striations showed a high Cx43 expression.

1.1.2.6. Tissue Engineering Using 3-D Culture Methods to Enhance HiPSC-CM Maturity

The myocardium is composed of a 3-dimensional (3-D) arrangement of rod-shaped cardiomyocytes as myofibers, which are influenced by surrounding interstitial fibroblasts, blood vessels, and ECM. Researchers have devised methods to combine physio-mimetic cues through the creation of 3-D polycaprolactone fibrous scaffolds with anisotropic patterning. Similar to cardiomyocytes grown on 2-D patterned surfaces, those grown in the 3-D aligned microenvironments exhibit morphology, alignment, gene expression and calcium handling more akin to mature cardiomyocyte tissue (Han et al. 2016). One major aspect of in vivo myocardial tissues that was yet missing was the mechanical load brought on by the constant cyclic strain of rhythmic heart beating. An experiment by Zimmerman et al. seeded NRVMs into 3-D matrixes of collagen I hydrogels plus basement membrane proteins (Zimmermann et al. 2002). These hydrogels were then subject to rhythmic mechanical stretch, and after 14 days the effects of this repeated stress on cardiomyocyte maturation were assessed. They found that the engineered NRVMs were interconnected into longitudinally oriented cardiac muscle bundles resembling adult heart tissue, had well-developed t-tubule networks, and dyad formation with the sarcoplasmic reticulum (SR). The tissue embedded within this matrix exhibited a high twitch to resting tension ratio, a strong β -adrenergic response, as well as action potentials with more mature characteristics: faster upstroke, prominent plateau phase, lower resting membrane potential. This method has been touted to grow NRVMs closest to adult cardiomyocytes in morphology and

electrophysiology (Yang, Pabon, and Murry 2014). Building on this methodology, Liau et al. added elliptic pores to tissue patches on which mouse ESC-CMs were seeded (Liau et al. 2011). These pores enhanced oxygen and nutrient diffusion, and aligned the tissue into a functional 3-D syncytium when supplied with non-myocytes, purified cardiovascular progenitors differentiated into cardiomyocytes, smooth muscle cells, and endothelial cells. Cardiomyocytes in the syncytium were dense, uniformly aligned, electromechanically coupled, with contractile force up to 2mN, and have conduction velocities between 22 and 25 cm/s. Comparably, neonatal mouse cardiomyocytes have conduction velocities of approximately 29 cm/s (Vaidya et al. 2001), while adult mice hearts have 62 cm/s (Gutstein et al. 2001).

Eventually the hydro-gel based 3-D tissue engineering methods were applied to hiPSC-CMs, to generate engineered human tissues (Tulloch et al. 2011). The hiPSC-CMs were cast in a 3-D collagen matrix including 11% mouse basement membrane extract and 57% human embryoid body medium, which was then subjected to uniaxial mechanical stress. This mechanical loading significantly increased proliferation rate (21%), alignment and size (2.2-fold) of cardiomyocytes. Furthermore, addition of endothelial cells enhanced proliferation by 14% to 19%, and addition of stromal supporting cells enhanced formation of vessel-like structures by approximately 10-fold. They found that their constructs generate Frank-Starling curves, which describe a ratio of myocardial fibre length to contractile force where this force is maximal at a certain length (Delicce and Makaryus 2018). Transplantation of these tissues into athymic rats resulted in the formation of grafts closely apposed to host myocardium, with human micro-vessels that are perfused by host coronary circulation. A 2013 study developed a biowire system, a platform that combines architectural and electrical cues into a micro-environment that matures cardiomyocytes derived from 3-D

tissues (Nunes et al. 2013). hiPSC-CMs and supporting cells from directed differentiation methods were seeded into a PDMS channel around a sterile surgical suture in type I collagen gels. In one week, cells remodel and contract the collagen matrix until 40% compaction is achieved and the biowire may then be removed from the PDMS template. Biowires subjected to electrical field stimulation showed an increase in myofibril ultrastructural organisation, enhanced conduction velocity, and altered electrophysiological and Ca^{2+} handling compared to controls.

Another variation on the 3-D tissue engineering approaches came in 2014 when Bian et al. cultured NRVMs on a 3-D hydrogel using elastomeric moulds with hexagonal posts orientated along directions derived from diffusion tensor magnetic resonance imaging maps of human ventricle (Bian et al. 2014). After 3 weeks of culture on 2.5cm^3 cardiac tissue patches with cardiomyocyte alignment that follows human epicardial fibre orientation, the tissues were compared to age-matched 2-D monolayers. The 3-D tissues showed presence of dense and aligned electromechanically coupled cardiomyocytes, quiescent fibroblasts, interspersed capillary-like structures, action potential propagation with conduction velocity close to that of adult tissue, directional dependence on local cardiomyocyte orientation, robust T-tubules aligned with Z-disks, co-localisation of L-type Ca^{2+} channels with ryanodine receptors and faster Ca^{2+} kinetics. Then a different study used a similarly structured tissue patch, but used a fibrin-based cardiac patch and seeded with hESC-CMs at a cardiomyocyte purity of 48% to 65% (Zhang et al. 2013). The high purity ensured longer sarcomeres, higher conduction velocities, and a higher expression of genes associated with contraction. In 2016 a technology reminiscent of the biowires was developed, cylindrically shaped engineered cardiac tissues dubbed “cardiobundles” were anchored within flexible porous frames (Jackman, Carlson, and Bursac 2016). These cardiobundles support both chronic auxotonic

loading and free-floating culture of NRVM or hiPSC-CM tissues. Cardiobundle cultured NRVM had significantly increased expression of sarcomeric proteins, 2.1-fold increase in size, 3.5-fold increase in contractile force and a 1.4-fold increase in conduction velocity. Their contractile characteristics matched or approached those of adult rat myocardium. Cardiobundles cultured without mechanical loading showed inferior function, but this could be rescued with a transfer to dynamic conditions. Finally, one study took an in-depth analysis of maturing effects of ECM combined with 3-D environments on hiPSC-CMs. Seeded into a 3-D cardiac ECM scaffold and compared with a 2-D culture, the hiPSC-CMs showed increased expression of calcium handling genes, Junctin, *CaV1.2*, *NCX1*, *HCN4*, *SERCA2 α* , Triadin, and *CASQ2*. Unsurprisingly they found that calcium transient amplitudes as well as maximum up- and downstroke were also increased compared to cells cultured in 2-D conditions.

1.1.2.7. Mechanical Loading to Enhance hiPSC-CM Maturity

As previously discussed, mechanical stimuli are an important physical cue for cardiomyocyte development and maturation. Mature myofibrils are generated by constant forces taxing the tissue during systole and passive stretch, but in addition to structural maturation we also find changes in gene expression (Tulloch et al. 2011). Genes upregulated due to mechanical loading include cell junction proteins such as Cx43 (Salameh et al. 2010) and N-Cadherin (Matsuda et al. 2004), which have been the focus of many studies. Cardiomyocytes exposed to cyclic uni-axial stretch 3 hours after seeding were found to be aligned in the direction of the applied force and had N-Cadherin proteins localised at the poles of cardiomyocytes. This contrasts with the even distribution found in cells not subject to mechanical stretch (Matsuda et al. 2004). Meanwhile, Cx43 was predominantly found at the cell-cell border after a 24-hour session of mechanical stretch to 110% cell length (Salameh

et al. 2010). In addition to Cx43 up-regulation, this protocol resulted in increased pERK 1 and 2, glycogen synthesis kinase-3 β , AKT, and growth factors such as myostatin, atrial natriuretic peptide, and TGF- β 1 (Shyu et al. 2005; Ruwhof et al. 2000). The protocol of a 24-72 hour stretch at a 1 Hz 10-20% elongation quickly became a standard used in many studies (Dhein et al. 2014; Matsuda et al. 2004; Salameh et al. 2010). Contrastingly, a more recent study found that exposure of embryonic mouse cardiomyocytes to cyclic stretch induced a decrease in TGF- β 1, and showed an increased maturation reflected by size, genetic profile, myofibril protein assessment, and proliferation rate (Banerjee et al. 2015). A very recent study showed that the forces of the contracting heart can regulate localisation and activation of vinculin, a cytoskeletal protein (Fukuda et al. 2019). Vinculin (VCL) is reported to be essential for myofilament maturation, as indicated by the co-immunoprecipitation derived interactome in contracting versus non-contracting cardiomyocytes. Identified was the slingshot protein phosphatase (SSH1), an activator of the actin depolymerising factor (CFL), which regulates F-actin rearrangement and promotes myofilament maturation. The reported VCL-SSH1-CFL axis provides a link between mechanical forces and myofilament maturation. Effects of higher stretch frequency were investigated in hESC-CMs, showing that at 3 Hz this significantly increased cardiomyocyte specific structures, and expression of cardiomyocyte specific markers (Shimko and Claycomb 2008). Indeed, the effects of cyclic stretch on cardiomyocyte and ECM alignment, hypertrophy, proliferation, myofibril generation, and sarcomere banding were also seen in hiPSC-CMs (Tulloch et al. 2011) and when combined with electric stimulation further increased contractility, as well as RYR2 and SERCA2 expression levels (Ruan et al. 2016).

1.1.2.8. Biochemical Stimulation to Enhance Cardiomyocyte Maturity

1.1.2.8.1. Thyroid Hormone

Various biochemical agents have been used in the maturation of cardiomyocytes. Triiodothyronine is a thyroid hormone that enters cardiomyocytes through membrane transporters or produced by conversion of thyroxine (Takasu 2006). In the nucleus, triiodothyronine binds to receptors in regulatory regions of target genes, positively regulated genes include MYH6 and SR/ER calcium ATPase 2. Negatively regulated genes include MYH7 and SERCA2 inhibitor phospholamban. SERCA2 promotes the reuptake and release of calcium from the SR during diastole, leading to improved ventricular relaxation (Hoit et al. 1997). Furthermore, triiodothyronine has a direct inotropic effect on the heart through upregulation of β_1 -AR expression (Fazio et al. 2004). It is known that triiodothyronine suppresses proliferation of ovine cardiomyocytes in vitro, possibly indicating a role in maturation (Chattergoon et al. 2012). Chattergoon et al. studied the in vivo maturation of cardiomyocytes by triiodothyronine in 3 groups of sheep fetuses, finding increases in cell width, binucleation percentage, SR/ER calcium ATPase2a expression, and ryanodine receptor 2 expression, while a reduction in proliferation was found (Chattergoon et al. 2012). An RT-PCR, cellular electrophysiology, and confocal calcium imaging based study on differentiation of murine ESC-CMs showed that triiodothyronine supplementation increased the number of ESC-CMs while also heightening expression of cardiac markers: Nkx2.5, myosin light chain-2V, α - and β -MHC (Lee et al. 2010). Electrophysiology showed a more negative resting membrane potential, closer to adult-like values, but no difference in AP duration. Finally, calcium-handling showed more mature properties as well: larger calcium transients, faster rate of rise and decay of calcium transients, and a larger internal store of calcium.

1.1.2.8.2. Insulin-Like Growth Factor-1

Another biochemical cue important in cardiomyocyte maturation is IGF-1. IGF-1 signalling is essential for regulation of contractility, metabolism, hypertrophy, autophagy, senescence, and apoptosis in the heart (Troncoso et al. 2014). IGF-1 works through the receptor tyrosine kinases IGF-1 receptor and the insulin receptor, which activate the PI3K-AKT and RAF-MEK-ERK pathways. NRVM treatment with IGF-1 increases myosin light chain-2 and troponin-I expression, doubling of cell size, and an increase in protein synthesis as assessed by leucine incorporation. Further studies show that IGF-1 enhances metabolic maturation through increased expression of fatty acid oxidation enzymes medium chain acyl-CoA dehydrogenase and the muscle-type carnitine palmitoyl-transferase I, and enhanced effect of nuclear receptor/transcription factor peroxisome proliferator-activated receptor α (Montessuit et al. 2006). In hESC-CMs, IGF-1 has been shown to initiate mitosis (McDevitt, Laflamme, and Murry 2005), and is linked to the Wnt, Hippo and PI3K pathways for coordination of cardiac chamber morphogenesis and embryonic heart size. Cardiac overexpression of IGF-1 stimulates cardiac proliferation, while constitutive overexpression has been shown to prevent cell death after myocardial infarction (Hashmi and Ahmad 2019). Recently, it has been shown that a combination of the biochemical factors; thyroid hormone, dexamethasone, and IGF-1 have a maturing effect on HiPSC-CM in 3D cardiac micro-tissues. Measurement of gene expression profiles and structural, ultrastructural, and electrophysiological characteristics, as well as mechanical and pharmacological properties of these cardiomyocytes showed enhanced SR function, contractile properties consistent with the positive results of other maturation methods, and an overall higher fidelity adult cardiac phenotype (Huang et al. 2020).

MiRs have also been identified as possible modulators of cardiomyocyte maturation. MiRs have pivotal roles in heart tissue development (Zhao et al. 2007; Mishima, Stahlhut, and Giraldez 2007), and MiR-1 is known to play an important role in heart disease (Zorio et al. 2009; Silvestri et al. 2009; Cai, Pan, and Lu 2010).

Analysis of expression profiles in hESCs, hESC-CMs, fetal human and adult ventricular cardiomyocytes showed that overexpression of MiR-1, -133, and -499 displayed the largest fold differences in gene clusters associated with cardiac differentiation (Fu et al. 2011). Furthermore, it was found that MiR-499 promotes the differentiation of hESC to ventricular cardiomyocytes, while MiR-1 facilitates electrophysiological maturation as indicated by augmented Ca^{2+} transient amplitude and kinetics, decreased AP duration, and hyperpolarised resting membrane and maximum diastolic potential. Other studies investigated MiR-208, a family of MiRs that are potential candidates for modulators of maturation that is involved in thyroid hormone responsiveness and switching of the myosin isoform. MiR-208a is encoded within an intron of alpha-cardiac muscle *MYH6*, while MiR-208b is encoded within a *MYH7* intron (Callis et al. 2009). Overexpression of MiR-208a in the heart induces hypertrophic growth and arrhythmias in mice, and results in thyroid hormone-associated protein 1, myostatin inhibition. Inhibition of these proteins results in upregulation of muscle growth and consequently hypertrophy. However, MiR-208 knockouts show that it is required for proper cardiac conduction, expression of cardiac transcription factors including key cardiac development factor GATA4, cardiac growth modulator homeodomain-only protein, and gap junction protein Cx40 (Van Rooij et al. 2007).

1.1.2.8.3. Circulating Fatty Acids

Fatty acid circulation at birth may contribute to cardiomyocyte maturation, palmitate is one of the primarily studied fatty acids in the culture of engineered cardiac tissues. Palmitate is a long-chain free fatty acid and can be followed using tracer compounds, which in neonatal human cells show already similarities with the adult free fatty chain transport (Bougnères et al. 1982). Findings show that a switch to fatty acid metabolism is a central driver of cardiac maturation, with cells grown on a palmitate substrate exhibiting enhanced cardiac function, reduced proliferation due to repression of β -catenin and Yes-associated protein 1, and increased expression of myosin light chain 2 (Mills et al. 2017). Further study of this substrate showed additional effects of maturation in increased mitochondrial respiratory capacity, changes in calcium dynamics and fatty acid oxidative capacity (Yang et al. 2019), though it should be noted that oxygen levels may also affect maturation of hiPSC-CMs. In vitro, hypoxia can impair differentiation and maturation through a hypoxia-inducible factor 1 α (Medley et al. 2013), while high oxygen tension will inhibit this factor and promote a metabolic switch to oxidative phosphorylation (Menendez-Montes et al. 2016). The inhibition of hypoxia-inducible factor 1 α results in an enhanced metabolism, mature cardiomyocyte associated gene expression, sarcomere organisation, and contractility (Hu et al. 2018).

Adrenergic receptor activation as a method of maturing cardiomyocytes has been extensively studied in rodents, showing pathological hypertrophy. α - and β -ARs are activated by norepinephrine and are part of cyclic nucleotide signalling pathways, with protein kinases as the main effectors, that end in positive and negative inotropic and chronotropic effects in cardiomyocytes. These pathways will be discussed in detail in chapter 1.2. In efforts to increase NRVM and mouse myocyte maturation, norepinephrine's

effect on β -ARs has been found to significantly increase protein content, in addition to inducing hypertrophy in mouse myocytes only (Deng, Rokosh, and Simpson 2000). In hESC-CMs, α -AR stimulation through the agonist phenylephrine has also been shown to increase protein synthesis (Földes et al. 2011). In addition, phenylephrine enhances sarcomere structure organisation, and increases cell area 1.8-fold and cell number 3.8-fold. Taken together these findings reveal an important role for protein kinase signalling in growth and hypertrophy of early and stem-cell derived cardiomyocytes.

1.1.2.9. Metabolic Maturation of HiPSC-CM

The heart has a high energy consumption driven by myosin ATPases required for sarcomere contraction and SERCA required for Ca^{2+} clearance and sarcomere relaxation (Lopaschuk and Jaswal 2010). The underdeveloped heart mainly relies on glycolysis for ATP production, while the adult human heart produces ATP primarily through oxidative phosphorylation using lipid substrates such as fatty acid beta-oxidation. ATP is produced in mitochondria, which occupy up to 40% of the cell volume in adults (Schaper, Meiser, and Stammer 1985). During maturation, mitochondria become associated with sarcomeres and have been suggested to have a functional link between their morphologies. Cristae, densely organised inner membrane foldings, are found in mature mitochondria and are a marker of cardiomyocyte maturation. Unsurprisingly, HiPSC-CMs rely on glycolysis for energy production (Kim et al. 2013). Recently, a group developed an arrhythmogenic right ventricular dysplasia/cardiomyopathy model from patients with mutant plakophilin-2 gene (Kim et al. 2013). HiPSC-CMs derived from these patients' cells show abnormal plakoglobin nuclear translocation and decreased β -catenin activity, but otherwise showed no signs of pathology until induced from a glycolysis dependent metabolism to a lipid oxidation based one, resulting in exaggerated lipogenesis and apoptosis. A study on HiPSC-CMs

differentiated in chemically defined conditions found that high glucose inhibits maturation at genetic, structural, metabolic, electrophysiological, and biomechanical levels. This impairment is achieved through promotion of nucleotide biosynthesis through the pentose phosphate pathway. This was reflected in models of diabetic pregnancy in mice, with cardiomyocytes showing increased mitotic activity and decreased maturity (Nakano et al. 2017). Surprisingly little work has been done in the study of metabolism in maturation of hiPSC-CMs, considering the large demand in proteins and energy production for the development of sarcomere, SR, membrane and mitochondrial structures.

1.1.2.10. Electric Stimulation to Enhance hiPSC-CM Maturity

Internal electrical signals constantly spur cardiomyocytes to contract, and electric signalling networks activate surrounding myocytes to join in a synchronous pulsation of contraction and relaxation. It has been hypothesised that excitation-contraction coupling through intercellular electrical signalling is a main contributor to in vivo maturation of cardiomyocytes, and that this effect may be replicated through electrical stimulation in hiPSC-CMs. In 2004 a study applied electrical field stimulation to NVRMs seeded in ultra-foam collagen sponges over 8 days and found improved cardiomyocyte alignment, increased amplitude of synchronous construct contraction 7-fold, and enhanced ultrastructural organisation (Radisic et al. 2004). These structural and electrophysiological changes are attributed to gap junction enabled connections forming between cells, allowing for propagation of electrical signal. Furthermore, increased expression of sarcomere and gap-junction related proteins α -MHC, β -MHC, CK-MM, Cx43, and TnI was found. Other studies in NVRMs have found increased presence of sodium-calcium exchanger, longer action potentials, enhanced conduction velocity (Sathaye et al. 2006), increased mitochondrial content and activity (Xia et al. 1997). Similarly, hESC-CMs grown under conditions of

electrical stimulation showed longer action potentials, as well as a higher calcium-flux and increased inward-rectifier potassium ion channel Kir2.1 expression (Deng, Rokosh, and Simpson 2000; Martherus et al. 2010). In a combination of electrical stimulation with previously discussed topographical cues, NRVMs plated on a micro-grooved polystyrene chip for 7 days were elongated, aligned along the micro-grooves, formed a well-developed sarcomere structure, and had gap junctions dotted over the entire surface of the cells. Contrastingly, when bi-phasic electrical pulses were applied to the chip, gap junctions were found to be isolated to cell-cell end junctions. Furthermore, as a result of electrical stimulation elongation was improved parallel to the vector of the electrical field (Heidi Au et al. 2009).

1.2. Cyclic Nucleotide in Cardiomyocytes

Two well-studied cyclic nucleotides, cAMP and cGMP, are important regulators of cardiac function (Ogawa and Imura 1982). Stimulation by catecholamines of G-protein coupled receptors anchored to various locations on the inside of a cell activates adenylyl cyclase to synthesise cAMP out of ATP (Ghigo and Mika 2019). Similarly, cGMP is synthesised out of GTP by either membrane bound pGCs activated by natriuretic peptides (NPs) (Moltzau et al. 2017), or by sGCs activated by NO (Hammond and Balligand 2017). The main downstream effectors of cAMP and cGMP are PKA and PKG respectively (Lin, Kass, and Lee 2017), which have opposing influences on cardiac contraction and relaxation. cAMP and cGMP have a complex crosstalk by virtue of PDEs (Hammond and Balligand 2017, Zaccolo and Movsesian 2007). These PDEs come in many varieties differing in subcellular localisation, affinity and specificity and can bind to either cAMP, cGMP or both, and have a cAMP degrading

enzymatic function which is regulated by cGMP (Conti 2000). Through this crosstalk, the concentration of cGMP can effectively regulate that of cAMP.

Correct secondary messenger signalling is only possible in well-structured and healthy cardiomyocytes (Lyon et al. 2009). GPCRs are specialised transmembrane proteins consisting of an extracellular amino terminus, seven transmembrane alpha-helices, and an intracellular carboxyl terminus. These receptors influence extracellular signal transduction from neurotransmitters, chemical stimuli, hormones, and other agents. Ligand-binding leads to a conformational change and subsequent coupling of the GPCR with a heterotrimeric G-protein, followed by the exchange of a G-protein-bound GDP for GTP. The G-proteins can be divided into a variety of sub-families with various down-stream effects, for example the activation or inhibition of cyclases. These cyclases in turn can generate signalling molecules such as cAMP or cGMP with down-stream PKA and PKG mediated pathways (Hammond and Balligand 2012). Generation of the ubiquitous second messenger cAMP from ATP follows the activation of AC co-localised at the membrane with the β_1 - or β_2 -AR. The generation of cGMP from GTP can follow several pathways which will be thoroughly dissected in chapter 1.2.2.

Belonging to this family of transmembrane proteins are the β -ARs, which can be divided into the sub-types β_1 -, β_2 -, and β_3 -AR, with β_1 being the highest expressed in cardiomyocytes and β_3 the lowest (Bylund et al. 1994). β -ARs and their second messengers such as cAMP, cGMP, and Ca^{2+} are known for signalling pathways that are highly organised and tightly regulated inside of “nano-domains” (Evans et al. 2010). Interestingly, in contrast with β_1 - and β_2 -AR, the β_3 -AR is resistant to agonist-induced desensitization, (Liggett et al., 1993; Nantel et al., 1993) and shows an enhanced expression in heart failure, sepsis, and diabetic

cardiomyopathy (Amour et al., 2007; Moniotte et al., 2007; Moniotte et al., 2001). On stimulation, β_1 - and β_2 -ARs induce positive chronotropic and inotropic effects via Gs-coupling. β_3 -ARs differ quite a bit in that they lack PKA phosphorylation sites. β_3 -ARs have been shown to be involved in the production of cGMP through activation of eNOS (Dessy and Balligand 2010), eventually resulting in PKG-mediated down-stream effects such as negative inotropy and positive lusitropy (Mongillo et al. 2006; Gauthier et al. 1998). It was suggested early on that the increased cardiac contraction resulting from β_1 - and β_2 -AR stimulation could be rescued through the β_3 -AR mediated pathway, thereby ameliorating the cardiotoxic effects of prolonged β_1 - and β_2 -AR stimulation, protecting against pathological hypertrophy, and cardiac remodelling (Gauthier, Langin, and Balligand 2000). Recently, a study evidenced this effect by showing that β_3 -AR over-expression in transgenic mice leads to protection against hypertrophy and cardiac remodelling induced through catecholaminergic stimulation (Belge et al. 2014).

The nano-domains that the effectors of β -adrenergic stimulation function in are small pockets of intracellular space restricted either physically or through protein-interactions. Nano-domains of cAMP were first found through stimulation of subcellular fractions isolated through separation with ultracentrifugation, where prostaglandin E stimulation showed differential cAMP accumulation in particulate versus soluble fractions (Buxton and Brunton 1983). Compartmentation of cAMP was further investigated in adult rats and mice using a combination of FRET and SICM microscopy techniques showing that cAMP responses to stimulated β_1 -ARs were distributed across the whole cell surface, while signals in response to β_2 -ARs were primarily localised to T-tubules and caveolae. Remarkably, in rats with chronic heart failure the β_2 -ARs redistribute to the cell crest, leading to diffuse cAMP

signalling (Nikolaev et al. 2010). β_3 -ARs, like β_2 -ARs, are localised together with eNOS in caveolae-enriched membrane fractions (Belge et al. 2014).

Further evidence to the existence of nano-domains was provided using a FRET-based sensor CUTie, which was generated as a localised cAMP sensor through fusion with AKAP79 resulting in localisation at membrane-bound AC; with AKAP18 δ resulting in localisation at SR-bound PLB; or with TnI resulting in localisation at MyBPC (Surdo et al. 2017). It was shown that acute cAMP elevation after β -adrenergic stimulation is mostly present at plasmalemma targeted by AKAP79-CUTie, slightly limited at the SR, and barely present at the TnI sites.

1.2.1. cAMP in Cardiomyocytes

The ubiquitous second messenger cAMP is extensively studied for the wide variety of biological functions it regulates, including cardiac contractility (Zagotta et al. 2003). cAMP is generated after stimulation of GPCRs, which signal via cAMP through activation of adenylyl cyclases that catalyse the conversion of ATP to cAMP. Stimulation of GPCRs such as β -ARs with isoprenaline (ISO) or prostaglandin receptors with prostacyclin results in cAMP release through the G-stimulatory pathway. Interestingly however, only cAMP generated through β -AR stimulation enhances cardiomyocyte contraction. The discovery of EPAC instigated the creation of a FRET sensor using the EPAC binding domain flanked by fluorophores. With this Epac1-camps sensor it was possible to find, through real-time FRET studies, that both β -ARs and prostaglandin receptors generate spatially distinct pools of cAMP with different downstream effects through the activation of different subsets of PKA enzymes (Snir et al. 2003).

1.2.2. cGMP in Cardiomyocytes

There are three triggers for the production of cGMP in cardiomyocytes—the NO-pathway: diffusion of NO into the cell with subsequent activation of sGC, the β_3 -AR pathway: activation of NOS through β_3 -AR stimulation with subsequent activation of sGC (Chinkers 1989), or the NP-pathway: stimulation of NPRs by natriuretic peptides resulting in subsequent activation of pGC (Takimoto 2005). Concentrations of cGMP can be also modulated by stimulation with ACh (Bork and Nikolaev 2018), however this pathway is outside of the scope of this thesis. In chapter 5. we gather the first major body of data on cGMP and its compartmentation in HiPSC-CMs aged to D30 or D90.

1.2.2.1. β_3 -AR and NO-Diffusion Pathways

Stimulation of sGC by free radicals, nitrovasodilators, and similar molecules was first reported in 1977, suggesting a subsequent increase in intracellular cGMP as a result of free radical diffusion across the cell membrane (Arnold et al. 1977). The first isolation of sGC from bovine lungs revealed that this regulation is mediated by heme as a prosthetic group (Gerzer et al. 1981). It was subsequently found that endothelium-derived nitric oxide (NO) is the major sGC ligand. It was further shown that interaction mediates cGMP release in vascular smooth muscle and facilitates vasodilation (Friebe and Koesling 2003). In cardiomyocytes, NO donors have been shown to modulate β -adrenergic inotropic responses in many models, reducing this response at lower doses while increasing it at higher doses (Massion et al. 2003). NO donors are converted into NO through eNOS, which has been found in close proximity to β_3 -AR in cardiomyocyte caveolae and t-tubules. A more recently discovered source of NO in cardiomyocytes is the nNOS, which differs from eNOS in its localisation as well as physiological and pathological functions in the cardiovascular system (Zhang et al. 2014). nNOS is localised primarily in the vicinity of RyR at the SR and α -

syntrophin at the crest (Zhang et al. 2014). Recent consensus indicates that nNOS is a key protein in cardiac protection under pathology-induced cardiac stress (Zhang 2017). Recent clinical studies show that the effect of an NO-donor infusion in human adults reduces LV peak and end-systolic pressure through positive lusitropic effect (Paulus 2020).

In chapter 6.2.3. we investigate a possible differential physiological effect of cGMP produced as a result of NO diffusion and cGMP produced through stimulation of β_3 -AR.

1.2.2.2. NP-Pathway

Synthesis of cGMP from GTP through the NP-pathways can be triggered through one of three natriuretic peptide receptors: NPR-A, NPR-B, and NPR-C, of which the first two can also be referred to as pGC-A and pGC-B respectively. While there is a total of seven pGCs (pGC-A through pGC-G), only these three have had ligands identified for them (Kuhn 2003). In this study we turn our gaze to GC-A and GC-B, stimulation of which has been shown to have a positive effect on cGMP levels in cardiomyocytes (Schulz et al. 1989; Lowe et al. 1989; Chinkers et al. 1989), but focus our experiments on GC-B. The natriuretic factors presence in atria was first discovered by De Bold et al. in 1981, who thereby revealed an endocrine signalling axis between the heart and the kidney (de Bold et al. 1981). Mammalian cardiac-expressed NP members are ANP, BNP, and CNP, furthermore it has been suggested that musclin and osteocrin may have a role here as well (Potter, Abbey-Hosch, and Dickey 2006). The amino acid sequence of ANP was derived in 1983 by purifying the natriuretic peptide from rat (Flynn, de Bold, and de Bold 1983), pig (Del Ry et al. 2007), and human atria (Kangawa and Matsuo 1984), and follow-up studies identified two novel peptides with similar amino acid sequences: BNP (Sudoh et al. 1988) and CNP (Sudoh et al. 1990). These peptides were found to be essential in maintaining physiological homeostasis as vasodilators, with dysfunction contributing to cardiovascular, and renal remodelling and

dysfunction (Von Lueder et al. 2013). Mice with a knockout of ANP or GC-A exhibit hypervolemic arterial hypertension and cardiac hypertrophy (Chan et al. 2005), while those with an overexpression show hypotension (Steinhelper, Cochrane, and Field 1990). BNP-deficiency results in blood pressure independent cardiac fibrosis (Tamura et al. 2000).

The third natriuretic peptide discovered, CNP, binds to the GC-B membrane receptor at an affinity 50- or 500-fold higher than ANP or BNP respectively (Koller et al. 1991). CNP is sourced from vascular endothelium and functions as an antagonist of the renin-angiotensin system, causing a suppression of the vasoconstrictive effects of angiotensin I (Davidson, Barr, and Struthers 1996). The first clinical study measuring CNP plasma levels in heart failure, through immunohistochemistry and radioimmunoassay, reported an elevated atrial but not systemic concentration in heart failure patients compared to control patients (Wei et al. 1993). The cardiovascular actions of CNP depend on its interaction with GC-B and the subsequent release of cGMP. The function of GC-B can be studied both in vivo and in vitro by using rats transgenic for a dominant GC-B knockout gene (Langenickel et al. 2006). Sequence identification in *sus scrofa* (mini-pig) led to several studies investigating the GC-B expression in normal and failing minipig hearts which showed that CNP generation in early left ventricular dysfunction depends on endocrine signalling in the myocardium (Del Ry et al. 2009). In this model, CNP protein and gene expression were shown to be inversely affected by down-regulation of GC-B in heart failure (Del Ry et al. 2008).

1.2.3. Phosphodiesterases and Compartmentation

As discussed previously, signalling proteins are subject to compartmentation through both localisation of receptors and synthases to membrane structures, as well as the physical barriers these structures form. A more specialised form of compartmentation takes place in

the cytosol through cGMP and cAMP hydrolysing enzymes called PDEs, which turn these signalling molecules into inactive GMP and AMP respectively to control their cellular levels. 21 genes encoding PDE have been described, which can be subdivided into 11 numbered PDE families. 7 of these have been investigated in the heart: PDE1, PDE2, PDE3, PDE4, PDE5, PDE8, and PDE9 (Figure 5). PDE1, PDE2, PDE3, PDE10, and PDE11 are dual-substrate specific, having the ability to hydrolyse both cAMP and cGMP, thus facilitating cross-talk between these two pathways. While PDE3 has a 4-10 times higher affinity for cAMP over cGMP, it can be competitively inhibited by binding cGMP resulting in a positive cross-talk. Allosteric activation of PDE2 can result in enhanced degradation of cAMP pools, causing a negative cross-talk. PDE4, PDE7, and PDE8 are specific for cAMP. PDE5, PDE6, and PDE9 are specific for cGMP (Bork and Nikolaev 2018). The differential localisation of PDEs infers varying forms of compartmentation on the different cAMP and cGMP pathways (Figure 6).

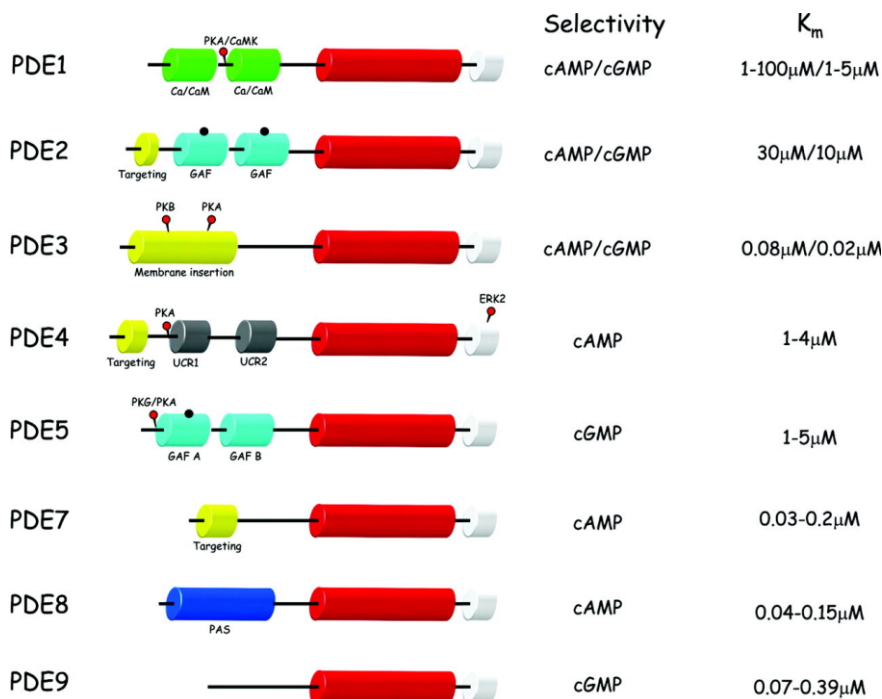


Figure 5. PDE families 1 to 9, showing structure, selectivity, and affinity. Image modified from (Zaccolo and Movsesian 2007).

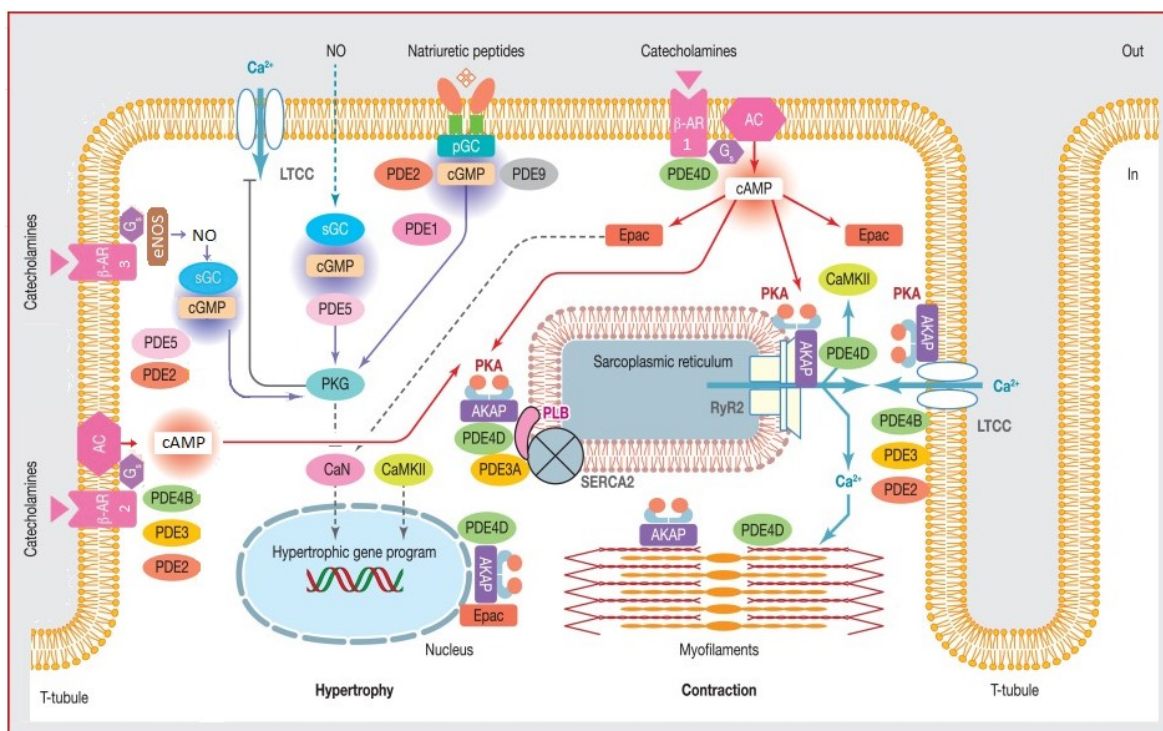


Figure 6. Schematic overview of PDE localised functions, image modified from (Bobin et al. 2016)

1.2.4.1. PDE1

PDE1, canonically known as the calmodulin-activated PDE, has two sites for either calmodulin or Ca^{2+} at the N-terminal, which can enhance its activity 10-fold (Kokkonen and Kass 2017). The three isoforms PDE1A, PDE1B, and PDE1C are all found expressed in the heart, but PDE1A and PDE1C are predominant there, with PDE1A being the most prevalent in mice and PDE1C in humans. At Ser120 in the N-terminal there is a phosphorylation site that can be modified by PKA in PDE1A and by CamKII in PDE1B. Binding to this site decreases the affinity of the PDE to calmodulin and Ca^{2+} , reducing overall activity. In human and mice, both isolated and hypertrophied cardiomyocytes exhibit heightened PDE1 expression. It has been shown using various loss-of-function strategies in NRVMs and ARVMs that PDE1A regulates hypertrophy in cardiomyocytes, a control which is dependent on cGMP/PKG

signalling (Miller et al. 2009). It was further shown that PDE1 inhibitors can reduce myocyte hypertrophy induced in mice by ISO treatment. Another study shows that PDE1 inhibitors can counter-act upregulation of PDE1A following myocardial infarction in activated myofibroblasts, thus preventing down-stream expression of fibrotic genes (Miller et al. 2011). In this interaction a known cAMP pathway for anti-fibrosis dependent on cAMP-Epac1-Rap1 was activated, as well as an anti-fibrotic sGC-cGMP signalling pathway through inhibition of non-canonical TGF β signalling (Beyer et al. 2015; Lu et al. 2013). Activity of cAMP-PKA can also suppress fibrosis, although sustained activation is profibrotic (Iwase et al. 1996). The NP-pathway also has an anti-fibrotic effect with ANP-induced PKG activation blocking pSMAD3 nuclear translocation, which in turn interferes with TGF β -driven fibrosis (P. Li et al. 2008). Recently, a clinical study has shown inotropic effects after inhibition of PDE1 by ITI-214 at a single oral dose of 30 or 90 mg in adult HFrEF patients (Gilotra et al. 2021). We see through these studies that inhibition of PDE1 in various nanodomains can activate various cooperative pathways.

1.2.4.2. PDE2

As with PDE1, PDE2 is dual-substrate with three isoforms: PDE2A1, PDE2A2, and PDE2A3, which all differ in their N-terminus and localisation. PDE2A3 is the only membrane localised PDE2, which may be due to differences in amino termini hydrophobicity between the different PDEs (Rosman et al. 1997). Other than the membrane and cytosol, PDE2 can be found in the nuclear envelope, the Golgi body, and the SR (Lugnier et al. 1999). Furthermore, it finds itself in the same compartments as cAMP produced as a result of β_1 - and β_2 -AR activation. This regulation is coupled to cGMP produced by the β_3 -AR-pathway (Mongillo et al. 2006; Geoffroy et al. 1999). The function of PDE2 as a mediator of cross-talk stems from the binding of cGMP to the GAF-B domain in the N-terminus resulting in a

conformational change increasing the affinity of PDE2 for cAMP by 10-fold (Zaccolo and Movsesian 2007; Martinez et al. 2002).

PDE2A is up-regulated with heart failure (Mehel et al. 2013), which results in more rigid tissue due to activation of myofibroblasts despite a lack of profibrotic factors (Vettel et al. 2014). It is hypothesised that this profibrotic effect manifests through the effect PDE2 has on cAMP and cGMP, which have been known to be anti-fibrotic (Sassi et al. 2014; Lu et al. 2013). Suppression of PDE2A increases a cAMP pool that activates PKA, phosphorylating nuclear factor of activated T-cells, preventing their nuclear import, thus blocking hypertrophic gene programs, and finally blunting maladaptive hypertrophy (Zoccarato et al. 2015). Suppression of PDE2A has further been shown to reduce pulmonary hypertension through the NP-pathway, specifically by regulating cGMP generated by the NPR-A. Though it must be noted that PDE2A predominately regulates cAMP levels rather than cGMP (Castro et al. 2006). With its effect on the symptoms of various cardiovascular diseases, PDE2 is a good target for study. While overexpression models are in use, unfortunately PDE2A^{-/-} mice do not survive the embryonic stage (Maurice et al. 2014).

1.2.4.3. PDE3

The double esterase containing PDE3 has two isoforms, PDE3A and PDE3B, with PDE3A having three splice variants PDEA3A1, PDEA3A2, and PDEA3A3. PDE3A is more sensitive to cGMP than PDE3B. Opposite to PDE2, PDE3 has its cAMP hydrolysis activity competitively inhibited by cGMP (Mehats et al. 2002). The splice forms of PDE3A vary in N-terminus sequence and localisation: PDE3A1 localises to the membrane and is found solely in microsomal fractions, while PDE3A2 and PDE3A3 localise to the cytosol and can be found in both the microsomal as well as cytosolic fractions (Vandeput et al. 2013). PDE3A and PDE3B

are both expressed in the heart, with PDE3A being predominantly present (Liu and Maurice 1998; Shakur et al. 2000). PDE3 inhibition displays inotropic qualities which are absent in PDE3A knockout mice, while wild-type and PDE3B knockout mice show similar responses to inhibitors. This indicates that PDE3A is the main target of current PDE3 inhibitors (Beca et al. 2013). PDE3A is downregulated in human and animal models of heart failure, with PDE3 inhibition exacerbating symptoms including hypertrophy, arrhythmia, and myocyte apoptosis (Packer et al. 1991; Smith et al. 1997; Ding et al. 2005). After phosphorylation by PKA at Ser292/293 PDE3A1 regulates basal contractility and SR Ca²⁺ by forming complexes with SERCA2a, PLB, AKAP18, PKA, and protein phosphatase-2A, controlling PLB phosphorylation and SERCA activity (Beca et al. 2013). PKA phosphorylation also enhances hydrolytic activity on cAMP (Ahmad et al. 2015).

1.2.4.4. PDE4

PDE4 and all of its 20 isoforms are cAMP specific, with PDE4A, 4B, and 4D being expressed in various nano-domains of the heart (Richter et al. 2011), including co-localisation with β_1 - and β_2 -ARs, The LTCC, RyR2, PLB, SERCA2a, and TnI (Kokkonen and Kass 2017). PDE4 is the main regulator of basal contractility, a control which is achieved through regulation of cAMP modulation of SERCA2a and LTCC. PDE4D in particular only regulates cAMP in the SERCA2a nano-domain (Beca et al. 2011). Decline of PDE4D in heart failure is associated with arrhythmias, risk for ischemic stroke, and atrial fibrillation (Jørgensen et al. 2015). Increased PDE4D results in a switch from B-AR G_s α subunit to the G_i α subunit, which reduces cAMP production (Baillie et al. 2003).

1.2.4.5. PDE5

PDE5 is cGMP specific and has three isoforms expressed in humans: PDE5A1-3 (Lin et al. 2000). These isoforms have no known difference in function or localisation and co-localise with α -actinin in the Z-disc of cardiomyocyte sarcomeres (Lee et al. 2015). This localisation shifts to a diffuse pattern upon disruption of eNOS, in late-stage hypertrophy and dilation, and in failing hearts (Senzaki et al. 2001; Zhang et al. 2008; Takimoto, Champion, Belardi, et al. 2005). This shift can be undone through sGC stimulation, indicating that localisation is dependent on cGMP produced through sGC (Zhang et al. 2012). PDE5A contains GAF regulatory domains which are activated by PKG phosphorylation (Kass 2012; Thomas, Francis, and Corbin 1990) and this activity selectively regulated cGMP produced through the NO-pathway (Takimoto, Champion, Belardi, et al. 2005; Takimoto et al. 2007). PDE5A has value as a therapeutic target, as it has been shown that its inhibition blocks multiple pro-hypertrophic and pro-fibrotic signalling pathways (Kass, Champion, and Beavo 2007), thereby counteracting maladaptive structural and functional remodelling in both ischemic (Salloum et al. 2008) and hypertrophic heart disease (Takimoto, Champion, Li, Belardi, et al. 2005). Furthermore, infarct size and apoptosis induced by ischemia-reperfusion can be ameliorated by PDE5A inhibitors by allowing mitochondrial K_{ATP} channels to open (Das et al. 2006; Ockaili et al. 2002).

While PDE5 inhibitors like sildenafil, tadalafil, and vardenafil are sold as commercial drugs to treat erectile dysfunction and pulmonary hypertension (Bender and Beavo 2006), clinical studies have found that inhibitors can ameliorate various heart diseases (Guazzi et al. 2011; Guazzi, Vicenzi, and Arena 2012). Contrasting evidence shows no such effect (Redfield et al. 2013), which may be due to selectivity of PDE5 for NO-pathway produced cGMP since this pathway is suppressed in heart failure with reduced NO synthesis (Takimoto, Champion, Li,

Ren, et al. 2005; Moens et al. 2008), sGC activity (Neo, Kandhi, and Wolin 2011), and subsequent cGMP production (Carnicer et al. 2013; Karbach et al. 2014). In female mice and in oestrogen treated ovariectomised mice, PDE5 inhibition can rescue heart disease caused by mechanical overload or excessive $G_q\alpha$ stimulation (Sasaki et al. 2014). This may indicate a use for PDE5 blockers in post-menopausal women, though clinical studies are lacking.

1.2.4.6. PDE8

PDE8 is another cAMP-specific PDE, with isoforms PDE8A and PDE8B (S. H. Soderling, Bayuga, and Beavo 1998), though studies focus on PDE8A. PDE8A knockout mice cardiomyocytes show altered excitation-contraction coupling, having higher levels of Ca^{2+} transients, greater basal Ca^{2+} spark frequency, and increased LTCC current upon ISO stimulation, suggesting a role in RYR2 activity (Patrucco et al. 2010). PDE8 appears to be active within a specific compartment, as global PKA activity is not increased in PDE8A knockout cardiomyocytes. It has been found that a rs4704397 SNP in PDE8B is associated with increased thyroid stimulating hormone levels and increased risk of myocardial infarction (Jorde et al. 2014). Isoform specific inhibitors are currently not available.

1.2.4.7. PDE9

PDE9 is a cGMP-specific PDE and of all the PDE families, it has the highest affinity for cGMP. It is expressed at both mRNA and protein level in mammalian hearts, including those of humans (Soderling, Bayuga, and Beavo 1998; Lee et al. 2015). Pathway specificity was tested using a PDE9 inhibitor in adult and neonatal rat cardiomyocytes transfected with the FRET sensor FlincG (Lee et al. 2015). These cells were stimulated with the NOS inhibitor L-NAME, the NO donor DEANO, or the GC-A/B stimulator ANP and it was found that PDE9 specifically targets cGMP produced through the GC-A/B pathway. The same study found that the intra-

cellular localisation of PDE9 is in the T-tubules and SR, based on a SERCA2a immunohistochemistry study. This study also showed that murine pre-existing heart disease can be reversed independent of NOS activity through the use of PDE9A inhibitors, while the effects of PDE5A inhibitors depend on the NOS pathway. Interestingly, this shows that the two cGMP-specific PDEs, PDE5 and PDE9, are localised in different compartments, which may be part of why PDE5 acts upon the NO-pathway while PDE9 acts upon the NP-pathway (Redfield et al. 2013). Heart failure increases PDE9 levels, particularly in HfpEF in which PDE5 inhibitors have failed to yield positive outcomes (Hoendermis et al. 2015). Cardiac hypertrophy in mice caused by transaortic constriction has its symptoms of fibrosis, increased size, and maladaptive signalling ameliorated by deletion of the PDE9A gene or inhibition of its expression (sLee et al. 2015).

1.2.4. FRET Investigations of the cGMP Pathways

FRET-based studies investigating the cGMP pathways are few and far apart. Various studies have investigated the effects of the NP-, β_3 - and NO-pathways on CM contractility, taking into account parameters of compartmentation both structural and cytosolic such as in the case of PDEs.

In 2014 cGMP was studied in adult mouse ventricular cardiomyocytes using a red cGES-DE5 sensor. They found very low cytosolic levels of cGMP at approximately 10 nmol/L, which could be measured to increase upon a 10-minute stimulation with 100 nmol/L ANP, 100 nmol/L CNP, or 100 μ mol/L SNAP in the presence of 100 μ mol/L IBMX. PDE1 inhibitor alone had no effect on basal cGMP levels, while PDE2 and PDE5 inhibitors showed only negligible effects. However, the PDE3 inhibitor cilostamide at 10 μ M/L was found to increase cGMP levels as strongly as IBMX alone, indicating a basal cGMP production. The same model but

with trans-aortic constriction applied showed no difference in cGMP response to CNP, but an increased effect of the PDE5 inhibitor. To ascertain the source of this basal cGMP production they inhibited either the sGC or the pGC using 50 $\mu\text{mol/L}$ ODQ or 50 $\mu\text{mol/L}$ A71915 respectively. Inhibition of the sGC reduced the measured FRET ratio by $\sim 4\%$, while also abolishing the effect of IBMX. Inhibition of the pGC however had no effect. Finally, cAMP-cGMP crosstalk was studied by sequential stimulation with ISO, ANP, cilostamide, and then IBMX in cardiomyocytes transgenic for the cAMP sensor Epac1-camps. It was shown that CNP did not lead to any significant response, but the PDE3 inhibitor cilostamide increased cAMP. This effect was not reciprocated by the PDE2 inhibitor. FRET responses of ANP and CNP after ISO were abolished in cells that were incubated with cilostamide prior to the experiment, indicating a central role for PDE3 in the cAMP-cGMP cross-talk. The PDE5 inhibitor did not have this effect, rather it strongly changes the response to SNAP, indicating that PDE5 has a role in the NO-pathway rather than the NP-pathway (Götz et al. 2014). This study was the first to extensively monitor changes in cGMP in live and intact cardiomyocytes and set an example for future studies.

The effects of cAMP and cGMP cross-talk on cell function in early cardiac disease were studied in 2015 through the use of a trans-aortic constriction mouse model, discovering positive inotropic and chronotropic effects of ANP after β -AR stimulation. This was found by using mice transgenic for either Epac1-camps or plasma membrane targeted cAMP sensor called pmEpac1. The differences in measurable FRET responses to PDE2, 3, and 4 after either β_1 -AR specific antagonist CGP20712A or β_2 -specific antagonist ICI118,551 demonstrated a functional redistribution of PDE2 and PDE3 between β_1 - and β_2 -AR nano-domains in heart failure (Perera et al. 2015). This may represent a compensatory mechanism, responding to enhanced cardiac demand due to pressure overload. However,

the study did not investigate the possibility of redistribution of the β -ARs themselves. It was published a month later, through SICM combined with FRET, that indeed β_2 -ARs redistribute from t-tubules to the crest in failing cardiomyocytes (Balycheva et al. 2015). A more recent study investigated the redistribution of β_3 -AR due to heart failure. It is well known that β_3 -ARs are mostly confined to the T-tubules in healthy rat cardiomyocytes and this study found that myocardial infarction can cause a decrease of the cGMP generated by these receptors. While no significant differences were found in FRET responses to PDE1, PDE2, PDE3, or PDE5 between healthy and failing cardiomyocytes, the PDE2-mediated cross-talk after β_3 -AR stimulation was found to be impaired. Furthermore, it was found that PDE2 and PDE5 predominantly regulate the β_3 -AR pathway in healthy and failing adult cardiomyocytes (Schobesberger et al. 2020).

1.3. Tools and Techniques Used in cGMP Studies

Several techniques have been developed and applied to study cAMP and cGMP in living cells and tissues. Traditional histochemistry-based methods are quite sensitive but lack the possibility for use in live cells as well as sufficient spatial resolution. Sensitivity is often also an issue, such that these methods often employ PDE-inhibitors to increase cGMP to measurable levels, reducing physiological relevance of data acquired. A now widely used method for the real-time measurement of cAMP and cGMP is the use of FRET. FRET sensors are designed to have a change in their conformation upon the binding of target molecules (Jares-Erijman and Jovin 2003). The binding domain is flanked by two fluorophores which are engaged in the transfer of energy from a higher energy donor fluorophore to a low energy acceptor. This transfer is highly dependent on the distance between the fluorophores.

1.3.1. Non-FRET Methods

Prior to the advent of FRET as the preferred method of measuring signalling nucleotide changes in cardiomyocytes, various other methods had been used. For instance, fractionation followed by immuno-assays allows the comparison of cAMP or cGMP measurements in cytosolic versus membrane fractions (Méry et al. 1993). Another method of measuring ex vivo cAMP or cGMP is to use scintillation proximity assays, a method that involves radiolabelling of the signalling molecules followed by their binding with reactive beads that emit light upon this binding (Johnson et al. 2012). Finally, ELISA kits exist for the detection of cGMP through the use of specific antibodies (KEILBACH, RUTH, and HOFMANN 1992).

1.3.2. FRET Tools and Methods

FRET techniques and tools have been developed and improved on for quite some time. Prior to these FRET techniques, cAMP (Rich et al. 2000) and cGMP (Baylor, Lamb, and Yau 1979) were measured using modified cyclic nucleotide-gated channels as sensors. The first cyclic nucleotide signalling FRET study created and used the sensor F1CRhR, which was generated by labelling recombinant catalytic and regulatory subunits of PKA with fluorescein isothiocyanate and tetramethyl-rhodamine isothiocyanate fluorophores respectively. The labelling was done in presence of ATP to preserve PKA activity. The cAMP concentration-response curve of this sensor matched curves describing PKA activation and the sensor was shown to be responsive to various cAMP modulators. 100 nM ISO, 50 μ M Forskolin, and 250 μ M dibutyryl cAMP increased the FRET ratio of 500-530/570 nm, while 100 nM propranolol decreased it (Adams et al. 1991).

Soon thereafter numerous FRET sensors for both cAMP and cGMP would be developed. In 2004 several sensors were constructed based on the Epac binding domain, a Rap guanine nucleotide exchange factor activated directly by cAMP. These sensors were made by PCR amplification of human Epac1, murine Epac2, or murine PKA regulatory type II β subunit to create DNA constructs. These constructs are then cloned into pcDNA3 vector along with amplification constructs from pEYFP and pECFP, in order to generate the cDNA for an Epac binding domain flanked by YFP at the C-terminus and CFP at the N-terminus. Out of the resulting sensors Epac1-camps and Epac2-camps were widely used in studies of cAMP (Nikolaev et al. 2004). Testing of this sensor followed previously established methods wherein cells were grown on coverslips and maintained in a FRET buffer were placed on an inverted microscope with a 63x oil immersion objective. Samples were excited at 436 ± 10 nm (within the CFP excitation range), while emissions were measured at 535 ± 15 nm and 480 ± 20 nm using a beam splitter. However, cells were not visualised, rather avalanche photodiodes were used to detect signals which were digitalised using an AD converter and stored using Clampex 8.1 software (Villardaga et al. 2003). Clampex is a software suite typically used for patch-clamp data acquisition and analysis, it is not suited to FRET studies as it only reads electrical signals and has no options for common imaging corrections. The scientists that generated the Epac1-camps moved away from this by using MetaMorph 5.0 instead. MetaMorph is far more suited to real-time FRET measurements and its only downsides seem to be that it is a proprietary software tool and that it cannot be modified as source-code is unavailable.

cGMP sensors suffer to a strong requirement for specificity, due to the low concentration of cardiomyocyte intracellular cGMP at $0.01 \mu\text{M}$ (Götz et al. 2014) compared to cAMP at $1 \mu\text{M}$ (Börner et al. 2011). Studies using early cGMP sensors showed ambiguous effects that could

be ascribed to either cAMP or cGMP due to the lack of selectivity. Two reports had described attempts to develop sensors with high selectivity based on the partially truncated GKI domain fused between ECFP and YFP. These sensors were called CGY and Cygnets but their use was deemed limited due to a lack of selectivity or temporal resolution (Honda et al. 2001; Sato et al. 2000). In 2006 the first cGMP sensor with adequate sensitivity and selectivity for cGMP over cAMP was generated using human PDE5A1 cGMP binding domain with YFP fused to Glu154 and CFP fused to Ala308. Through comparing EC₅₀ for the cyclic nucleotide proteins, this sensor was found to be 420 times more selective towards cGMP than to cAMP. While this selectivity is far greater than most cGMP sensors and deemed adequate for monitoring of intracellular cGMP, it is below that of Cygnet 2.1 at >600 cGMP/cAMP. However, the dynamics of Cygnet's response in response to cGMP were called rather slow in comparison to those of CGES-DE5 (Nikolaev, Gambaryan, and Lohse 2006).

Another line of cGMP sensors was created in 2007 from the binding domain of PKG fused to ECFP and EYFP. The resulting cGi500, cGi3000, and cGi6000 sensors displayed EC₅₀s of 500 nM, 3 μM and 6 μM respectively. cGi500 proceeded to outperform the other two sensors in both an in vitro dose-response curve as well as in transfected HEK293 cells stimulated with 200 μM DEANO and 20 μM sGC activator YC-1. This sensor was found to be 100-fold more selective for cGMP over cAMP, theoretically straddling the line for adequate selectivity (Russwurm et al. 2007).

In an interesting study in 2009, a red CGES-DE5 was created by swapping out the CFP and YFP with Sapphire and RFP fluorophores. The excitation/emission ranges of this sensor made it possible for it to be co-transfected along with Epac1-camps for simultaneous measurements of cAMP and cGMP in HeLa cells. A Quad-View beam splitter was used to

split the image into four channels allowing different wavelength bands to pass, though bringing the side-effect of geometrical distortion caused by misalignment of mirrors. Unfortunately, the emissions overlapped too much causing bleed-through of signal between the different channels. It was attempted to digitally unmix these signals through linear unmixing corrections. In pre-processing, a projective transformation was applied to the images to reduce geometric distortions. Unfortunately, uneven distribution of fluorescence intensity in each channel still remained. This was countered by normalising the distribution to pre-recorded reference images of a dye mixture solution. Finally, linear unmixing was applied as described by a previous study. The linear unmixing involves multiplying the inverse of the contribution ratio of each fluorophore contributing to a pixel in the channel in question, as determined using reference images, with the contribution of the intended channel FP signal. This can be represented for each pixel with the unknown contribution of each fluorescent protein X, the mixed fluorescence signal acquired in each channel Y, and a spectral matrix S composed with references of individual FPs as:

$$\begin{bmatrix} S_{CFP/C.ch.} & S_{Sapphire/C.ch.} & S_{YFP/C.ch.} & S_{RFP/C.ch.} \\ S_{CFP/G.ch.} & S_{Sapphire/G.ch.} & S_{YFP/G.ch.} & S_{RFP/G.ch.} \\ S_{CFP/Y.ch.} & S_{Sapphire/Y.ch.} & S_{YFP/Y.ch.} & S_{RFP/Y.ch.} \\ S_{CFP/R.ch.} & S_{Sapphire/R.ch.} & S_{YFP/R.ch.} & S_{RFP/R.ch.} \end{bmatrix} \begin{bmatrix} X_{CFP} \\ X_{Sapphire} \\ X_{YFP} \\ X_{RFP} \end{bmatrix} = \begin{bmatrix} Y_{C.ch.} \\ Y_{G.ch.} \\ Y_{Y.ch.} \\ Y_{R.ch.} \end{bmatrix}$$

In addition to these corrections, 3x3 binning was used to reduce noise and background was subtracted before image processing. All these corrections were applied through programs written in ANSI C. The result showed no cAMP response when stimulating cGMP and vice versa. However, signal-to-noise ratio was quite high, particularly for the cGMP response (Niino, Hotta, and Oka 2009). While quite promising, this toolset may affect measurements through its unmixing correction and thorough applications are yet to be seen. The authors

published a second paper after construction of a blue cGMP sensor named Cygnus using the PDE5 binding domain fused to a dark YFP sREAcH as a quenching acceptor and mTagBFP as a blue fluorescent donor. Using a confocal laser microscope, it was possible to perform triple-parameter imaging, wherein Cygnus, a Ca²⁺ dye Fura Red, and Epac1-camps were measured simultaneously, allowing Ca²⁺, cAMP and cGMP dynamics to be monitored. It appeared that with this microscopy technique there was no spectral bleed-through unless one biosensor was present in a substantially higher concentration (Niino, Hotta, and Oka 2010).

The established real-time FRET protocol was documented in full detail in 2011, starting from the transfection of cells plated in glass-bottom dishes, to the use of the microscope and the MetaMorph software to acquire data, to finally the “offline” analysis of saved FRET data in MetaMorph. Described are simple ratio-metric calculations wherein uncorrected Donor-FP/Acceptor-FP ratios are calculated on a pixel-by-pixel basis, as well fully corrected calculations wherein background corrections, subtraction of photobleaching, corrections for channel cross-talk, and corrections for cross-excitation are applied (Börner et al. 2011).

While MetaMorph has been the norm for quite some time, in 2012 a protocol paper described the use of ImageJ with live ratio-metric FRET macros for use as a free-ware alternative, using Micro-Manager to control the hardware. This paper describes in detail the steps needed to set up ImageJ-MicroManager and the hardware, which includes an Arduino I/O board to facilitate communications between the computer and the light source. The data acquisition macro involves a simple selection of a region of interest on an on-going Micro-Manager MDA image, in which it will average all the pixels per channel per time interval, ratio the channels, and display the FRET signal on a graph versus number of captured frames (Sprenger et al. 2012). However, corrections are limited to background

corrections, the macros need to be modified per system, and the static nature of these modifications makes it unfit for use with a QuadView beam-splitter which suffers from geometric distortions that may change with each use. Furthermore, due to the nature of macros and their limited control the macros work on the ImageJ application thread, making it impossible to interact with ImageJ while the macros run. As with MetaMorph, the acquired data requires further “Offline” analysis, which is performed by running the data files through a second macro involving re-selection of the regions of interest, as well as a background region to be subtracted from the images. Note that the live acquisition or “Online” macro does not display any background corrected data.

In chapter 3. we discuss our microscope system incorporating a motorized sample stage and our new software plug-in for Micro-Manager named MultiFRET, which allows for higher throughput real-time ratio-metric FRET experiments. While the MultiFRET software can be used for other types of luminescent measurements, our focus in this thesis is on FRET using biosensors designed for FRET.

1.3.3. Other relevant tools and techniques

When whole cell physiological data is required, one often uses a patch-clamp: a method involves the penetration of the cell membrane using a micropipette filled with an electrolyte solution, allowing measurement of action potential through a recording electrode within the pipette (Sakmann and Neher 1984). For cell morphology, a non-invasive method called SICM is employed. SICM is a non-contact scanning technique which employs a nanopipette filled with electrolytes which change in electrical properties when the nanopipette approaches the cell surface. This change can be measured and converted into a map of the cell surface (Lab et al. 2013). This can be combined with a microscope geared for FRET

studies as described before. Through the use of SICM in combination with FRET sensors, one can locally measure cyclic nucleotides at cell surface structures such as T-tubules, Z-grooves, and the crest. SICM not only allows detection of cell and tissue structures, but also to record ion channel currents and to apply local nanopipette stimulation. These possibilities combined make it an interesting tool to investigate compartmentation of cyclic nucleotides (Nikolaev et al. 2010).

1.4. Hypotheses and Aims

In summation there are many methods available to mature HiPSC-CMs and to assess said maturation. However, studies involving the cGMP pathways in HiPSC-CMs are completely lacking despite its significant role in regulating mature cardiomyocyte contractility.

In this work we hypothesise that cGMP signalling, including the compartmentalising effects of PDEs and structural elements on it, change during the aging of HiPSC-CMs, which could provide a means of assessing different stages of maturation.

To prove this, we first aimed to fill the gap in availability of high-throughput FRET tools. We thus develop a high-throughput FRET system, which allowed us to gather sufficient data for a large number of experimental conditions. In chapter 3. we discuss the creation and experimental validation of MultiFRET. We then aimed to select a suitable cGMP sensor which would be effective at measuring changes in cGMP throughout the aging process of HiPSC-CMs. In chapter 4. we compare several sensors to fill the knowledge-gap left by a lack of sufficient FRET studies on cGMP in HiPSC-CMs. We compare two sensors primarily used in rat and mouse models, cGi500 and CGES-DE5, as well as a novel ScGi sensor. We chose ScGi for follow-up experiments and additionally found some interesting preliminary age-related differences between D30 HiPSC-CMs and NRVMs. In the same chapter, we aim to enhance

the efficiency of these experiments and to enhance the ability to perform multiplexed FRET sensor studies of cross-talk between cAMP and cGMP, as we found current methods lacking. To do this we lay the groundwork for the generation of a transgenic IMR-90 HiPSC line expressing the cAMP sensor Epac1-camps.

We then aimed to test various concentrations of cGMP-relevant PDE-inhibitors for use in D30 and D90 HiPSC-CMs, as these have not been used in HiPSC-CMs prior to our work.

In chapter 5. we aim to follow studies on cAMP which had tested the effects of various PDE inhibitor concentrations in cardiomyocytes, applying the same concept to cGMP. We set up a dose-response curve and find that PDE2, 3, 5, and 9 can best be used at 10 μ M to maximise response. We further take together the tools and findings of our first three aims and proceed to generate a large data set of cGMP data under various conditions of maturation, PDE inhibition, different cGMP pathway stimulants, and modulators of structural compartmentation. We additionally examine expression of PDEs, NP-pathway receptors and proteins, and B-ARs through qPCR and western blot. Finally, in chapter 6. we aim to tie our findings to physiological measurements using a CytoCypher device to acquire contraction and calcium data under several conditions of cGMP stimulation and PDE inhibition.

- **Aim 1:** Development of a High-throughput FRET software.
- **Aim 2:** Selection of suitable cGMP sensor and creation of transgenic IMR-90 lines expressing this sensor.
- **Aim 3:** Finding suitable PDEi concentrations in D30 and D90 HiPSC-CMs.
- **Aim 4:** Measurement of cGMP under different conditions of maturation, PDE inhibition and cyclic nucleotide stimulation.

- **Aim 5:** CytoCypher measurement of contraction and calcium under these conditions in HiPSC-CMs.

Chapter 2: General Methods

2.1. Adult Mouse Cardiomyocytes isolation

All procedures were carried out under the Animals (Scientific Procedures) Act 1986 Amendment Regulations 2012, and EU directive 2010/63/EU. A previously described protocol was used to isolate adult mouse cardiomyocytes (Wright 2013). Adult mice were sacrificed through cervical dislocation after brief isoflurane anaesthesia. The heart was removed and placed into cold HEPES buffer (113 mM NaCl, 4.7 mM KCl, 0.6 mM KH₂PO₄, 0.6 mM Na₂HPO₄, 1.2 mM MgSO₄, 12 mM NaHCO₃, 10 mM KHCO₃, 10 mM HEPES and 30 mM taurine). The aorta was cannulated, and the heart perfused with HEPES buffer at 37°C. trypsin/liberase solution (HEPES plus 13µM CaCl₂, 0.05 mg/ml liberase, 0.3 mg/ml trypsin) was added to perfusate after exiting fluid became clear. After 10 minutes the heart was diced, shaken, and triturated with a needleless 1 mL syringe until all material had broken down. The suspension was centrifuged, the pellet was resuspended in blocking buffer (HEPES buffer plus 1%BSA and 50µM CaCl₂) to inhibit enzymatic breakdown by the trypsin/liberase solution, and the cells were then washed and maintained in myocyte culture medium (MEM no L-glutamine, 0.1%, 1% BSA penicillin/streptomycin, 2 mM L-glutamine, 10mM BDM and 1x ITS-Supplement).

2.2. Neonatal Mouse and Rat Cardiomyocyte isolation

Neonatal ventricular mouse cardiomyocytes were isolated from one to two-day old pups according to the protocol provided by the manufacturer of our Neonatal Cardiomyocyte Isolation Kit (Miltenyi Biotech, Germany) (www.miltenyibiotec.com/protocols). The pups were sacrificed by cervical dislocation followed by decapitation. The hearts were excised using sterilised scissors and forceps and were washed in Hank's Buffered Salt Solution (HBSS) to remove blood. The ventricles were minced into 1mm cubes and harvested tissue

transferred into a gentleMACS C tube containing 2.5 ml enzyme mix before being incubated at 37 °C for 15 minutes. The tissue fragments were subjected to mechanical dissociation process using gentleMACS dissociator (Miltenyi Biotech, Germany). This step (enzymatic digestion and tissue dissociation) was repeated three times. After the third time, 7.5 ml of culture medium 199 (M199), supplemented with 10% (v/v) FCS, 1% (v/v) VitB12, 1% (v/v) L-glutamine, 200 µg/ml streptomycin and 200 U/ml penicillin, was added into the tube before passing the sample through a 70 µm gauge mesh filter insert to remove large particles. The filtrate was centrifuged at 1000 xg for 5 min, and the supernatant was removed. The pellet was suspended in fresh supplemented M199 and incubated for one hour at 37 °C at 1% CO₂ to allow for a separation between the cardiac fibroblasts and cardiomyocytes; fibroblasts adhere faster to the surface of the flask compared to the cardiomyocytes. After one hour the medium with cardiomyocytes was collected in a tube and centrifuged at 1000 xg before being counted and plated onto Fibronectin-coated glass-bottomed MatTek dishes with RB+ with 10% FBS and 10 µM RI. The medium is replaced with RB+ on the next day and ready for experimental use.

2.3. Generating HiPSC-derived Cardiomyocytes

The human IMR-90 stem cell line (Wicell, Madison, WI, USA) was differentiated using a protocol based on what was described by Xiaojun Lian et al. 2012, which was a culmination of previous studies all aimed at increasing the efficiency of the differentiation (Lian et al. 2013). With this approach we pre-treat D0-1 HiPSCs maintained in E8 medium (ThermoFisher, US) on Matrigel (Corning, US)-coated Falcon 6-well plates (Corning, US) with 6µM of the Glycogen synthase kinase-3B (GSK3B) inhibitor CHIR99021 (Tocris, UK). This leads to β-catenin accumulation within the nuclear membrane through the canonical Wnt

signalling pathway and promotes cardiac differentiation. Starting D2 we switch medium to RPMI medium (Sigma-Aldrich, MO, USA) with insulin-negative B27 supplement (RB-) (Thermo Fisher, MA, USA), which has been found to increase cardiomyocyte yield compared to previously used serum-based EB differentiation methods (Laflamme et al. 2007; Melkounian et al. 2010). From D3-4 we further inhibit the Wnt pathway with 2.5 μ M Wnt-C59 (Tocris, UK). During D5-10 the cells are left to complete their growth into cardiomyocytes and on D11-14 we apply a metabolic selection using RPMI-1640 without glucose. During this selection step the undifferentiated cells which have a higher glucose dependence die off leaving only the cardiomyocytes. On D15 we rescue the cardiomyocytes from starvation with RPMI with insulin positive B27 supplement (RB+), after which they are dissociated using EDTA with trypsin and replated in RB+ with 10% FBS and 10 μ M RI (Tocris, UK) to Fibronectin (Sigma Aldrich, UK)-coated 12-well plates at 600,000 cells per well. The medium is replaced with RB+ on the next day and the cells are then maintained on 1.5mL of RB+, which is refreshed every 2 days, until they are at the desired age. On D30, D60 or D90 the cardiomyocytes are dissociated using CDS (Cell dissociation solution: 20 mL RPMI, 20 mL cell dissociation buffer, 10 mL Trypsin) and replated onto Fibronectin-coated glass-bottomed MatTek dishes with RB+ with 10% FBS and 10 μ M RI. The medium is replaced with RB+ on the next day and ready for experimental use.

2.4. Sensors used

Refer to table 2 for an overview of all sensors used during this project.

2.4.1. Sensors used: Validation experiments

For the validation experiments five different sensors were used (Table 2). The Epac1-camps sensor contains a truncated EPAC1 protein with only the cAMP binding domain, flanked by

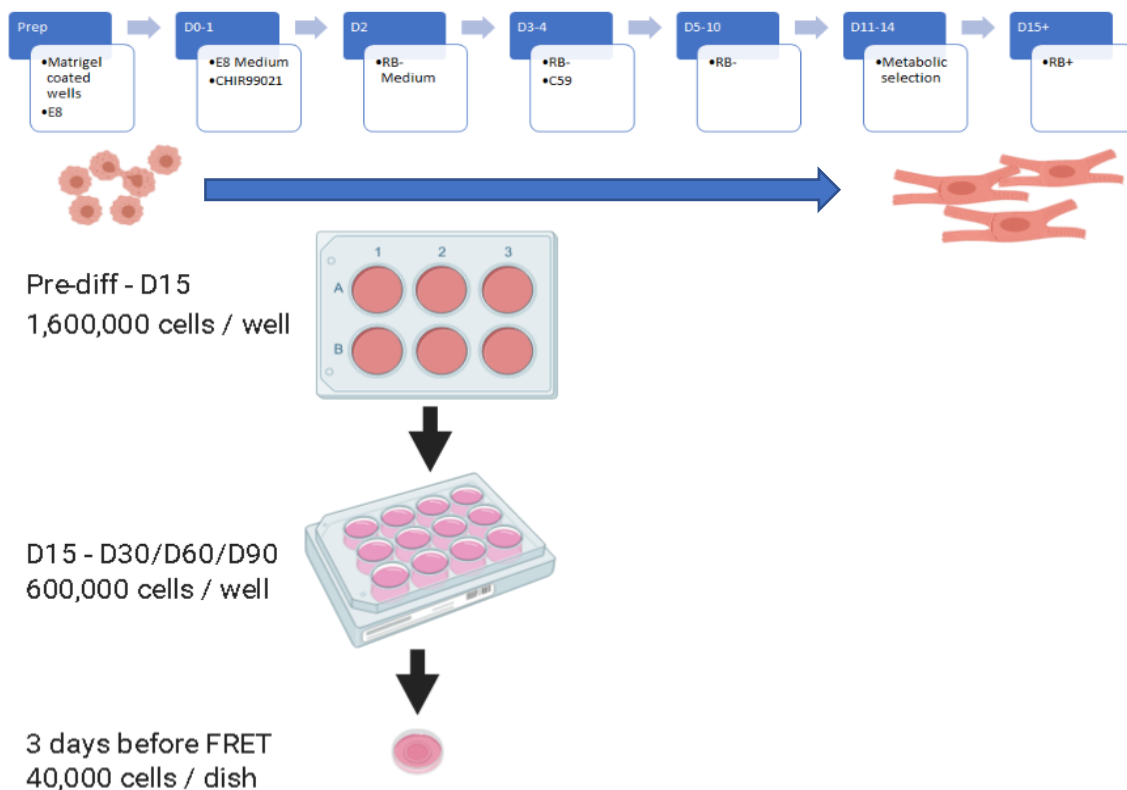


Figure 7 Protocol for the differentiation of IMR-90 HiPSCs to cardiomyocytes, and replating for FRET experiments.

the ECFP (ex. 434 nm, em. 477 nm) and Venus (ex. 515 nm, em. 528 nm) fluorophores (see Table 2). The cAMP sensor Epac1-camps is well-documented within our lab and shows a high sensitivity to changes evoked by isoproterenol, PDE inhibitors, and AC stimulation. We additionally used the Epac-S^{H74} sensor (Klarenbeek et al. 2011) which contains a mutated full-length EPAC1 protein as a sensor, flanked by mTurquoise (ex. 434 nm, em. 474 nm) as donor fluorophore and a Venus dimer as acceptor. Furthermore, we used two localised versions of the Epac1-camps sensor expressed in transgenic mice. One of these is named pmEpac1 (Perera et al. 2015) (gift from Professor V Nikolaev, Hamburg University, Germany) and is targeted to the plasma membrane, while the other is named Epac1-PLN and is localised at the SR. We also used a localised AKAP79-targetted CUTie sensor (Surdo et al. 2017) (kind gift from Manuela Zaccolo, Oxford university, UK), which has cAMP-binding

domain of protein kinase A regulatory subunit type II beta and uses ECFP as the donor and EYFP (ex. 513 nm, em. 527 nm) as the acceptor. Importantly, upon binding of cAMP the AKAP79-CUTie sensor shows an increase in FRET, while the other two sensors show a decrease in FRET.

2.4.2. Sensors used: cGMP studies

cGMP has been studied for a while now and several sensors had been made starting with parallel development of CGY-Del1 and Cygnet both based on cGMP-dependent protein kinase isozyme α (cGKI α), which is more sensitive to cGMP than the beta variant (Newman, Fosbrink, and Zhang 2011; Sprenger and Nikolaev 2013). As with cAMP sensors, these consist of a binding domain flanked on both sides by CFP and YFP fluorophores. However sensitivity of the sensors was found to be lacking so two more were developed, cGi-500 (EC₅₀ = 0.5 μ M) which was based on Cygnet truncated at the C-terminal, deleting the catalytic domain in the process (Russwurm et al. 2007). The resulting shorter sensor was much more sensitive and faster. When cGi-500 binds to cGMP, the fluorophores part, resulting in a decrease in measured FRET. In tandem a sensor based on the PDE5 cGMP binding GAF domain was developed and named CGES-DE5 (EC₅₀ = 1.5 μ M) (Bork and Nikolaev 2018; Jalink 2006; Nikolaev, Gambaryan, and Lohse 2006). The cGi-500, and CGES-DE5 sensors have since been modified with the enhanced eCFP and cpVenus fluorophores, and a yet unpublished ScGi sensor (gift from K. W. Andressen) has been made as an improvement on cGi-500 by implementing a C173R mutation in the A domain of PKG-I. The cGi-500 and CGES-DE5 sensors have been documented in several model organisms and tissues, these models however do not appropriately describe the function of these sensors as per our own goals. cGi-500 has been used in adult mouse smooth muscle cells and has been shown yield a decreased YFP/CFP ratio under stimulation with the NO donor DEANO

and natriuretic peptide CNP (Götz et al. 2014). CGES-DE5 has shown similar FRET dynamics in adult rat cardiomyocytes stimulated with natriuretic peptide CNP and PDE blocker IBMX (Subramanian et al. 2018).

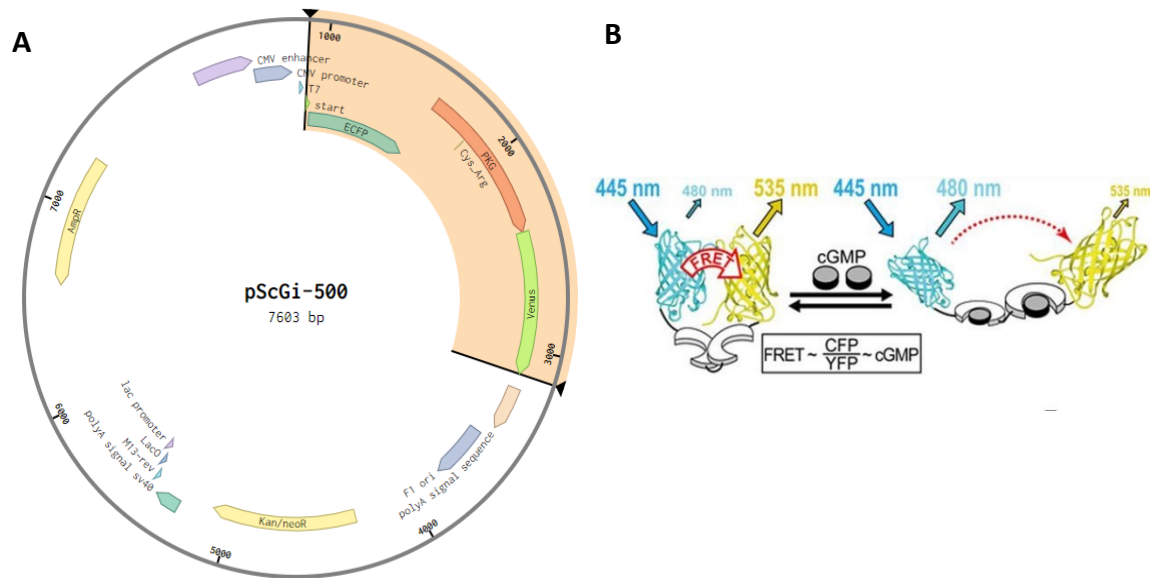


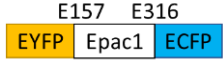

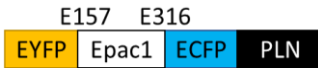

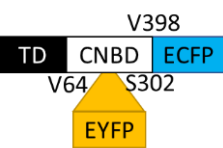
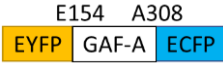
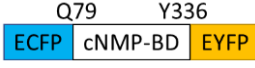
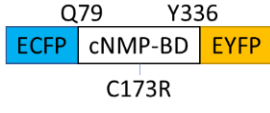
Figure 8 A. ScGi plasmid with highlighted in orange the transcribed sensor. The Cysteine to Arginine mutation of the PKG-I domain is indicated. B. Schematic representation of the effect of cGMP binding to the FRET sensor.

We compared three cGMP sensors: cGi-500 (EC50 = 0.5 μ M), CGES-DE5 (EC50 = 1.5 μ M) and ScGi (EC50 0.2 μ M). The first two sensors use the fluorophores ECFP (ex. 434 nm, em. 477 nm) and EYFP (ex. 513 nm, em. 527 nm), while ScGi features a Venus fluorophore (ex. 515 nm, em. 528 nm) rather than EYFP.

2.5. Transfection

HiPSC-CMs and NRVMs were transfected with a plasmid containing a desired FRET sensor using Lipofectamine3000 (Thermo Fisher) in Opti-MEM (Thermo Fisher) as per the manufacturer's guidelines and incubated for 2 days before use.

Table 2 FRET sensors used in this project.

Sensor	Binding domain	EC ₅₀	Selectivity cGMP/cAMP	Reference	Structure	FRET Response
Epac1-camps	Epac1	2.4 μM	-	(Nikolaev et al. 2004)		↓
pmEpac1	Epac1	9.1 μM	-	(Perera et al. 2015)		↓
Epac1-PLN	Epac1	5.3 μM	-	(Sprenger et al. 2015)		↓
Epac-S^{H74}	Epac1	Unknown	-	(Klarenbeeck et al. 2011)		↓
AKAP79-CUTie	Prkar2 β	7.4 μM	-	(Surdo et al. 2017)		↓
CGES-DE5	PDE5	1.5 μM	420 cGMP/cAMP	V.O. (Nikolaev, Gambaryan, and Lohse 2006)		↑
cGi-500	PKG	0.5 μM	100 cGMP/cAMP	(Russwurm et al. 2007)		↓
ScGi-500	PKG	0.2 μM	500 cGMP/cAMP	Kjetil W. Andressen et al., unpublished		↓

For human adult cardiomyocytes we used a viral vector to deliver the ScGi sensor. This virus was used at an MOI of 500, with an original PFU of 1.4×10^{10} / mL. We used 11 μL of the viral solution to transfect ~300,000 cells.

2.6. FRET Experimental protocol

Coverslips or MatTek dishes containing transfected cells were washed with a physiological buffer at pH 7.4 for FRET (purified Milli-Q water containing 144 mM NaCl, 5 mM KCl, 10 mM HEPES and 1 mM MgCl₂) and then imaged in 500 μ L of this buffer. For each coverslip or dish a single fluorescent cell was chosen and the continuous measurements were started. FRET signals were recorded every 6th second using 20 ms of exposure and 4x4 binning, meaning that each set of 16 pixels in a square are averaged into a square of 4 pixels in order to reduce noise. We measured the YFP/CFP FRET ratio to obtain a starting plateau. A dose of cGMP production stimulating drug was added in-between two frames of recording. In our experiments we use CNP (100 nM), GSNO (100 μ M), ISO (30 nM) after a 10-minute CGP (100 nM) + ICI (50 nM) incubation, or BAY58-2667 (100 μ M). Once the effect of CNP on the FRET ratio reaches a plateau, we may add a PDE inhibitor and monitor the response until it reaches another plateau. Finally, we add IBMX (100 μ M) as a saturator and measurements continue until the final plateau had been reached. In later experiments an additional step of adding GSNO and awaiting a plateau was added between the initial plateau and the addition of CNP. All experiments were performed at room temperature (\sim 22 $^{\circ}$ C).

2.7. FRET calculations

Upon acquisition of each frame, the mean intensity of signal (\bar{F}) in each ROI is calculated following formula (1), where n is the number of pixels in ROI and x is the intensity of a single pixel i . These fluorescence signals are then used to calculate the FRET ratio in formula (2) by first subtracting background signal and then dividing the background-corrected donor signal by the background-corrected acceptor signal.

$$\bar{F} = \frac{1}{n} \left(\sum_{i=1}^n x_i \right) \quad (1)$$

$$\text{FRET} = \frac{\bar{F}_{\text{donor}} - \bar{F}_{\text{donor background}}}{\bar{F}_{\text{acceptor}} - \bar{F}_{\text{acceptor background}}} \quad (2)$$

When data acquisition is completed, the data is sent to an Excel file containing formulae for the calculation of FRET response per stimulant. We first calculate a baseline plateau (P_{base}), with plateau in the sense of a stable intensity over a period of time resulting in a flat line on our graphs, by calculating the mean of the FRET ratios of the last 10 acquisitions before adding the first stimulant. Then, for each stimulant we first calculate a plateau (P_{stim}) by calculating the mean of the FRET ratios of the last 10 acquisitions before adding a new stimulant. These means are used to calculate a change (C) from the baseline caused by each stimulant (3), this shift is then normalised to the change of the final plateau from base (S_{max}) caused by addition of a signal maximiser and a % FRET shift is calculated (4).

$$C = \frac{P_{\text{base}} - P_{\text{stim}}}{P_{\text{base}}} \quad (3)$$

$$\% \text{ FRET shift} = \frac{100C_{\text{stim}}}{C_{\text{max}}} \quad (4)$$

2.8. FRET statistical analysis

Data is normalised to IBMX, setting the IBMX plateau to 100% FRET response. Statistical analysis is performed using GraphPad Prism 8. For our sensor comparison (chapter 4) and dose response (chapter 5) analyses we used one-way anova in order to compare multiple groups under the existence of an independent variable: sensor in the sensor comparisons tests or dosage in the dose response tests. Tukey post-hoc test was used in these analyses to compare the experimental conditions in a pair-wise fashion, allowing us to see if there is

a significant change between two sensors or two dosages. For comparisons of our data from the cardiomyocyte aging experiments in chapter 5 we chose the Welch's t-test, an adaptation of the Student's t-test that is more reliable when two samples have unequal variances and/or unequal sample sizes. P values less than 0.05 were considered statistically significant.

Chapter 3: MultiFRET Development

3.1. Introduction

At the start of this project the main method for the real-time FRET analysis consisted of the use of a set of ImageJ macros named FRET-online and FRET-offline as described by (Sprenger et al. 2012). The FRET-online macro would run a series of ImageJ functions cropping out the channels generated by the beam-splitter and prompting the user to draw an ROI for the cell of interest and a background selection. It would then draw a pair of graphs, one set for our YFP/CFP ratio and one set for the RFP/OFD ratio. Once the experiment was completed, image stacks were saved and analysed using the FRET-offline macro, which would analyse the data in a similar fashion and print out a data table that could be copied into Excel. Unfortunately, there were some glaring faults with this procedure. A major issue stems from the fixed coordinates used to crop out the beam-splitter channels. These coordinates were obtained with a time-consuming manual method of recording pixel counts from a capture, but more importantly they were often faulty due to beam-splitter being prone to minute changes in mirror orientation over use. This would result in mispositioned ROIs leading to the FRET ratio being calculated from different parts of the same cell, or even from the area around the cells. To minimise inaccurate data the macro would have to be modified with almost every use of the system, a technical feat that not all users of the system could achieve. A second flaw with this macro-based approach was that the macro occupied ImageJ's main worker thread, rather than running on a separate thread. This not only makes functions of ImageJ and by extension Micro-Manager unusable during the FRET-online macro's run, but even makes it so the windows that show up such as the graphs cannot be moved if one wants to look at the MDA captures underneath them. Attempts to move these graphs while the macro was working would result in a crash and loss of data. Finally, a problem that underlines the obtuseness of these macros is the separation between online

and offline. Essentially, this almost doubles the work-load by requiring researchers to capture (FRET-online), analyse (FRET-offline) and then reanalyse (Excel, SPSS, Graphpad Prism, etc.) their data separately. This type of offline/online split work-flow was also seen in older methods using Clampex (Villardaga et al. 2003) or Metamorph software (Börner et al. 2011).

Initially, I was to modify the ImageJ macro in order to be able to run two sensors by reading 4 channels simultaneously. However, I set out to correct all the flaws by generating an entirely new software plugin coded in Java. Java is the high-level object-based programming language that ImageJ and all of its off-shoots were created with, so a Java plugin would easily interface with existing image capture and analysis tools. At the time I found the existence of Icy, a modern bioimaging suite and ImageJ off-shoot with a few exceptional features that made it stand out from older tools. What is immediately striking is the UI, a JDesktopPane-based interface which allows for internalised windows. This would immediately reduce the window clutter that comes from using traditional ImageJ tools where every window was its own separate entity in the windows explorer. Secondly, Icy comes with an integrated Micro-Manager plugin which draws from an existing MM installation to run it inside of Icy. Since MM generates a great number of windows during its MDA, being able to have all of these internalised provides a great improvement in overall UI visibility. However, the greatest advantage of an integrated MM stems from the development tools Icy provides through its API. The Icy API comes with a great number of classes that reduce the work required from developers, much of this comes in the form of the EzPlug SDK. EzPlug can automatically generate elegant interfaces for users to set-up and run their plugin through, and also takes care of threading issues that may be tedious to most. While EzPlug was initially used in the development of MultiFRET, the need for

increased flexibility in later interfaces made me rework the plugin without the use of EzPlug. MultiFRET does however make use of other features of the application programming interface (API), most prominently of which the classes that capture the MM acquisition engine. This engine allows us to control MM, as it is run through the Icy MM plugin, through MultiFRET. This feature is used to read the positions list, listen to MDA captures, stop the Acquisition when the experiment has concluded, and is used in an automatic cell-finding feature that is still in an early development phase as of now.

The first iteration of MultiFRET had the functionality to use a set of special ROIs contouring the channels shown in the camera output to extract all contoured channels. The full potential of this function is brought to bear by a plugin made by Dr. Alexandre Dufour, Pierre & Marie Curie university, named “Active Contours”, which uses edge-detection to draw tightly fitting contour ROIs (Figure 9). Active Contours is developed for use in cell-detection, but with the right settings can be used to automatically and precisely find our channels (Dufour 2021). While these contours can be used to crop out the channels as images by way of the built-in visualisation toolkit (VTK)-based methods that Icy provides, MultiFRET could at most correct for location, skewing, and size. While most of the time, this proved to be sufficient for accurate channel alignment provided, the channels could at times show a disruptive amount of rotation that could not be compensated. I then added an advanced alignment correction function to MultiFRET, which would apply an affine transformation to each of the channels in order to correct for any rotation. An affine transformation is a form of projective transformation that requires 3 known points of an image to scale, rotate, skew, and distort that image (Weisstein 2011). The way the affine transformation would eventually be used was to take the corners of each channel and relocate them to each respective corner of an image viewport. With this method, each

channel would end up with the same size, and their rotation and skewing would be undone by setting the points back into a level rectangular shape. However, to make all of this work there was one major conundrum to be settled: programmatically finding the corners of these contours. Contours made by Active Contours would be generated as polygons consisting of hundreds of individual points, while their shapes would be rectangular due to fitting to the rectangular channels, they have no point that serves specifically as a corner. Thus, a corner point needed to be extrapolated from these polygons. I set up a procedural algorithm that would read the points of the polygon in sets of 10, generate a line formula based on these, and then using a distance-to-line calculation evaluate whether the following points are part of this line. As soon as a point would stray more than a certain threshold, this difference would be taken as proof of a corner. In this way, polygons would be scanned in their entirety until 4 corners were found, and these were then used as parameters for the affine transformation. The affine transformation itself would conveniently come as a method in the popular image processing library OpenCV (Bradski and Kaehler 2000), which I used within a Java wrapper. While the procedural algorithm may take approximately 10 seconds to run, it only needs to be run once in order to obtain the coordinates of the corners. Afterwards any affine transformation can be performed within a timespan of micro-seconds.

With aligned channels, measurements could now be made accurately. MultiFRET analyses FRET ratios from images in real-time and yields a graph showing background-corrected data. These graphs are generated using JFreeChart, a Java library dedicated to producing any kind of graph. At the end of an experiment data is exported to Excel using the Apache POI Java API for Microsoft documents. The export follows a set template; however a separate template can be set up that will be appended to the export following the writing of data. In

this way, formulae can be set to automatically be copied into every sheet in the Excel workbook containing the exported data (Figure 10).

Our group then came upon funding to purchase new hardware and, upon my suggestion, this was used to obtain a mechanical stage for software-controlled movement in the X- and Y-axes, a Z-motor for software-controlled movement in the Z-axis, and a joystick to indirectly control these features. These additions would allow us to make full use of the features of Micro-Manager's Multi-Dimensional Acquisition, which allows selection of any number of positions of interest within a given sample. In our experiments this translates to the ability to select multiple cells to visualise and record FRET ratios simultaneously, a feature not found previously in non-proprietary software tools. It should be noted that other high-throughput FRET screening assays exist, however these do not visually record the cells and only take measurements of whole-well fluorescence by using 96-well plates with a compatible fluorescent plate reader (Zhu, Fu, and Luo 2012). MDA generates a new sequence for each position and updates these sequences every time a frame is captured, temporally spaced with a user-set time. MultiFRET would quickly be adapted in order to apply the beam-splitter corrections and generate a separate graph for each sequence, increasing the number of cells that can be measured within one experiment from a single to any number supported by the computer's graphical memory capacity (Figure 11A). The taxation on the computers graphical memory could be circumvented in the future by closing the images as they are captured by MM, after converting these images to data bytes. The plethora of windows generated increased in proportion to the dramatic increase in the number of concurrent cell measurements, initially using approximately 15-25 cells per experiment but later increasing beyond this amount as both MultiFRET and our transfection method were optimised. These windows were cumbersome even in the Icy desktop pane

designed to reduce clutter (Figure 11B). My answer to this problem was to create the Workspace feature within MultiFRET, a separate tab in the MultiFRET main window which would house all of the alignment-corrected sequences and all graphs within a JScrollPane nested within a JTabbedPane (Figure 11C). This would allow the user to set tab-limit, a number of sequences with corresponding graphs, to be neatly organised by a BorderLayoutManager within a pane that does not expand, rather creating a scroll bar when its contents exceed its size. When the user-set limit is reached, a new tab is created to house the next set of sequences and graphs in the same manner. Splitting the sequences and graphs between multiple tabs reduces taxation on the computer's graphical processing capability by only loading and updating the tab-limit number at any time, while also enhancing the user experience through the splitting of what would be one large set of sequences into multiple sets.

In future development, it will be vital to expand the compatibility of MultiFRET with hardware such as a spinning disc shutter, which will enable MultiFRET to be used on more machines and thus in more laboratories. Furthermore, plans are in place for the addition of a dish-scanning cell detection method powered by the same ActiveContours. This would drastically reduce amount of human participation running an experiment requires and freeing time. However, due to the inability of ActiveContours to distinguish unwanted luminescence from target luminescence, this will require a final human selection from a list of potential-target positions. Eventually, it may be possible to apply a machine learning protocol, which may be trained upon any type of luminescent target and eventually find suitable cells automatically. Such AI platforms already exist, but would need some modification to work within our system (Wang et al. 2020).

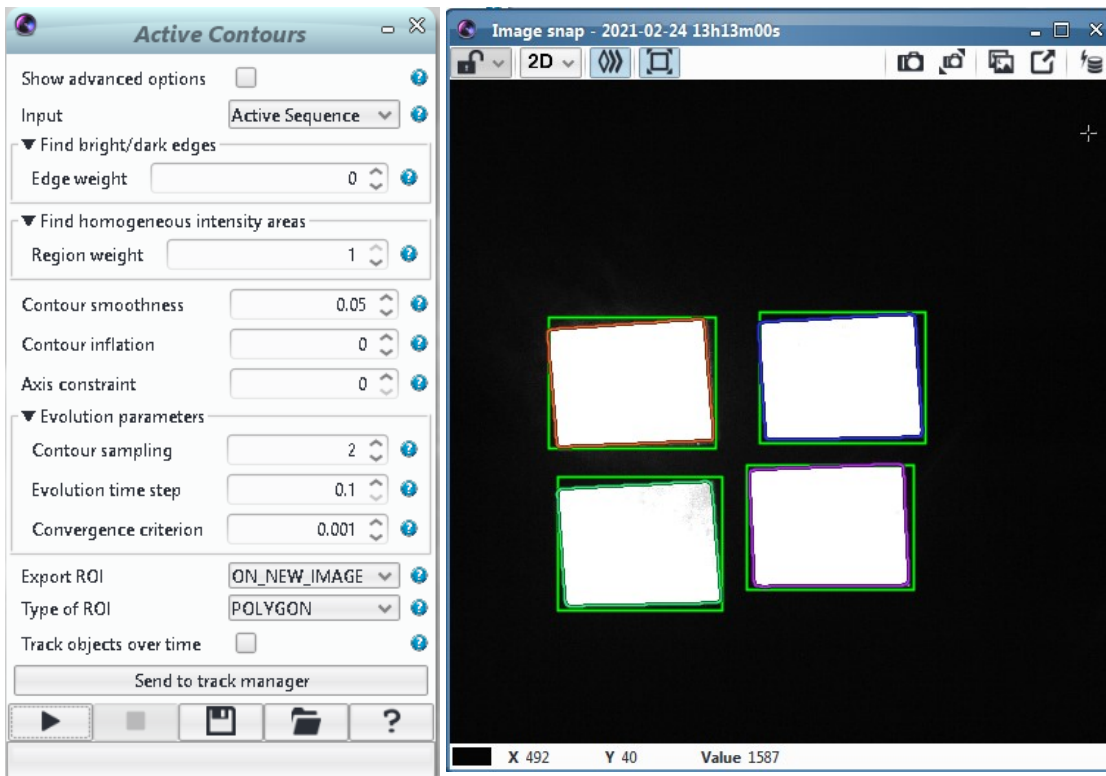


Figure 9. Active Contours used with default settings save for the Export ROI and Type of ROI. Settings window on the left, image with input ROI (green squares) and contours (coloured borders around the white channels) on the right.

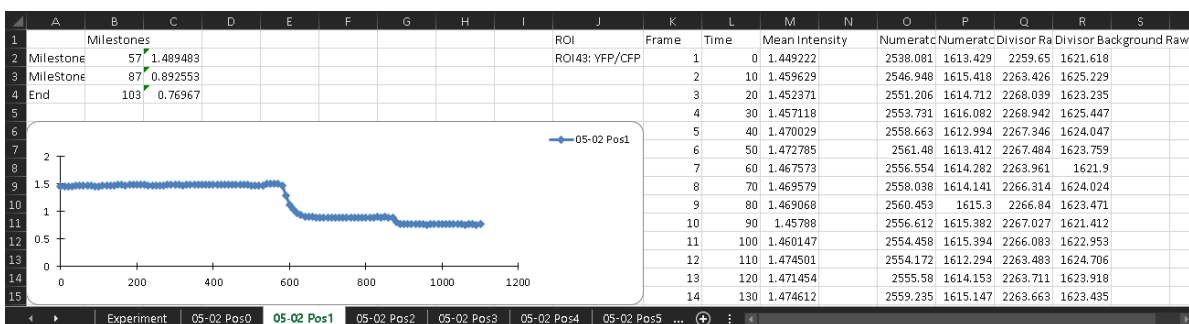


Figure 10. Default automated Excel output shows on the right-hand side the number of each frame, the time at which it was recorded, the mean FRET ratio intensity as calculated by $(\text{Numerator} - \text{Numerator Background}) / (\text{Divisor} - \text{Divisor Background})$. On the left-hand side a list of milestones set by the user are listed, showing the average of the 10 time-points

before it. Furthermore, a graph is generated based on the columns for Time and Mean Intensity.

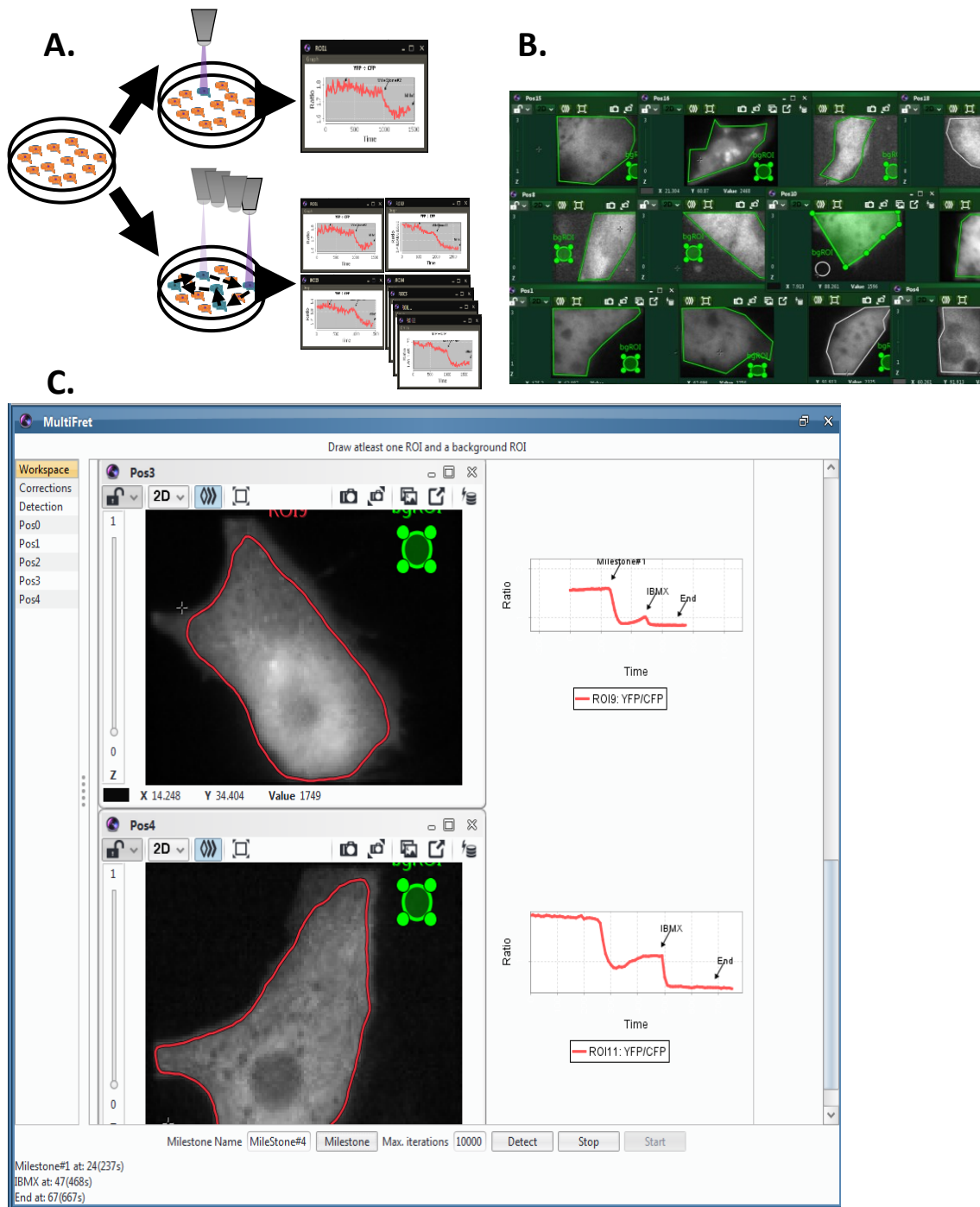


Figure 11. **A.** Old method of single cell analysis vs new software. Using the new software we can use a mechanised stage to capture and analyse as many cells as wanted in real-time. At each time-interval of user-set length, the stage will cycle through all designated cells and a frame will be captured and analysed for each one. This repeats after every interval. **B.** Channel image stacks of HiPSC-CMs with Regions of Interest being simultaneously measured. **C.** Workspace running FRET analysis on multiple cells.

3.2. Methods

3.2.1. Multiplexed FRET System Design

We select four fluorophores and design a system of light filters and dichroic mirrors to separate their signal. Our available cGMP sensors use eCFP and cpVenus with excitation peaks at 433 nm and 500 nm respectively, and emission peaks at 475 and 520 nm respectively. Compatible fluorophores selected were LSSmOrange and MKate2 with excitation peaks at 437 nm and 588 nm respectively, and emission peaks at 572 nm and 633 nm respectively. We chose these fluorophores in order to separate the signals as much as possible, additionally the large Stokes shift of LSSmOrange allows simultaneous excitation of the donor fluorophores of both the new cAMP sensor and the cGMP sensors at a bandwidth around 435 nm.

3.2.2. Software development

The new MultiFretIcy plugin was developed using the Java Integrated Development Environment (IDE) provided by the Eclipse tools platform. The plugin was developed for the Icy bioimaging suite and it makes use of the following libraries in addition to the ones required for Icy to function:

- OpenCV 3.3.0 is a software library dedicated to virtual imaging and machine learning. We use this library for its Affine transformation method, to correct for QuadView-induced misalignment.
- Apache-POI 4.0.1 is a Java API for Microsoft Documents developed by the Apache POI team in 2018 and allows software to easily hook into and run functions on existing Microsoft Office applications. We use this library to output data into Excel.

- mXparser v.4.3.0 is a rich and highly flexible math expression parser library developed by Mariusz Gromada in 2019. It has an easy-to-use API for Java, Android and C#. We use this library for a custom corrections module.

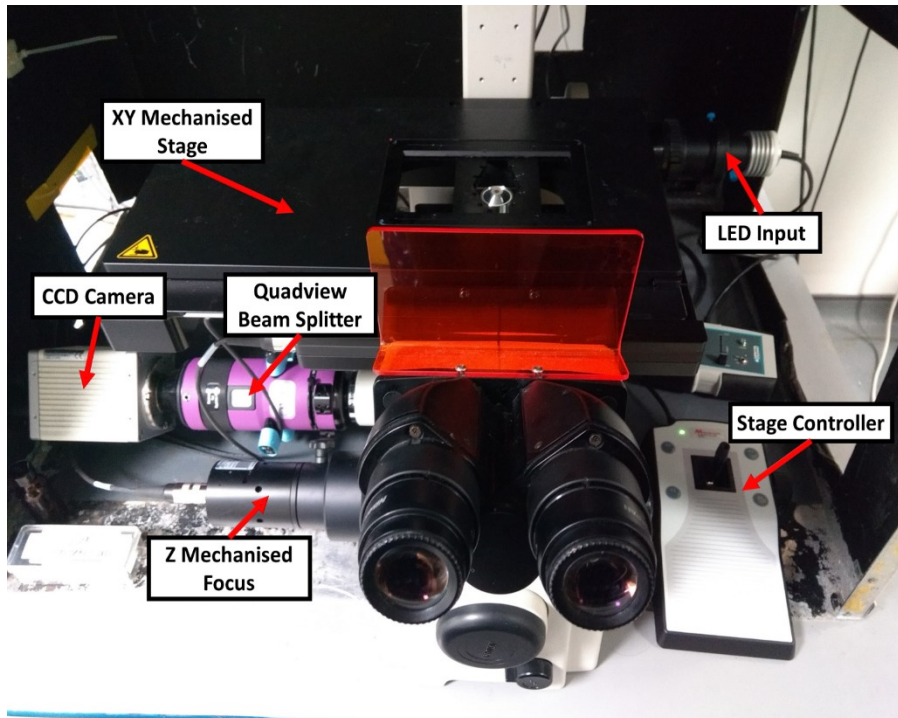


Figure 12. Cells are visualised using an inverted Nikon TE2000 microscope with as a light source a 30W Dia lamp using a 436/20nm excitation filter and a DM455 dichroic mirror. A QuadView beam-splitter precedes the ORCA-ER CCD camera (Hamamatsu Photonics, Welwyn Garden City, UK).

MicroManager 1.4 is a freeware that allows control of hardware elements such as a camera, mechanical stage, shutters, etc. We use this library to hook into the MicroManager plugin built into Icy in order to control acquisition and obtain images.

3.2.3. QuadView-Based Microscopy System

Our microscopy system is based on the same principles as shown by J. U. Sprenger et al. 2012, but with the addition of a mechanised sample stage and focus drive (Märzhäuser

Wetzlar, Wetzlar, Germany) that allow higher throughput acquisition of multiple fields of view in one experiment. The software for the recordings was MicroManager 1.4 (Vale Lab, University of California, San Francisco), integrated into the Icy imaging suite.

Luminescent cells are visualised using our inverted Nikon TE2000 microscope a 30WDia lamp using a 436/20nm excitation filter and a DM455 dichroic mirror. Recordings were made using an ORCA-ER CCD camera (Hamamatsu Photonics, Welwyn Garden City, UK), we use a QuadView (Optical Insights) to split the light into four channels before it reaches the camera.

We have selected this splitter to enable measurements of four different wavebands simultaneously, allowing measurement of two different sensors. The beam splitter has a filter cube consisting of Semrock FF01-433/24, FF01-530/11, FF01-572/15 and Omega 700LP filters for acquisition of fluorophores that emit cyan, yellow, orange and red light respectively (Figure 13). A major problem arises from the use of a beam-splitter, namely the mis-alignment of channels due to imperfections in the orientations of the various mirrors inside the beam-splitter. These orientations may be subject to change when the machine is used, the resulting variation in mis-alignment is unpredictable and requires automated correction.

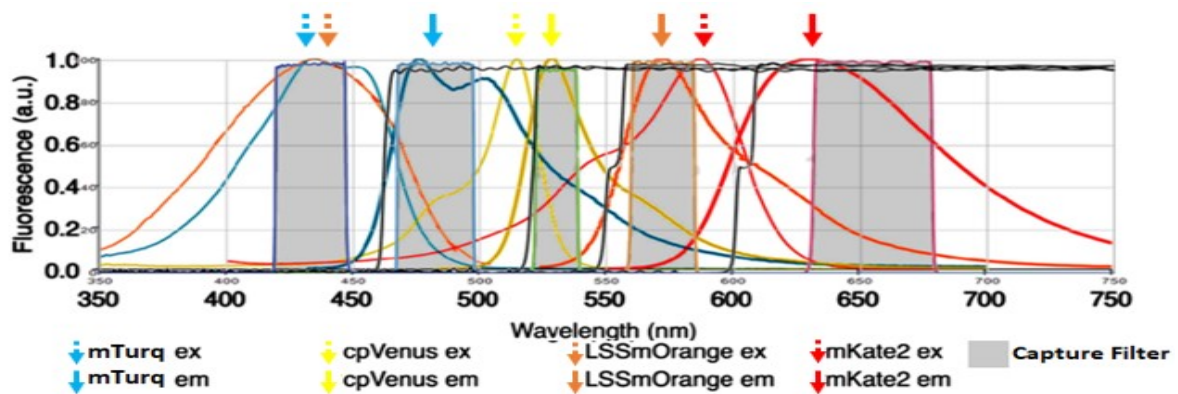


Figure 13. A system of fluorophores, mirrors and filters that will work in conjunction while minimizing overlap between signals. We've selected a previously used ECFP-ScGi-Venus sensor and designed an LSSmOrange-Epac1-mKate2 sensor to function in parallel.

3.2.5. Corrections and Analyses

We modified the MultiFRET software to allow analysis of multiple channels simultaneously, and to correct for beam-splitter misalignment and bleed-through by employing three levels of corrections: Transformative correction of the images, live data corrections and a post-acquisition Excel analysis.

The image transformations and live corrections are performed after each individual image acquisition and are set-up by the user to fit their experiment. For the image transformations we use ActiveContours by A. Dufour 2011 to create tightly fitting polygons around the channels as they appear on the CCD camera chip. The number of channels are determined by this initial step, which can also be performed manually, thus enabling the user to indicate four channels for multiplexed FRET experiments. Points from these polygons are used to calculate a projective transformation of each channel's size and shape to be identical, thus correcting for mis-alignment by QuadView mirrors (Figure 14). Each cell is then designated using a Region Of Interest (ROI), similarly a background ROI is indicated. By default a background correction is available and will, for each channel separately, deduct the

background intensity for that channel from the cell intensity for that channel. The resulting corrected intensities are then divided as selected by the user to obtain the FRET ratio. Additionally, custom corrections may be given to the software as a separate text file, the plugin makes use of a freely available mXparser library to convert simple mathematical notation into live corrections to be used during acquisition, allowing use of bleed-through correcting formulae and other calculations.

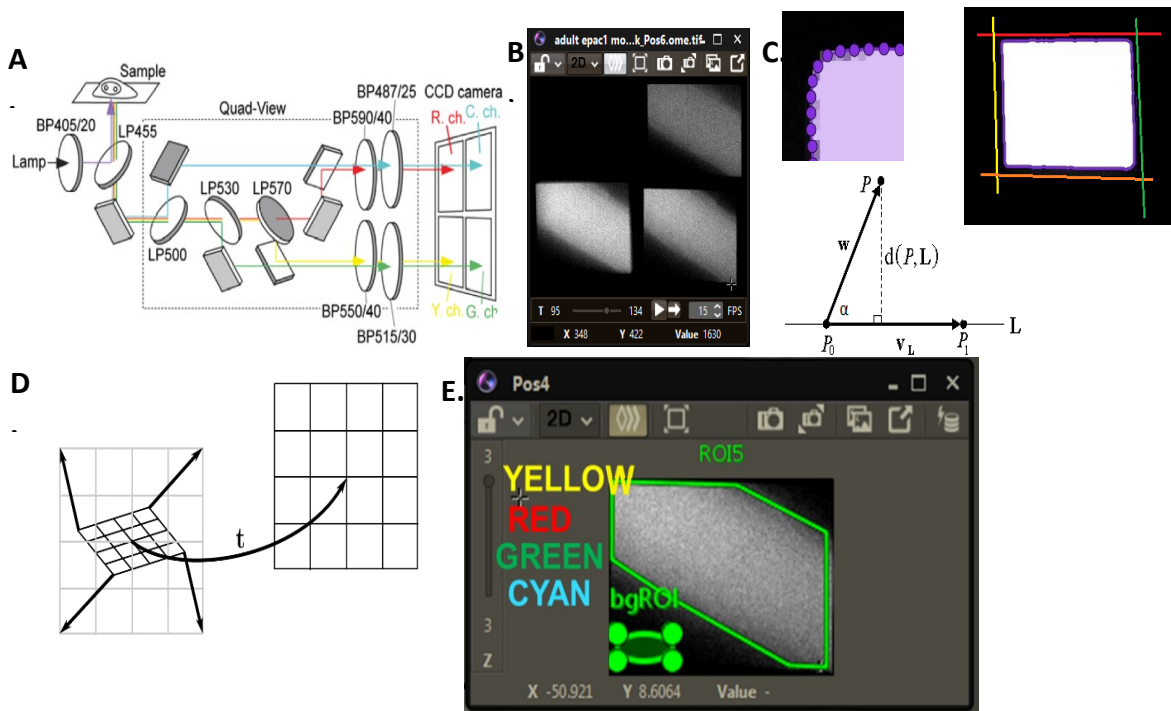


Figure 14. **A.** We use a QuadView beam-splitter to split our image into four channels. **B.** Due to the nature of this device, images arrive at the camera chip distorted and misaligned. The cell shown is an adult mouse CM transgenic for the *epac1-camps* sensor **C.** Through the use of the open-source ActiveContours plugin by A. Dufour, we automatically draw channel fitting polygons, which are made up of many 2-dimensional points. This step can also be performed manually. Using a distance-to-line approach we procedurally calculate average lines between sets of points and obtain corner points at the line intersections. **D.** These corners are then used for a projective transformation, using the VTK toolkit, of each channel into a standard shape and size. **E.** The end-result consists of all four channels having been molded into the same shape and size, eliminating all distortions. These corrected images are then concatenated into one image with a channel slider.

3.2.6. Software Validation Through FRET

Adult mouse cardiomyocytes transgenic for either epac1-camps, Epac1-PLN or pmEpac1 are isolated and cultured as described in chapter 2.1. These cardiomyocytes are then prepared for FRET as described in chapter 2.6., stimulating with 30 nM β_2 -AR agonist isoproterenol hydrochloride (ISO), followed by 100 μ M PDE inhibitor IBMX. We replicated this experiment using both our new plugin and the old macro and compare results. This experiment was repeated with neonatal mouse cardiomyocytes isolated using the method described in chapter 2.2. D30 HiPSC-CM cultured using the method described in chapter 2.3. The NRVM and HiPSC-CM were transfected with AKAP79-CUTie and Epac1-S^{H74} respectively using the transfection method described in chapter 2.5. Data analysis is performed as described in chapter 2.8.

3.3. Results

3.3.1. MultiFRET Protocol

This chapter contains an excerpt of a detailed protocol and troubleshooting segment from my methods paper “MultiFRET: A Detailed Protocol for High-Throughput Multiplexed Ratiometric FRET” that is in press for publication in the Springer journal’s “Methods in Molecular Biology”. This protocol will detail the necessary steps to set up the software, the protocol for running an experiment, variations on the protocol, and lists references to the notes for potential trouble-shooting steps in chapter 3.3.1.8. After describing the software set up, several optional steps are detailed that may be taken to customise your experiment and data output. We then detail the sample preparation, using NRVMs transfected with Epac-S^{H74} as an example. Finally, we run through every step of running the MultiFRET plugin.

While we demonstrate the protocol using two spectral channels of our four-channel system. MultiFRET is, as previously mentioned, compatible with any number of spectral channels.

3.3.1.1. Icy Setup

- 1) Download the Icy Bioimaging suite at <http://icy.bioimageanalysis.org/download/>.
- 2) The same page contains a download link for Java, if your device does not have Java 7 or higher installed make sure to download and install the proper version of Java 7 or higher for your OS architecture. This is important as Icy does not come in separate 32/64 bit versions, but rather runs in either mode depending on the Java installation it finds. If you are not sure if Java is installed, confirm installation through the methods listed below. Note that Java version is noted as “1.X.0 ###”, with X being the number referred to when Java 7 or 8 is mentioned, and ### being an indicator of the current build of said version.
 - i) In Windows: WIN+R -> Type “cmd” and hit ENTER -> Type “java -version” and hit ENTER.
 - ii) On a Mac: Command key -> hit the SPACEBAR -> Type “terminal” and hit ENTER -> Type “java -version” and hit ENTER.
 - iii) On Linux: Open a Terminal (method depending on your distribution) -> Type “java -version” and hit ENTER.
- 3) The MultiFRET plugin comes as a MultiFRET.jar file and should be copied into the Plugins folder under your Icy installation. MultiFRET is available on request from m.ramuz17@imperial.ac.uk (alternatively masoud.ramuz@gmail.com) . (see **Note 1**).
- 4) Install Micro-Manager 1.4, obtained from <https://micro-manager.org>.
- 5) Start Icy by running Icy.exe or any shortcuts generated by the installer. (see **Note 2**).

- 6) Using either the top-side search bar or the **Online Plugins** button under the top-side **Plugins** tab, confirm that your installation of Icy came with **Active Contours** and **Micro-Manager For Icy** installed. (see **Note 3**).
- 7) When attempting to start the Micro-Manager plugin for the first time, you are prompted to indicate the location of your Micro-Manager installation. This links the plugin to the actual installation. (see **Note 4**).
- 8) The Micro-Manager plugin works almost identically to the stand-alone installation, as such it will start with a prompt to select a configuration file. This is the file that can be set-up through the Micro-Manager configurations wizard and contains all the information needed for Micro-Manager to control your hardware. Within Icy, this wizard can be opened through the menu that follows when clicking on the top-left of the Micro-Manager main window. Set-up of the configurations file is performed through the self-explanatory wizard, and a list of compatible devices can be found here: https://micro-manager.org/wiki/Device_Support (see **Note 5**).

3.3.1.2. Initial Set-up of MultiFRET

At this point it is assumed that you have a microscope configured with an automated stage, shutter-controlled excitation light, camera and the appropriate lenses/splitters needed for the experiment. If not, refer to Sprenger et al. 2012 for basic instruction and to the Methods section of this chapter for our modifications. In this section we show how to either manually select a set of regions of interest (ROI) or use the Active-Contours plugin to generate a contour-file, used to correct for beam-splitter channel misalignment. We further set up our MDA settings, and optionally prepare an Excel output template and custom calculations file.

3.3.1.3. Active Contours


- 1) With no dish on the microscope, turn on the brightfield illumination source, open Icy, then open the Micro-Manager plugin, make sure you have selected the correct binning for your camera (we use 4x4 binning) and activate **Live** capture.
- 2) Increase brightfield illumination source until the corners of your channels are clear and sharp in the viewport, but make sure that the light does not “spill over” into the camera chip around the channels, see Figure 15. (see **Note 6**).
- 3) On the Micro-Manager main window, click **Snap** to capture a still frame.
- 4) In the Icy top-side pane **Region of Interest** tab, find the buttons for Rectangle, Circle, Free-hand, etc. ROI drawing tools. Draw an ROI around each of your channels. Rectangle is recommended but any of them will work. (see **Note 7**).

Use the search bar to find and run the **Active Contours** plugin by A. Dufour et al. 2011, this will open a plugin window with many adjustable settings and a Run (▶) button at the bottom, see 16. **Input** is by default set to the **Active Sequence**, meaning the last image you have had as the active window, either make sure that the capture from step 3 with ROIs from step 4 is the active window or select it from the Input drop-down selection box. The only settings that need to be changed are:

- i) **Export ROI** to **ON_NEW_IMAGE** or **ON_INPUT**
- ii) **Type of ROI** to **POLYGON**.

(see **Note 8**).

- 5) Hit the ▶ button to run Active Contours, which will draw out contours starting from each of your drawn ROI and, using an edge-detection algorithm, tightly fit these contours to each channel. The contours are a polygon-ROI with many procedurally generated points. These and all other ROI are listed on the right-side pane of the Icy

main window under the **ROI** tab. If the right-side pane is not visible, there will be a very small  arrow on the right border of the Icy main window which expands this pane. (see **Note 9**).

- 6) In the right-side pane under the **ROI** tab, find and rename all the ROI to appropriate channel names. In traditional fashion, the F2 key may be used to start renaming a selected entry. Thus, using the F2, ENTER, and the arrow keys allows for a faster conclusion over mainly using the mouse. Make sure there are no duplicate names, and then select all of the contours and save them to an accessible location using the **Save ROI(s)** button in the **Region of Interest** tab of the Icy main window top-side pane. Selection follows typical modern computer selection methods such as SHIFT+leftclick to select all entries between the currently selected and the one clicked on, and CTRL+leftclick to select one additional entry. If you have chosen **ON_INPUT** in step 5, make sure you are not selecting the initial ROI drawn in step 4. ROI may be deleted by selecting them and hitting the DEL key. Note that it is recommended that contour files are saved with a date, so that they can be used to re-analyse any saved image-stacks from that period.

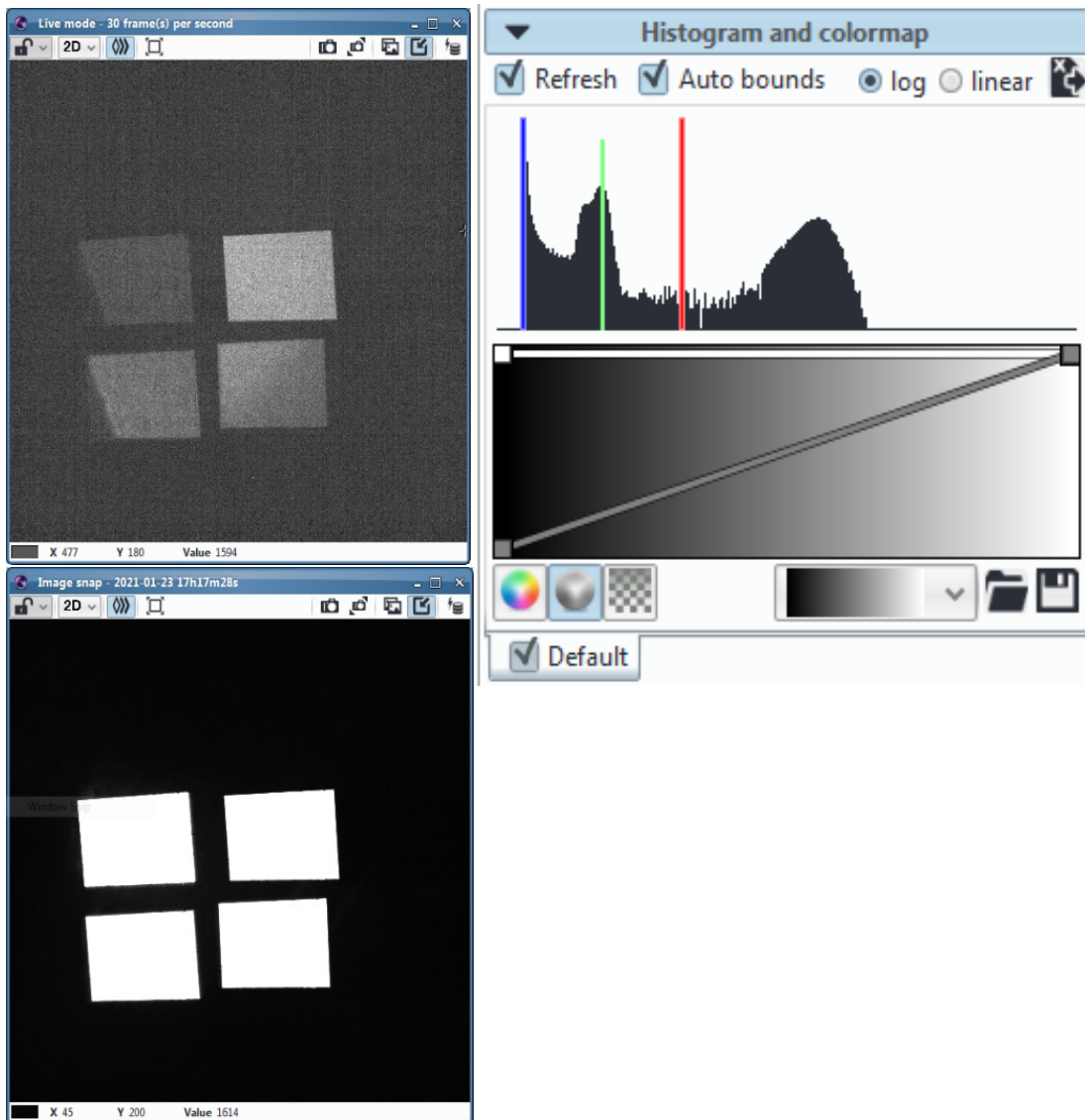


Figure 15. Uniformly lit channels can be generated by increasing the intensity of bright-light or by tweaking the image settings (dragging the blue and red lines in the Histogram pane to encompass only parts of the tonal distribution representing the bright channel). Top left: Before histogram modification. Bottom left: After modification. Right: Histogram pane showing histogram corresponding to the image after modification shown in top/bottom left.

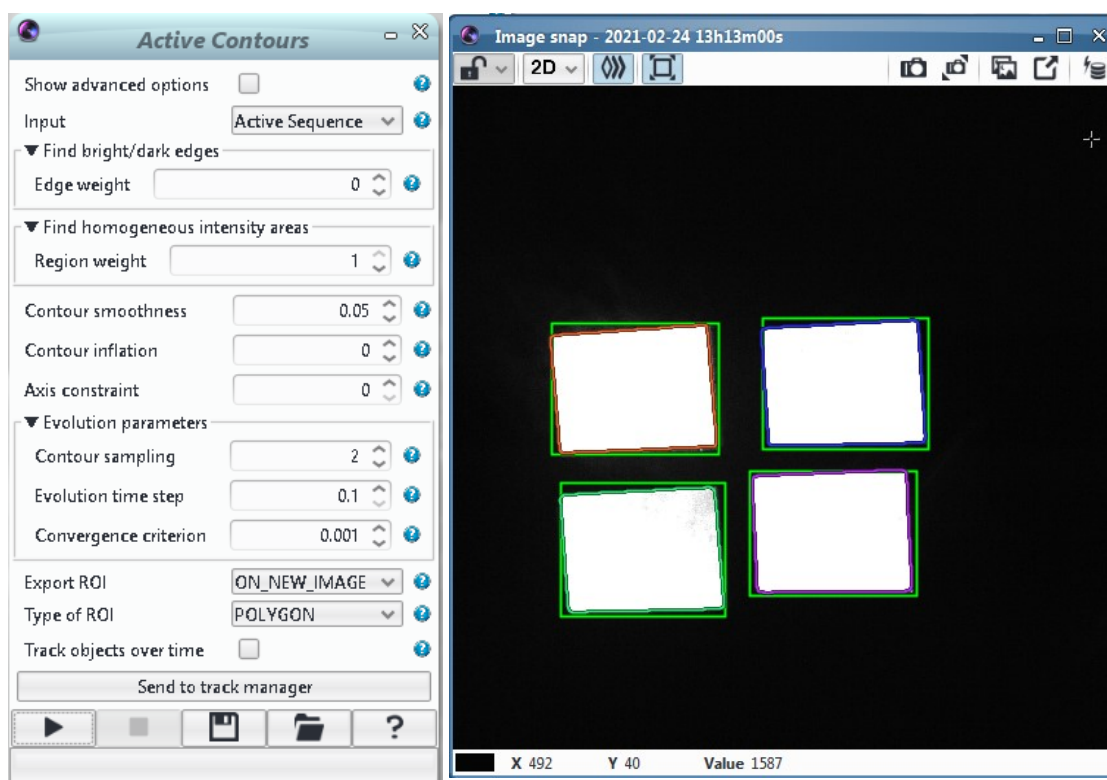


Figure 16. An example of Active Contours pane with typical settings to extrapolate freely drawn ROIs (green rectangles) into tight POLYGON contours (coloured rectangular shapes).

3.3.1.4. Excel Output Template (Optional)

Upon completion of data acquisition, MultiFRET prompts Excel to write to a user-designated workbook. In this workbook every run of MultiFRET will create a header sheet named “Experiment#<x>” where x is an incremental integer counting the number of experiments in the workbook. This header sheet will contain a screen capture of the final state of MultiFRET, including all graphs and sequence viewers. After each header sheet, data sheets will appear named “<Day-Month> <Target name>” with the target name being a user-designated label for each position in the sample marked for data acquisition, defaulting to “Pos<n>” with n ranging from 0 to the number of positions acquired minus one. Each of these sheets contains data following the template shown in Figure 17, with columns for milestones, frame number, frame capture time in seconds, mean intensity, and raw data.

Furthermore, a graph based on the mean intensity and time columns is generated. In this template, the column showing the mean intensity of signal (\bar{F}) for the target ROI is calculated using Equation 1 with the number of pixels in the ROI n and the intensity x of each single pixel i . If enabled, there will be a further background correction applied to the mean intensity column using Equation 2. The milestones shown in this template are user-marked events in time that occur during the experiment such as the addition of a drug. For convenience, each milestone comes with a formula next to it which calculates the average over the last 10 frames captured up to and including the milestone. Using the FRET ratio plateau averages provided by milestones, responses can easily be normalised to an experimental condition chosen to saturate the response of the biosensor, allowing a % FRET change to be calculated (Equation 3.). In this section, we detail the steps needed to set up a custom template on top of the one described above.

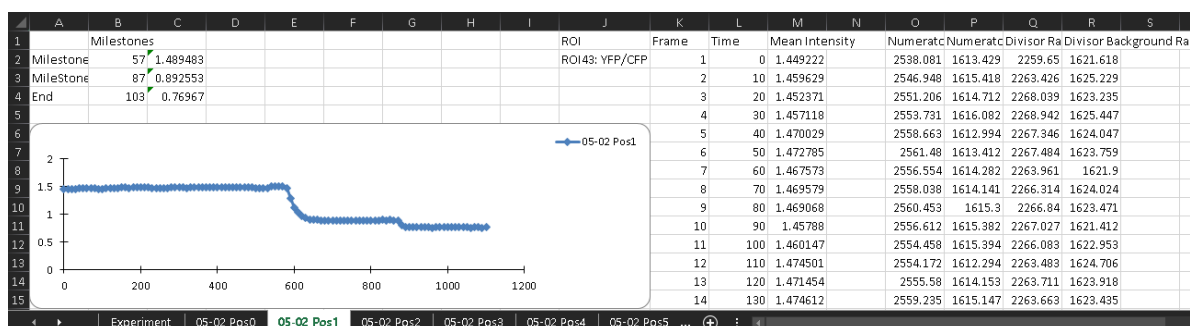
$$\bar{F} = \frac{1}{n} \left(\sum_{i=1}^n x_i \right) \quad \text{(Equation 1.)}$$

$$\text{FRET} = \frac{\bar{F}_{\text{donor}} - \bar{F}_{\text{donor background}}}{\bar{F}_{\text{acceptor}} - \bar{F}_{\text{acceptor background}}} \quad \text{(Equation 2.)}$$

$$\text{FRET \% Change} = 100 * \frac{\bar{F}_{\text{stimulant_plateau}}}{\bar{F}_{\text{saturator_plateau}}} \quad \text{(Equation 3.)}$$

1. Open either the Excel workbook you intend to use or create and open a new one.
2. Create a new sheet at the start of the workbook, that is the left-most sheet, and name it “template”.
3. In this sheet, fill in any formulae and indicators you require while avoiding use of cells that are already in use by the default template.

- After a completed run of MultiFRET that uses this workbook as its output workbook, any new datasheets will have the contents of your template sheet automatically copied into them before MultiFRET fills these sheets with data and the original template.
- Depending on your version of Excel, it may be required to force Excel to re-calculate any formulae added to your datasheets in this manner. This may be done using the hotkey CTRL+ALT+F9 to force re-calculation on all open worksheets or with



CTRL+ALT+SHIFT+F9 to do so for all sheets.

Figure 17. Example of an Excel output workbook with a typical data sheet showing Milestones listed on the left with the C-column containing the average of the last 10 frames before milestone mark. On the ROI name, frame number, recording time (s), mean intensity, and raw data can be found in order. The sheet further contains an automatically generated graph with mean intensity on the Y axis and time on the X axis.

3.3.1.5. Custom Calculations (Optional)

MultiFRET is able to parse mathematical formulae through the use of the mXparser by M. Gromada 2010. MultiFRET implements this parser by scanning a user-designed formula for variables that can be linked to the data obtained from specified ROI. Such a formula can be created in any text editor such as Notepad and stored as a text file (*.txt) with the header

for each formula denoted by a “>” at line start, the variable names comma-separated and denoted by a “>>” at line start, and the formula itself denoted by a “>>>” at line start. For example, the bleed-through correction formula in Equation 4, with example bleed-through co-efficients 1.468 for the CFP channel to YFP channel and 9.610 for the YFP channel to CFP channel, can be written as in Equation 5. When saved as a *.txt file, using for example Notepad.exe in Windows, it can be selected in MultiFRET, which gives the option to designate values obtained from a specified ROI as those to be used for e.g. CellMeasurement or BackgroundMeasurement. The text in square brackets is used to indicate the named spectral channel of this ROI that should be used. Thus, this example lets us measure both the fluorescence signal (e.g. YFP) from a cell (CellMeasurement[YFP]) and the signal from a selected background region in both the YFP channel (BackgroundMeasurement[YFP]) and in the CFP channel (BackgroundMeasurement[CFP]), then perform the custom calculation. For simple expressions, it is enough to write them as one would on a graphical calculator, with the exception that any word followed by square brackets will be detected by MultiFRET as a variable, and needs to be designated in the “>>” denoted line. For more complex functions, comprehensive documentation can be found here: <https://mathparser.org/mxparser-tutorial/>

$$F_{Corrected\ ratio} = \frac{(F_{YFP} - F_{YFP\ background}) - \frac{(F_{CFP} - F_{CFP\ background})}{1.468}}{(F_{CFP} - F_{CFP\ background}) - \frac{(F_{YFP} - F_{YFP\ background})}{9.610}} \quad (\text{Equation 4.})$$

```

1 >bleedthrough
2 >>CellMeasurement, BackgroundMeasurement
3 >>>{(CellMeasurement[YFP] - BackgroundMeasurement[YFP]) -
      (CellMeasurement[CFP]-BackgroundMeasurement[CFP])/1.468) /
      ((CellMeasurement[CFP] - BackgroundMeasurement[CFP]) -
      (CellMeasurement[YFP]-BackgroundMeasurement[YFP])/9.610)

```

(Equation 5.)

3.3.1.6. Sample Preparation (Example)

Neonatal ventricular mouse cardiomyocytes (NRVMs) were isolated from one to two-day old pups according to the protocol provided by the manufacturer of the dissociation kit (Miltenyi Biotec, Germany) (www.miltenyibiotec.com/protocols). Myocytes were plated on glass-bottomed Mattek dishes (13mm culture well diameter, 35mm dish diameter) in culture medium (90ml M199 medium, 10ml neonate serum, 0.5ml antimicotic/antibiotic solution (100x), 1ml L-Glutamax (100x), 0.5 ml Vitamin B12 stock (0.4mg/ml)) and cultured in an incubator with 1% CO₂ supply.

While MultiFRET works with any luminescent material, we provide here an example procedure for transfection of the cultured NRVMs with a plasmid encoding the Epac-S^{H74} sensor.

1. In a sterile hood, prepare two Eppendorf tubes containing 25 μ L of Opti-mem medium per dish to be transfected.
2. In the first tube add 1 μ g of plasmid DNA per dish to be transfected
3. To the same tube, add 1 μ L of P3000 reagent per dish to be transfected.
4. Incubate this tube at room temperature for one minute while preparing the second tube.
5. In the second tube, add 1 μ L of Lipofectamine3000 reagent per dish to be transfected.
6. Slowly pipette the contents of the second tube into the first, slowly moving the pipette tip throughout the length of the tube while releasing the mixture. Do not mix.
7. Incubate the combined mixture for 20 minutes at room temperature. (see **Note 10**).
8. Directly pipette 50 μ L of the transfection mixture onto the glass-bottom well of a Mattek dish. (see **Note 11**).

9. Incubate at 37°C in 5% CO₂ for 48 hours.

3.3.1.7. Running MultiFRET

At this point in the protocol, it is assumed you have previously completed the Initial Setup section of this chapter and have an up-to-date contour-file that represents the current position of your channels on the camera chip. Position the dish onto the microscope stage; immersion oil is required for the 60x lens.

1. Start Icy and open the Micro-Manager plugin, selecting the appropriate configuration file for your system.
2. Set the appropriate binning (4x4 is appropriate in our system)) and exposure time for your camera and experiment. Note that higher levels of binning reduce the impact of readout noise in exchange for a reduction in spatial resolution. The binning you select must be the same as used when setting up the contour file.
3. Click on the **Multi-D Acq.** button on the Micro-Manager window to open the MDA window, see Figure 18.
4. Make sure that the only checkboxes enabled are **Time points**, **Multiple positions (XY)**, and **Save images**. Depending on your hardware, **Autofocus** may also be used.
5. Under **Time points**, set the **Number** of time points to an arbitrarily high integer that will not be reached during your experiment, but is low enough not to require more memory than is available. An estimation of the memory cost and experiment duration are given in the **Summary** box. (see **Note 12**).
6. Under **Time points**, set the **Interval** to a duration appropriate to your experiment, but that will give your stage enough time to loop through all selected cells. The duration

selected here is the minimum total time any single cycle of measurements will take. That is, if your cells have all been recorded throughout a current cycle, MDA will wait until the interval duration elapses before starting the next cycle. However, you need to make sure the time it takes for the stage to scan through all the selected cells does not exceed the time interval you have set between your consecutive measurements of the same cell. In our hands, with the time-lapse intervals of 6-10 seconds, the number of cells you can measure is 15-25, depending on how close the cells are located in a dish.

7. Under **Save images**, set a suitable Directory root for your image-stacks to be saved under as well as a suitable Name prefix for the image-stack files. Image-stacks will be saved in a sub-folder named `<Name prefix>_<Incremental number starting at 1>` as `<Name prefix>_<Incremental number as inferred from the folder name>_MMStack_<Position name>.ome.tif`.
8. Under **Multiple positions (XY)**, click on **Edit position list...** to bring up the **Stage Position List** window. Here at the bottom of the window, un-check the use of the Z stage if your machine lacks the capability of digitally tracking vertical movement of the stage. All marked targets after this un-checking will only have their XY coordinates recorded. (see **Note 13**).
9. You are now ready to start selecting cells. Click on **Live** on the **Micro-Manager For Icy** main window. A sequence viewer window with a live camera feed will open. You are now ready to locate and select cells using either the camera or the microscope optics. Note that depending on your microscope you may need to switch between camera and optics output using a switch, valve, or lever on the microscope itself.

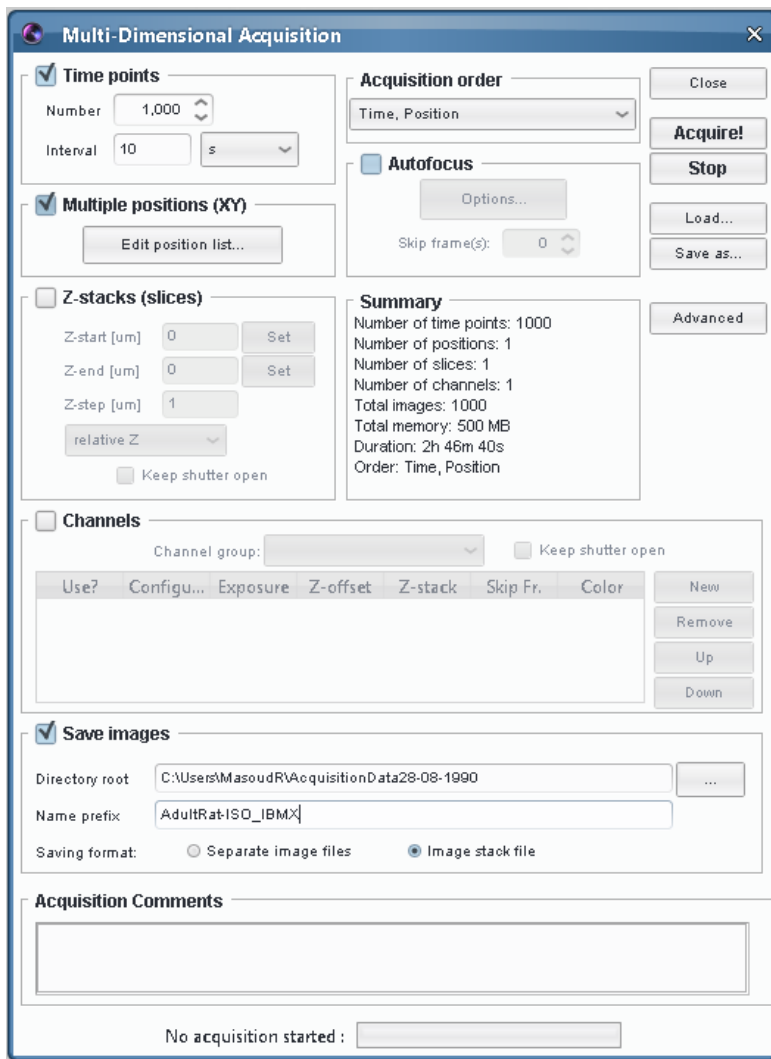




Figure 18. Example MDA set-up.


10. Using only a 3D joystick, move the stage until a target of interest is centred in your channels output. If available, use a mechanised vertical stage that uses either an encoder to inform Micro-Manager of vertical changes and record Z-coordinates in addition to X and Y, or an auto-focussing mechanism. You may use the manual focus knob on the microscope but beware that bringing a later target into focus may result in loss of focus for previous targets. With the lack of an encoder or auto-focus, you must find targets that are roughly within the same focal plane and you may use either the 3D

Joystick to focus or the manual focus knob on the microscope but beware that bringing a later target into focus may result in loss of focus for previous targets.

11. To select the target of interest, click  Mark on the **Stage Positions List** window. Note that the number of targets MultiFRET can support relies solely on your PC's hardware. Once an adequate number of targets have been selected, you may close the **Stage Positions List**.

i. To correct a mistakenly selected target, click on the entry within the **Stage Positions List** and then click the  Remove button on the same window.

ii. Targets listed in the **Stage Positions List** may be renamed by double clicking on the entry's label, or by selecting them and hitting the F2 key. Type in a unique label and hit the ENTER key to confirm.

iii. To check a previously marked target, select it in the **Stage Positions List** and then click on the  Go to button.

iv. Note that the positions list may be saved once selections are complete by clicking on the Save As... button in the **Stage Positions List** window. This will prompt you to save your currently marked targets and allows them to be loaded if you wish to restart Icy due to any mistakes. Loading a positions list is done by clicking on the Load button on the same window.

12. Start the MDA by clicking the **Acquire!** button on the **Multi-Dimensional Acquisition** window. This will open a sequence containing an image-stack for each position marked in the previous step. Every interval the stage will move to and capture a frame at each position, updating the sequences in the process. Each sequence viewer has a slider at the bottom which allows you to scroll through the image-stack. Note that

even when the sequence viewers are closed, Micro-Manager is still collecting frames for them in the background as the sequences themselves are still open.

13. Now start MultiFRET, either from the plugins tab on the top pane of the Icy main window or through the search bar. The first run of this plugin will show a terms of service window, if you wish to continue you must agree to the terms. Agreement will be saved in `C:\Users\\MFIOptions.cfg`. Note that this is a local home directory, not a network one.
14. A changelog message will pop-up in the lower right corner of Icy, showing the current version, date of the current version, as well as any fixes and new features that have been added in the current version. This message dismisses itself in 30 seconds, or when clicked on.
15. A Settings window will open containing several rows of options that may be enabled or disabled.
 - i. `Transform`: Enables the use of an algorithm to increase accuracy of channel alignment. Rotationally distorted channels in particular will benefit from this option. For this algorithm to function contour edges need to contain minimal deformities, as the algorithm uses the straight lines to detect channel corners. Note that there will be a few seconds of lag upon clicking the `Ok` button on this settings window, while the plugin runs its calculations. The run itself is further unaffected. It is recommended to keep this option on unless an error pops up after clicking the `Ok` button. The protocol will run with adequate accuracy regardless of this option if the channels are not rotated excessively.
 - ii. `Offline`: Enable this option if you are loading image-stacks into Icy for 'offline' analysis. 'Offline' analysis implies running through the rest of this protocol on not a

live captured image-stack, but on a previously saved one. A microscope and Micro-Manager are not required for an offline run, but you must use a contour created for the state of the beam-splitter at the time of the capture. Alternatively, you may use the image-stack to create a new contour file for it. The following steps are the same for either an online or an offline run, but the plugin will run much faster in the offline mode, as it will not need to wait for captures.

- iii. **CustomCalcs**: Enables the use of a custom calculations file as set up in the Custom calculations section of this chapter.
- iv. **Workspace**: Enables a convenient 'workspace' tab in the window that opens during the run. This tab will place all sequence viewers and graphs conveniently inside a scrollable section of the window, making them easier to manage. Recommended to be on for most purposes unless it is of utmost importance to be able to view all graphs or sequences, or both, simultaneously.
- v. **Select Contour-file**: Prompts you to select your contour-file. This is mandatory for the run.
- vi. **Select Calculations**: Prompts you to select your custom calculations file, as set up in the Custom calculations section of this chapter. The **CustomCalcs** checkbox on the previous row must be enabled.
- vii. **Save Settings**: This will save all options on this window to `C:\Users\\MFIoptions.cfg`. These will be automatically loaded on the next start-up of MultiFRET.
- viii. **Open a File**: This button opens a prompt for you to choose an output Excel workbook or a folder. Alternatively, you may manually enter a file or folder location in the adjacent text-box. If a folder is selected, a Datasheet.xlsx file will

automatically be generated. If an existing used Excel workbook is chosen, data will be amended to the end of this workbook in the form of new sheets. It is recommended to frequently change the used workbook, as interruptions of the run may result in corruption of the file.

- ix. Between the settings and the confirmation buttons you will find a real-time log of the settings loaded and changed in this window.
- x. Under the log you will find the **Ok** button which is used to confirm the settings, and the **Cancel** button which is used to close MultiFRET.

16. When the settings are as desired, click on the **Ok** button. If **Transform** was enabled, the next window may take a few seconds to load. All MDA acquisition windows are automatically minimised at this point. The **MultiFRET** window appears and contains a set of tabs on the left, one of which is **Workspace** (if it is enabled, which is recommended) and contains the sequence viewers. Otherwise, along with the **MultiFRET** window, a window for each of your marked positions will appear. Whether the sequence viewer is shown in the **Workspace** or as a separate window, these viewers contain a slider on the left allowing you to switch through channels in alphabetical order (as named during contour generation). Note that while the **MultiFRET** window is active, any frames captured by the MDA will automatically be stored for analysis by MultiFRET. This means that your data collection includes the time it takes for you to set up the ROIs in the following steps in your experiment (see section 21).

17. The mean intensity of fluorescence is calculated using Equation 1. wherein the mean intensity of signal (\bar{F}) in each ROI is calculated from the number of pixels n in the ROI and the intensity x of each single pixel i . Under the **Corrections** tab, enable any

further live corrections required. By default, this tab will contain the option to enable live background correction on a per-channel basis using Equation 2.

18. If enabled, custom calculation will also appear here. Save the enabled calculations for future runs by clicking the `Save corrections and last ROI channel selection` button at the bottom of this tab.

19. To proceed, you must draw an ROI for each region of interest in your sequences, and a single background ROI for each position (each sequence). Note that a sequence may have multiple ROI that will all be corrected against the same background ROI. These ROI can be drawn manually using the ROI tools in the `Region of interest` tab in the Icy main window top pane. It is recommended to use `Polygon` ROIs for your targets, and to save time use either `Circle` or `Square` ROIs for the background ROIs. ROIs can be selected on the image or in the right-pane ROI tab, be moved through dragging or editing the position values in the right-side pane, be deleted using the DEL key, and modified in every way including colour and label. As always, if you change the labels make sure they are unique.

20. The tab-list on the left side of the MultiFRET window also contains a tab for each of your marked positions. Every ROI drawn on your images will appear in the appropriate tab as a series of settings. The first drop-down list chooses the numerator for the fluorescence ratio calculation, while the second drop-down list chooses the divisor. Finally, there will be a checkbox to designate the ROI as a background ROI. Doing so will ignore and grey out the numerator/divisor settings. If enabled, custom calculations checkboxes will appear after the background checkbox. Each ROI may be designated to be used as one of the variables in your custom calculation equation. Importantly, selection of any of the basic settings here will be committed to memory and

automatically applied to any ROI drawn hereafter. This makes it efficient to first draw a single target ROI, adjust the settings, and then draw the rest of them. Similarly, it is most efficient to draw one background ROI, designate it as such, and then draw the rest of them. The memory of the last chosen ROI settings may be saved to `C:\Users\\MFIoptions.cfg`, using the `Save corrections and last ROI channel selection button` at the bottom of the corrections tab.

21. As an alternative method and time-saver compared to manually drawing the ROIs for your targets, you may use the `Detect` button at the bottom of the `MultiFRET` window to use the automatic detection function to draw a single ROI per sequence automatically. Under the `Detection` tab, you may choose the method for an automatic ROI drawing functionality built on the Active Contours plugin by A. Dufour et al. 2011.

- i. `Max Pixel`: This method will find the highest intensity pixel in your image and use it as a starting point to draw your ROI. This method is recommended unless your sample features bright artifacts.
- ii. `Whole Frame`: This method will use the borders of your channel as the starting point to draw your ROI.

22. At the bottom of the window, find the `Max. Iterations` text-box and its `Detect` button. `Max. Iterations` controls the amount of time afforded for the automatic ROI drawing function. It is at 10000 by default, which is normally sufficient. This may be raised if ROIs are drawn unfinished but doing so will increase the duration of the automatic detection procedure.

23. Note that the automatic detection of ROI is not always perfect, so make sure to double-check all ROI. Note that the **Detect** button will first clear any currently drawn ROIs and will not draw background ROIs. (see **Note 14**).
24. If using multiplexed biosensors with the adequate number of channels to measure each separately, you may duplicate your target ROI as many times as required and assign different numerator and divisor channels to each.
25. Finally, one of the last few buttons at the bottom of the **MultiFRET** window is the **Milestone** button. This will create a mnemonic marker allowing you to designate when you have applied experimental events such as the addition of a drug. This button's effects are only visible once the Start button has been clicked and the graphs are generated but it may be used during the ROI set-up phase, allowing experimental events to be registered even while setting up the MultiFRET live calculations.
26. Click on the **Start** button at the bottom of the **MultiFRET** window when all sequence viewers contain at least one target ROI designated with the correct numerator/divisor, and exactly one background ROI designated as such, see Figure 7. All frames captured by the MDA between the appearance of the **MultiFRET** window and now will automatically be processed, generating a graph with all live corrections for each sequence. These graphs will either show as separate windows or inside the **workspace** tab if it is enabled. All further captured frames will automatically be processed and shown in the same way after every capture interval. Every Milestone will appear both as a list at the bottom of the **MultiFRET** window as well as a marker on the graphs. Graphs may be zoomed in and out on, and a right-click brings up options to set automatic axis constraints.

27. When your experiment has concluded, first, make sure the designated output Excel workbook is not open, then click on the **Stop** button; this will bring up a prompt window allowing you to select whether the MDA should also be stopped, and whether its sequences should be closed. When stopped, MultiFRET will close and instruct Excel to write the data into a workbook and open it. Excel may take a few seconds to complete this procedure, and it is important to keep Icy open until the Excel workbook appears. Premature closure may corrupt the workbook. (see **Note 15**).
28. To proceed to the next experiment, you have to clear the positions list using the **Clear All** button in the MDA **Stage Position List** window; make sure all sequences have been closed and repeat this protocol from step 7.

3.3.1.8. MultiFRET Protocol Notes

- 1)
 - a) As the provided email address refers to a university account, it may be closed in the future. As such feel free to CC the personal account at masoud.ramuz@gmail.com, or if privacy is a concern contact the account at masoud.ramuz@tutanota.com.
- 2)
 - a) In Windows: When starting Icy, if an error message is encountered saying that the JAVA_HOME environmental variable is not set, first locate your Java installation directory (example: `C:\Program Files\Java\jre1.8.0_251`), then hit WIN+R and enter `SystemPropertiesAdvanced` and click on Environment Variables in the subsequent window, next add a new system variable with the name `JAVA_HOME` and the path to your java installation directory, and finally adjust the system Path variable by adding `%JAVA_HOME%\bin` as a new entry.

b) On Mac: If your security settings deny access to Icy, you will need to use

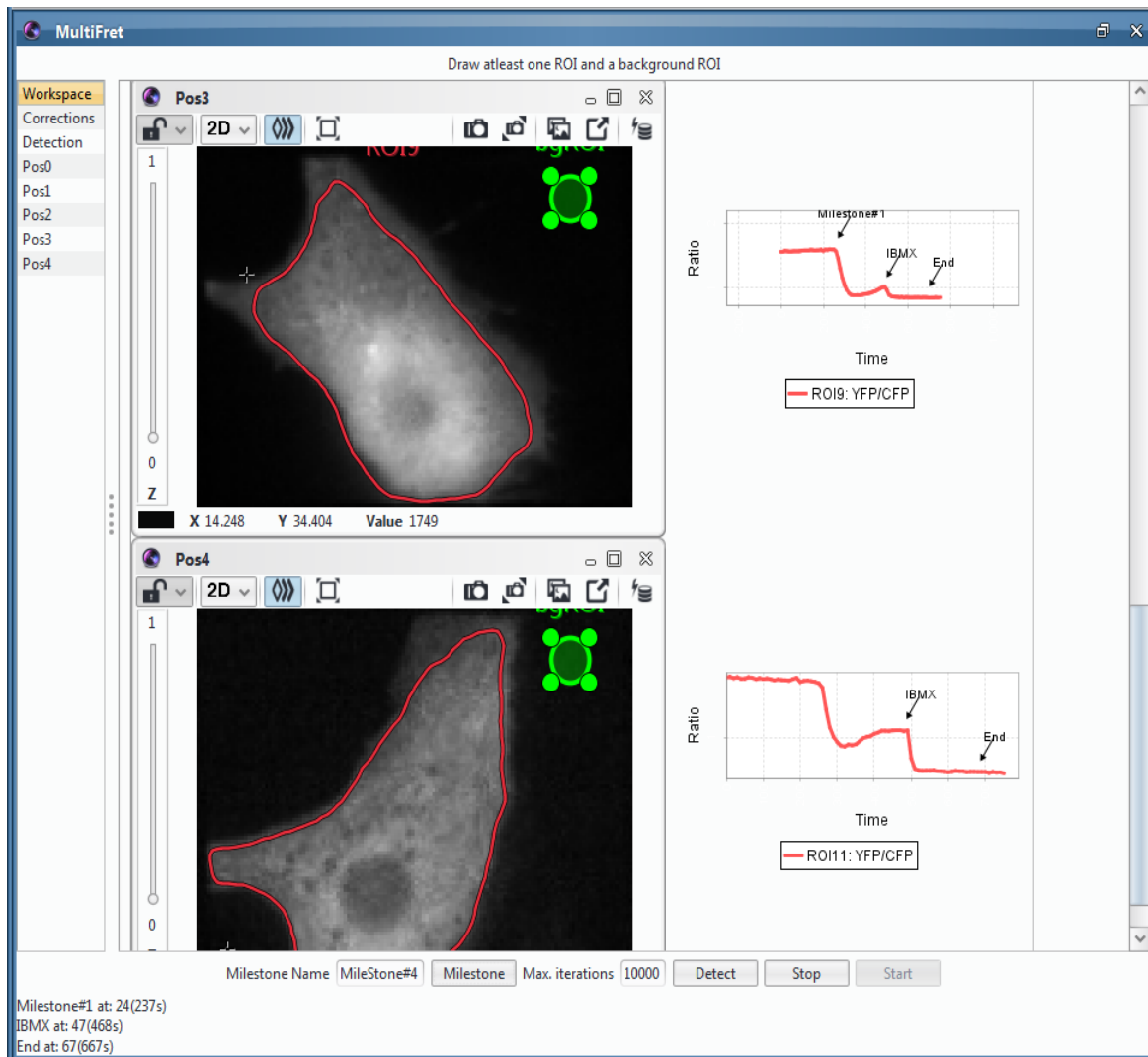


Figure 19. An example of MultiFRET workspace showing 2 viewports of different position captures and their corresponding live charts. NRVMs were transfected with Epac- S^{H74} cAMP sensor and the YFP/CFP ratio was displayed upon stimulation with 100 nM isoproterenol, designated as the automatically generated “Milestone#1”. After a plateau was established, cells were saturated for cAMP by use of phosphodiesterase inhibitor IBMX, designated by the user-generated “IBMX” marker. Finally, the End of the experiment was also marked by the user. Note that the top chart has been zoomed out for demonstration purposes.

control+click and choose **Open**, to bypass them.

c) On Linux: Make sure to start Icy from its folder to ensure proper loading of VTK libraries. If your distribution shows incompatibilities, you may need to install or

compile the dedicated VTK package with java wrapper and move the library (*.so) files to the icy `lib/linux64/vtk` folder.

3)

- a) Icy has a built-in Plugin installer which can be accessed from the plugins tab, or through the search-bar. Additionally, any uninstalled plugins searched for through this same bar can be installed by clicking on the search result. Currently, MultiFRET is not included in the automated plugin installer, however the ActiveContours plugin needed for this protocol is. Icy should come with a Micro-Manager plugin installed, if not this can also be acquired in the same way. Do note that this plugin is not an actual Micro-Manager installation, Micro-Manager 1.4 or later should be installed separately from <https://micro-manager.org>. A link to this download is also provided if the plugin is launched without a Micro-Manager installation.

4)

- a) Note that after this initial setup, the Micro-Manager plugin may not work initially and yield an error when launched. This can be resolved by restarting Icy. If a further error is encountered this may indicate a conflict between the OS architecture the downloaded micro-manager installation is built for and that of the Java version installed. To clarify, if 64-bit Java 8 is installed Icy will launch in 64-bit and be unable to launch a 32-bit Micro-Manager installation through its plugin, and vice versa.
- b) When launching Micro-Manager within Icy you may be prompted to register, unless you have already done so or already clicked “Never” within the standalone Micro-Manager application. You may notice that the registration window within Icy lacks the “Ok”, “Later”, and “Never” buttons, this is a result of the way Icy internalises windows. The buttons are still present, but the layout will not show them.

However, one may still navigate to and use the hidden “Never” button by activating the lowest text input field and using three presses of the Tab key followed by Enter or Spacebar.

5)

- a) If your hardware is not yet supported by Micro-Manager, either search online for a compatible driver built by someone or to build your own driver refer to this guide:

https://micro-manager.org/wiki/Building_Micro-Manager_Device_Adapters

6)

- a) If your brightfield illumination source does not have sufficient power to clearly illuminate the channels, you may use the brightness and contrast controls after capturing a frame in step 3 to achieve the same effect.
- b) If a channel is not lit up evenly, i.e. there is a gradient, you may have to adjust the positions of your mirrors if you are using a beam-splitter.

7)

- a) As the next step uses an edge-detection tool designed for cells, you may be quite rough and inaccurate with the ROI drawings.
- b) If for any reason you prefer to contour your channels manually and skip the next step, it is recommended to use the polygon ROI tool to do so. Using the mouse-wheel allows you to zoom in and out on the capture, for enhanced accuracy. Note that for comprehensive realignment algorithms to work, you require the plethora of only points provided by the next step.

8)

- a) If for any reason Active Contours did not come installed, install in either the same way as launching it through the search bar, through the Online Plugin installer, or from this URL: <http://icy.bioimageanalysis.org/plugin/active-contours/>

9)

- a) If the contour encompasses dead space around the channel, this may be resolved by increasing contrast between channel space and the unused camera chip space around it in the following ways:
 - i) Increase bright-light output and further close diaphragm.
 - ii) Use the **Histogram and colormap** settings on the right-side pane under the **Sequence** tab to enhance contrast by dragging the lines in the histogram to bound only relevant intensities (typically a peak) and drag a point upwards in the colormap to further increase the brightness.
- b) If too many contours are shown in the ROI list, this may be due to accidental duplication of initial ROIs, or by running **Active Contours** again while the contours are already present. Since contours are ROI themselves, they may be used as new starting-off points for subsequent contours.

10)

- a) If at any point you see a precipitate forming in the first tube, this could be the result of either too much DNA or adding your reagents before adding the DNA. Make sure to add DNA to the Opti-mem before any lipofectamine reagents.

11)

- a) For enhanced transfection efficiency, there are two alternative methods you may use:
 - i) Mix the transfection mixture with the cell suspension just before plating.

- ii) Aspirate the medium from the Mattek dish, add the transfection mixture onto the glass-bottom well containing the cells and then incubate for 3 hours before adding fresh medium on top.

12)

- a) Memory here refers to storage memory, you can increase the amount available to your computer by upgrading your HDD, SSD, or connecting an external drive of either type.

13)

- a) Note that the `Stage Position List` window is not an Icy internalised window. This may be resolved in a future update to Icy, but currently brings with it several issues:
 - i) The `Stage Position List` window may be hidden behind the Icy main window. Hold down the ALT key and hit the TAB key multiple times to cycle through open desktop windows, find it and release ALT bring it back to the front.
 - ii) Experience has prompted the theory that resizing or perhaps even moving the `Stage Position List` window may result in a crash while running the MDA later. It is best to leave the dimensions and position of this window alone once it is open, and close it when you are finished using it. If a crash occurs, it is important to terminate any lingering Icy process. Do to so use CTRL+SHIFT+ESC to open the task manager, click on More Details on the bottom left if needed (depending on your version of Windows and previous task manager usage), then find and end every instance of the `Java(TM) Platform SE binary`, or `Java.exe`. On any other operating system, use the appropriate process manager to do the same.

14)

- a) Using the automatic detection function will save much time in this process, but it is not a one-button solution. ROIs may be drawn in the wrong position or may incorrectly include background space. Importantly, ROIs automatically drawn may also encompass the area outside of the bounds of your image (Figure 20). This makes it important to quickly zoom out on each image, using the mouse-wheel, to see if the ROI is put where it should be. Should there be one or more erroneous ROIs, it is important to replace these: select them either through the right-hand pane **ROI** tab or by simply clicking on the ROI in the viewport, then hit the DELETE key, and finally replace the ROI using the **Polygon** tool under the top-side **Region Of Interest** tab.
- b) For increased efficiency, copy and paste the same background ROI quickly into each sequence and drag them to a suitable location. This saves the time of having to click on the ROI drawing tool over and over.

15)

- a) If your experiment concludes prematurely for any reason and your Excel workbook output has not been completed, it is still possible to retrieve your data. All data acquired automatically has a back-up amended to a text-file in real-time. This text-file may be found in **C:\Users\\MFI**, along with a log file containing run-time information useful for debugging.
- b) If you end your experiment but MultiFRET cannot find your designated Excel workbook or the workbook is opened or busy for any other reason, you will get a prompt when hitting the **Stop** button. This prompt contains a **Retry** and a **Choose other .xlsx file...** button. **Retry** allows you to close the Excel workbook or place it in the designated location and have MultiFRET attempt to

write to it again. `Choose other .xlsx file...` opens a file chooser, allowing you to select a folder where a Datasheet.xlsx file will be generated or an existing .xlsx file. Alternatively, you may type in the name of a non-existing .xlsx file and it will be generated for you.

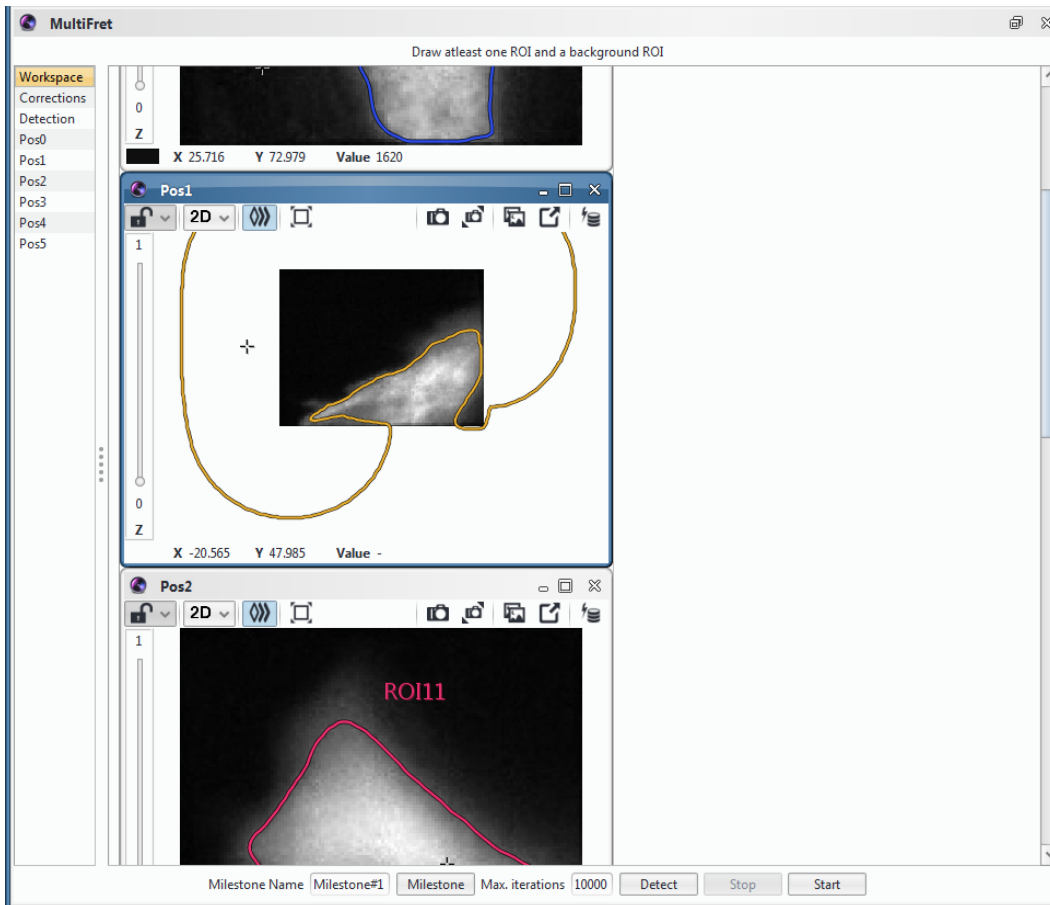


Figure 20. The Pos1 viewport shows a possible error in cell-detection when using the automatic cell contouring function. Note that the viewport has been zoomed out to fully display the nature of this error.

3.3.2. Software validation

We validated our software by measuring FRET in various cardiomyocyte models transgenic for cAMP sensors with both the new MultiFRET plugin and the old low-throughput macro that has been used for FRET experiments in many previous studies. Comparing the software in adult epac1-camps transgenic mice stimulated with 30nM β - AR agonist Isoproterenol

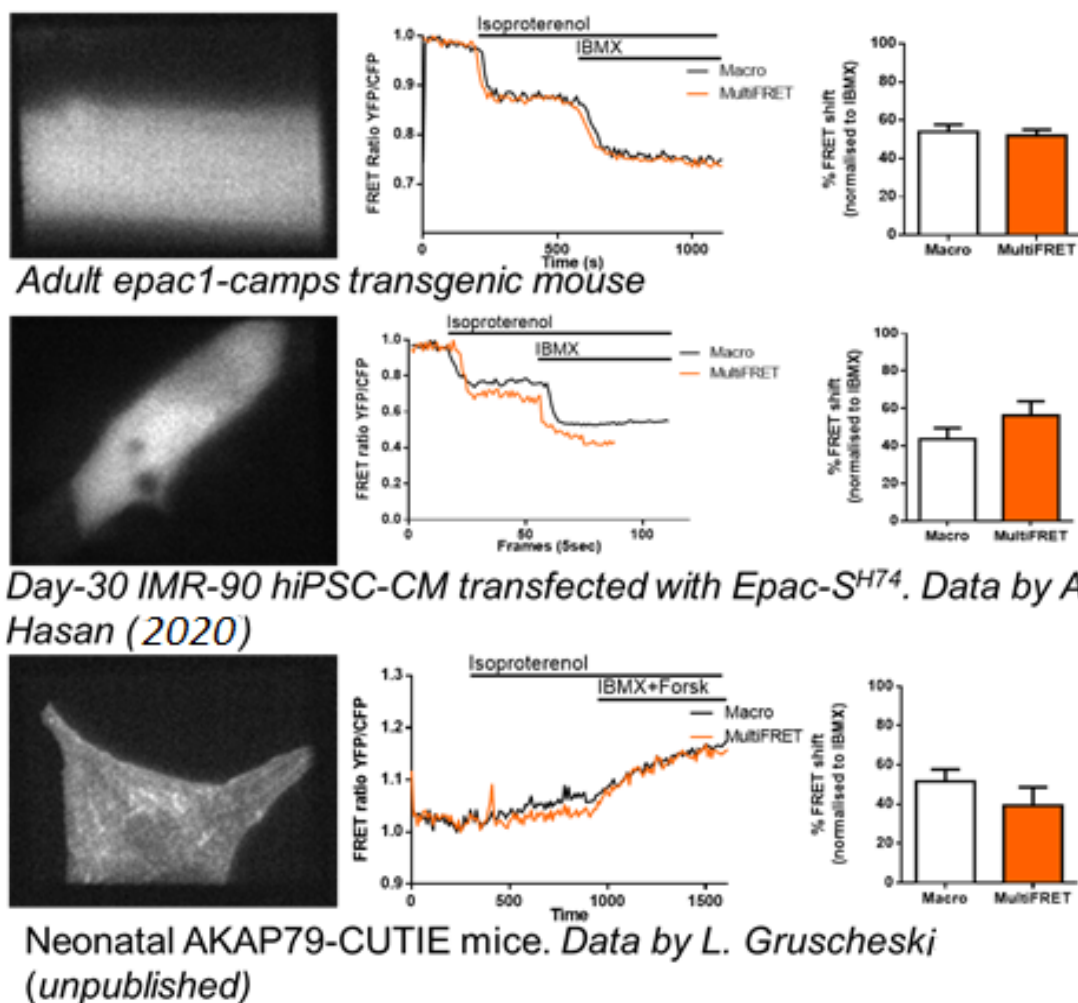


Figure 21. Comparison of MultiFRET to the previously standard macro in various models

for cAMP detection shows no significant difference between the software. ns with $P \geq 0.05$

Welch's unequal variances t-test

and normalising against 3-isobutyl-1-methylxanthine (IBMX) we find no significant difference between the macro and MultiFRET (Figure 21). This is similar to experiments by A. Hasan (unpublished) in D30 HiPSC-CMs, which following the same experimental protocol

showed no significant difference between the macro and MultiFRET. Another dataset acquired by L. Gruscheska (unpublished) shows the same non-significance in neonatal mice transgenic for the AKAP79-targetting CUTiE sensor.

3.4. Discussion

We have developed a new high-throughput software plugin that will allow researchers unprecedented efficiency, increasing the number of cells that can be obtained from a single dish of cultured cells and experimental protocol by over 50-fold, a number that is only currently limited by the power of our own computer's hardware. Our new software boasts high flexibility, ease of use and is usable with any model that expresses bioluminescence. We show evidence that the new software yields data per cell that is not significantly different from the methods discussed in the introduction of this chapter that have been used for almost a decade in any way other than the rate of data output and ease of acquisition. The software is made to be future-proof, and as such is open-source and allows easy addition of new features that may be required by future experiments. The MultiFRET software is already under extensive use within our own research group, which has yielded user-feedback driven improvements. While the software had existed for less than a year at the time, an early version of MultiFRET was successfully used in a study of cAMP in maturing HiPSC-CM (Hasan et al. 2020). Our validation data along with the MultiFRET tool have been published [Cells – IF 4.829] Special Issue "New Advances in Cyclic AMP Signalling" (Ramuz et al. 2019). We additionally have a paper under preparation, focused more on the protocol and technical aspects of using the MultiFRET software, to be published in the Springer journal special edition "Methods in Molecular Biology".

3.5. Limitations and Future Work

Our primary limitations ensue from the lack of hardware. While this is to be expected as MultiFRET is designed to work on limited hardware, for the sake of flexibility it would be beneficial to have access to different types of FRET microscopes. One major example of this is a spinning disc microscope. While our systems use beam-splitters to visualise multiple channels of light, spinning disc microscopes quickly switch between different filtration mirrors through a rotary mechanism. While MultiFRET should in theory function on such a device, there had been no possibility to test whether it does.

MultiFRET was initially designed to support viewing more than two channels simultaneously and while it has been found capable of doing so in-silico by using demo camera feeds, we lacked the compatible sources of luminescence to test this under our microscope.

Finally, since MultiFRET values efficiency above all else, it was my idea that a dish-scanning functionality would aid in completely freeing up the user during the now most time-consuming part of the protocol: finding appropriate targets in the sample. Initial work has been done towards this goal, with a dish scanner moving between two user-designated X/Y boundary coordinates in increments calculated through a calibration step to be the visual window. This feature of MultiFRET records a still image after each increment of movement, finally giving the user a list to choose from upon completion of the scan. After selecting images from this list, the coordinates associated with each image are then fed into Micro-Manager's MDA, allowing the rest of the protocol to be followed as described previously. However, since the calibration steps are not user-friendly and hardware control could risk damage to the device, I decided not to release this feature until further optimisation and testing had been completed. Finally, once all of this has been completed the next and final

step for MultiFRET would be in the use of supervised machine learning to automatically select images from the list obtained by scanning a sample. While such approaches require calibration per cell-type and microscopy set-up, and may yet not be without false positives, there would still be a rise in efficiency and these issues could be solved with user-guidance.

Chapter 4: Sensor Selection and Transgenic Line Development

4.1. Introduction

Here we compare available cGMP sensors to find a suitable one for further study of the cGMP pathway in aging HiPSC-CMs and multiplexed FRET together with a cAMP sensor to examine cross-talk in HiPSC-CMs. We also perform work towards generation of a transgenic line expressing a cAMP biosensor to remove the need for transfection. The three sensors examined in this chapter have not previously been compared in aging HiPSC-CMs. As discussed in chapter 1.2. both cAMP and cGMP are essential for the regulation of contraction in aging cardiomyocytes, yet there is a lack of developmental knowledge of the cGMP pathways as only recently have sensors been made available that are sensitive enough to measure the low cytosolic cGMP levels (Götz and Nikolaev 2013). In particular, we want to select the optimal sensor for multiplexed FRET with an extensively used TEV sensor for cAMP, allowing us to examine cross-talk between the cAMP and cGMP pathways.

The sensors were studied under conditions of stimulated cGMP production in order to choose a suitable sensor for follow-up experiments. The three sensors compared here all have suitable selectivity towards cGMP over cAMP to overcome the 100-fold difference in cytosolic concentration (Börner et al. 2011; Götz et al. 2014) and were compared based on reproducibility of results as well as function within the cytosol. Secondary to this first aim we wanted to create transgenic HiPSC lines bearing cAMP and cGMP FRET sensors, which would eliminate the need of transient transfection of subsequently produced HiPSC-CMs. For this we first aimed to generate CRISPR/Cas9 gene editing plasmids to create a transgenic cAMP line, with the intention to reiterate this with our cGMP sensor once chosen. A transgenic HiPSC line expressing a biosensor would drastically increase yield of cells viable for experimentation as well as reduce costs in transfection reagents.

4.1.2. *Measuring cyclic nucleotides with FRET*

Since its discovery more than 50 years ago (Ashman et al. 1963), cGMP has been studied extensively and several sensors have been made starting with parallel development of CGY-Del1 and Cygnet, both based on cGKI α , which is more sensitive to cGMP than the beta variant (Newman, Fosbrink, and Zhang 2011; Sprenger and Nikolaev 2013). As with cAMP sensors, these consist of a binding domain flanked on both sides by CFP and YFP fluorophores (Figure 22). However sensitivity of the sensors was found to be lacking so two more were developed, first, cGi-500 which was based on Cygnet truncated at the C-terminal, deleting the catalytic domain in the process (Russwurm et al. 2007). The resulting shorter sensor was much more sensitive and faster. When cGi-500 binds to cGMP the fluorophores part, resulting in a decrease in measured FRET. Second, a sensor based on the PDE5 cGMP binding GAF domain was developed and named CGES-DE5 (Bork and Nikolaev 2018; Jalink 2006; Nikolaev, Gambaryan, and Lohse 2006). In contrast to the cGi-500 sensor, the CGES-DE5 sensor closes the distance between their fluorophores when binding cGMP, resulting in an increase in measured FRET. The cGi-500, and CGES-DE5 sensors have since been modified with the enhanced eCFP and cpVenus fluorophores, and a novel yet unpublished ScGi sensor has been made as an improvement on cGi-500 (Table 3). ScGi was kindly donated to us by the group of Dr. Kjetil W. Andressen and is made through a single amino acid mutation (C173R), unpublished data shared with us through personal communication from Dr. Andressen shows that it has a high EC₅₀ of 0.2 μ M and is 500 times more selective for cGMP over cAMP. These numbers dwarf both the high affinity of the cGi-500 sensor with an EC₅₀ of 0.5 μ M (Russwurm et al. 2007), as well as the selectivity of the CGES-DE5 sensor which is 420 times more selective for cGMP over cAMP (Nikolaev, Gambaryan, and Lohse 2006). The cGi-500 and CGES-DE5 sensor function has been tested in

several model organisms and tissues which do not appropriately describe their function as per our own goals. cGi-500 has been used in adult mouse smooth muscle cells and has been shown to yield a decreased YFP/CFP ratio under stimulation with the NO donor DEANO and natriuretic peptide CNP (Götz et al. 2014). CGES-DE5 has shown similar FRET dynamics in adult rat cardiomyocytes stimulated with natriuretic peptide CNP and PDE blocker IBMX (Subramanian et al. 2018). In this chapter we show experiments that for the first time test these sensors in HiPSC-CMs aged to day 30, then we compare these results to data we obtain from identical experiments in NRVMs used as a more mature cardiomyocyte model. We use an early version of the MultiFRET software, development of which was described in chapter 3., which lacks the high-throughput capability and uses a rudimentary but functional, albeit less accurate, computational method for the correction of channel misalignment described in chapter 3.1. This means that only a single cell was measured per dish and that it was necessary to take great caution in regard to calibration of the beam-splitter and selection of ROIs. We use an experimental protocol similar to Gotz et al. 2014 by stimulating with CNP, which they have shown to yield the highest cGMP response out of the three main natriuretic peptides ANP, BNP, and CNP, and by normalising to an IBMX saturation plateau.

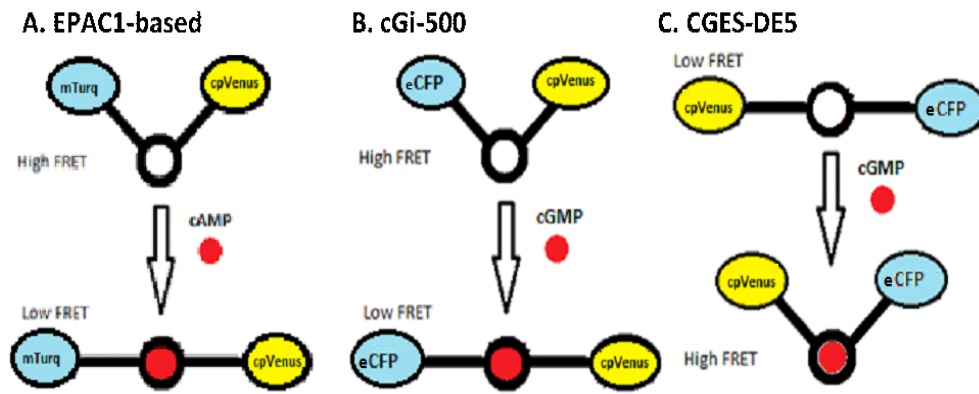


Figure 22. Schematic representation of sensors used in this project, drawn from N to C terminus. A) Epac1-based sensor flanked by mTurquoise and cpVenus. B) cGKI α -based sensor flanked by CFP and YFP. C) PDE5-based sensor flanked by CFP and YFP.

Table 3. cGMP sensors compared in this chapter.

Sensor	Binding Domain	EC50	Selectivity cAMP/cGMP	Source	Sequence schematic	FRET direction
CGES-DE5	PDE5	1.5 μ M	420	V.O. Nikolaev, Gambaryan, and Lohse 2006, Nature Methods		↑
cGi-500	PKG	0.5 μ M	100	Russwurm et al. 2007, The Biochemical Journal		↓
ScGi	PKG	0.2 μ M	500	Kjetil W. Andressen et al., unpublished		↓

4.1.3. Transgenic Line Development

For the generation of our transgenic line we decided on the use of CRISPR/Cas9, for which there are several methods available: conventional homology-directed repair (HDR) based insertion, nickase HDR-based insertion, piggyBac transposon-based insertion and HDR using targeting by single-stranded oligo DNA nucleotides (ssODN). Conventional CRISPR/Cas9 insertion involves the use of two plasmids, the first of which has a guide RNA (gRNA) sequence which is complementary to the target region and the Cas9 coding gene which will introduce a double-stranded break (DSB) in the target region (Mali, Yang, et al. 2013). The target region needs to be directly adjacent to a Protospacer Adjacent Motif (PAM) sequence which serves as a binding signal for the Cas9 protein, with the exact PAM sequence depending on the Cas9 protein used. After the DSB, DNA can be repaired through either

non-homologous end-joining (NHEJ) which causes indels, or HDR which uses the DNA we provide in a second plasmid as a template. This second plasmid contains the gene of interest flanked by arms homologous to the target region (Figure 23A). The nickase method (Figure 23B) uses a modified Cas9 that generates a nick rather than a DSB. For this method two gRNAs are required to target opposite DNA strands in order to create a double nick which can be repaired via NHEJ or HDR (Mali, Aach, et al. 2013). The advantage of the nickase method lies in the need for two distinct gRNAs, increasing the specificity of the insertion (Shen et al. 2014). The more recently developed piggyBac transposon-based method (Figure 23C) relies on a combination of a transposon and a transposase originally discovered in moths in 1983. With this method the transposase inserts the gene of interest into a random TTAA site throughout the genome. Three major advantages of this method are a significantly enhanced insertion efficiency, a one-step insertion and the possibility to remove the inserted DNA seamlessly (S. Li et al. 2017). Gene editing using ssODN-mediated CRISPR/Cas9 is a method similar to conventional CRISPR/Cas9 except in the use of a single-stranded DNA (ssDNA) donor rather than a double-stranded one (dsDNA). dsDNA donors are more likely to be incorporated in the genome through NHEJ, which results in duplicate homology arms or partial incorporation of the template. The tendency to be used in NHEJ also increases the likelihood of insertions into off-target or naturally occurring DSBs. ssDNA donors show greater efficiencies and allow shorter homology arms, but their major downside is that only small edits can be made in this way, as larger ssODN bring severely increased cytotoxicity (Okamoto et al. 2019). ssODN are generally between 60-200nt in size, with most of these nucleotides being the homologous arms flanking the mutation (Yang et al. 2013; Yang, Wang, and Jaenisch 2014). For our gene editing purposes we made use of the conventional CRISPR/Cas9 method, as there were ready-to-use and well-documented

plasmids available. We used the pAAVS1-Nst-CAG-DEST plasmid which contains a CAG promoter and homologous arms for the AAVS1 locus, a locus that has been shown to not yield any noticeable physiological changes when modified. This plasmid has been shown to yield successful results when used with the pXAT2 plasmid containing a compatible gRNA and a Cas9 sequence (Oceguera-Yanez et al. 2016). For the selection procedure we use a combination of the protocol detailed by Hendriks et al. 2015 and an in-house protocol which has previously been found successful.

4.1.4. Aims

- ❖ To select a suitable FRET sensor out of three available sensors with high cGMP selectivity.
- ❖ To create two transgenic IMR-90 lines expressing cAMP and cGMP sensors respectively.

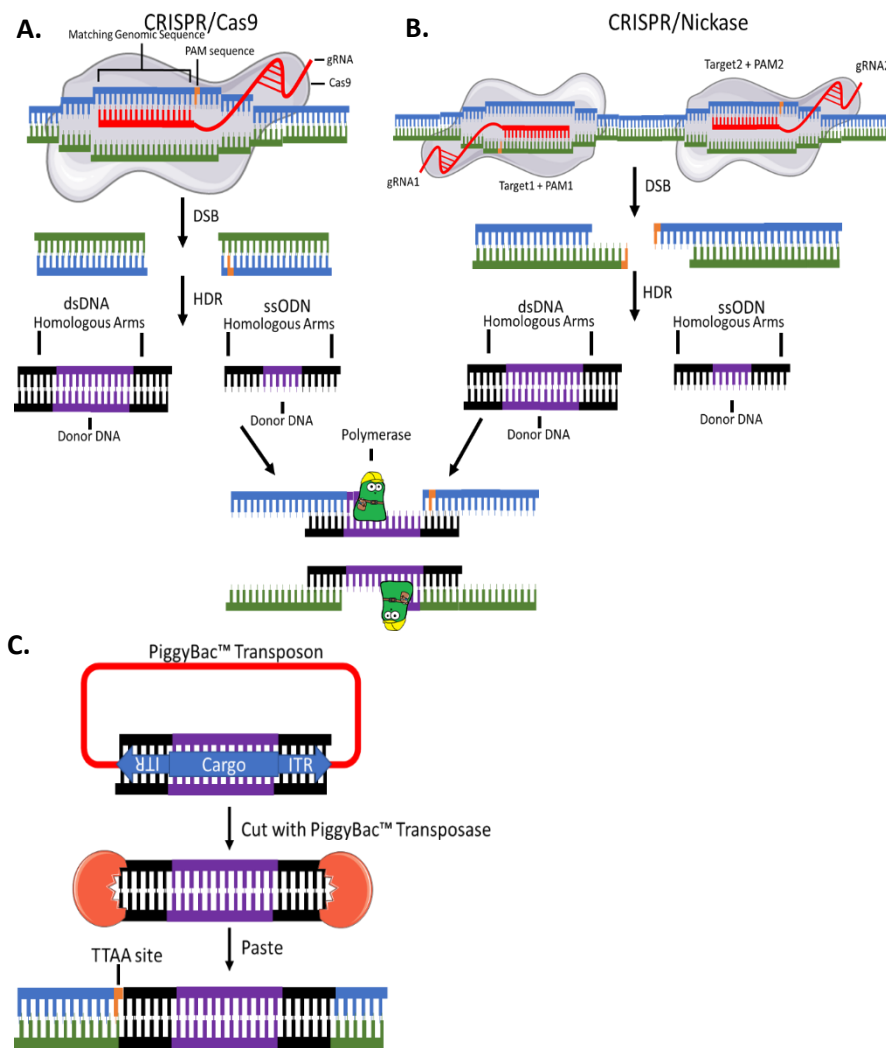


Figure 23. **A.** Schematic representation of the conventional CRISPR/Cas9 method as well as the use of ssODN instead of dsDNA. The gRNA guides Cas9 to the target sequence at a PAM site, Cas9 then creates a DSB which can be repaired through NHEJ or HDR. During HDR donor DNA can be inserted into the host genome. **B.** Similarly a schematic representation of CRISPR/Nickase using two gRNAs making single-stranded breaks at two locations. **C.** Schematic representation of the PiggyBac™ transposon system using Transposase to cut a cassette containing Cargo DNA flanked by two Inverted Terminal Repeats (ITR), and paste this in any TTA site in the host genome.

4.2. Methods

4.2.1. FRET Microscopy Preparation

NRVMs and HiPSC-CMs were obtained as described in chapters 2.2. and 2.3. respectively. Cells were plated in MatTek dishes, as described in chapter 2.3. and transfected as described in chapter 2.5. with one of three of the sensors described in chapter 2.4. as well as in Table 3.: CGES-DE5, cGi-500, or ScGi. The medium in a MatTek dish containing transfected cardiomyocytes is aspirated and replaced with 500 μ L of pH 7.4 FRET buffer (purified Milli-Q water containing 144mM NaCl, 5mM KCl, 10mM HEPES and 1mM MgCl₂) before being firmly affixed onto the stage of our QuadView microscopy system and lowered onto a 60x Nikon oil immersion lens with a droplet of oil on top. The MultiFRET protocol detailed in 3.3.1. is followed but adjusted to an older version of the software, which lacked workspace, high-throughput, and enhanced transformation options. Micro-Manager MDA is set to measure each selected cell every 10 s and save to an image-stack for back-up. Background correction is used for both the CFP and YFP channels and MultiFRET is set to yield YFP/CFP ratio-metric data. During the experiment, drugs are added diluted in volumes of 500 μ L of FRET buffer to ensure rapid circulation into the dish's buffer.

4.2.2. cGMP FRET sensor comparison

The FRET sensors CGES-DE5, cGi-500, and ScGi (for details see section 2.4.) were compared using either 100 nM CNP, 100 μ M GSNO, or 100 μ M GSNO followed by 100 nM CNP as a stimulant of cGMP release. After the cGMP response plateaued the cells were saturated with 100 μ M of IBMX, to which the ratio-metric YFP/CFP FRET response obtained from the cGMP stimulant was normalised.

4.2.3. Primer Design

PCR primers for the generation of aavsCAGdest-scgi were designed in the multi-purpose suite Benchling and were ordered from Sigma-Aldrich in a desalted dry format. Primers were diluted to 10 μ M before use. Sequencing primers were designed using Primer3Plus, only forward primers were used in this case. See Table 4.

Table 4. Primers used in this work. Cyan highlighting indicates complementary sequence, while greyed out bases are overhangs. Lower-case bases indicate restriction enzyme sites, with the restriction enzyme indicated in the primer name. Number ranges in the primer names indicate the sequence range covered for sanger sequencing.

PRIMER NAME	PRIMER SEQUENCE
SCGIF-SBFI-6BP	5' TATAATcctgcaggACTAGAGAACCCACTGCTTACT 3'
SCGIR-PACI-6BP	5' ACGGTAttaattaaTGAACAAGAGTCCACTATTAA 3'
AAVSCAGDEST-SCGI 5535-5554	5' CATTGCCTTTTATGGTAATC 3'
AAVSCAGDEST-SCGI 6935-6956	5' GGTAAGGTTGAAGTTACAAAAG 3'
AAVSCAGDEST-SCGI 7662-7680	5' TGACCCTGAAGCTAATCTG 3'
AAVSCAGDEST-SCGI 8338-8355	5' TAGTTGCCAGCCATCTGT 3'
AAVSCAGDEST-SCGI 9063-9080	5' ATCTCTCTCCTTGCCAGA 3'
AAVSCAGDEST-TEV 7008-7026	5' AGATGATTTTGGACAGCTG 3'
AAVSCAGDEST-TEV 8424-8441	5' AGTCCGGAAGCTGTACTC 3'
AAVSCAGDEST-TEV 9789-9806	5' GACCCTGAAGCTGATCTG 3'
AAVSCAGDEST-TEV 10486-10507	5' GTCTCCTGATATTGGGTCTAAC 3'

4.2.4. Restriction Enzyme Digest

Restriction enzymes purchased from NEB were incubated with purified DNA in the appropriate NEB buffer at 37 °C for 1 hour, after which an enzyme deactivation step was used depending on the enzyme.

4.2.5. Ligation

For our ligation we followed manufacturer protocol, using 1 μ L T4 ligase in 20 μ L 1 X T4 DNA Ligase Buffer with a Vector:Insert ratio of 1:4. The ligation mix was incubated at 37 °C for 10 min after which the mixture was used to transfect competent cells.

4.2.6. Gel electrophoresis and Purification

Agarose gel is made by dissolving agarose powder in 1 X TAE buffer (diluted from 50 X TAE: 2 M Tris, 50 mM EDTA disodium salt, 1 M acetic acid in 1 L deionised water) at 1% to separate bands under 8 kb and 0.5% for larger bands. The agarose mixture is microwaved until the powder dissolves and when it cools down to \sim <40 °C 2.5 μ L of ethidium per 50 μ L of agarose mix is added. The mixture is poured into a tray with a comb to create slots for the DNA. After the gel cools down and solidified 1 X loading buffer is added to the DNA which is loaded into the slots on the gel. The gel electrophoresis is run for 2-3 hours at 80V to separate the DNA bands. These bands are then imaged and cut out under UV light after which purification was performed using a Qiagen gel purification kit.

4.2.7. Bacterial Culture

NEB 5-alpha Competent E. coli cells were thawed on ice from -80 °C, 100 ng of plasmid DNA was added to the cells and the tube was flicked 4-5 times to mix. The mixture was placed on ice for 30 min before a heat shock is applied at 42 °C for 45 seconds. Afterwards the mixture was placed on ice for 5 min, then 950 μ L of room temperature SOC medium (nutrient-rich culture medium: 2% tryptone, 0.5% yeast extract, 10 mM NaCl, 2.5 mM KCl, 10 mM MgCl₂, 10 mM MgSO₄.7H₂O, 20 mM glucose) was added, the mixture was kept at 37 °C for 1 hour, vigorously shaken and then plated on warm selection plates containing LB medium with antibiotics specific to the plasmid used. After an overnight incubation, a single colony was selected and grown out overnight in a 15mL tube containing 4 mL of LB medium with

antibiotics. Plasmids were then purified from this mixture according to a Qiagen midiprep kit protocol.

4.2.8. CRISPR/Cas9 Transfection

A transfection mixture was made using 1.5 µg of both the AAVS1-sensor plasmid and the pXAT2 plasmid were mixed with 5 µL of P3000 per well in 100 µL of Optimem medium. To this P3000 mixture, 3.75 µL of Lipofectamine3000 was added and the mixture was left to incubate in room temperature for 5 min. IMR-90 stem cells (0.6 million) were dissociated using CDS as in 2.3. and spun down for 4 min at 300 x g. The liquid was aspirated leaving a pellet which was resuspended in the transfection mixture and left to incubate for 15 min at room temperature. 1 mL of E8 with 10 µM RI is added to the cell suspension, which is then plated in a 6-well plate well coated with fibronectin for a minimum of one hour. The plate is shaken to ensure equal distribution of cells along the surface of the well. Medium must be replaced after 48 hours after which selection may begin.

4.2.9. Transgenic Line Selection

Antibiotic G418 is added at recommended concentration for mammalian cells of 200-500 µL. Cells are imaged over 3 days to find the persistent fluorescence indicative of successful gene insertion. 2.5×10^4 of surviving cells are replated to a 10 cm plate to split into single cells, fed with 7 mL of E8 + RI. Medium is replaced with E8 lacking RI after cells appear in groups of 2 or more. Colonies are manually collected into 24-well plate wells coated with Matrigel and fed with E8 + RI until confluent. Confluent wells may be harvested for sequencing and restriction enzyme-based confirmation of intended gene insertion.

4.3. Results

4.3.1. cGMP Sensor Comparison

GSNO stimulation showed significantly higher response than cumulative CNP in HiPSC-CM with ScGi ($P=0.0005$, Figure 24A), cGi-500 ($P=0.0008$, Figure 24B), and CGES-DE5 ($P=0.0007$, Figure 24C) and a lower response in NRVM with ScGi ($P=0.0289$, Figure 25A). We find no statistical significance in differences between our stimulant responses in NRVM transfected with cGi-500 (Figure 25B) or CGES-DE5 (Figure 25C). These data reflect what we see in the representative curves (Figure 24G-I and Figure 25G-I) and shows a stark contrast between the GSNO response in HiPSC-CM and NRVM. These data reflect what we see in the representative curves (Figure 25D-F). Furthermore, CNP-only showed a significantly higher response than cumulative CNP in HiPSC-CM with ScGi ($P=0.0008$, Figure 24A) and CGES-DE5 ($P=0.0018$, Figure 24C), providing evidence supporting a shared pool of resources for cGMP generation after stimulation with GSNO and CNP.

Comparison of cGMP FRET sensors (Figure 26) in HiPSC-CM using GSNO showed a FRET response of $71.99 \pm 12.88\%$ of the value of the IBMX response with the ScGi sensor, $73.26 \pm 13.09\%$ with cGi-500, and $90.63 \pm 14.84\%$ with CGES-DE5, showing no significant difference between the sensors using a one-way ANOVA with Tukey's post-hoc test ($P=0.5581$, Figure 26A). Contrastingly, in NRVM the same experiment showed a $4.71 \pm 4.76\%$ response using the ScGi sensor, similarly $8.99 \pm 6.93\%$ with its offshoot, the ScGi sensor, and a striking $49.77 \pm 13.83\%$ response with the CGES-DE5. While the CGES-DE5 response was significantly different from the other sensors ($P=0.0083$, Figure 26B), it should be noted that CGES-DE5 had a much wider spread than either of the other two sensors. Addition of CNP after GSNO showed none to a small further increase in FRET response in HiPSC-CM (ScGi: $5.96 \pm 3.63\%$;

cGi-500: $9.63 \pm 7.37\%$; CGES-DE5: $16.05 \pm 11.56\%$) with no significant difference between the sensors ($P=0.7049$, Figure 26C), while the response much more pronounced in NRVMs (ScGi: $39.39 \pm 12.78\%$; cGi-500: $17.24 \pm 6.15\%$; CGES-DE5: $41.64 \pm 11.46\%$) with no significant difference between the sensors ($P=0.2155$, Figure 26D). CNP alone in HiPSC-CM and NRVMs (Figure 26E) showed a similar response with ScGi ($41.24 \pm 7.27\%$) and cGi-500 ($21.34 \pm 10.15\%$), but CGES-DE5 ($76.23 \pm 5.79\%$) showed a significantly higher response than both ScGi ($P=0.0304$) and cGi-500 ($P=0.0263$). We see an interesting difference here between the responses of HiPSC-CM and NRVMs with GSNO showing a high response in HiPSC-CM and next to none in NRVM, while this situation is reversed using CNP. This may indicate a difference in mechanisms of cGMP production between the cells of different levels of developmental maturity. Finally, experiments in NRVM using only CNP followed by and normalised to IBMX (ScGi: $33.37 \pm 7.67\%$; cGi-500: $33.21 \pm 13.91\%$; CGES-DE5: $49.21 \pm 14.76\%$) showed no significant difference between the sensors ($P=0.5547$, Figure 26F).

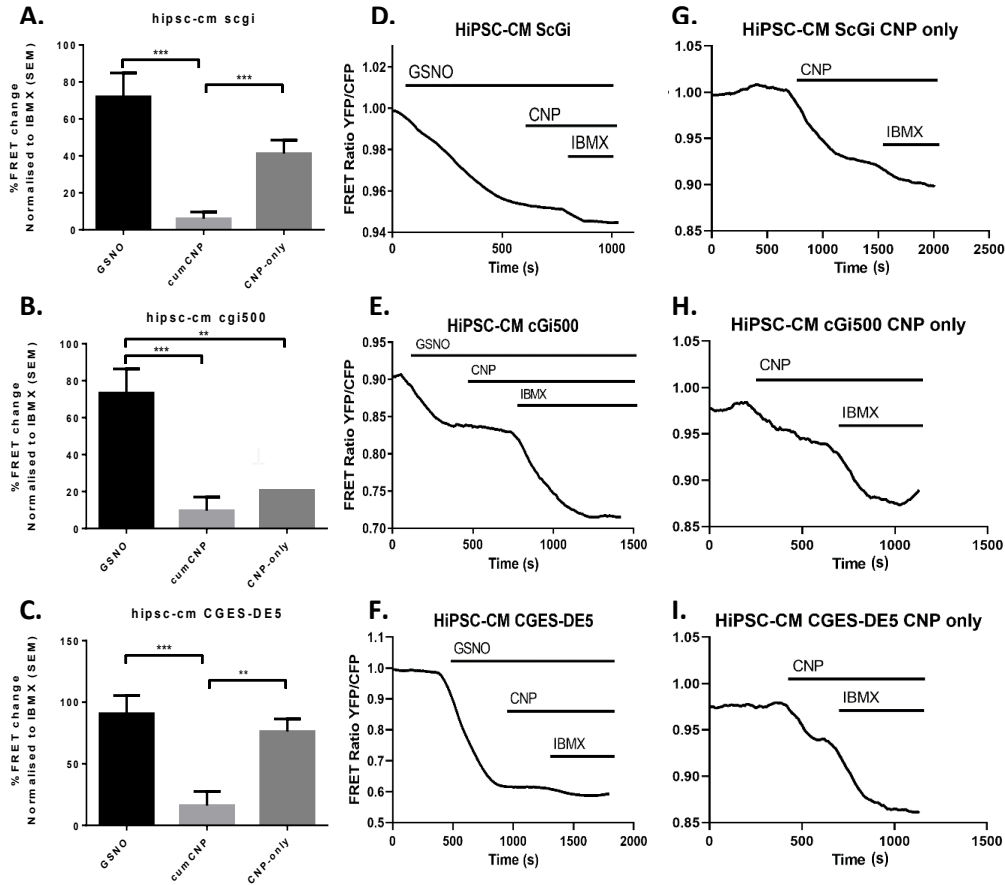


Figure 24. A-C. Comparisons of FRET responses to cGMP production stimulants in HiPSC-CM. **D-I.** Representative curves for each experiment are shown. Production of cGMP in HiPSC-CM was stimulated with either 100 μ M GSNO followed by 100 nM CNP and finally 100 μ M IBMX (cumCNP, A: $n = 10/3$; B: $n = 10/3$; C: $n = 12/3$), or with 100 nM CNP followed by 100 μ M IBMX (CNP-only, A: $n = 10/3$; B: $n = 2/2$; C: $n = 5/3$). Curves have been smoothed, averaging every 8 neighbours to the 0th order of the smoothing polynomial. Significance tested using one-way ANOVA using cells for the n -values with Tukey's post-hoc test (* $P = 0.05$, ** $P = 0.005$). Data are presented as mean \pm SEM. $n =$ cells/batches.

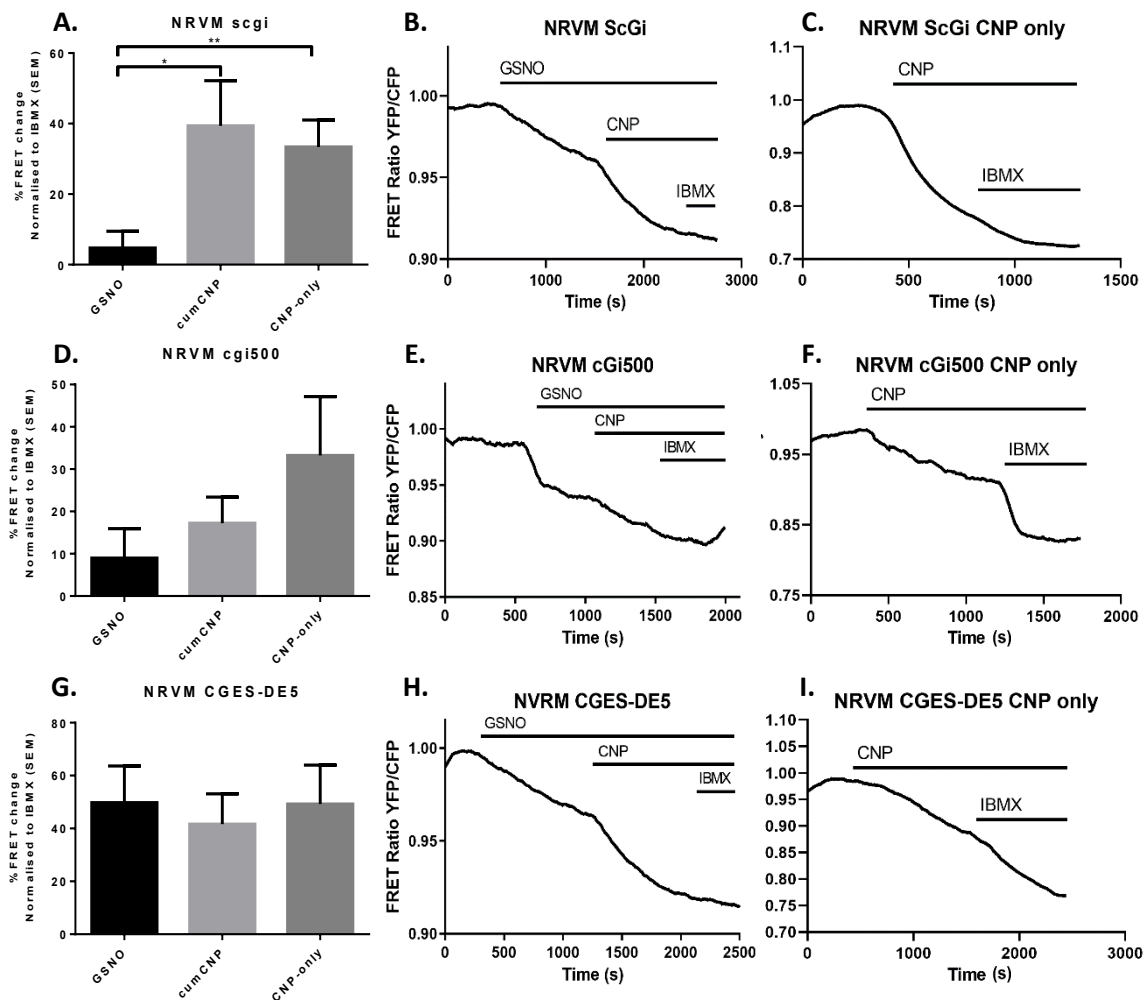


Figure 25. **A-C.** Comparisons of FRET responses to cGMP production stimulants in NRVM. **D-I.** Representative curves for each experiment are shown. Production of cGMP in isolated NRVM was stimulated with either 100 μ M GSNO followed by 100 nM CNP and finally 100 μ M IBMX (cumCNP, A: $n = 9/3$; B: $n = 11/3$; C: $n = 14/3$), or with 100 nM CNP followed by 100 μ M IBMX (CNP-only, A: $n = 7/3$; B: $n = 4/2$; C: $n = 5/2$). Curves have been smoothed, averaging every 8 neighbours to the 0th order of the smoothing polynomial. Significance tested using one-way ANOVA using cells for the n -values with Tukey's post-hoc test (* $P = 0.05$, ** $P = 0.005$). Data are presented as mean \pm SEM. $n =$ cells/batches.

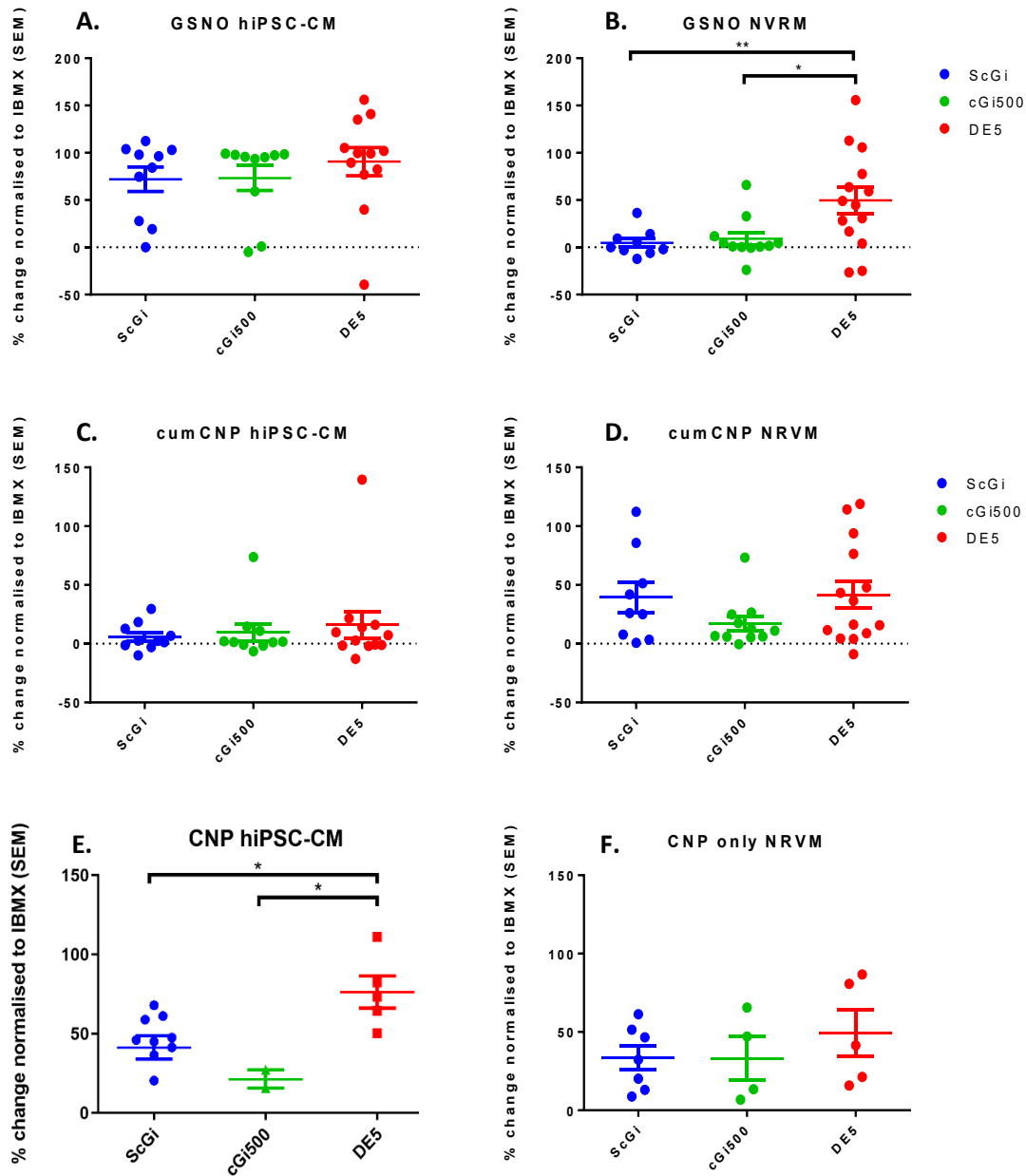


Figure 26. Comparison between ScGi (A,C: $n = 10/3$; B,D: $n = 9/3$; E: $n = 10/3$; F: $n = 7/3$), cGi500 (A,C: $n = 10/3$; B,D: $n = 11/3$; E: $n = 2/2$; F: $n = 4/2$) and CGES-DE5 (A,C: $n = 12/3$; B,D: $n = 14/3$; E: $n = 5/3$; F: $n = 5/2$) sensors for cGMP. Production of cGMP in hiPSC-CM or isolated NRVM was stimulated with either $100 \mu\text{M}$ GSNO followed by 100 nM CNP and finally $100 \mu\text{M}$ IBMX, or with 100 nM CNP followed by $100 \mu\text{M}$ IBMX. Significance tested using one-way ANOVA with Tukey's post-hoc test (* $P = 0.05$, ** $P = 0.005$). $n = \text{cells/batches}$.

4.3.2. Transgenic line development

We generated a plasmid containing the DNA coding for our cAMP sensor flanked by AAVS1 homologous arms (HA-L and HA-R) through the design of primers targeting the sensor DNA and inserting a pair of additional restriction enzyme binding sites for SBF-I and PAC-I, which allowed us to take a restriction/ligation approach to generate the 12 kb aavsCAGdest-TEV plasmid (**Error! Reference source not found.**). An aavsCAGdest-scgi plasmid was generated using an identical process

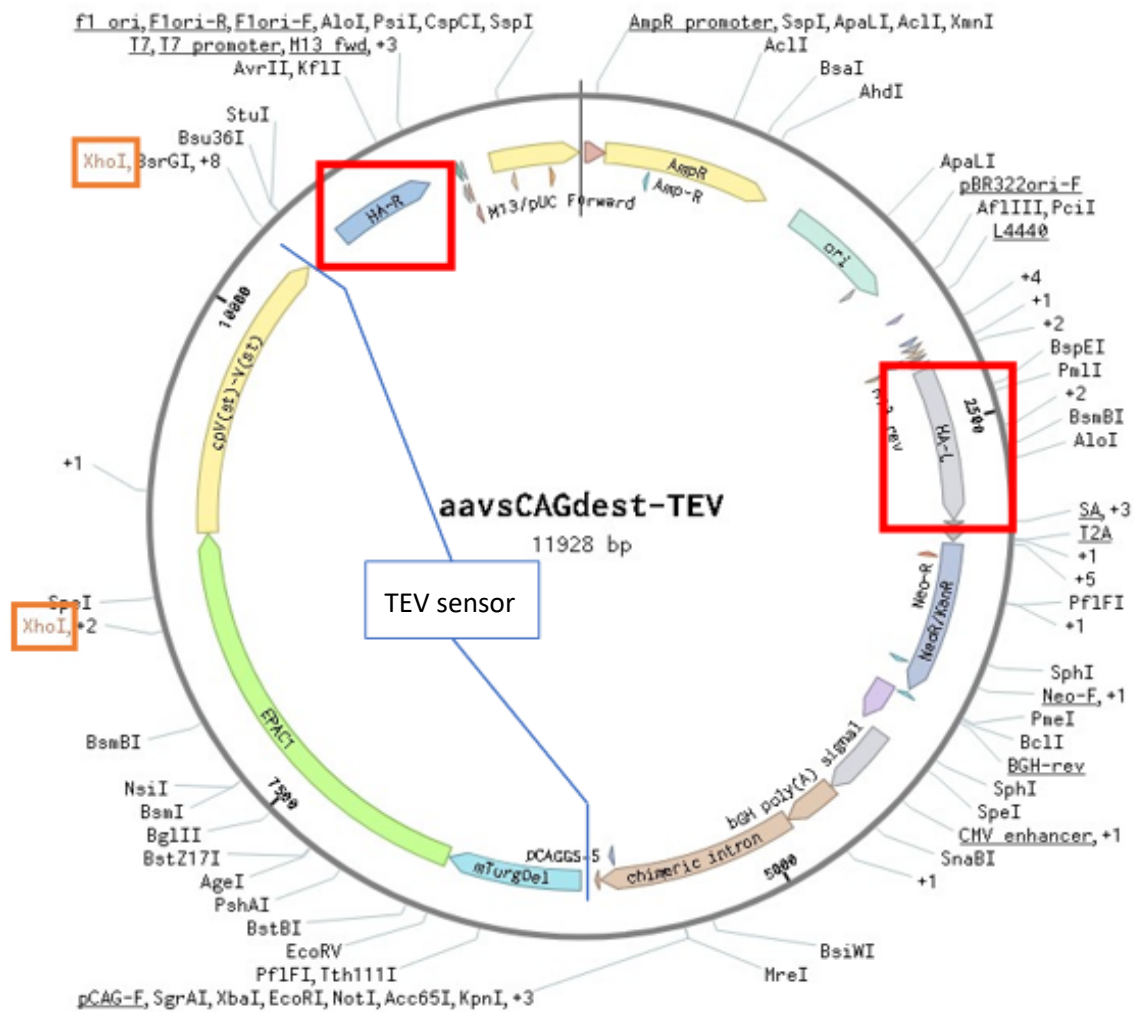


Figure 27. CRISPR-ready *aavsCAGdest-TEV* plasmid containing in blue square: our TEV sensor for cAMP, in red squares: homologous arms HA-L and HA-R for integration into the AAVS1 safe locus, in orange squares: *Xho*-I cutting sites used to test correct plasmid construction, and the CAG promoter.

with a different set of primers and the plasmid containing the ScGi sensor coding region. These plasmids were then amplified through inoculation of chemically competent *E. coli* bacteria. Plasmid DNA for TEV was isolated and tested to be valid through restriction enzyme cuts with *Xho*-I (Figure 28). Co-transfection of IMR-90 cells with one AAVS-sensor plasmid and the CRISPR/Cas9 coding region containing pXAT2 plasmid resulted in a transient expression of the fluorescent sensors (Figure 29) but the selection process left no live cells,

future work may use an altered selection protocol to obtain a transgenic line using the plasmid generated here.

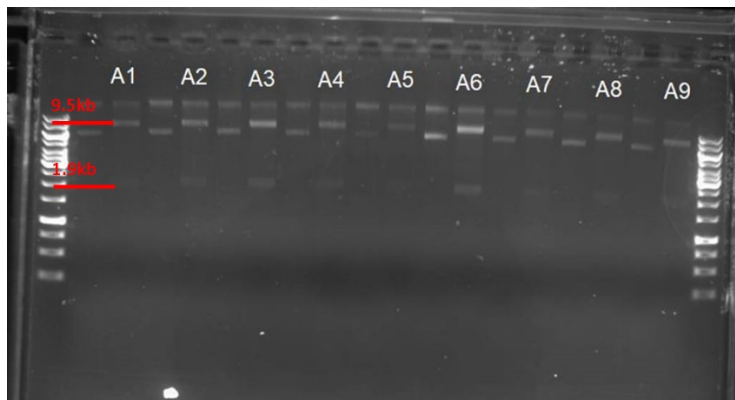


Figure 28 Test-cuts of aavsCAGdest-TEV using Xho-I, yielding expected 9.5kb and 1.9kb bands in 9 plasmid isolations A1 – A9 from different bacterial colonies.

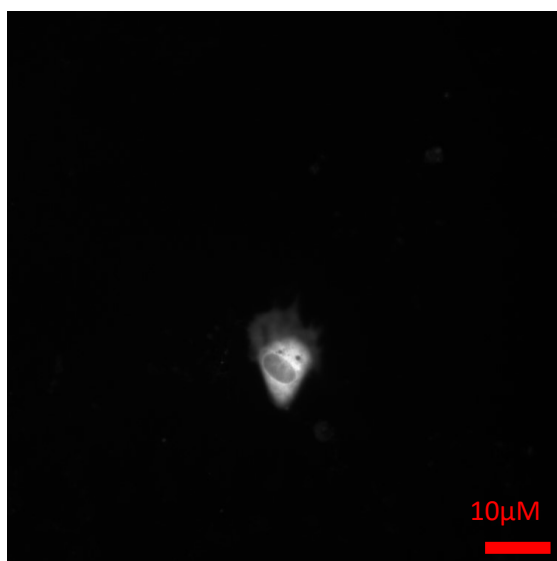


Figure 29. IMR-90 cell 2-days post transfection with aavsCAGtev and pXAT2 shows fluorescence at 480 nm and 535 nm. Scale is shown in red.

4.4. Discussion

In the experiments described above two cellular models were used; human stem cell derived CMs and rat neonatal CMs. The differences we have found between these models

are interesting ones showing a striking contrast between the hiPSC-CM which have a very primitive and underdeveloped biology, and the NRVM which while far from mature show many more hall-mark characteristics of adult cardiomyocytes. The contrasting response when using GSNO shows that quite early in development, cardiomyocytes switch away from a nitric oxide-based system for cGMP production, and into a more specialised natriuretic peptide-based system. Indeed, it has been shown decades ago that NO has a prominent role as a signalling molecule during early development of cardiomyocytes, with eNOS expression decreasing with development while iNOS expression in particular mostly stops at E15.5 in rat cardiomyocytes (Bloch et al. 2001). At the same time the effects of CNP in rat cardiomyocytes can still be found in adult cells (Brusq et al. 1999). More recent evidence shows an absence of GC-A and NO-GC in adult rat cardiomyocytes compared to neonatal rat cardiomyocytes (Feil et al. 2021), to which the contrast we show might be an early indicator. We additionally show that while CNP after GSNO shows no further effect in hiPSC-CM, CNP alone shows a clear response, albeit lower than with GSNO. This indicates that GSNO-stimulated cGMP production can either saturate the available biosensors or fully deplete or occupy pools of GTP required for cGMP production, which it shares with the natriuretic peptide pathway during this stage.

The comparisons between sensors show a consistent similarity between ScGi and cGi-500, which can be expected as ScGi is an offshoot of cGi-500. Meanwhile, CGES-DE5 which is based on a PDE5 binding domain shows increased activity in GSNO stimulated NRVMs compared to the almost completely absent response in the other two sensors. This may be caused by the difference in cyclic nucleotide binding domains between CGES-DE5 and the PKG-based sensors (Russwurm et al. 2007; Niino, Hotta, and Oka 2009). Though it has been

shown that PDE5 is localised in nano-domains (Castro et al. 2006; Lee et al. 2015), the PDE5 sensor lacks any localisation signal and is entirely cytosolic (Jalink 2006).

We find an easily noticeable change in FRET response upon stimulation with CNP, which is found to be lower in adult rats (Götz et al. 2014). While NPR1 moves to the t-tubules in adults, NPR2 which is the primary receptor for CNP, remains expressed on the entire cell surface (Subramanian et al. 2018). Indeed, CNP response can still be measured in adult mouse cardiomyocytes and CGES-DE5 is sufficiently sensitive for this purpose, whereas cGi-500 was deemed lacking (Götz et al. 2014). The change in NPR1 localisation raises the question of whether ANP or BNP, which have a much higher affinity for this receptor (Lumsden, Khambata, and Hobbs 2011), would be more interesting to study in the context of aging cardiomyocytes. However, NPR1 and NPR2 are functionally redundant in the case of ANP or BNP stimulation even in neonatal rat cardiomyocytes (Becker et al. 2014) and in this work we do not study the NP-pathway beyond the neonatal stage.

We were reluctant to use the CGES-DE5 sensor for our future PDE studies as our results show it to be deviant from the other two sensors, but also due to its consistently wide deviation between experiments. For these reasons as well as unpublished data on ScGi's affinity and selectivity, we decided to move forward and exclusively use this sensor for our future cGMP measurements. We have tested these sensors in HiPSC-CM for the first time, showing they function even in these underdeveloped cells, and selected an optimal sensor for future studies.

4.5. Limitations and future work

Generation of cAMP and cGMP sensor expressing IMR-90 lines would have greatly accelerated future experiments, however due to time constraints we were not able to

obtain a transgenic line for cAMP, nor a validated aavsCAGdest-scgi plasmid. Death of cells under antibiotic is most likely the effect of insufficient co-transfection of aavsCAGdest-TEV with pXAT2. It could also be theorised that death of cells neighbouring those that may have undergone a successful gene editing could diminish the chances of survival through release of apoptotic factors and toxins, or reduction of pH despite the recommended daily change of medium (Hendriks et al. 2015). Cell survival may already be affected by such factors during the transfection phase, but could possibly be ameliorated, , as one protocol suggests (Ran et al. 2013), by slowly adding warm incubation medium 24 hours after transfection rather than changing the medium after 48 hours. A major limitation of our tools when selecting for transgenic, fluorescent cells is caused by the lack of a microscope that can hold and image our 6-well plates. Cells are known to have reduced viability when grown on glass, however this is a necessity to measure fluorescence in our system. Thus, before cell selection through antibiotics can be evaluated, they must be transferred to glass-bottom MatTek dishes. This process results in a loss of around 40% of the cells, reducing chances of finding a transgenic cell. While we found fluorescence 2 days after transfection, this was most likely due to the transient transfection with the aavsCAGdest-TEV plasmid and did not indicate cells with persistent resistance to the G418 selection antibiotic.

Future work should use the generated plasmids and apply several variations on the protocol described in this work, as well as employing troubleshooting steps described in the papers cited here. When successful, the TEV-transgenic line may be used together with MultiFRET for efficient study of the cAMP pathway, or transfected with a cGMP sensor for study of cross-talk. When a successful method has been established, this may be used to generate an ScGi line as well and potentially a line transgenic for both TEV and ScGi.

Chapter 5: Age-Dependent Compartmentation of cGMP signalling in HiPSC-CMs -role of PDEs

5.1. Introduction

After selecting a suitable cGMP sensor we then moved to test dosages of inhibitors of relevant PDEs on D30, D60 and D90 hiPSC-CMs after stimulation with either GSNO or CNP. The different PDEs examined in these experiments each have a different localisation and/or affinity to cAMP and cGMP. Seven PDE families have been identified and investigated in the heart: PDE1, PDE2, PDE3, PDE4, PDE5, PDE8, and PDE9 (Fischmeister et al. 2006; Bork and Nikolaev 2018). We chose PDEs shown to have a capacity to modulate the presence of cGMP or facilitate cross-talk between cAMP and cGMP in the heart. Of these, PDE2 and PDE3 are dual-substrate specific for both cAMP and cGMP and may effect cross-talk between pools of these cyclic nucleotide proteins. PDE2 is involved in a negative form of cross-talk whereby the PDE is allosterically activated by cGMP to hydrolyse cAMP (M. Zhang and Kass 2011). The PDE2-inhibitor EHNA at 10 μ M was shown to significantly increase cGMP-gated current generated through the sGC pathway under the influence of the nitric oxide donor SNAP (Castro et al. 2006). PDE3 in particular is well investigated and known as the cGMP-inhibited PDE and main effector of positive cAMP-to-cGMP cross-talk. While it specifically hydrolyses cAMP at a maximum velocity ratio of 4-10 cAMP/cGMP, it can be competitively inhibited by cGMP (Beavo 1995). Using Cilostamide as a PDE3-inhibitor at 10 μ M in adult mice cardiomyocytes transfected with the FRET sensor CGES-DE5, an increase in cGMP levels similar to that with 100 μ M of the universal PDE inhibitor IBMX was observed (Götz et al. 2014). PDE5A is a cGMP specific PDE expressed in cardiomyocytes, primarily localised to the Z-discs (SENZAKI et al. 2001). Increased cGMP levels and subsequent PKG activity stimulate PDE5A to reduce cGMP, forming a negative feedback loop on the NO-sGC pathway. Contrastingly, it has also been found that cGMP generated by the NP-pGC pathways is positively regulated by PKG (Castro, Schittl, and Fischmeister 2010). The first

major PDE5-inhibitor used in cardiovascular research was Sildenafil at 1 mM, which was demonstrated to counteract an ISO-driven increase in contraction rate. When blocking both β_1 - and β_2 -ARs, contraction rate is unaffected by either ISO or PDE5. Furthermore, a cGMP-dependant activation of PDE2 was shown to attenuate cAMP levels generated by ISO stimulation, as well as produce a negative chronotropic effect (Isidori et al. 2015). PDE9 is the most recently discovered cGMP-selective PDE and has the highest affinity and was only described in brain or systemic studies during our experiments. In a study, PDE9 inhibitor PF044 at 5 μ M was found to further increase FRET response by ~5% when added to neonatal mouse ventricular myocytes pre-treated with SNAP (Brescia et al. 2020). PDE9 regulates cGMP signalling independent of the NO-pathway, having a role in regulating cGMP generated by the NP-pathway instead (Lee et al. 2015). Similarly PDE2 was also found to specifically control the NP-pathway, while the NO-pathway is predominantly controlled by PDE3 and PDE5 (Götz et al. 2014; Castro et al. 2006).

We have performed a set of experiments testing how our HiPSC-CMs at D30 or D90 are affected by PDEis for PDE2, 3, 5, and 9 at 1 μ M, 5 μ M, and 10 μ M after treatment with 5 μ M of either GSNO or CNP.

In 2016 a study by Jung et al. examined the expressional differences between HiPSC, D30 HiPSC-CMs, D60 HiPSC-CMs, and D90 HiPSC-CMs for the following genes: *ADRB1* (β_1 -AR), *ADRB2* (β_2 -AR), *ADRB3* (β_3 -AR), *ADCY5*, *ADCY6*, *CASQ2*, *Cav3*, *CaMKII δ* , and *MURC*. Gene expression was normalised to *GAPDH* or *actin*. Notably, for *Cav3* and *MURC* which are both important in the function of caveolae, as well as for *ADRB1*, *ADRB2*, *CASQ2*, *ADCY5*, and *ADCY6* relative gene expression normalised to iPSC was significantly upregulated in D90 HiPSC-CM compared to any of the younger groups. Protein expression of *Cav3* was found to

already be significantly upregulated in D60 and immunostaining showed clusters of Cav3 at the cell membrane in D60 HiPSC-CM and older. *CaMKII δ* showed no protein expression in iPSC in contrast to showing a clear band in D30 and was significantly reduced going from D30 to D60 to D90 (Jung et al. 2016).

These data was supported using our own differentiation protocol and IMR-90 HiPSC cell line, showing again a significant increase in relative gene expression for Cav3 and β_2 -AR in D90 compared to D30 HiPSC-CM. It was additionally shown that the ratio of β_2 -AR/ β_1 -AR significantly increases towards D90. This study also investigated the compartmentalising role of PDE2, PDE3, and PDE4 on the β_1 -AR-cAMP and β_1 -AR-cAMP pathways by stimulating with isoprenaline (30 μ M) in the presence of either the β_1 -AR blocker CGP (100 nM) or the β_2 -AR blocker ICI (50 nM). These experiments were performed in D30 and D90 HiPSC-CM, with cAMP responses being measured through the use of the Epac-S^{H74} FRET sensor and the MultiFRET software. Finally, the effect of cholesterol depletion through M β CD (cyclodextrin) was used to investigate the association of the β -AR-cAMP pathways and their compartmentalisation by PDEs with caveolae. Caveolae were found to be significantly reduced in both D30 and D90 HiPSC-CM after M β CD treatment. Though the initial number of caveolae was much higher in D90 at 0.6 caveolae / μ m compared to 0.2 / μ m in D30, after treatment both were found at around 0.1 / μ m. (Hasan et al. 2020).

In this chapter we follow the example of the previously performed experiments by A. Hasan et al. 2020 in the cAMP pathways, but study the cGMP pathways using PDEi that affect cGMP at concentrations we determine through PDEi dose-response curves. We thus thoroughly examine difference in the effects of PDEi for PDE2, 3, 5, and 9 after 5 μ M GSNO or 500 nM CNP between HiPSC-CMs of 30- or 90-days post initiation of differentiation. We

additionally test the generation of cGMP through the β_3 -AR in 30- or 90-days old hiPSC-CMs by blocking the β_1 - and β_2 -AR with a 10-minute pre-treatment using 100 nM CGP and 50 nM ICI respectively, before adding 100 nM of the β -AR activator ISO.

5.1. Aims

- ❖ To determine effective concentrations of PDEis vinpocetine, EHNA, cilostamide, sildenafil, and PF in D30 and D90 IMR90 hiPSC-CM.
- ❖ To study the roles of PDEs and caveolae on compartmentation of cGMP produced through the NO-, NP-, and β_3 -pathways.

5.2. Methods

5.2.1. cGMP FRET PDEi dose-response curve

We tested various concentrations of PDE inhibitors on iPSC-CMs 30- and 90-days post initiation of differentiation, which were transfected with the ScGi sensor two days prior. A concentration of 1 μ M, 5 μ M, or 10 μ M PDE inhibitor (PDEi) for PDE2 (EHNA), PDE3 (CILO), PDE5 (SILD) or PDE9 (PF) was applied after a 100 nM CNP or 100 μ M GSNO FRET response plateau. The PDEi plateau was then followed by 100 μ M IBMX as a saturator to which all data was normalised.

5.2.2. D30 vs D90 FRET experiments

We tested various PDE inhibitors on iPSC-CMs 30- and 90-days post initiation of differentiation, which were transfected with the ScGi sensor two days prior. For experiments on the NO- or NP-pathway, cells were stimulated to produce cGMP using 5 μ M GSNO or 500 nM CNP respectively. For our β_3 -pathway experiments, cells were pre-treated with 100 nM of the β_1 -blocker CGP and 50 nM of the β_2 -blocker ICI for 20 minutes before

cGMP stimulation with 100 nM ISO. After a plateau of the response, the one of the following PDE inhibitors was added at 10 μ M: Vinpocetine (PDE1 inhibitor), EHNA (PDE2 inhibitor), Cilostamide (PDE3 inhibitor), Sildenafil (PDE5 inhibitor), PF-449076 (PF, PDE9 inhibitor). The PDEi plateau was then followed by 100 μ M IBMX as a saturator to which all data was normalised.

5.2.3. D90 Cyclodextrin Pre-Treatment

ScGi transfected HiPSC-CM of 90-days post initiation of differentiation were subjected to caveolae removal by 1-hour incubation with 1 mL RPMI medium containing 1.3 g/L cyclodextrin. Afterwards, cells are washed with FRET buffer, and the medium is replaced with 1 mL FRET buffer.

5.3. Results

5.3.1. PDEi dose-response results

PDEi's for PDE2 (EHNA), PDE3 (CILO), PDE5 (SILD) and PDE9 (PF) were tested on a dose-response curve on ScGi-transfected D30 and D90 HiPSC-CMs, using 1 μ M, 5 μ M or 10 μ M of PDEi after stimulation with 5 μ M of CNP (Figure 30) or GSNO (Figure 31). Values are calculated as a % FRET change from baseline to IBMX response, with significance testing through one-way ANOVA with Tukey's post-hoc test. D60 HiPSC-CMs were initially included but this experimental condition was scrapped in order to increase the number of replicates for D90 HiPSC-CMs, which showed a higher rate of experimental failure due to cell-death.

We found no significant change in FRET response with all doses of EHNA after CNP treatment in D30 HiPSC-CMs (Figure 30A), and only a minor significant change D90 HiPSC-CMS from CNP to 10 μ M EHNA (21.02 ± 4.63 to 39.91 ± 5.04) (Figure 30B). The same drug after GSNO treatment resulted in a strong significant increase in FRET response from 1 μ M

to 5 μM in D30 (12.73 ± 2.94 to 57.37 ± 7.10) (Figure 31A), and from 5 μM to 10 μM in D90 (29.74 ± 7.33 to 99.56 ± 7.31) (Figure 31B). CILO showed a gradual increase in FRET response after CNP in D30, with a significant increase between 5 μM CNP and 5 μM CILO (46.83 ± 8.54 to 82.40 ± 4.63), and 5 μM CNP and 10 μM CILO (9.99 ± 4.56 to 17.83 ± 4.35) (Figure 30C). In D90 HiPSC-CMs after CNP treatment, CILO shows no change with 1 μM CILO, but a large increase with 5 μM (29.55 ± 5.53 to 81.15 ± 4.15) and no further change on further increasing the concentration to 10 μM (Figure 30D). Minimal change is seen with CILO in both D30 and D90 HiPSC-CMs after GSNO, showing only a significant change when increasing from 5 μM to 10 μM (D30: 60.58 ± 6.55 to 95.87 ± 1.25 , D90: 29.55 ± 5.53 to 77.82 ± 8.09) (Figure 31C-D). In D30, CNP-SILD shows no significant change at any SILD concentration (Figure 30E), but in D90 there is a small significant increase after 5 μM (23.16 ± 4.68 to 40.80 ± 5.07) and a much larger increase after 10 μM (40.80 ± 5.07 to 74.37 ± 4.80) (Figure 30F). SILD after GSNO shows only a significant increase after 10 μM in D90 (23.32 ± 9.59 to 84.58 ± 2.04) (Figure 31F), however it must be noted that our pool of D30 data consists only of $n=9$ cells (Figure 31E), the lowest in all of these experiments, partly due to cell death mid-experiment. The PDE9 inhibitor PF shows the most consistent changes between the different concentrations in D30s after CNP (Figure 30G), with a significant increase at every concentration (CNP to 1 μM : 10.42 ± 3.42 to 45.54 ± 4.94 , 5 μM : 82.27 ± 3.26 , 10 μM 104.7 ± 2.31). In D90s this is less pronounced with a significant increase only between CNP and 5 μM (20.12 ± 9.49 to 82.45 ± 10.50) and a lesser significant increase between 1 μM and 10 μM (41.26 ± 11.28 to 89.14 ± 11.02), however the number of replicates is much lower than with our D30s (Figure 30H). D30 GSNO-PF shows significant increases between 1 μM (20.55 ± 4.71), 5 μM (59.35 ± 4.53) and 10 μM (83.97 ± 5.83) (Figure 31G), while in D90s we found a significant increase between all conditions, with 1

μM giving the largest response (GSNO to 1 μM : 4.419 ± 3.73 to 48.57 ± 7.48 , 5 μM : 69.74 ± 5.75 , 10 μM : 93.71 ± 4.38) (Figure 31H). We conclude that for maximised response, the simplest strategy is to use inhibitors for PDE2, 3, 5, and 9 at 10 μM each.

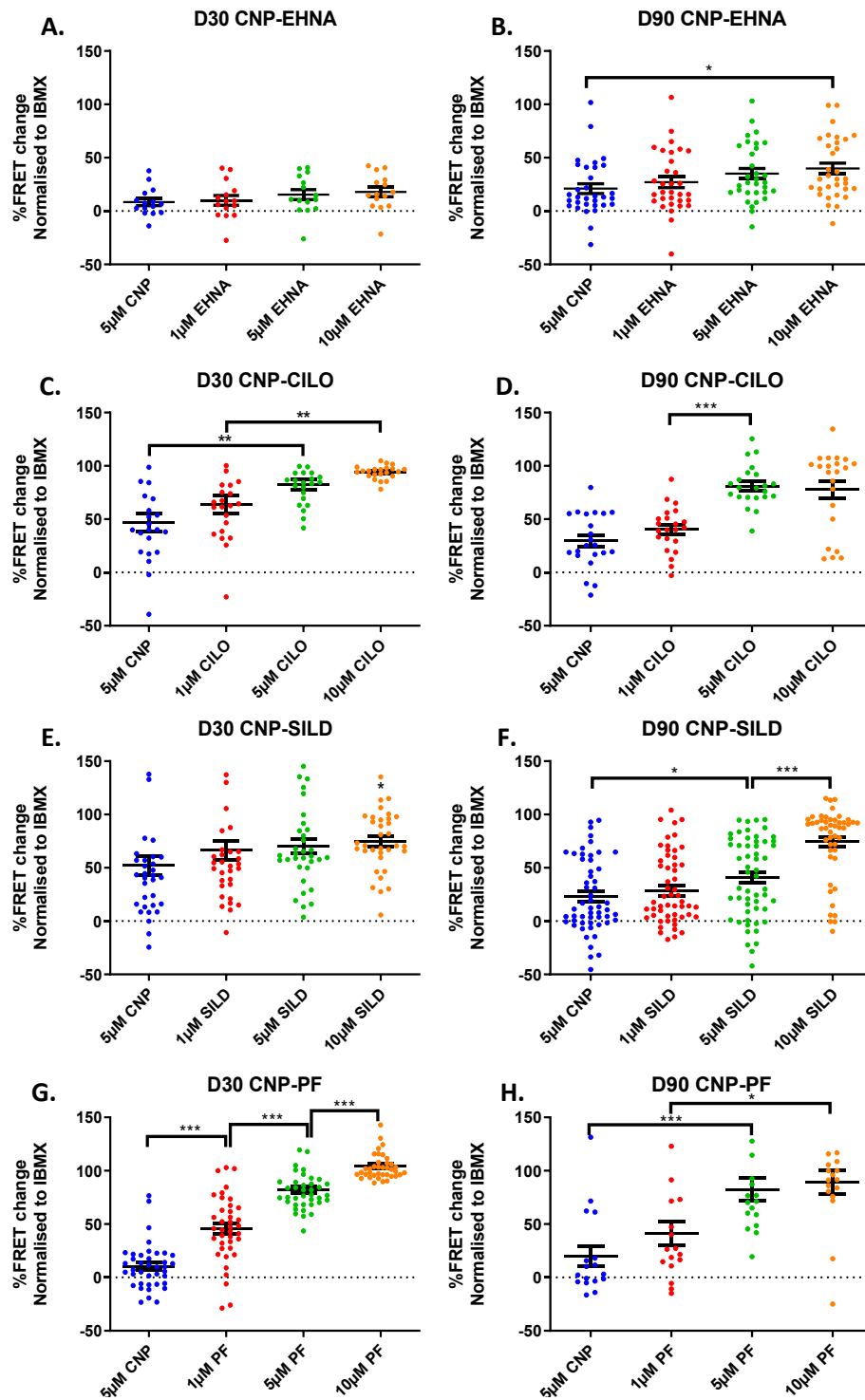


Figure 30. Dose-response of FRET-sensor transfected hiPSC-CM cells after stimulation with 5 μ M CNP followed by 1 μ M, 5 μ M, or 10 μ M of PDE inhibitor for PDE2 (EHNA), PDE3 (CILO), PDE5 (SILD), or PDE9 (PF). FRET change was normalised to the response after a saturating dose of 100 μ M IBMX. Significance tested using one-way ANOVA with Tukey's post-hoc test (* $P = 0.05$, ** $P = 0.005$, and *** $P \leq 0.001$). Data are presented as mean \pm SEM. $n =$ cells/batches with **A**: $n=15/4$, **B**: $n=34/4$, **C**: $n=22/4$, **D**: $n=29/4$, **E**: $n=32/3$, **F**: $n=50/4$, **G**: $n=39/4$, **H**: $n=21/4$. Total: $n=242/20$.

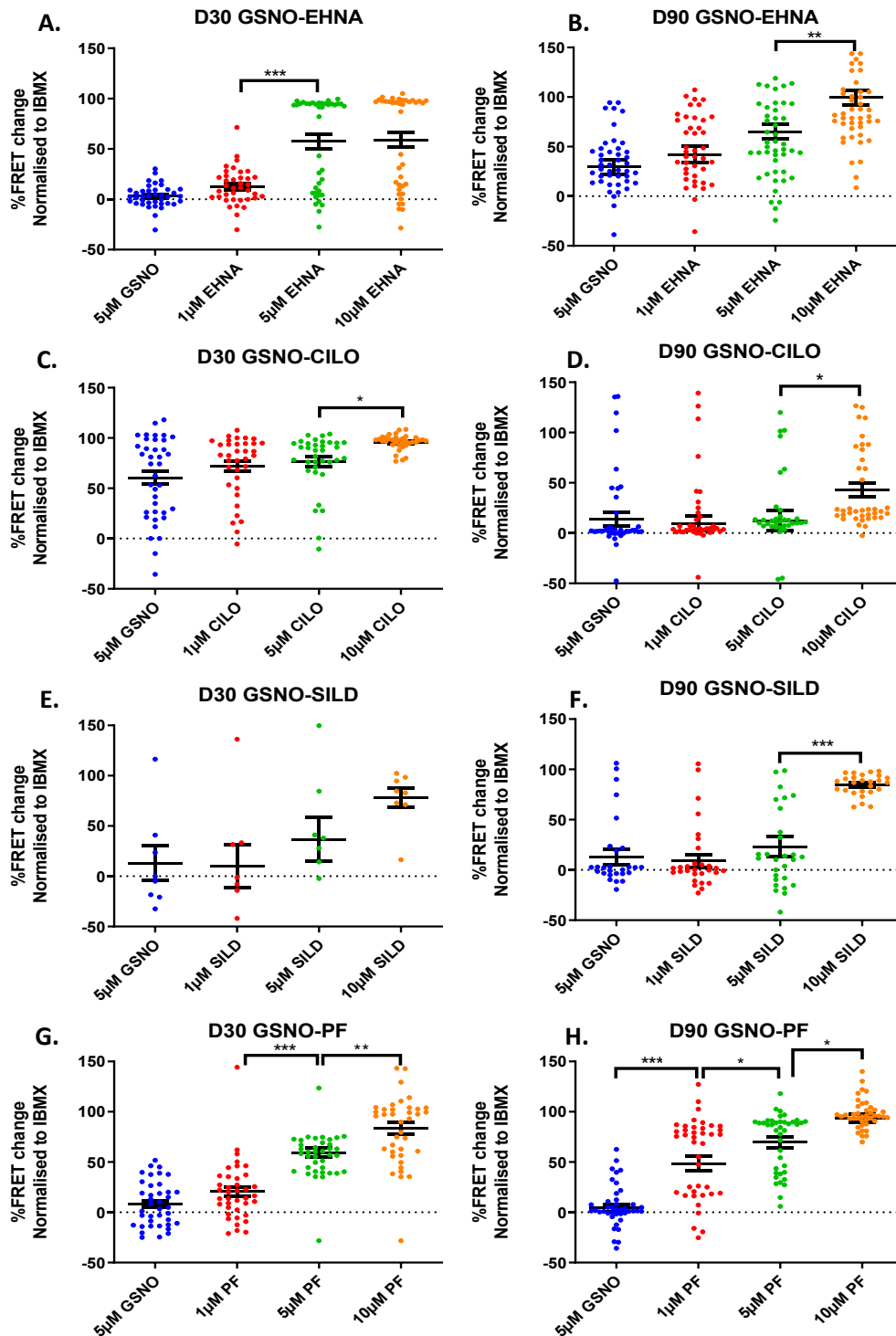


Figure 31. Dose-response of FRET-sensor transfected H1PSC-LM cells after stimulation with 5 μ M GSNO followed by 1 μ M, 5 μ M, or 10 μ M of PDE inhibitor for PDE2 (EHNA), PDE3 (CILO), PDE5 (SILD), or PDE9 (PF). FRET change was normalised to the response after a saturating dose of 100 μ M IBMX. Significance tested using one-way ANOVA with Tukey's post-hoc test (* $P = 0.05$, ** $P = 0.005$, and *** $P \leq 0.001$). Data are presented as mean \pm SEM. $n =$ cells/batches with **A**: $n=41/4$, **B**: $n=45/4$, **C**: $n=38/4$, **D**: $n=42/4$, **E**: $n=9/4$, **F**: $n=28/4$, **G**: $n=39/4$, **H**: $n=40/4$. Total: $n=282/20$.

5.3.2. FRET PDEi D30 vs D90 in IMR-90 HiPSC-CM

In our experiments comparing the NP-pathway between D30 vs D90 IMR-90 HiPSC-CM, we apply PDEi1, 2, 3, 5, or 9 after CNP and normalise the response to IBMX. The response to CNP alone showed no significant difference between D30 and D90 ($P = 0.1224$) (Figure 32A). The representative curves show the drug-response dynamics found in most of our experiments for the shown conditions, with a small response to CNP, a varying PDEi response depending on the drug, and a consistently high response to IBMX (Figure 32B-F). We find significant differences in the PDEi response between D30 and D90 when using cilostamide ($P = <0.0001$), sildenafil ($P = 0.0012$) and PF ($P = <0.0001$), but not vinpocetine ($P = 0.7344$) nor EHNA ($P = 0.1410$) (Figure 32G). Using cilostamide, the D30 mean response (7.729%) was lower than in D90 (2.223%). Using sildenafil, the D30 mean response (3.897%) was lower than in D90 (1.935%). Using PF, the D30 mean response (3.297%) was lower than in D90 (1.580%). The responses of IBMX after all our experiments taken together for D30 and D90 showed no significant difference between these ages ($P = 0.0528$) (Figure 32H).

In our experiments comparing the NO-pathway between D30 vs D90 IMR-90 HiPSC-CM, we apply PDEi1, 2, 3, 5, or 9 after GSNO and normalise the response to IBMX. The response to GSNO alone showed a significant difference between D30 and D90 ($P = <0.0001$), with D30 showing a higher mean response (8.723%) than D90 (4.385%) (Figure 33A). Here, representative curves showcase the difference in GSNO response between D30 and D90. Notably, sildenafil shows a slow response dynamic here (Figure 33E) as it did in the previous set of curves (Figure 3E), while D30 PF shows a much faster response (Figure 33F). We find significant differences in the PDEi response between D30 and D90 when using vinpocetine ($P = 0.0053$), cilostamide ($P = <0.0001$), and sildenafil ($P = <0.0001$), but not EHNA ($P = 0.0273$) nor PF ($P = 0.3817$) (Figure 33G). Using vinpocetine, the D30 mean response

(4.278%) was lower than in D90 (9.066%). Using cilostamide, the D30 mean response (5.831%) was higher than in D90 (1.840%). Using sildenafil, the D30 mean response (3.344%) was lower than in D90 (9.363%). The responses of IBMX after all our experiments taken together for D30 and D90 showed no significant difference between these ages ($P = 0.0180$). In our experiments comparing the β_3 -pathway between D30 vs D90 IMR-90 HiPSC-CM, we apply PDEi1, 2, 3, 5, or 9 after ISO on cells pre-treated with β_1 - and β_2 -blockers ICI and CGP, then normalise the response to IBMX. The response of pre-treatment and ISO alone showed no significant difference between D30 and D90 ($P = 0.2908$) (Figure 34A). The low signal from our experiments on this pathway are reflected in the erratic course of some of our representative curves, as lesser responses enhance visibility of noise (Figure 34B-F). We find significant differences in the PDEi response between D30 and D90 when using vinpocetine ($P = <0.0001$), EHNA ($P = <0.0001$), cilostamide ($P = <0.0001$), and sildenafil ($P = <0.0001$), but not PF ($P = 0.0848$) (Figure 34G). Using vinpocetine, the D30 mean response (2.069%) was higher than in D90 (0.7314%). Using EHNA the D30 mean response (1.477%) was higher than in D90 (-0.8284%). Using cilostamide, the D30 mean response (1.820%) was higher than in D90 (-0.3763%). Using sildenafil, the D30 mean response (0.8098%) was higher than in D90 (-0.2755%). The responses of IBMX after all our experiments taken together for D30 and D90 showed a significant difference between these ages ($P = 0.0002$), with the D30 data showing a lower mean response (6.629%) than the D90 data (5.252%).

5.3.3. FRET PDEi Untreated vs Caveolae Disruption through Cyclodextrin in IMR-90 HiPSC-CM

In our experiments comparing untreated and cyclodextrin treated cells by applying PDEi1, 2, 3, 5, or 9 after CNP and normalising the response to IBMX, we find significant differences in the PDEi response between untreated and cyclodextrin when using sildenafil ($P = 0.0042$),

but not when using vinpocetine ($P = 0.1078$), EHNA ($P = 0.4202$), cilostamide ($P = 0.3624$), nor PF ($P = 0.4405$). Using sildenafil, the untreated mean response (3.264%) was lower than in cyclodextrin treated cells (8.253%). The responses of IBMX after all our experiments taken together showed a significant difference between these groups ($P = <0.0001$), with untreated (15.17%) giving a higher response than cyclodextrin (10.02%). The response to CNP alone showed no significant difference between untreated cells and cyclodextrin treated cells ($P = 0.1183$) (Figure 35).

In our experiments comparing untreated and cyclodextrin treated cells by applying PDEi1, 2, 3, 5, or 9 after GSNO and normalising the response to IBMX, we find significant differences in the PDEi response between untreated and cyclodextrin when using vinpocetine ($P = <0.0001$), EHNA ($P = <0.0001$), sildenafil ($P = <0.0001$), and PF ($P = 0.0172$), but not when using cilostamide ($P = 0.2385$). Using vinpocetine, the untreated mean response (18.21%) was higher than in cyclodextrin treated cells (3.623%). Using EHNA, the untreated mean response (10.34%) was higher than in cyclodextrin treated cells (-0.3126%). Using sildenafil, the untreated mean response (10.18%) was higher than in cyclodextrin treated cells (1.629%). Using PF, the untreated mean response (8.088%) was higher than in cyclodextrin treated cells (5.030%). The responses of IBMX after all our experiments taken together showed a significant difference between these groups ($P = <0.0001$), with untreated (14.97%) giving a higher response than cyclodextrin (9.873%). The response to GSNO alone showed a significant difference between untreated and cyclodextrin ($P = 0.0007$), with untreated cells (4.492%) showing a higher response than in cyclodextrin treated cells (2.261%) (Figure 36).

In our experiments comparing untreated and cyclodextrin treated cells by applying PDEi1, 2, 3, 5, or 9 after ISO in the presence of CGP and ICI before normalising the response to IBMX, we find significant differences in the PDEi response between untreated and cyclodextrin when using EHNA ($P = <0.0001$) and PF ($P = <0.0001$), but not when using vinpocetine ($P = 0.0262$), cilostamide ($P = 0.0697$) nor sildenafil ($P = 0.1331$). Using EHNA, the untreated mean response (-0.03211%) was lower than in cyclodextrin treated cells (2.543%). Using PF, the untreated mean response (2.423%) was lower than in cyclodextrin treated cells (6.742%). The responses of IBMX after all our experiments taken together showed no significant difference between these groups ($P = 0.6017$). The response to pre-treatment and ISO alone showed a significant difference between untreated and cyclodextrin ($P = <0.0001$), with untreated cells (1.744%) showing a lower response than in cyclodextrin treated cells (3.149%) (Figure 37).

cGMP Production upon NP Stimulation

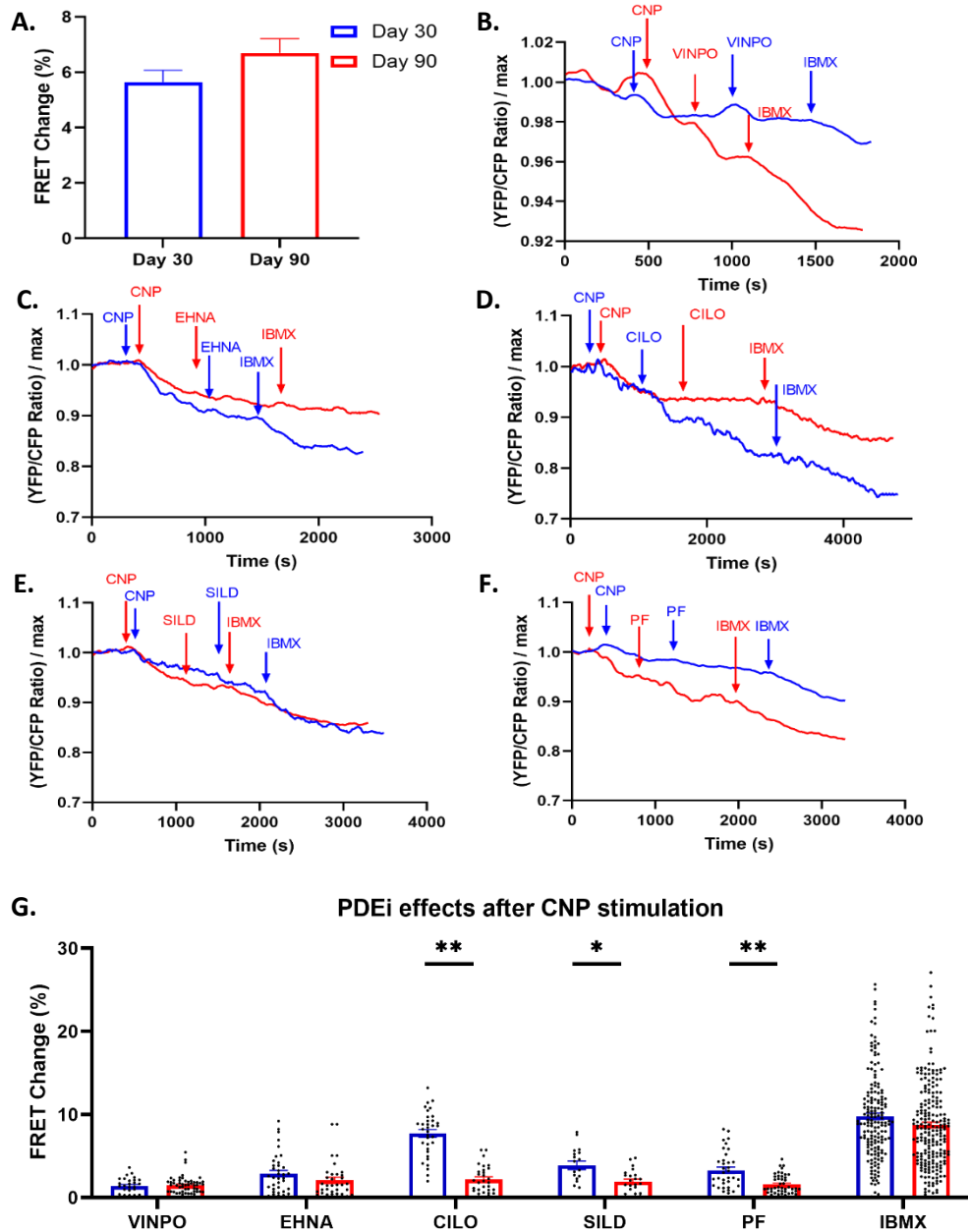


Figure 32. D30 vs D90 in FRET-sensor transfected IMR90 HiPSC-CM after stimulation with 500 nM CNP followed 10 μ M of PDE inhibitor for PDE1 (VINPO), PDE2 (EHNA), PDE3 (CILO), PDE5 (SILD), or PDE9 (PF). FRET change was normalised to the response after a saturating dose of 100 μ M IBMX. **A.** cGMP stimulant alone. **B-F.** representative curves. **G.** PDEi comparison. Significance tested using unpaired T-tests with Holm-Šídák post-hoc test (* $P = 0.05$, ** $P = 0.001$). Data are presented as mean \pm SEM. $n =$ cells/batches with **A:** D30 $n = 170/15$ D90 $n = 148/15$, **G:** VINPO D30 $n = 28/3$ D90 $n = 54/3$, EHNA D30 $n = 37/3$ D90 $n = 34/3$, CILO D30 $n = 34/3$ D90 = 30/3, SILD D30 $n = 18/3$ D90 $n = 23/3$, PF D30 $n = 35/3$ D90 $n = 46/3$, IBMX D30 $n = 169/15$ D90 = 218/15.

cGMP Production upon NO Stimulation

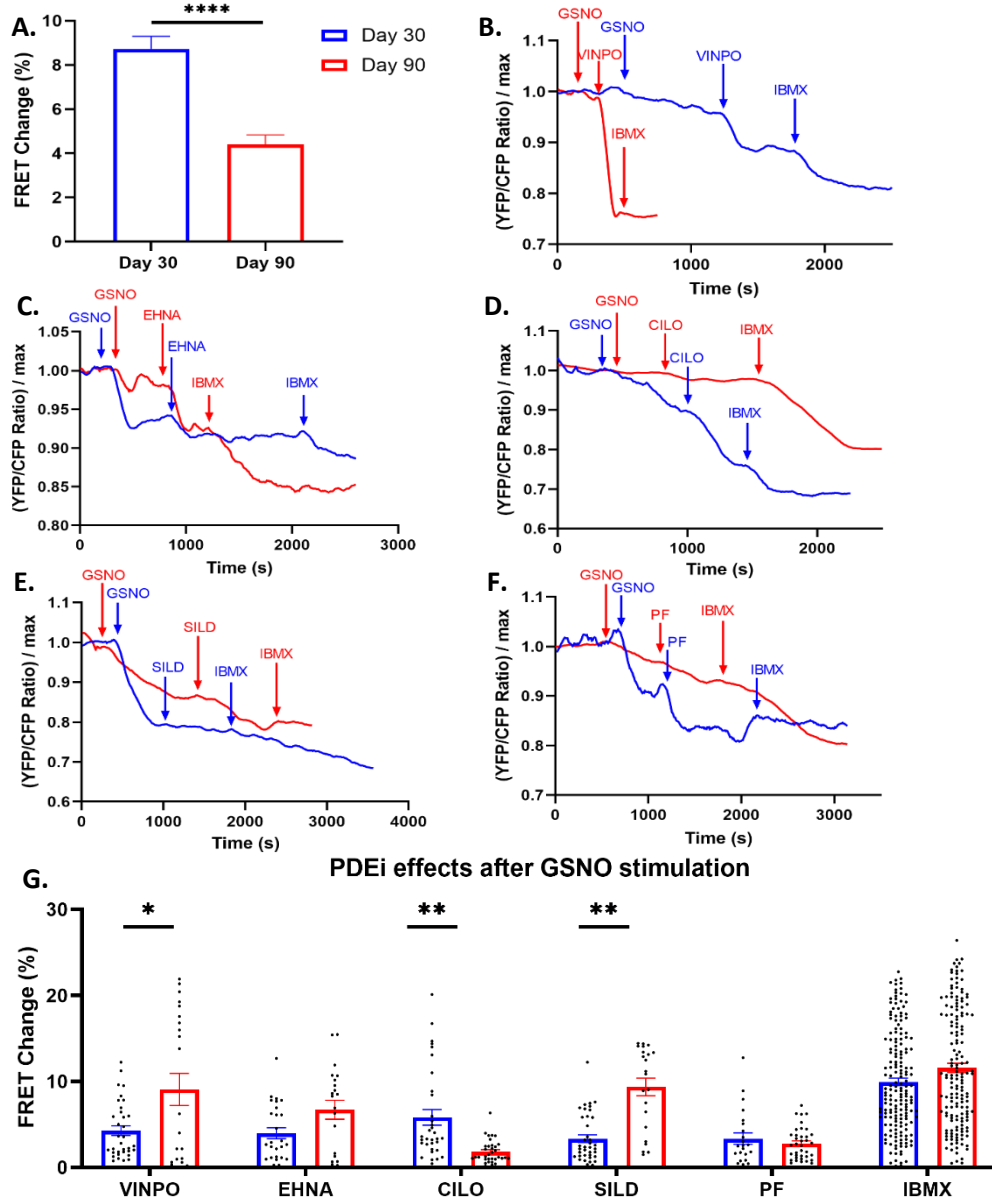


Figure 33. D30 vs D90 in FRET-sensor transfected IMR90 HiPSC-CM after stimulation with 5 μM GSNO followed 10 μM of PDE inhibitor for PDE1 (VINPO), PDE2 (EHNA), PDE3 (CILO), PDE5 (SILD), or PDE9 (PF). FRET change was normalised to the response after a saturating dose of 100 μM IBMX. **A.** cGMP stimulant alone. **B-F.** representative curves. **G.** PDEi comparison. Significance tested using unpaired T-tests with Holm-Šidák post-hoc test (* $P = 0.05$, ** $P = 0.001$). Data are presented as mean \pm SEM. $n = \text{cells/batches}$ with **A:** D30 $n = 186/15$ D90 $n = 110/15$, **G:** VINPO D30 $n = 34/3$ D90 $n = 22/3$, EHNA D30 $n = 27/3$ D90 $n = 21/3$, CILO D30 $n = 33/3$ D90 = $34/3$, SILD D30 $n = 38/3$ D90 $n = 22/3$, PF D30 $n = 23/3$ D90 $n = 37/3$, IBMX D30 $n = 178/15$ D90 = $162/15$.

cGMP Production upon β_3 Stimulation

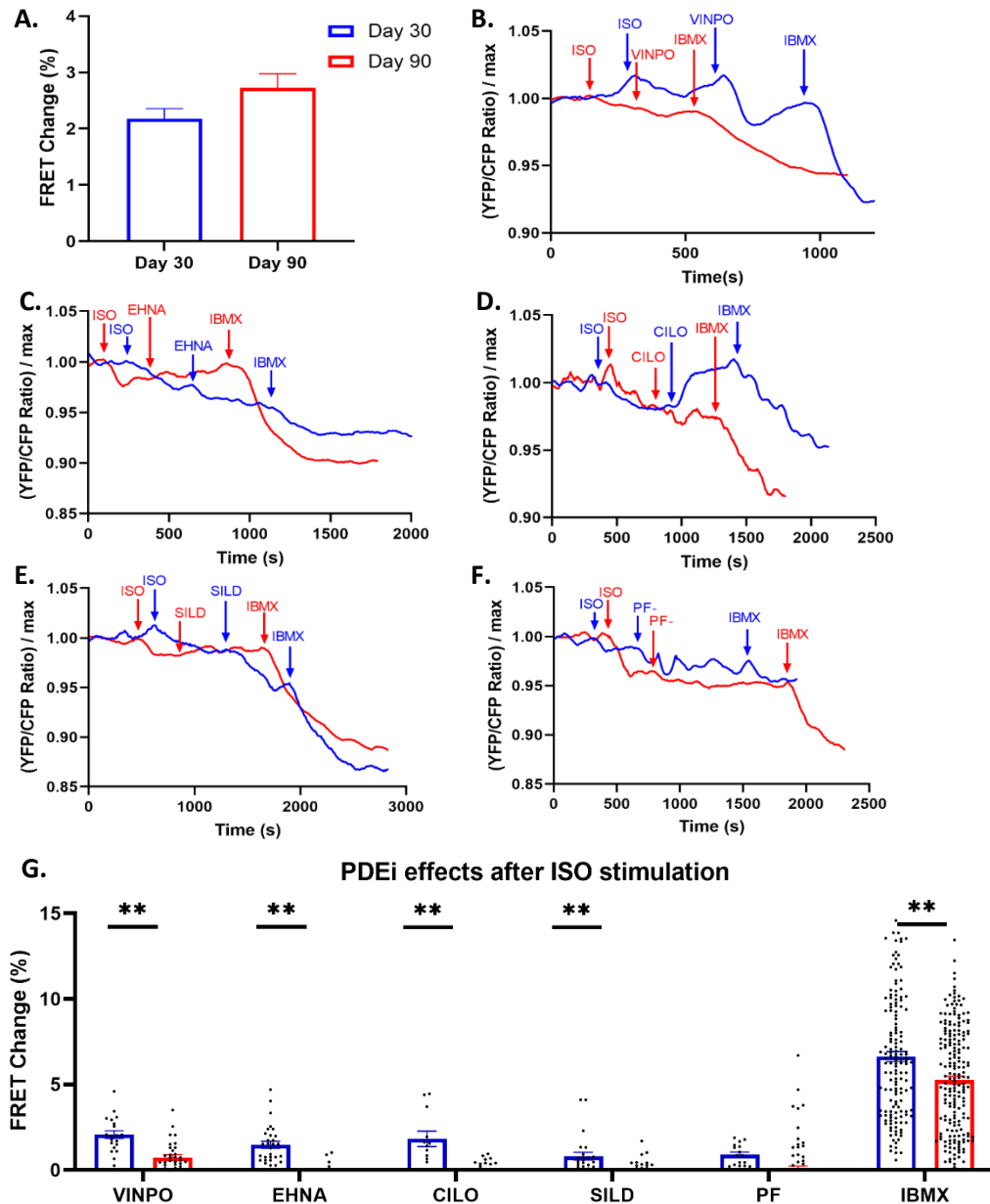


Figure 34. D30 vs D90 in FRET-sensor transfected IMR90 HiPSC-CM after stimulation with 100 nM ISO after a 10-minute CGP (100 nM) + ICI (50 nM) incubation, followed by 10 μ M of PDE inhibitor for PDE1 (VINPO), PDE2 (EHNA), PDE3 (CILO), PDE5 (SILD), or PDE9 (PF). FRET change was normalised to the response after a saturating dose of 100 μ M IBMX. **A.** cGMP stimulant alone. **B-F.** representative curves. **G.** PDEi comparison. Significance tested using unpaired T-tests with Holm-Šidák post-hoc test (* P = 0.05, ** P = 0.001). Data are presented as mean \pm SEM. n = cells/batches with **A:** D30 n = 136/15 D90 n = 105/15, **G:** VINPO D30 n = 20/3 D90 n = 33/3, EHNA D30 n = 30/3 D90 n = 33/3, CILO D30 n = 12/3 D90 = 25/3, SILD D30 n = 25/3 D90 n = 40/3, PF D30 n = 16/3 D90 n = 51/3, IBMX D30 n = 150/15 D90 = 200/15.

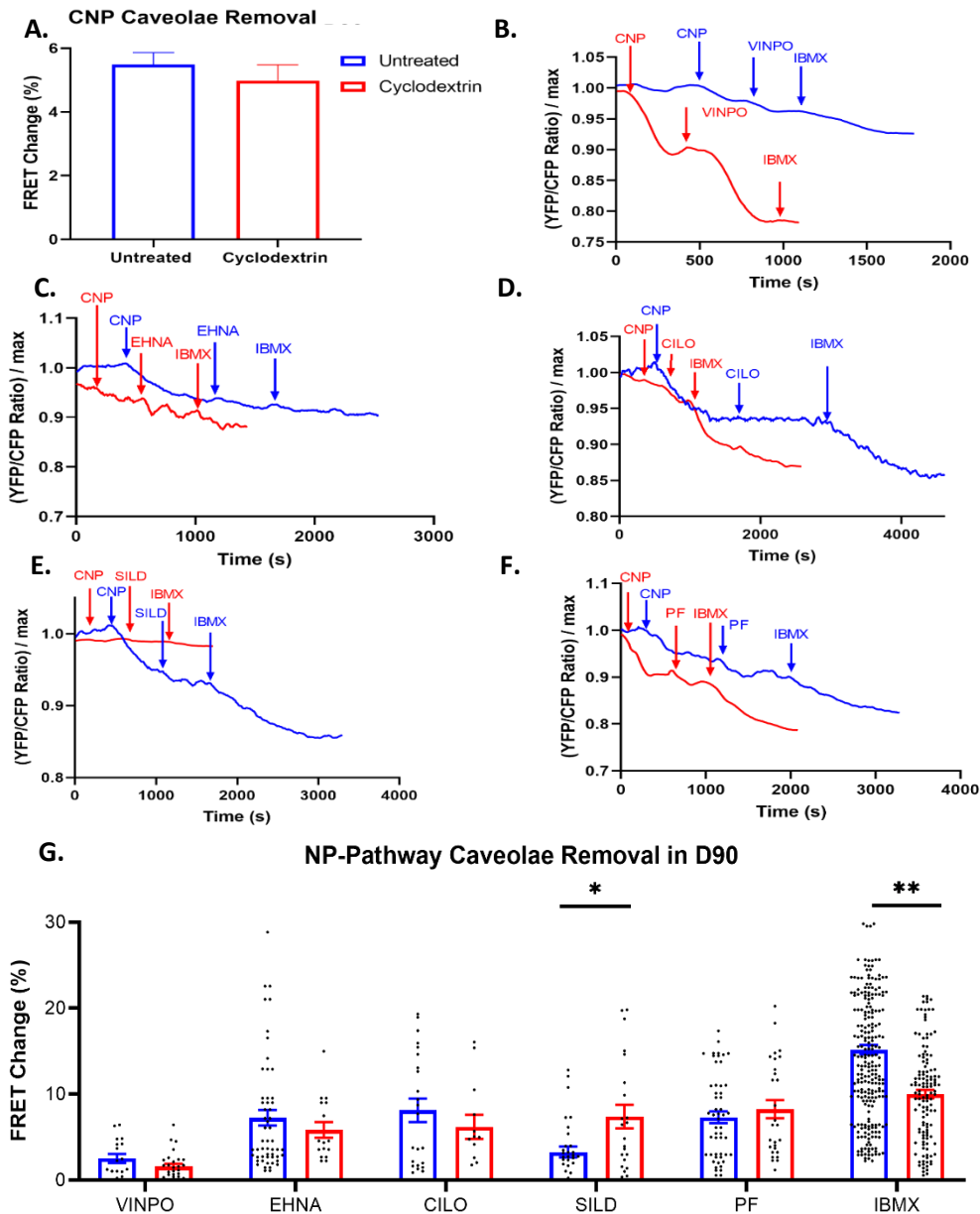


Figure 35. D90 untreated vs D90 cyclodextrin in FRET-sensor transfection IMR90 HiPSC-CM after stimulation with 500 nM CNP followed 10 μ M of PDE inhibitor for PDE1 (VINPO), PDE2 (EHNA), PDE3 (CILO), PDE5 (SILD), or PDE9 (PF). FRET change was normalised to the response after a saturating dose of 100 μ M IBMX. **A.** cGMP stimulant alone. **B-F.** representative curves. **G.** PDEi comparison. Significance tested using unpaired T-tests with Holm-Šidák post-hoc test (* $P = 0.05$, ** $P = 0.001$). Data are presented as mean \pm SEM. $n =$ cells/batches with **A:** D30 $n = 242/15$ D90 $n = 130/15$, **G:** VINPO D30 $n = 18/3$ D90 $n = 28/3$, EHNA D30 $n = 54/3$ D90 $n = 16/3$, CILO D30 $n = 23/3$ D90 = $13/3$, SILD D30 $n = 32/3$ D90 $n = 22/3$, PF D30 $n = 53/3$ D90 $n = 28/3$, IBMX D30 $n = 248/15$ D90 = $130/15$.

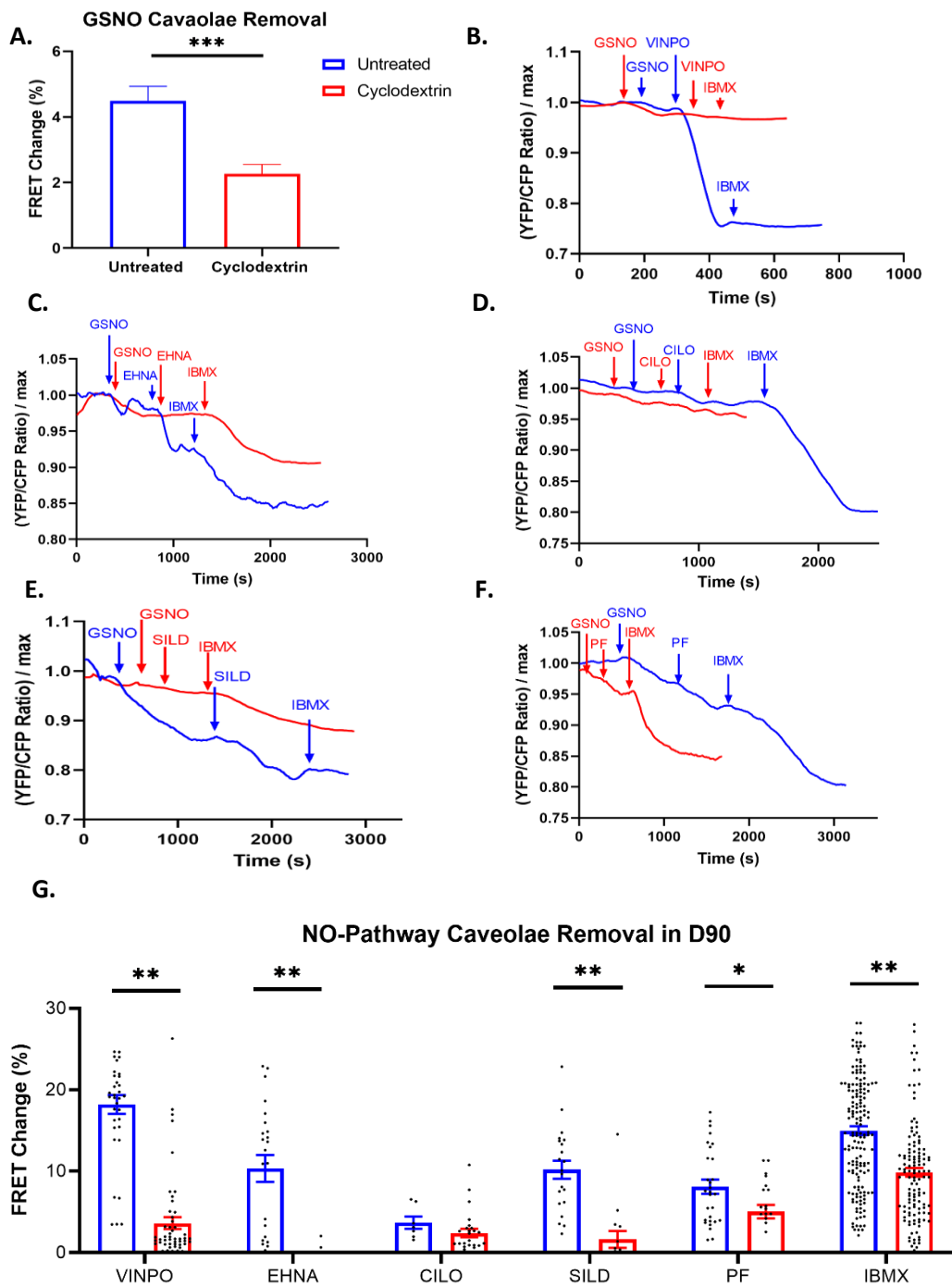


Figure 36. D90 untreated vs D90 cyclodextrin in FRET-sensor transfection IMR90 HiPSC-CM after stimulation with 5 μ M GSNO followed 10 μ M of PDE inhibitor for PDE1 (VINPO), PDE2 (EHNA), PDE3 (CILO), PDE5 (SILD), or PDE9 (PF). FRET change was normalised to the response after a saturating dose of 100 μ M IBMX. **A.** cGMP stimulant alone. **B-F.** representative curves. **G.** PDEi comparison. Significance tested using unpaired T-tests with Holm-Šidák post-hoc test (* $P = 0.05$, ** $P = 0.001$). Data are presented as mean \pm SEM. $n =$ cells/batches with **A:** D30 $n = 187/15$ D90 $n = 125/15$, **G:** VINPO D30 $n = 35/3$ D90 $n = 51/3$, EHNA D30 $n = 23/3$ D90 $n = 13/3$, CILO D30 $n = 7/3$ D90 = 25/3, SILD D30 $n = 21/3$ D90 $n = 15/3$, PF D30 $n = 29/3$ D90 $n = 21/3$, IBMX D30 $n = 164/15$ D90 = 125/15.

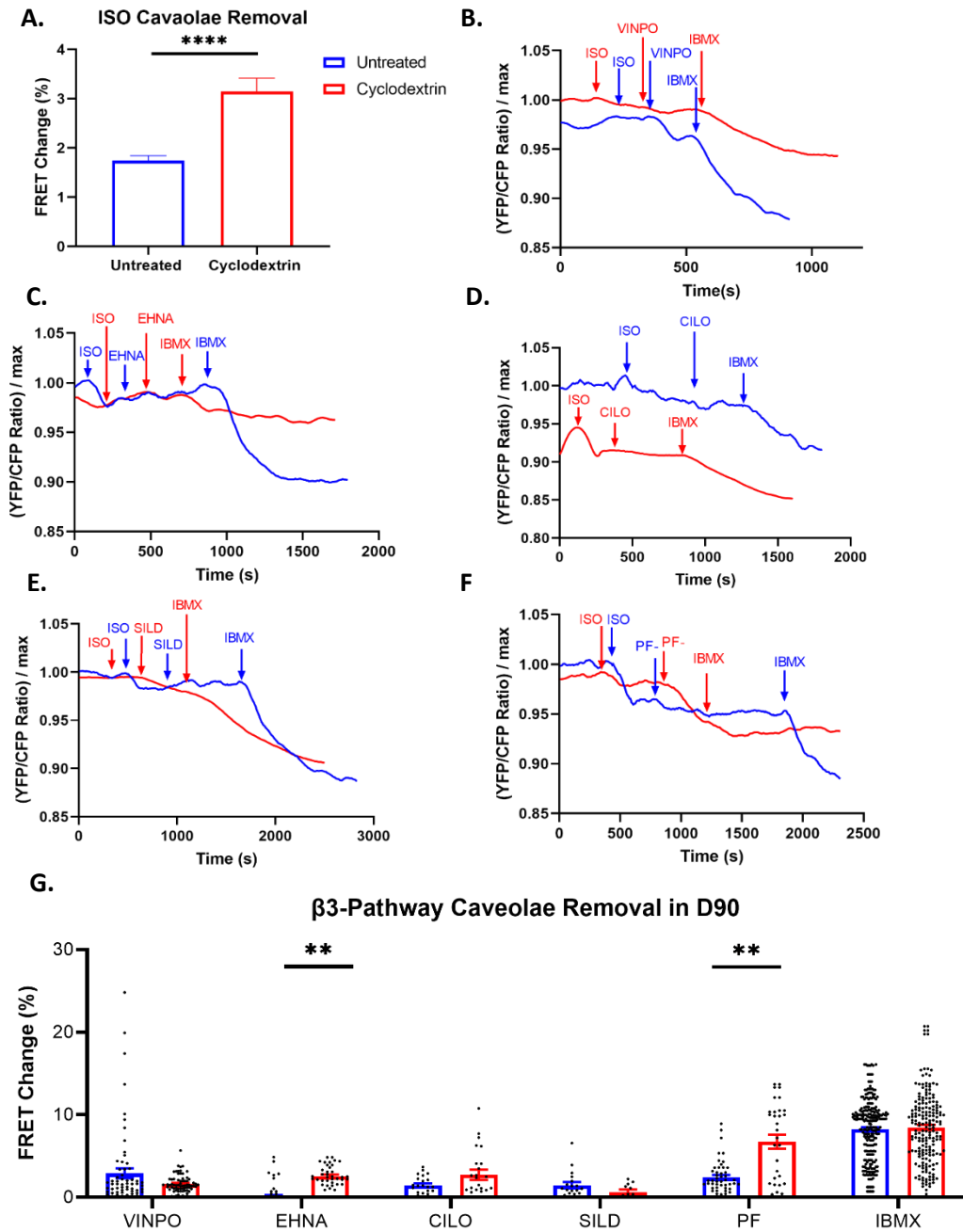


Figure 37. D90 untreated vs D90 cyclodextrin in FRET-sensor transfection IMR90 HiPSC-CM stimulated with 100 nM ISO after a 10-minute CGP (100 nM) + ICI (50 nM) followed by 10 μ M of PDE inhibitor for PDE1 (VINPO), PDE2 (EHNA), PDE3 (CILO), PDE5 (SILD), or PDE9 (PF). FRET change was normalised to the response after a saturating dose of 100 μ M IBMX. **A.** cGMP stimulation alone. **B-F.** representative curves. **G.** PDEi comparison. Significance tested using unpaired T-tests with Holm-Šidák post-hoc test (* $P = 0.05$, ** $P = 0.001$). Data are presented as mean \pm SEM. $n =$ cells/batches with **A:** D30 $n = 251/15$ D90 $n = 177/15$, **G:** VINPO D30 $n = 65/3$ D90 $n = 71/3$, EHNA D30 $n = 36/3$ D90 $n = 39/3$, CILO D30 $n = 22/3$ D90 = $24/3$, SILD D30 $n = 19/3$ D90 $n = 11/3$, PF D30 $n = 49/3$ D90 $n = 32/3$, IBMX D30 $n = 252/15$ D90 = $188/15$.

5.4. Discussion

The lacklustre response with EHNA after CNP compared to the remarkable response after GSNO indicates that PDE2 may be mainly compartmentalising cGMP produced through the sGC-NO pathway. This is in line with previous, albeit conflicting, data on the localisation of PDE2 in cardiac cells. In healthy adult human cardiomyocytes, PDE2A was only found in the cytosolic fraction, which supports its primary role in compartmentalising cGMP from the cytosolic sGC-NO pathway (Sugioka et al. 1994). However, guinea pig cardiac ventricles PDE2A activity was found in both cytosolic and membrane preparations (Muller, Stoclet, and Lugnier 1992). To further complicate matters, immunohistochemistry data in rat ventricular myocytes show that PDE2A is localised to the plasma membrane, cell-to-cell junctions, and sarcomeric Z-lines. Additionally, PDE2A activity in rat ventricular myocytes was only found in membrane fractions (Mongillo et al. 2006). Whether this conflicting data is as it seems, simply due to the difference between human and animal models, or has a deeper meaning is yet difficult to say with certainty. While it is difficult to compare HiPSC-CM to that from adult human cardiomyocytes, the nano-domain switch in adult human cardiomyocytes previously discussed shows that our cells may shift from a 'healthy' configuration where PDE2 is localised to the plasma membrane together with the β_1 -AR as well as cGMP produced through β_3 -AR activation, to the 'early disease' configuration where PDE2 is localised to the β_2 -AR where it has been found to be interact mostly with cGMP from the NP-pathway (Perera et al. 2015). It should be noted however, that the study which found this nano-domain switch investigated adult human cardiomyocytes. These hold T-tubules to which β_2 -AR localise even in early disease, while our D90 HiPSC-CM would lack or have a very rudimentary version of such a structure. Additionally, HiPSC-CM FRET data investigating the compartmentalising effects of PDE2 on cAMP do not show a significant aging-dependant

change between D30 and D90, but find that PDE2 within this age range predominantly affects cAMP pools produced through β_2 -AR stimulation (Hasan et al. 2020).

In D30 HiPSC-CM with CILO we find the opposite: much more noticeable increase in FRET response after CNP compared to GSNO. Furthermore, we find a small change to the graduality of the dose-responsiveness between D30 and D90 after CNP, with D90s jumping up in response on 5 μ M while D30s increased more gradually with a small increase at 1 μ M. However, the response in D90 HiPSC-CM with GSNO-CILO is varied but overall low compared to D30 or CNP experiments. PDE3 has been shown to mainly affect pools of cAMP produced by β_2 -AR in HiPSC-CM of D30 to D90 (Hasan et al. 2020). Combined with our data showing a much lesser effect of PDE3 on the NO-pathway in D90 HiPSC-CM, we find a possible switch of PDE3 from favouring the NO-pathway to favouring the NP-pathway.

The contrast between D30 and D90 response to SILD indicates a developmental change whereby PDE5 starts to take a role in cGMP down-regulation only after a time in development. This follows expression profiling data of PDE5A that shows a rise in its expression as HiPSC-CM age (Wu et al. 2015). PF has the most consistent gradual increase with dosage, a trait which we find in every experimental condition that uses PF, indicating a strong role of PDE9-based cGMP control. Unfortunately, there is no aging-based difference in response, making PDE9 a poor indicator of development between D30 and D90 HiPSC-CM. Studies in adult and neonatal rat cardiomyocytes show that PDE9 predominantly affects the NP-pathway (Redfield et al. 2013), however such studies have not been performed in HiPSC-CM. Additionally, we tally the number of successful cells, i.e. experiments where a given cell shows a response to any stimuli and is not subject to any optical or mechanical interference, versus cells which fail these conditions. We find that in D90s the failure rate is

almost tripled (33 vs 86), which may be an indicator of decreased cell viability as the HiPSC-CM are cultured for a prolonged time (Figure 38).

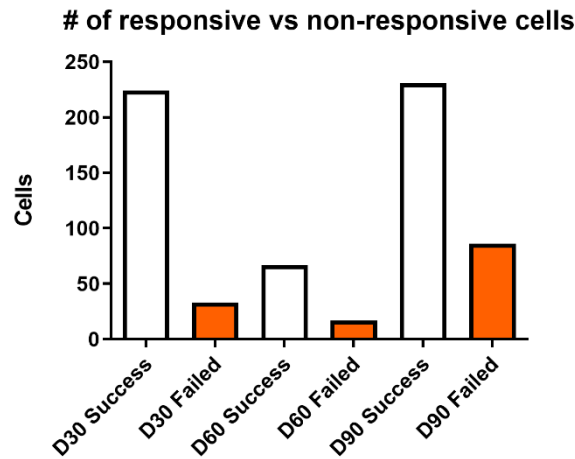


Figure 38. Successful and failed experiments for each age of HiPSC-CM. Failure criteria are the lack of response to any stimuli, any optical interference, or any mechanical interference.

In our single dose D30 vs D90 studies, we find that PDE3 is the predominant cGMP regulator in D30 for both the NP- and NO-pathways. This role is significantly diminished in all three pathways in D90. This is in opposition to data we gathered in during the dose-response experiments, where we found that PDE3 would switch from favouring the NO-pathway in D30 to favouring the NP-pathway in D90. The large changes we find in D30 vs D90 for PDE3 are in accord with recent FRET data showing that maturation of IMR90 HiPSC-CM drastically changes the activities of PDE3 (Hasan et al. 2020).

The NO-pathway shows that the dominance of PDE3 in D30 is shifted onto PDE1 and PDE5 in D90. It's been shown that PDE1 is available in much higher levels than PDE5 in adult human myocardium (Movsesian and Kukreja 2011). The similar response we find when blocking PDE1 and PDE5 may be caused by a reduction in PDE1's effect on cGMP due to its dual-

substrate nature, or due to PDE5 being localised closer to sites of NO-cGMP production. It should be noted that a study in mouse cardiomyocytes found PDE1 primarily expressed in non-myocyte cells (Bode, Kanter, and Brunton 1991), which could mean that as our HiPSC-CMs mature or as HiPSC-CM differentiation tools become more accurate, we would start to see a decline in the role of PDE1.

In the NP-pathway, there is a significant reduction in the effects of PDE3, PDE5, and PDE9 but no concurrent increases. At the same time, FRET response to CNP stimulation increases while response to GSNO stimulation decreases. Taken together these results show that while the NP-pathway has a larger presence in D90 HiPSC-CM, their compartmentalisation depends less on PDEs and perhaps shifts to structural elements.

The ISO-pathway shows a low effect of all tested PDEs, which is reduced to almost no detectable effect in D90. Recent data from healthy and failing rat adult cardiomyocytes had shown an increase in the effect of PDE2i on cGMP generated through cGMP stimulation, suggesting disruption of compartmentalising structures (Schobesberger et al. 2020). Our findings corroborate this, indicating that D30 is more akin to failing than healthy cardiomyocytes. However, comparing our cells to adult rat cardiomyocytes is difficult and no data using closer models currently exists. Notably, no difference is seen in PDE1, PDE3, nor PDE5 in healthy vs failing adult rat cardiomyocytes.

PDE9 which has only recently been found expressed in mammalian hearts is known to primarily regulate the NP-pathway over the NO-pathway (Lee et al. 2015), with no β_3 -pathway data available until now. While there is a tendency towards a reduced role in D90 vs D30, we find no significant change in the β_3 -pathway FRET response after blocking PDE9.

We find an overall increase in cGMP generated through the β_3 -pathway after disruption of caveolae structures. We also find a reduction in the role of PDE1 in its regulation, as well as a large increase in the role of PDE9 in regulating this cGMP. Surprisingly, we find no difference in PDE2 which was shown to have an enhanced effect on β_1 -pathway but not β_2 -pathway cAMP after cyclodextrin treatment (Hasan et al. 2020). This shows that, as one may expect from two similarly localised receptors, the β_2 and β_3 -pathways are similarly affected by removal of caveolae.

In the NO-pathway, caveolae removal results in a significant reduction of cGMP production after GSNO stimulation as well as a reduced effect of all tested PDEs with the exception of PDE3i. This is in opposition to literature which shows that PDE3 (Götz et al. 2013) and PDE5 (Nagayama et al. 2008) are the main regulators of NO-cGMP, though it should be noted that this data was obtained from adult rats and mice respectively.

Caveolae removal seems to have no significant effect on the cGMP production through the NP-pathway. We only find PDE5 to be significantly affected by caveolae removal, having a greater effect on produced cGMP after cyclodextrin treatment. This can be ascribed to the release of PDE5 from caveolar compartments where it has a role in regulating β_3 -pathway cGMP (Bork and Nikolaev 2018). Notably, we find a significant decrease in response to IBMX after cyclodextrin treatment, possibly implying the involvement of an un-tested PDE.

5.5. Limitations and future work

We did not set-up a dose-response curve for PDE1 inhibitor, as we had not decided to use it in our follow-up experiments before being some ways through our D30 vs D90 experiments. We instead used PDE1 inhibitor concentrations found in literature studying cAMP in HiPSC-

CMs. It would be beneficial to increase the number of the D30-GSNO-SILD dose-response experiments, as these had many failed experiments reducing their number. If there was more time, an interesting point to pursue is the relation between shape and other characteristics of hiPSC-CMs and the failure rate and deviation of FRET response from the median. Furthermore, to get a better picture of the limits of the cardiomyocytes we could lower or increase the concentration further in experiments where the response has not shown a plateau. However, we find that this dose-response is sufficient for further investigations into cGMP compartmentalisation of aging cardiomyocytes.

Future work on the comparisons between ages would benefit from increased time-points selections, such as D60 and comparisons to adult human cardiomyocytes. An attempt was made to include adult human cardiomyocytes in this thesis, however viral transfections did not take. It was deemed that our supply of FRET sensor inducing virus had degraded.

Similarly, our caveolae studies would benefit from more time-points, but also from additional and more selective methods of caveolae removal. While cyclodextrin treatment significantly diminishes the presence of caveolae, the lipid depletion may have unwanted side-effects.

Chapter 6: Analysis of Gene and Protein expression, Contractility, and Calcium Dynamics in D30 and D90 HiPSC-CM in relation to cGMP Pathways

6.1. Introduction

In this chapter we compare our findings from chapter 5. to data on gene expression, protein expression, calcium handling, and contraction. We check our previous conclusions by using RT-qPCR, with the first dataset on PDE gene expressions for *PDE1A*, *PDE1B*, *PDE1C*, *PDE2A*, *PDE3A*, *PDE3B*, *PDE5A*, and *PDE9A* in HiPSC-CMs. We also measure expression of relevant receptors *NPR1*, *NPR2*, and *ADRB3*. And finally, we measure expression of NP precursors *NPPA*, *NPPB*, and *NPPC*. We show western blot data for the protein expression of *PDE1C*, *PDE2A*, *PDE3A*, and *PDE5A* in IMR-90- and CDI-derived HiPSC-CMs. CDI follow a different differentiation protocol and are compared between D20 and D40. We expand the data available on cGMP-related gene expression in HiPSC-CMs by comparing the previously mentioned genes in D30 vs D90 in IMR-90 derived cardiomyocytes.

Finally, we couple our findings to physiological data through calcium and contraction measurements obtained using CytoCypher. The CytoCypher is a brand-new microscopy device whose true innovation lies in the use of pixel correlation (PC) algorithm to measure the movement of cardiomyocyte contraction in many cells both simultaneously and in a sequenced fashion, resulting in massive data yield (Cao, Manders, and Helmes 2021). The down-side to this PC method is that measurements are delivered in arbitrary units, allowing normalised comparisons but giving no means to compare to older studies wherein contraction may be given in nanometre measurements. Based on our results from chapter 5., we chose to use the CytoCypher to measure changes in contraction and calcium-handling when stimulating the NP- and β_3 -pathways under conditions of PDE3i using Cilostamide and lipid depletion using M β CD. Additionally, we now use Cinaciguat as a direct and more powerful sGC stimulant. We chose these experiments to see our FRET results reflected in

other aspects of the cell's physiology. In particular, we wanted to study whether contractility and calcium dynamics provide similar conclusions to our FRET studies which have showed that PDE3 is the main regulator of NPR-2 mediated cGMP response in D30, the significance of PDE3 in all pathways is significantly reduced in D90, the lack of effect from NO-stimulation in D90, the lack of effect of PDE3 inhibition in the NO-pathway of D30 HiPSC-CM pre-treated with cyclodextrin, and finally the minimal effect of β_3 -AR stimulation on cGMP.

6.1.1. Aims

- To perform qPCR of genes relevant to the NP-, NO-, and β_3 -pathways in D30 and D90 HiPSC-CMs
 - PDEs: *PDE1A*, *PDE1B*, *PDE1C*, *PDE2A*, *PDE3A*, *PDE3B*, *PDE5A*, and *PDE9A*
 - NP precursors: *NPPA*, *NPPB*, and *NPPC*
 - Receptors: *NPR1*, *NPR2*, and *ADRB3*
- To look into the expression of genes for expression of relevant PDEs to protein, normalised to *GAPDH* protein expression, in D30 and D90 HiPSC-CMs
 - *PDE1C*, *PDE2A*, *PDE3A*, and *PDE5A*
- To relate our findings to physiology by examining the contraction and calcium-handling of D30 and D90 HiPSC-CMs under conditions similar to our FRET experiments
 - D30 vs D90 | CNP, PDE3i, IBMX
 - D30 vs D90 | sGC-agonist BAY58-2667 (Cinaciguat) at 100 μ M, IBMX
 - D30 vs D90 | cyclodextrin, Cinaciguat, IBMX
 - D30 vs D90 | β_1 - and β_2 -AR blockers, ISO, IBMX

6.2. Methods

6.2.1. RT-QPCR

Primer name	Primer sequence
ADRB3_FWD ADRB3_REV	GACCAACGTGTTTCGTGACTTC GCACAGGGTTTCGATGCTG
hGAPDH_FWD hGAPDH_REV	AATCCCATCACCATCTTCCA TGGACTCCACGACGACTCA
PDE1A_FWD PDE1A_REV	TTGGCTTCTACCTTTACACGGA AGGGCAAATACATCGAAAGACC
PDE1B_FWD PDE1B_REV	ATGAGACACGGCAAATCTTGG TGCACAATGCTTCGGAACCTG
PDE1C_FWD PDE1C_REV	GATGTGGACAAGTGGTCCTTTG GGGGATCTTGAAACGGCTGA
PDE2A_FWD PDE2A_REV	CCTCCTGTGACCTCTCTGACC TGAACCTGTGGGACACCTTGG
PDE3A_FWD PDE3A_REV	TCACAGGGCCTTAACCTTTACAC GGAGCAAGAATTGGTTTGTCC
PDE3B_FWD PDE3B_REV	CCTCAGGCAGTTTATACAATG TGCTTCTTCATCTCCCTGCTC
PDE5A_FWD PDE5A_REV	GCAGAGTCCTCGTGCAAGATAA GTCTAAGAGGGCCGGTCAAATTC
PDE9A_FWD PDE9A_REV	GACTCCTCGACGCGATGTTC TTTCTGTAGTTGTCGTGGACG
NPR1_FWD NPR1_REV	CTTCGGTGTCAAGGACGAGTA GGTAGGCGTAGAGCATGAGC
NPR2_FWD NPR2_REV	TGACCCCGACCTGCTGTTA CGAACCAGGGTACGATAATGG
NPR3_FWD NPR3_REV	AGCTAAGCAAGCATACTCGTCC GCTTCAAAGTCGTGTTTGTCTCC
NPPB_FWD NPPB_REV	TGGAAACGTCCGGGTACAG CTGATCCGGTCCATCTTCCT
NPPC_FWD NPPC_REV	GCAAATACAAAGGAGCCAACAAG CATGGAGCCGATTCGGTCC
NPPA_FWD NPPA_REV	CAACGCAGACCTGATGGATTT AGCCCCCGCTTCTTCATTC

Table 5. RT-qPCR primers.

RNA was extracted using the RNeasy Mini Kit (Qiagen, Manchester, United Kingdom) according to manufacturer's guidelines. Concentrations were measured using a NanoDrop UV-Vis Spectrophotometer (Thermo-Fisher Scientific, Loughborough, United Kingdom). An

iTaq SYBR Green qPCR kit (Bio-Rad, the Netherlands) was used to perform RT-QPCR with the primers listed in Table 5.

6.2.2. Western Blot

Wells of D30 and D90 HiPSC-CMs were washed with room-temperature PBS, detached using 0.5 mL of CDS (Cell dissociation solution: 20 mL RPMI, 20 mL cell dissociation buffer, 10 mL Trypsin). Cell suspensions were spun down at 300 RPM for 4 minutes, the supernatant was aspirated, and the pellet was washed with PBS before being transferred to 1.5 mL Eppendorf tubes. The cells were pelleted again using the same settings and subsequently frozen in -80°C. Tubes containing our frozen samples were shipped to the N. Vaicheslav laboratory where the rest of the protocol was performed. Cells were resuspended in homogenisation buffer (1 mM EGTA, 10 mM HEPES, 150 mM NaCl, 300 mM sucrose, 1% triton, phosphatase and protease inhibitors (Roche)). Cells were homogenised for three times 20 seconds with an Ultra Turrax (T-10 basic, IKA). Lysates were centrifuged at 13000 RPM, 4°C for 10 minutes and supernatant was used with a Pierce BCA protein assay kit (Thermo Scientific) to determine protein concentrations. Lysates were mixed with 3 x SDS Stop for a 10-minute denaturation at 70°C and then stored at -20°C. 10-30 µg of protein samples were loaded on 8-15% SDS polyacrylamide gels for size-separation through electrophoresis. Protein size standards Protein marker V (PeqLab) or Precision Plus Protein Dual Color (Biorad) were used as size standards. Using a tank-blot method, proteins were transferred to a nitrocellulose or PVDF membrane (Amersham and Biorad). Here, immunodetection was carried out using antibodies for GAPDH (1:160000 dilution, Bio Trend #5G4), PDE1C (1:1000 dilution, generous gift from C. Yan), PDE2A (1:500 dilution, Fabgennix #PD2A-101AP), PDE3A (1:1000 dilution, generous gift from C. Yan), PDE4B (1:2500 dilution, abcam #ab170939), and PDE4D (1:2500 dilution, abcam #ab171750).

6.2.3. CytoCypher

The CytoCypher (Ionoptix, US) is a high throughput multicell system specifically built to test compounds on myocytes. The device contains an enclosed microscope, working at a 10x magnification, on a mechanical stage with X, Y, and Z motion. The device further contains a MyoCam-S3 camera used to find cells and measure contraction. The device is connected to a photometer, which can feed data to the IonWizard 7.3 software on calcium dynamics as displayed through our use of fura-2 as a calcium indicator.

Our general preparation protocol starts at the application of the Fura-2 AM dye. HiPSC-CMs of D30 or D90 old that have been plated in 35 mm glass-bottom MatTek dishes are gently washed twice with 1 mL of HBSS buffer (137 mM NaCl, 5.4 mM KCl, 0.5 mM MgCl₂-6H₂O, 0.4 mM MgSO₄-7H₂O, 0.44 mM KH₂PO₄, 0.34 mM Na₂HPO₄-7H₂O), then gently washed thrice with 1 mL HBSS+BSA (1 mg / mL of BSA mixed into HBSS), and finally 1 µL of a solubilised Fura-2 AM (1 g / L in DMSO), diluted and vortexed for 1 minute in 1 mL of HBSS+BSA, was added to the dish. The dish was then incubated at 37 °C and 5 % CO₂ for 45 minutes. In the case of experiments requiring cyclodextrin pre-treatment (1.3 g / L for 1 hour), this treatment was added during the dyeing step when 30 minutes remained. Cells were then washed 3 to 4 times with HBSS buffer and 2 mL was added to the dish, the dish was then placed back into the incubator. After 30 minutes of incubation, the dish was placed over the CytoCypher lens and an IonOptix MyoPacer was used to pace the cells at 40 V for 10 ms at 1 Hz intervals. For experiments requiring β-blocker pre-treatment (50 nM CGP + 50 nM ICI for 15 minutes), this treatment was added during the last 15 minutes of this 30-minute incubation. The lid of the CytoCypher device was closed, allowing the cells with now a light-sensitive dye to stay in darkness. Areas containing contracting cells were selected and the program was run to record at 250 frames per second during the experiment.

During the experiment we first recorded 5 seconds of baseline, then added a drug, recorded another 5 seconds, and so forth. Drugs added were CNP (100 nM), Cinaciguat (100 μ M), or ISO, followed by PDE3 (10 μ M), and finally IBMX (100 μ M).

The CytoCypher comes with a data analysis tool named CytoSolver, which parses the IonWizard data files and exports a plethora of calculated parameters to excel. From these parameters we further analysed time to peak (TTP), return velocity (RV), and percentage shortening (%S) for Pixel correlation (PC) based data and TTP, RV, and peak divided by baseline (PB) for the ratio-metric calcium (RMC) based data.

6.2.4. Statistics

Data analysis was performed within GraphPad Prism 8. Our RT-qPCR data was tested for statistical significance using an un-paired t-test with alpha set to 0.05. CytoCypher data was tested for statistical significance using a Nested one-way ANOVA with Tukey's multiple comparisons test with the alpha set to 0.05. Each CytoCypher measurement recorded 5 transients which were averaged and used as a data point for that cell under the relevant experimental condition. The western blot results were tested using an un-paired Mann-Whitney test with statistical significance defined by a $P < 0.05$.

6.3. Results

6.3.1. RT-qPCR

We tested the expression of several genes of interest, comparing them between D30 and D90, and normalising the data to the expression of *GAPDH*. We found no significant difference in gene expression of cAMP-targeting PDEs: PDE1A ($P = 0.1790$), PDE1B ($P =$

0.0099), PDE1C (P = 0.0752), PDE2A (P = 0.9968), PDE3A (P = 0.1547), nor PDE3B (P = 0.9087) in D30 vs D90 comparisons (Figure 39A). When looking at cGMP-specific PDEs: PDE5A was expressed at a significantly lower level (P = 0.0014) in D30 (mean DDcT = 0.1160) compared to D90 (mean DDcT = 0.3556) and so was PDE9A (P = 0.0047) in D30 (mean DDcT = 0.1513) compared to D90 (mean DDcT = 0.0398) (Figure 39B).

There was no significant difference in gene expression of receptors NPR1 (P = 0.0277), nor NPR2 (P = 0.7796) in D30 vs D90 (Figure 39C). However, ADRB3 showed significantly lower expression (P = 0.0146) in D30 (mean DDcT = 3.877) vs D90 (mean DDcT = 11.71) (Figure 39C). No significant differences were found for NPPA (P = 0.2145), NPPB (P = 0.0409), nor NPPC (P = 0.2449) (Figure 38D).

6.3.2. Western Blot

A western blot was performed using 6 different PDE antibodies and the data was normalised to GAPDH (Figure 39). We found significant differences between IMR90-derived cells of D30 and D90 for the protein expression of PDE1C (P = 0.0286) and PDE4B (P = 0.0571). PDE1C was reduced from D30 (0.7233 ± 0.0674 , n = 4) to D90 (0.3968 ± 0.0539 , n = 4). PDE4B was reduced from D30 (0.1227 ± 0.0647 , n = 4) to D90 (0.7778 ± 0.0492 , n = 3). No significant differences were found for PDE2A (P = 0.2860, n = 4), PDE3A (P = 0.8857, n = 4), PDE4D (P = 0.1143, n = 4), nor PDE5A (P = 0.4857, n = 4).

6.3.3. CytoCypher

Using the new CytoCypher device and software, we measured and analysed contraction data calculated through PC and RMC data measured by using a photometer with a Fura-2 dye. Our representative traces show 5 recorded peaks in accordance with our measurement

time of 5 seconds and our pacing frequency of 1 Hz (Figure 41 and Figure 42). Segments of traces in which no peak is found, such as in this case the end of the recording, are automatically rejected by the CytoSolver software (Figure 42). In 288 comparisons, we have found only 2 significant differences (

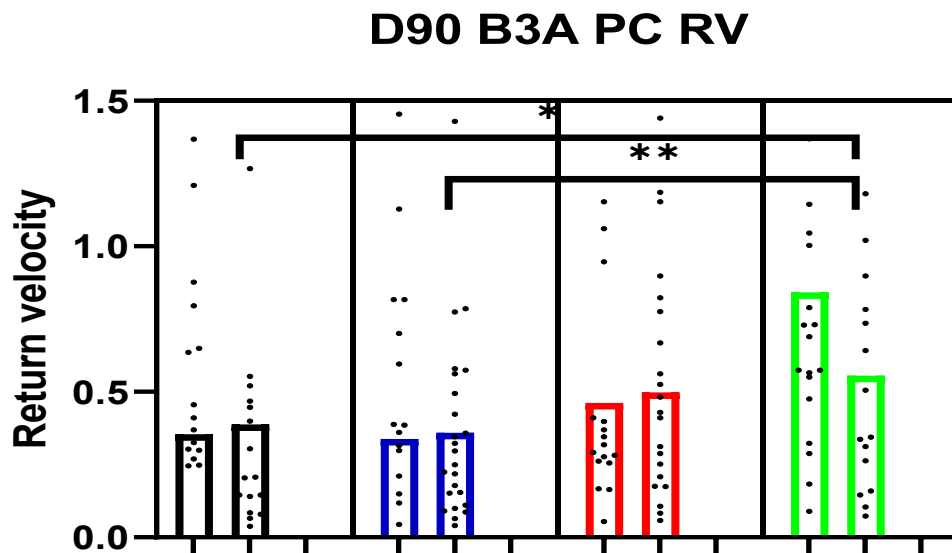


Figure 43). This was found in PC measurements of RV in our D90 experiment in which cells were stimulated with the B3A Cinaciguat, followed by PDE3 inhibition, and finally IBMX treatment. Significant difference was found between IBMX and baseline ($P = 0.0209$), as well as IBMX and Cinaciguat ($P = 0.0075$). Due to experimental failure and the lack of time needed to generate new cells the only experiment that showed any significant rejections of the null-hypothesis has only 2 replicates, adding a factor of uncertainty to the statistical findings. As the rest of these experiments have not provided sufficient information for valid conclusions to be drawn, we have omitted the graphs from this work.

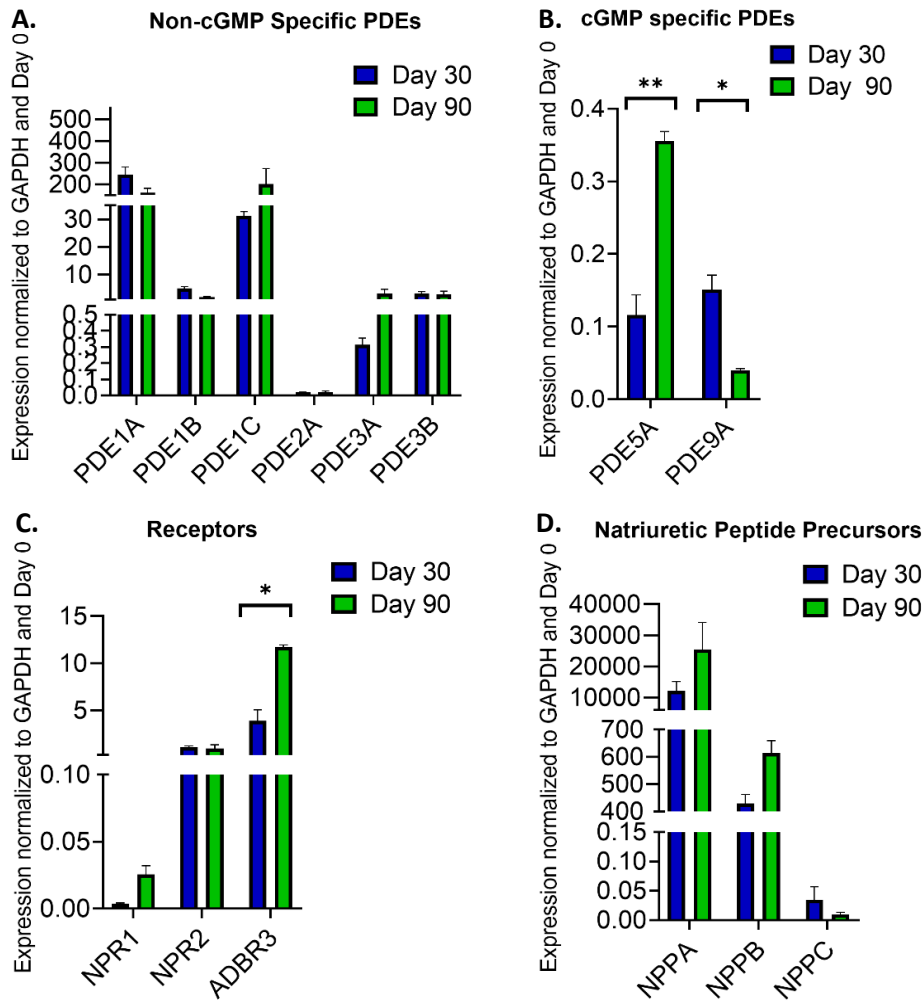


Figure 39. Expression of genes of interest measured in triplicates through RT-qPCR with RNA extracted from D30 and D90 HiPSC-CMs. Data normalised to GAPDH and expression of genes from Day 0 HiPSC-CMs. Data are presented as mean \pm SEM. Tested for statistical significance through T-tests with * $p \leq 0.05$ and ** $p \leq 0.01$.

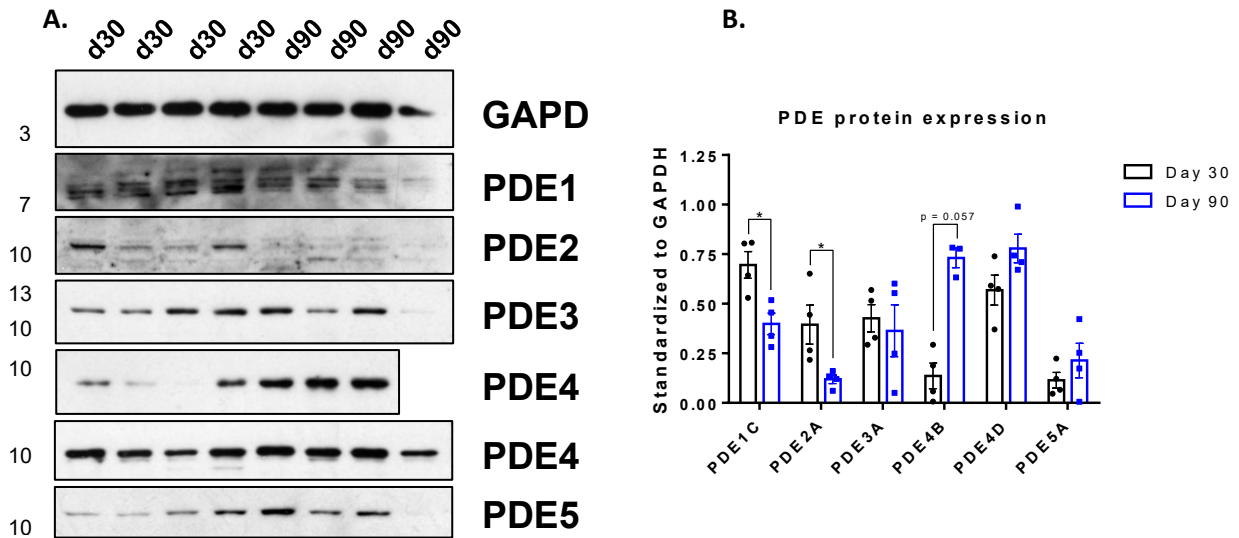


Figure 40. D30 vs D90 Western blot protein expression graciously performed by the N. Slava group using their probes. **A.** Blot images with band sizes shown. **B.** results from 4 batches of HiSPC-CM differentiations normalised to GAPDH. From each batch, a triplicate of suspensions containing 1 million cells were used and averaged. Data are presented as mean \pm SEM. Statistical significance tested using Mann-Whitney test with $*p \leq 0.05$.

Representative Trace Baseline D30 HiPSC-CM

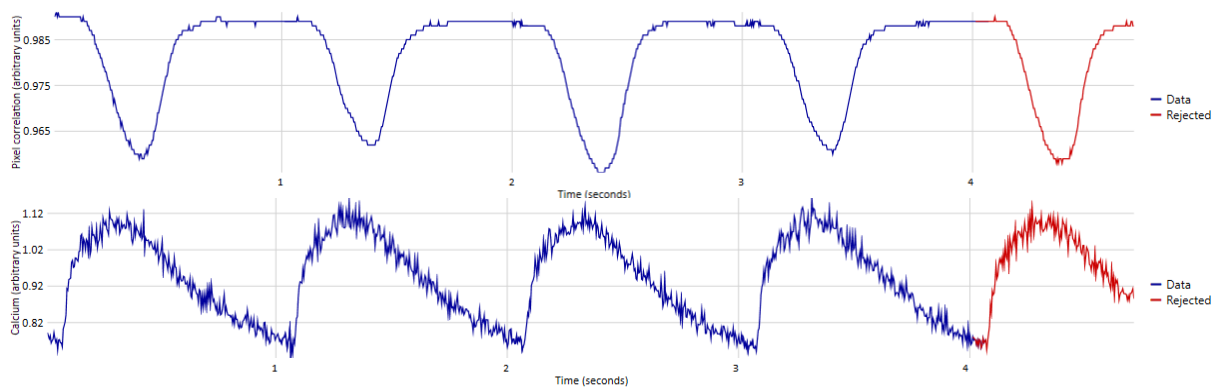


Figure 41. Representative trace of D30 HiPSC-CM PC and RMC baseline data. Data was recorded during the first 5 seconds of an experiment, prior to any drug-based stimulation. Cells were paced at 1 Hz, 40 V for 10 ms per pulse. Images were recorded at 250 Hz. Red segments of the graph show automatically rejected peaks that did not fix CytoSolver's criteria.

Representative Trace Baseline D90 HiPSC-CM

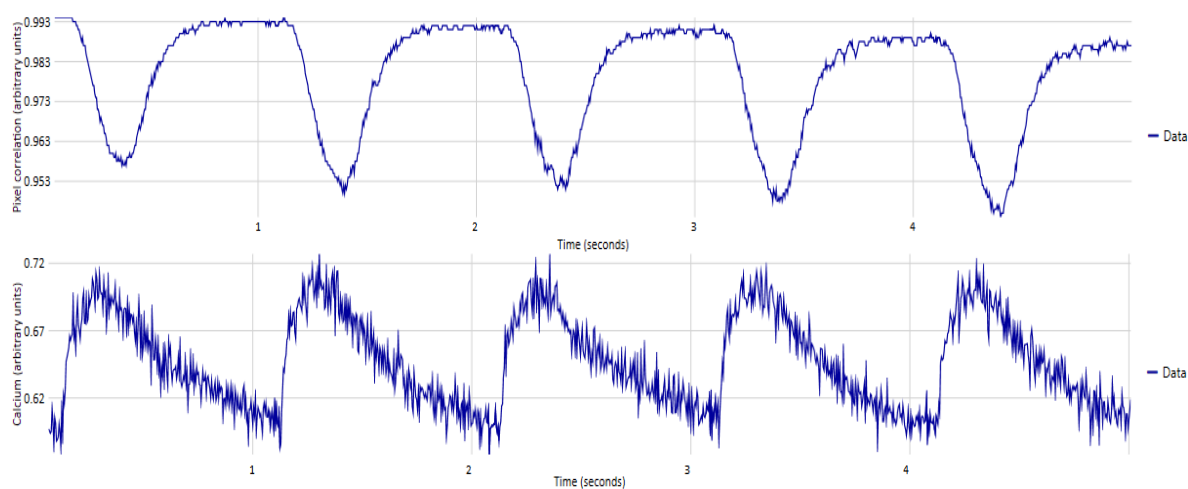


Figure 42. Representative trace of D90 HiPSC-CM PC and RMC baseline data. Data was recorded during the first 5 seconds of an experiment, prior to any drug-based stimulation. Cells were paced at 1 Hz, 40 V for 10 ms per pulse. Images were recorded at 250 Hz.

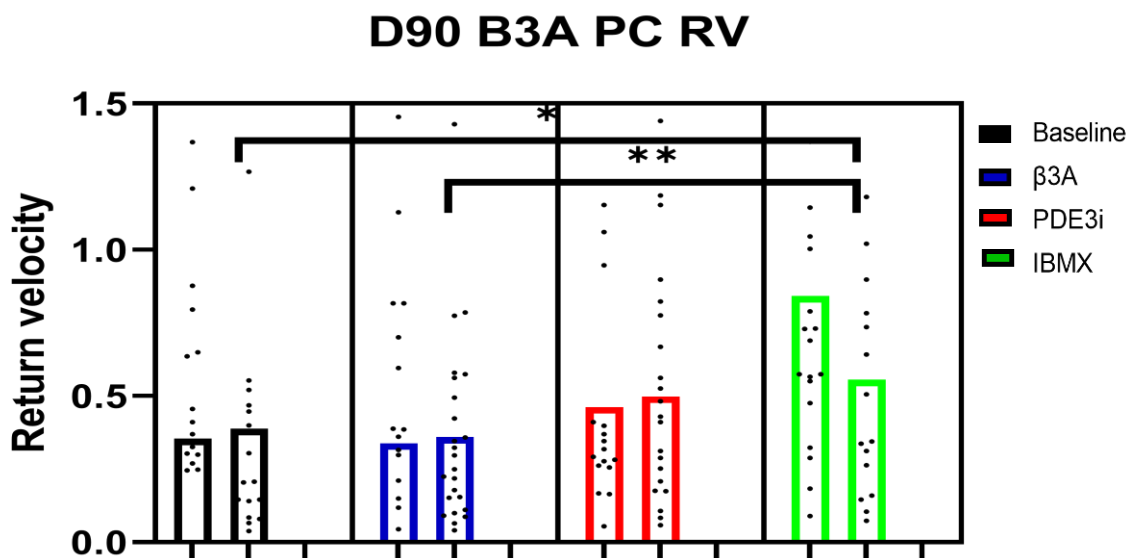


Figure 43. CytoCypher contraction (PC) and ratiometric calcium-handling (RMC) data measured from D90 HiPSC-CM under conditions of 100 μ M sGC stimulator cinaciguat, followed by PDE3 inhibition using 10 μ M cilostamide, and finally global PDE inhibition using 100 μ M IBMX. Recordings of 5 seconds were made after each drug addition. Cells were paced at 1 Hz interval for 10 ms at 40 V. Recordings of cells were made at a framerate of 250 Hz. Data are presented as mean \pm SEM. Statistical significance was tested using One-way ANOVA with * $p \leq 0.05$, ** $p \leq 0.01$. Measures of length and thus speed use an arbitrary unit by design. $n = 24/2$ cells/batches.

6.4. Discussion

In the 2016 paper by Jung et al., development of β -pathway signaling in HiPSC-CM maturing from D30 to D90 was studied in terms of expression of its constituents, coupling to physiology (Jung et al. 2016). It was found that β -AR genes *ADRB1* and *ADRB2*, but not *ADRB3* were upregulated through maturation. Additionally, structural genes *Cav3* and *Cavin4* were found upregulated in D90. Production of contraction-relevant proteins CaMKII and Tnl were also found to be enhanced at D90. More recently A. Hasan et al. confirmed *Cav3* gene upregulation in IMR90 HiPSC-CMs at D90 vs D30 as well as an upregulation of β_2 -

AR. β -AR was not found to be significantly upregulated after maturation in this study (Hasan et al. 2020).

NPPA and *NPPB* gene expression normalised to *GAPDH* were found to be relatively high in D30-D36 HiPSC-CMs grown in an EHT format (Mannhardt et al. 2017). Relative expression of these two genes grows from D2 to its peak at D14, after which it is reduced slightly before stabilising from D35-D42 (Puppala et al. 2013).

PDE gene expression in D15-D20 HiPSC-CMs grown in EHT format has shown *PDE3B* and *PDE4B* to be significantly higher than the similarly expressed *PDE3A*, *PDE4A*, *PDE4C*, and *PDE4D* (Saleem et al. 2020a). Interestingly, *PDE1A* and *PDE3B* were not detected in a qualitative RT-PCR, though it was noted that this method performed at a lesser sensitivity. *ADRB1* and *ADRB2* gene expression was measured in a 2D tissue of D30 HiPSC-CMs as well as EHT tissues of D50 and D80 HiPSC-CMs (de Lange et al. 2021). It was found that expression of *ADRB1* and *ADRB2* significantly increase as the cells mature over this range of time.

ADRB3 expression in D30, D60, and D90 HiPSC-CMs was compared to expression of fetal human heart tissue and adult human left ventricle tissue and was found to be much lower than either, though it was similar in expression to levels in adult human left atrial tissue (Jung et al. 2016). Furthermore, expression data for *ADRB3* shows that it is upregulated in D30 HiPSC-CMs when these cells are grown in a 3D culture (Giacomelli et al. 2019). In 2021 it was shown that *ADRA2A*, *ADRB2*, and *ADRB3* expression levels vary over the first 35 days of IMR-90 HiPSC-CM differentiation. While *ADRB2* does not significantly change during this maturation period, *ADRB3* shows a 100-fold increase by D20 and remains elevated at D30

and D35 (Hasan, 2020). This effect is greatly reduced through the use of a Cav β 2 mimetic peptide used to increase the depth of membrane invaginations such as caveolae.

In our studies we found a significant increase in PDE5A and ADRB3 gene expression from D30 to D90, along with a decrease in PDE9A expression. There was a disconnect between changes found in gene expression data versus protein expression data, wherein we only found PDE1C and PDE2A decreased, along with an increase in PDE4B.

The lack of any significant changes in PDE1-3, sGC, and NPP gene expression between D30 and D90 indicate that the differences we found in our FRET experiments are the result of other factors that influence their control on cGMP such as compartmentation or translation rate of mRNA. We find that despite this lack of change in PDE1 and PDE2 gene expression, there is a significant reduction in protein expression from D30 to D90. This contradicts our FRET data in the NO-pathway, which showed an increase here. This discrepancy could be the result of the subject of normalisation between experiments or indicate a compartmentation of these PDEs to a micro-domain where NO-cGMP does not sufficiently exist.

Supporting past studies (Wu et al. 2015) as well as our own FRET data, we find that expression of PDE5 increases during maturation. However, while our FRET data shows a major increase in the effect of PDE5 on the NO-pathway, a small decrease was noted in the NP-pathway and an even lesser one in the β_3 -pathway. It stands to reason that while the expression of PDE5 increases, increasing compartmentation after aging localises most of the PDE5 to nano-domains under the NO-pathway. PDE9 expression is shown to be increased in cardiac hypertrophy and heart failure resulting from HfPEF (Lee et al. 2015). The reduction in PDE9 gene expression we find shows conforms to the paradigm indicating that younger

HiPSC-CM more closely resemble failing cardiomyocytes and that maturation moves them away from this status. Our PDE9 expression data also supports our FRET data, though we unfortunately did not have any tested antibodies available to measure PDE9 protein content. Finally, we find a strong increase in PDE4B but not PDE4D protein expression in D90. The cAMP-specific PDE4B is known to primarily regulate cAMP produced through stimulation of the β_2 -AR in the T-tubules where it may affect PDE2 and PDE3 mediated cAMP-cGMP cross-talk, thus exhibiting a regulatory role on the T-tubule present β_3 -pathway (Bobin et al. 2016).

The lack of significant differences in contraction and calcium handling in our experimental conditions poses an interesting question of whether cGMP in these immature cells truly has no measurable effect, or if our experiments need to be bolstered with more repeats or a different approach. While studies of contraction and calcium handling in relation to cGMP stimulation in HiPSC-CM to compare to are few, one recent publication examined the role of PDE3 in HiPSC-EHTs. Though it should be noted that these cells were not stimulated for cGMP production, it was found that PDE3 inhibition significantly increased the contractile force as well as the calcium current in these cells (Saleem et al. 2020). It should also be noted that the study in question conforms to the recent standards of statistical analysis which state a minimum n of 5 (Curtis et al. 2018).

6.5. Limitations and Future Work

We had a lack of suitable probes with which to match our investigated genes to protein expression data. This issue stems from a lack of available probes, a lack of sufficient study of existing probes, as well as a lack of funding.

Initially, we aimed to fractionate our protein lysates in order to be able to differentiate between membrane and cytosolic fractions in our protein expression data. However, it quickly became apparent that protein concentrations in HiPSC-CMs are too low to be financially worthwhile to split between fractions. Since our current data shows some interesting results, it has become more appealing to sacrifice the large number of HiPSC-CMs needed for a fractionation study in the future.

For our CytoCypher work we did not have the remaining time to properly explore optimal experimental conditions, primarily in regards to cell density, selection, pacing, and analysis. Our analysis initially showed some significant differences between our experiments, however more accurate nested analysis grouping averaged transients between technical replicates negated any statistical rejections of the null-hypothesis. Future work should pursue a higher number of replicates, experiment with different plating densities, selection of grouped versus individual cells, and take into account naturally contracting HiPSC-CMs. Additionally, testing our other cGMP stimulants and PDE inhibitors would be interesting. The effects PDE9 in particular on contractility have currently not been explored.

Chapter 7: Final Discussion

7.1. Discussion and Conclusions

The primary aim of this thesis was to expand our knowledge on the signaling molecules behind contraction in HiPSC-CMs in order to compare their function and growth to that of more mature cells for an understanding and the generation of an assessment tool of maturation. Since cAMP has been extensively studied in these cells, we focussed on its counterpart cGMP. We further aimed to assess the role of compartmentation of the cGMP signal through caveolae and PDEs, as well as the changes in these mechanics throughout the growth of HiPSC-CM.

We initially compared several popular cGMP sensors and selected ScGi to proceed with. While ScGi didn't have any publications to its name, we found that it outperformed cGi500 and CGES-DE5. It became apparent early on that due to the low concentrations in which cGMP appears in these cells, we would need enhanced numbers to obtain statistical significance in our experiments. For this need, we developed MultiFRET. A software tool that is currently in use for many diverse projects, MultiFRET allowed us to gain numbers that would previously be impossible to obtain during a single project. While alternative tools exist as discussed in 1.3.2., many of them are proprietary, require specialised hardware, or do not work during live imaging. For example, Clampex and Metamorph have been used in the past, though Metamorph is the one that is truly FRET-focussed. The proprietary software Metamorph is compatible with a wide variety of third-party microscopes and boasts many features, further being usable for FRAP and motion studies as well. The benefit of MultiFRET over Metamorph however is that it is open-source, this would technically enable anyone to pick it up and add whatever features and compatibility they are missing. One of MultiFRET's major strengths but simultaneously its main drawback is the

dependence on the Icy bioimaging suite. Icy is currently still backed by a development team that develops various updates, though they may generally be positive advancements they may create an issue of incompatibility with MultiFRET over time. MultiFRET is currently used with the latest version of Icy 2.0.3.0, issues in the future may be resolved by reverting Icy to this version.

The CytoCypher is another example of a tool with competing functionality. Though where it has the advantage of a commercial interest and a support team that updates and maintains the product as well as its software, it requires specific hardware. The CytoCypher boasts the ability to automatically detect cardiomyocytes as well, though this feature was not yet implemented for HiPSC-CM that have a lesser defined structure. Communications revealed that this feature was in the works to be released soon. The sheer amount of data that CytoCypher puts out is staggering, creating a task to either examine every calculation result in the output for statistical and biological significance, or to use only a selection of calculations based on previous studies of physiology. Seemingly problematic, we found that our HiPSC-CM particularly contract in groups or clumps of cells. While the PC algorithm and RMC measurements still show biologically correct curves, it is left to the imagination what the effect of cells contracting in opposite directions could be on the PC calculation. Working with the CytoCypher has led to me considering adapting the PC contraction measurement algorithms for FRET experiments through MultiFRET. Since the PC method works through comparison of pixels in an initial frame to those in the next frames, not actually detecting or tracking shapes, it would be feasible to measure contraction in FRET sensor illuminated cells. Though bleaching and change in brightness due to drug application could be a problem in certain scenarios, these issues can be evaded by measuring in a short timespan on drug effect plateaus.

With our initial FRET data from the sensor studies, we found that stimulation of the NO-pathway produces only a 0-10% FRET response in accordance with previous data (Stangherlin et al. 2011). We further showed that indeed the NO-pathway is more active in less mature cardiomyocytes, indicating a link between dysfunctional cardiomyocytes and an activation of the NO-pathway, possibly as a compensatory mechanism. This is supported by the emerging consensus on the cardioprotective properties of the NO-pathway (Park, Sandner, and Krieg 2018). We then found that PDE2 is the main regulator for this pathway, though it is found that in adult cardiomyocytes this may switch to the NP-pathway as cardiomyocytes reach an early disease configuration (Perera et al. 2015). Unfortunately, our maturation protocol did not show any difference for PDE2 in D30 and D90. Strangely, we found little to no gene expression of PDE2A in our cells though the western blot did find an amount which was significantly decreased in D90. This is a maturation-related change that was not found in cAMP FRET studies either (Hasan et al. 2020), prompting a need for further evidence to its presence in D30 and D90 HiPSC-CM.

We found a strong role for PDE3 in managing the NO- and NP-pathways in D30, which is diminished in D90. Interestingly, aging related reduction is abolished for the NO-pathway in cells that are lipid-depleted through cyclodextrin pre-treatment. These results indicate that at least during immature stages, PDE3 has a stronger control over cGMP levels than previously thought (Götz et al. 2014; Chung et al. 2015). The diminishing role over aging may result from a combination of rising cAMP levels competing for PDE3 binding sites and increased structural compartmentation. While the role between cAMP and cGMP in relation to PDE3 has been established (Pavlaki and Nikolaev 2018), there is a lack of a simultaneous measurement of their levels in response to PDE3 inhibition in aging HiPSC-CM. In addition to the compartmentation by barriers created by the maturing cardiomyocyte structure, PDE3

and its binding sites such as SERCA, PLB, and AKAP18 δ also become more prevalent (Grancharova et al. 2021; Zhang and Morad 2020; Guo and Pu 2020). Though no effects of PDE3i could be found on the contraction and calcium handling dynamics in this study with any of the tested pathways, further research with altered parameters, tools, and increased replicates could confirm this lack or inform otherwise. Notably, previous work has shown that PDE3 inhibitors in adult mice and rat cardiomyocytes have a strong positive effect on the cardiac contractility as well as the amplitude of calcium transients (Mika et al. 2013; Maurice et al. 2003).

Previous studies on PDE5 found primarily an effect of it after stimulation of the NO-pathway. To be precise, it was found that while PDE5 inhibition does not ordinarily affect basal contractility, it reduced basal contractility only after activation of all β_3 -ARs and stimulation of the NO-pathway to produce cGMP (Borlaug et al. 2005). In our studies we found that aging affects the role of PDE5 in a manner contrasting to its effect on PDE3, showing a high impact of inhibition in D30 CNP, low in D30 GSNO, but low in D90 CNP and high in D90 GSNO. This coincides with an increase in PDE5 gene expression in D90. This switch from the NO-pathway to the NP-pathway hasn't been documented previously, making it an attractive target for further investigation.

PDE9 inhibition in D90 has a decreased effect in the NO-pathway after caveolae removal as well as the NP-pathway. We find the opposite effect on the β_3 -pathway after caveolae removal, with an increased FRET response. These opposing effects are possibly caused by redistribution of the β_3 -receptors due to the cyclodextrin treatment. Interestingly, this differs from previous experiments where it was found that PDE9 has no regulatory control over the NO-pathway mediated cGMP production, instead regulating cGMP produced in the

NP-pathway. It is interesting to note that these experiments were performed on NRVMs, making it likely that this disparity with our own data is due to either a difference between model organisms or the difference in the level of cardiomyocyte maturity between NRVM and D90 HiPSC-CM (Lee et al. 2015).

7.2. Limitations and Future Work

We forewent any further purchase and testing of sensors due to a combination of funding, adequate results from ScGi, and the pressure to move on to obtain publishable data. It would be interesting however to compare the dynamics of recent single-fluorophore cGMP sensors (Harada et al. 2017) or the most recent PKG based sensors (Calamera et al. 2019) to ScGi.

If any future work is to be done on MultiFRET, similar algorithms used in CytoCypher software could be applied to allow PC-based measurement of contraction (Kamgoué et al. 2009).

Currently the lack of study on the cGMP pathway creates difficulty in the interpretation of the results. It would be ideal if future research could explore the effects of all PDE inhibitors on the three cGMP pathways, as well as examine these conditions in more mature models such as NRVM or cardiomyocytes from donated adult human hearts for comparison. Furthermore, study of the cGMP-cAMP cross-talk is made easier through MultiFRET's compatibility with any number of beam-splitter channels. While previous work studies the cross-talk through stimulation of one pathway and FRET measurement of another (Götz et al. 2014) or report FRET data that was obtained using two sensors with an unfortunate amount of bleed-through (Niino, Hotta, and Oka 2009), tools and methods have improved to a point where it should be possible to delve beyond these issues.

References

- Adams, Stephen R., Alec T. Harootunian, Ying Ji Buechler, Susan S. Taylor, and Roger Y. Tsien. 1991. "Fluorescence Ratio Imaging of Cyclic AMP in Single Cells." *Nature* 349 (6311): 694–97. <https://doi.org/10.1038/349694a0>.
- Agarkova, Irina, and Jean Claude Perriard. 2005. "The M-Band: An Elastic Web That Crosslinks Thick Filaments in the Center of the Sarcomere." *Trends in Cell Biology*. Elsevier. <https://doi.org/10.1016/j.tcb.2005.07.001>.
- Ahmad, Faiyaz, Weixing Shen, Fabrice Vandeput, Nicolas Szabo-Fresnais, Judith Krall, Eva Degerman, Frank Goetz, Enno Klussmann, Matthew Movsesian, and Vincent Manganiello. 2015. "Regulation of Sarcoplasmic Reticulum Ca²⁺ ATPase 2 (SERCA2) Activity by Phosphodiesterase 3A (PDE3A) in Human Myocardium: Phosphorylation-Dependent Interaction of PDE3A1 with SERCA2." *Journal of Biological Chemistry* 290 (11): 6763–76. <https://doi.org/10.1074/jbc.M115.638585>.
- Arnold, W. P., C. K. Mittal, S. Katsuki, and F. Murad. 1977. "Nitric Oxide Activates Guanylate Cyclase and Increases Guanosine 3':5'-Cyclic Monophosphate Levels in Various Tissue Preparations." *Proceedings of the National Academy of Sciences of the United States of America* 74 (8): 3203–7. <https://doi.org/10.1073/pnas.74.8.3203>.
- Ashman, D. F., R. Lipton, M. M. Melicow, and T. D. Price. 1963. "Isolation of Adenosine 3',5'-Monophosphate and Guanosine 3',5'-Monophosphate from Rat Urine." *Biochemical and Biophysical Research Communications* 11 (4): 330–34. [https://doi.org/10.1016/0006-291X\(63\)90566-7](https://doi.org/10.1016/0006-291X(63)90566-7).
- Baillie, George S., Arvind Sood, Ian McPhee, Irene Gall, Stephen J. Perry, Robert J. Lefkowitz, and Miles D. Houslay. 2003. "β-Arrestin-Mediated PDE4 CAMP Phosphodiesterase Recruitment Regulates β-Adrenoceptor Switching from G_s to G_i." *Proceedings of the National Academy of Sciences of the United States of America* 100 (3): 940–45. <https://doi.org/10.1073/pnas.262787199>.
- Balycheva, Marina, Giuseppe Faggian, Alexey V. Glukhov, and Julia Gorelik. 2015. "Microdomain-specific Localization of Functional Ion Channels in Cardiomyocytes: An Emerging Concept of Local Regulation and Remodelling." *Biophysical Reviews* 7 (1): 43–62. <https://doi.org/10.1007/s12551-014-0159-x>.
- Banerjee, Indroneal, Katrina Carrion, Ricardo Serrano, Jeffrey Dyo, Roman Sasik, Sean Lund, Erik Willems, et al. 2015. "Cyclic Stretch of Embryonic Cardiomyocytes Increases Proliferation, Growth, and Expression While Repressing Tgf-β Signaling." *Journal of Molecular and Cellular Cardiology* 79 (February): 133–44. <https://doi.org/10.1016/j.yjmcc.2014.11.003>.
- Baylor, D. A., T. D. Lamb, and K. W. Yau. 1979. "The Membrane Current of Single Rod Outer Segments." *The Journal of Physiology* 288 (1): 589–611. <https://doi.org/10.1113/jphysiol.1979.sp012715>.
- Beavo, Joseph A. 1995. "Cyclic Nucleotide Phosphodiesterases: Functional Implications of Multiple Isoforms." *Physiological Reviews*. Vol. 75. <https://doi.org/10.1152/physrev.1995.75.4.725>.
- Beca, Sanja, Faiyaz Ahmad, Weixing Shen, Jie Liu, Samy Makary, Nazari Polidovitch, Junhui Sun, et al. 2013. "Phosphodiesterase Type 3A Regulates Basal Myocardial Contractility through Interacting with Sarcoplasmic Reticulum Calcium ATPase Type 2a Signaling Complexes in Mouse Heart." *Circulation Research* 112 (2): 289–97. <https://doi.org/10.1161/CIRCRESAHA.111.300003>.
- Beca, Sanja, Peter B. Helli, Jeremy A. Simpson, Dongling Zhao, Gerrie P. Farman, Peter P. Jones, Xixi Tian, et al. 2011. "Phosphodiesterase 4D Regulates Baseline Sarcoplasmic Reticulum Ca²⁺ Release and Cardiac Contractility, Independently of L-Type Ca²⁺ Current." *Circulation Research*

109 (9): 1024–30. <https://doi.org/10.1161/CIRCRESAHA.111.250464>.

- Becker, Jason R., Sneha Chatterjee, Tamara Y. Robinson, Jeffrey S. Bennett, Daniela Panáková, Cristi L. Galindo, Lin Zhong, et al. 2014. “Differential Activation of Natriuretic Peptide Receptors Modulates Cardiomyocyte Proliferation during Development.” *Development (Cambridge)* 141 (2): 335–45. <https://doi.org/10.1242/dev.100370>.
- Belge, Catharina, Joanna Hammond, Emilie Dubois-Deruy, Boris Manoury, Julien Hamelet, Christophe Beauloye, Andreas Markl, et al. 2014. “Enhanced Expression of B3-Adrenoceptors in Cardiac Myocytes Attenuates Neurohormone-Induced Hypertrophic Remodeling through Nitric Oxide Synthase.” *Circulation* 129 (4): 451–62. <https://doi.org/10.1161/CIRCULATIONAHA.113.004940>.
- Bender, Andrew T., and Joseph A. Beavo. 2006. “Cyclic Nucleotide Phosphodiesterases: Molecular Regulation to Clinical Use.” *Pharmacological Reviews*. Pharmacol Rev. <https://doi.org/10.1124/pr.58.3.5>.
- Bergmann, Olaf, Sofia Zdunek, Anastasia Felker, Mehran Salehpour, Kanar Alkass, Samuel Bernard, Staffan L. Sjöström, et al. 2015. “Dynamics of Cell Generation and Turnover in the Human Heart.” *Cell* 161 (7): 1566–75. <https://doi.org/10.1016/j.cell.2015.05.026>.
- Beyer, Christian, Christoph Zenzmaier, Katrin Palumbo-Zerr, Rossella Mancuso, Alfiya Distler, Clara Dees, Pawel Zerr, et al. 2015. “Stimulation of the Soluble Guanylate Cyclase (SGC) Inhibits Fibrosis by Blocking Non-Canonical TGF β Signalling.” *Annals of the Rheumatic Diseases* 74 (7): 1408–16. <https://doi.org/10.1136/annrheumdis-2013-204508>.
- Bhana, Bashir, Rohin K. Iyer, Wen Li Kelly Chen, Ruogang Zhao, Krista L. Sider, Morakot Likhitpanichkul, Craig A. Simmons, and Milica Radisic. 2010. “Influence of Substrate Stiffness on the Phenotype of Heart Cells.” *Biotechnology and Bioengineering* 105 (6): 1148–60. <https://doi.org/10.1002/bit.22647>.
- Bhavsar, Pankaj K., Gurtej K. Dhoot, Debbie V.E. Cumming, Gillian S. Butler-Browne, Magdi H. Yacoub, and Paul J.R. Barton. 1991. “Developmental Expression of Troponin I Isoforms in Fetal Human Heart.” *FEBS Letters* 292 (1–2): 5–8. [https://doi.org/10.1016/0014-5793\(91\)80820-S](https://doi.org/10.1016/0014-5793(91)80820-S).
- Bian, Weining, Nima Badie, Herman D. Himmel, and Nenad Bursac. 2014. “Robust T-Tubulation and Maturation of Cardiomyocytes Using Tissue-Engineered Epicardial Mimetics.” *Biomaterials* 35 (12): 3819–28. <https://doi.org/10.1016/j.biomaterials.2014.01.045>.
- Bird, S. D., P. A. Doevendans, M. A. Van Rooijen, A. Brutel De La Riviere, R. J. Hassink, R. Passier, and C. L. Mummery. 2003a. “The Human Adult Cardiomyocyte Phenotype.” *Cardiovascular Research* 58 (2): 423–34. [https://doi.org/10.1016/S0008-6363\(03\)00253-0](https://doi.org/10.1016/S0008-6363(03)00253-0).
- . 2003b. “The Human Adult Cardiomyocyte Phenotype.” *Cardiovascular Research* 58 (2): 423–34. [https://doi.org/10.1016/S0008-6363\(03\)00253-0](https://doi.org/10.1016/S0008-6363(03)00253-0).
- Blazeski, Adriana, Renjun Zhu, David W. Hunter, Seth H. Weinberg, Elias T. Zambidis, and Leslie Tung. 2012. “Cardiomyocytes Derived from Human Induced Pluripotent Stem Cells as Models for Normal and Diseased Cardiac Electrophysiology and Contractility.” *Progress in Biophysics and Molecular Biology*. NIH Public Access. <https://doi.org/10.1016/j.pbiomolbio.2012.07.013>.
- Bloch, Wilhelm, Klaus Addicks, Jürgen Hescheler, and Bernd K. Fleischmann. 2001. “Nitric Oxide Synthase Expression and Function in Embryonic and Adult Cardiomyocytes.” *Microscopy Research and Technique* 55 (4): 259–69. <https://doi.org/10.1002/jemt.1175>.
- Bobin, Pierre, Milia Belacel-Ouari, Ibrahim Bedioun, Liang Zhang, Jérôme Leroy, Véronique Leblais, Rodolphe Fischmeister, and Grégoire Vandecasteele. 2016. “Cyclic Nucleotide

- Phosphodiesterases in Heart and Vessels: A Therapeutic Perspective." *Archives of Cardiovascular Diseases* 109 (6–7): 431–43. <https://doi.org/10.1016/j.acvd.2016.02.004>.
- Bode, D. C., J. R. Kanter, and L. L. Brunton. 1991. "Cellular Distribution of Phosphodiesterase Isoforms in Rat Cardiac Tissue." *Circulation Research* 68 (4): 1070–79. <https://doi.org/10.1161/01.RES.68.4.1070>.
- Bold, A. J. de, H. B. Borenstein, A. T. Veress, and H. Sonnenberg. 1981. "A Rapid and Potent Natriuretic Response to Intravenous Injection of Atrial Myocardial Extract in Rats." *Life Sciences* 28 (1): 89–94. [https://doi.org/10.1016/0024-3205\(81\)90370-2](https://doi.org/10.1016/0024-3205(81)90370-2).
- Bork, Nadja I., and Viacheslav O. Nikolaev. 2018. "cGMP Signaling in the Cardiovascular System—the Role of Compartmentation and Its Live Cell Imaging." *International Journal of Molecular Sciences*. Multidisciplinary Digital Publishing Institute (MDPI). <https://doi.org/10.3390/ijms19030801>.
- Borlaug, Barry A., Vojtech Melenovsky, Tricia Marhin, Patricia Fitzgerald, and David A. Kass. 2005. "Sildenafil Inhibits β -Adrenergic-Stimulated Cardiac Contractility in Humans." *Circulation* 112 (17): 2642–49. <https://doi.org/10.1161/CIRCULATIONAHA.105.540500>.
- Börner, Sebastian, Frank Schwede, Angela Schlipp, Filip Berisha, Davide Calebiro, Martin J. Lohse, and Viacheslav O. Nikolaev. 2011. "FRET Measurements of Intracellular cAMP Concentrations and cAMP Analog Permeability in Intact Cells." *Nature Protocols* 6 (4): 427–38. <https://doi.org/10.1038/nprot.2010.198>.
- Bougneres, P. F., I. E. Karl, L. S. Hillman, and D. M. Bier. 1982. "Lipid Transport in the Human Newborn. Palmitate and Glycerol Turnover and the Contribution of Glycerol to Neonatal Hepatic Glucose Output." *Journal of Clinical Investigation* 70 (2): 262–70. <https://doi.org/10.1172/JCI110613>.
- Bradski, Gary, and A. Kaehler. 2000. "OpenCV." *Dr. Dobb's Journal of Software Tools*.
- Bray, Mark Anthony, Sean P. Sheehy, and Kevin Kit Parker. 2008. "Sarcomere Alignment Is Regulated by Myocyte Shape." *Cell Motility and the Cytoskeleton* 65 (8): 641–51. <https://doi.org/10.1002/cm.20290>.
- Brescia, Marcella, Ying Chi Chao, Andreas Koschinski, Jakub Tomek, and Manuela Zaccolo. 2020. "Multi-Compartment, Early Disruption of cGmp and cAMP Signalling in Cardiac Myocytes from the Mdx Model of Duchenne Muscular Dystrophy." *International Journal of Molecular Sciences* 21 (19): 1–19. <https://doi.org/10.3390/ijms21197056>.
- Brusq, Jean Marie, Eric Mayoux, Laurent Guigui, and Jorge Kirilovsky. 1999. "Effects of C-Type Natriuretic Peptide on Rat Cardiac Contractility." *British Journal of Pharmacology* 128 (1): 206–12. <https://doi.org/10.1038/sj.bjp.0702766>.
- Bryant, Simon M., Cherrie H.T. Kong, Judy J. Watson, Hanne C. Gadeberg, David M. Roth, Hemal H. Patel, Mark B. Cannell, Andrew F. James, and Clive H. Orchard. 2018. "Caveolin-3 KO Disrupts t-Tubule Structure and Decreases t-Tubular I_{Ca} Density in Mouse Ventricular Myocytes." *American Journal of Physiology - Heart and Circulatory Physiology* 315 (5): H1101–11. <https://doi.org/10.1152/ajpheart.00209.2018>.
- Buxton, I. L.O., and L. L. Brunton. 1983. "Compartments of Cyclic AMP and Protein Kinase in Mammalian Cardiomyocytes." *Journal of Biological Chemistry* 258 (17): 10233–39. [https://doi.org/10.1016/s0021-9258\(17\)44447-4](https://doi.org/10.1016/s0021-9258(17)44447-4).
- Bylund, D. B., D. C. Eikenberg, J. P. Hieble, S. Z. Langer, R. J. Lefkowitz, K. P. Minneman, P. B. Molinoff, R. R. Ruffolo, and U. Trendelenburg. 1994. "IV. International Union of Pharmacology

Nomenclature of Adrenoceptors." *Pharmacological Reviews*.

- Cai, B., Z. Pan, and Y. Lu. 2010. "The Roles of MicroRNAs in Heart Diseases: A Novel Important Regulator." *Current Medicinal Chemistry* 17 (5): 407–11.
<https://doi.org/10.2174/092986710790226129>.
- Calamera, Gaia, Dan Li, Andrea Hembre Ulsund, Jeong Joo Kim, Oliver C. Neely, Lise Román Moltzau, Marianne Bjørnerem, et al. 2019. "FRET-Based Cyclic GMP Biosensors Measure Low CGMP Concentrations in Cardiomyocytes and Neurons." *Communications Biology* 2 (1): 1–12.
<https://doi.org/10.1038/s42003-019-0641-x>.
- Callis, Thomas E., Kumar Pandya, Young Seok Hee, Ru Hang Tang, Mariko Tatsuguchi, Zhan Peng Huang, Jian Fu Chen, et al. 2009. "MicroRNA-208a Is a Regulator of Cardiac Hypertrophy and Conduction in Mice." *Journal of Clinical Investigation* 119 (9): 2772–86.
<https://doi.org/10.1172/JCI36154>.
- Campbell, Scott E., A. Martin Gerdes, and Teri D. Smith. 1987. "Comparison of Regional Differences in Cardiac Myocyte Dimensions in Rats, Hamsters, and Guinea Pigs." *The Anatomical Record* 219 (1): 53–59. <https://doi.org/10.1002/ar.1092190110>.
- Cao, L., E. Manders, and M. Helmes. 2021. "Automatic Detection of Adult Cardiomyocyte for High Throughput Measurements of Calcium and Contractility." *PLoS ONE* 16 (9 September): e0256713. <https://doi.org/10.1371/journal.pone.0256713>.
- Carnicer, Ricardo, Mark J. Crabtree, Vidhya Sivakumaran, Barbara Casadei, and David A. Kass. 2013. "Nitric Oxide Synthases in Heart Failure." *Antioxidants and Redox Signaling*. Antioxid Redox Signal. <https://doi.org/10.1089/ars.2012.4824>.
- Carson, Daniel, Marketa Hnilova, Xiulan Yang, Cameron L. Nemeth, Jonathan H. Tsui, Alec S.T. Smith, Alex Jiao, et al. 2016. "Nanotopography-Induced Structural Anisotropy and Sarcomere Development in Human Cardiomyocytes Derived from Induced Pluripotent Stem Cells." *ACS Applied Materials and Interfaces*. ACS Appl Mater Interfaces. <https://doi.org/10.1021/acsami.5b11671>.
- Castro, Liliana R.V., Julia Schittl, and Rodolphe Fischmeister. 2010. "Feedback Control through CGMP-Dependent Protein Kinase Contributes to Differential Regulation and Compartmentation of CGMP in Rat Cardiac Myocytes." *Circulation Research* 107 (10): 1232–40.
<https://doi.org/10.1161/CIRCRESAHA.110.226712>.
- Castro, Liliana R.V., Ignacio Verde, Dermot M.F. Cooper, and Rodolphe Fischmeister. 2006a. "Cyclic Guanosine Monophosphate Compartmentation in Rat Cardiac Myocytes." *Circulation* 113 (18): 2221–28. <https://doi.org/10.1161/CIRCULATIONAHA.105.599241>.
- . 2006b. "Cyclic Guanosine Monophosphate Compartmentation in Rat Cardiac Myocytes." *Circulation* 113 (18): 2221–28. <https://doi.org/10.1161/CIRCULATIONAHA.105.599241>.
- Chan, Joyce C.Y., Ole Knudson, Faye Wu, John Morser, William P. Dole, and Qingyu Wu. 2005. "Hypertension in Mice Lacking the Proatrial Natriuretic Peptide Convertase Corin." *Proceedings of the National Academy of Sciences of the United States of America* 102 (3): 785–90.
<https://doi.org/10.1073/pnas.0407234102>.
- Chattergoon, Natasha N., George D. Giraud, Samantha Louey, Philip Stork, Abigail L. Fowden, and Kent L. Thornburg. 2012. "Thyroid Hormone Drives Fetal Cardiomyocyte Maturation." *The FASEB Journal* 26 (1): 397–408. <https://doi.org/10.1096/fj.10-179895>.
- Chen, Fabian, Hyun Kook, Rita Milewski, Aaron D. Gitler, Min Min Lu, Jun Li, Ronniel Nazarian, et al. 2002. "Hop Is an Unusual Homeobox Gene That Modulates Cardiac Development." *Cell* 110 (6):

713–23. [https://doi.org/10.1016/S0092-8674\(02\)00932-7](https://doi.org/10.1016/S0092-8674(02)00932-7).

- Chinkers, Michael, David L. Garbers, Ming Shi Chang, David G. Lowe, Hemin Chin, David V. Goeddel, and Stephanie Schulz. 1989. "A Membrane Form of Guanylate Cyclase Is an Atrial Natriuretic Peptide Receptor." *Nature* 338 (6210): 78–83. <https://doi.org/10.1038/338078a0>.
- Cho, Gun Sik, Dong I. Lee, Emmanouil Tampakakis, Sean Murphy, Peter Andersen, Hideki Uosaki, Stephen Chelko, et al. 2017. "Neonatal Transplantation Confers Maturation of PSC-Derived Cardiomyocytes Conducive to Modeling Cardiomyopathy." *Cell Reports* 18 (2): 571–82. <https://doi.org/10.1016/j.celrep.2016.12.040>.
- Chung, Youn Wook, Claudia Lagranha, Yong Chen, Junhui Sun, Guang Tong, Steven C. Hockman, Faiyaz Ahmad, et al. 2015. "Targeted Disruption of PDE3B, but Not PDE3A, Protects Murine Heart from Ischemia/Reperfusion Injury." *Proceedings of the National Academy of Sciences of the United States of America* 112 (17): E2253–62. <https://doi.org/10.1073/pnas.1416230112>.
- Conti, Marco. 2000. "Phosphodiesterases and Cyclic Nucleotide Signaling in Endocrine Cells." *Molecular Endocrinology* 14 (9): 1317–27. <https://doi.org/10.1210/mend.14.9.0534>.
- Crompton, M., H. Ellinger, and A. Costi. 1988. "Inhibition by Cyclosporin A of a Ca²⁺-Dependent Pore in Heart Mitochondria Activated by Inorganic Phosphate and Oxidative Stress." *Biochemical Journal* 255 (1): 357–60. [/pmc/articles/PMC1135230/?report=abstract](https://pubmed.ncbi.nlm.nih.gov/articles/PMC1135230/?report=abstract).
- Curtis, Michael J., Steve Alexander, Giuseppe Cirino, James R. Docherty, Christopher H. George, Mark A. Giembycz, Daniel Hoyer, et al. 2018. "Experimental Design and Analysis and Their Reporting II: Updated and Simplified Guidance for Authors and Peer Reviewers." *British Journal of Pharmacology* 175 (7): 987–93. <https://doi.org/10.1111/bph.14153>.
- Dai, Dao Fu, Maria Elena Danoviz, Brian Wiczer, Michael A. Laflamme, and Rong Tian. 2017. "Mitochondrial Maturation in Human Pluripotent Stem Cell Derived Cardiomyocytes." *Stem Cells International* 2017. <https://doi.org/10.1155/2017/5153625>.
- Das, Anindita, Albert Smolenski, Suzanne M. Lohmann, and Rakesh C. Kukreja. 2006. "Cyclic GMP-Dependent Protein Kinase I α Attenuates Necrosis and Apoptosis Following Ischemia/Reoxygenation in Adult Cardiomyocyte." *Journal of Biological Chemistry* 281 (50): 38644–52. <https://doi.org/10.1074/jbc.M606142200>.
- Davidson, Neil C., Craig S. Barr, and Allan D. Struthers. 1996. "C-Type Natriuretic Peptide: An Endogenous Inhibitor of Vascular Angiotensin-Converting Enzyme Activity." *Circulation* 93 (6): 1155–59. <https://doi.org/10.1161/01.CIR.93.6.1155>.
- Delicce, Anthony V., and Amgad N. Makaryus. 2018. *Physiology, Frank Starling Law*. StatPearls. StatPearls Publishing. <http://www.ncbi.nlm.nih.gov/pubmed/29262149>.
- Deng, Xing Fei, D. Gregg Rokosh, and Paul C. Simpson. 2000. "Autonomous and Growth Factor - Induced Hypertrophy in Cultured Neonatal Mouse Cardiac Myocytes: Comparison with Rat." *Circulation Research* 87 (9): 781–88. <https://doi.org/10.1161/01.RES.87.9.781>.
- Dessy, Chantal, and Jean Luc Balligand. 2010. "Beta3-Adrenergic Receptors in Cardiac and Vascular Tissues. Emerging Concepts and Therapeutic Perspectives." In *Advances in Pharmacology*, 59:135–63. *Adv Pharmacol*. [https://doi.org/10.1016/S1054-3589\(10\)59005-7](https://doi.org/10.1016/S1054-3589(10)59005-7).
- Dhein, Stefan, Anna Schreiber, Sabine Steinbach, Daniel Apel, Aida Salameh, Franziska Schlegel, Martin Kostelka, Pascal M. Dohmen, and Friedrich Wilhelm Mohr. 2014. "Mechanical Control of Cell Biology. Effects of Cyclic Mechanical Stretch on Cardiomyocyte Cellular Organization." *Progress in Biophysics and Molecular Biology* 115 (2–3): 93–102. <https://doi.org/10.1016/j.pbiomolbio.2014.06.006>.

- Ding, Bo, Jun Ichi Abe, Heng Wei, Qunhua Huang, Richard A. Walsh, Carlos A. Molina, Allan Zhao, et al. 2005. "Functional Role of Phosphodiesterase 3 in Cardiomyocyte Apoptosis: Implication in Heart Failure." *Circulation* 111 (19): 2469–76. <https://doi.org/10.1161/01.CIR.0000165128.39715.87>.
- Doetschman, T. C., H. Eistetter, and M. Katz. 1985. "The in Vitro Development of Blastocyst-Derived Embryonic Stem Cell Lines: Formation of Visceral Yolk Sac, Blood Islands and Myocardium." *Journal of Embryology and Experimental Morphology*. Vol. VOL. 87. <https://doi.org/10.1242/dev.87.1.27>.
- Dolnikov, Katya, Mark Shilkrot, Naama Zeevi-Levin, Sharon Gerech-Nir, Michal Amit, Asaf Danon, Joseph Itskovitz-Eldor, and Ofer Binah. 2006. "Functional Properties of Human Embryonic Stem Cell-Derived Cardiomyocytes: Intracellular Ca²⁺ Handling and the Role of Sarcoplasmic Reticulum in the Contraction." *Stem Cells* 24 (2): 236–45. <https://doi.org/10.1634/stemcells.2005-0036>.
- Drouin, Emmanuel, Flavien Charpentier, Chantal Gauthier, Karine Laurent, and Herve Le Marec. 1995. "Electrophysiologic Characteristics of Cells Spanning the Left Ventricular Wall of Human Heart: Evidence for Presence of M Cells." *Journal of the American College of Cardiology* 26 (1): 185–92. [https://doi.org/10.1016/0735-1097\(95\)00167-X](https://doi.org/10.1016/0735-1097(95)00167-X).
- Dufour, Alexandre. 2021. "Active Contours." *Computer Vision*, 15–15. https://doi.org/10.1007/978-3-030-63416-2_300267.
- Evans, Bronwyn A., Masaaki Sato, Mohsin Sarwar, Dana S. Hutchinson, and Roger J. Summers. 2010. "Ligand-Directed Signalling at β -Adrenoceptors." *British Journal of Pharmacology*. Br J Pharmacol. <https://doi.org/10.1111/j.1476-5381.2009.00602.x>.
- Fazio, Serafino, Emiliano A. Palmieri, Gaetano Lombardi, and Bernadette Biondi. 2004. "Effects of Thyroid Hormone on the Cardiovascular System." *Recent Progress in Hormone Research*. Recent Prog Horm Res. <https://doi.org/10.1210/rp.59.1.31>.
- Feil, Robert, Moritz Lehnert, Daniel Stehle, and Susanne Feil. 2021. "Visualising and Understanding CGMP Signals in the Cardiovascular System." *British Journal of Pharmacology*. John Wiley and Sons Inc. <https://doi.org/10.1111/bph.15500>.
- Feinberg, Adam W., Patrick W. Alford, Hongwei Jin, Crystal M. Ripplinger, Andreas A. Werdich, Sean P. Sheehy, Anna Grosberg, and Kevin Kit Parker. 2012. "Controlling the Contractile Strength of Engineered Cardiac Muscle by Hierarchical Tissue Architecture." *Biomaterials* 33 (23): 5732–41. <https://doi.org/10.1016/j.biomaterials.2012.04.043>.
- Feinberg, Adam W., Alex Feigel, Sergey S. Shevkopyas, Sean Sheehy, George M. Whitesides, and Kevin Kit Parker. 2007. "Muscular Thin Films for Building Actuators and Powering Devices." *Science* 317 (5843): 1366–70. <https://doi.org/10.1126/science.1146885>.
- Fischmeister, Rodolphe, Liliana R.V. Castro, Aniella Abi-Gerges, Francesca Rochais, Jonas Jurevičius, Jérôme Leroy, and Grégoire Vandecasteele. 2006. "Compartmentation of Cyclic Nucleotide Signaling in the Heart: The Role of Cyclic Nucleotide Phosphodiesterases." *Circulation Research*. Lippincott Williams and Wilkins. <https://doi.org/10.1161/01.RES.0000246118.98832.04>.
- Flynn, T. Geoffrey, Mercedes L. de Bold, and Adolfo J. de Bold. 1983. "The Amino Acid Sequence of an Atrial Peptide with Potent Diuretic and Natriuretic Properties." *Biochemical and Biophysical Research Communications* 117 (3): 859–65. [https://doi.org/10.1016/0006-291X\(83\)91675-3](https://doi.org/10.1016/0006-291X(83)91675-3).
- Földes, Gábor, Maxime Mioulane, Jamie S. Wright, Alexander Q. Liu, Pavel Novak, Béla Merkely, Julia Gorelik, Michael D. Schneider, Nadire N. Ali, and Sian E. Harding. 2011. "Modulation of Human

- Embryonic Stem Cell-Derived Cardiomyocyte Growth: A Testbed for Studying Human Cardiac Hypertrophy?" *Journal of Molecular and Cellular Cardiology* 50 (2): 367–76. <https://doi.org/10.1016/j.yjmcc.2010.10.029>.
- Friebe, Andreas, and Doris Koesling. 2003. "Regulation of Nitric Oxide-Sensitive Guanylyl Cyclase." *Circulation Research*. Lippincott Williams & Wilkins. <https://doi.org/10.1161/01.RES.0000082524.34487.31>.
- Friedman, Clayton E., Quan Nguyen, Samuel W. Lukowski, Abigail Helfer, Han Sheng Chiu, Jason Miklas, Shiri Levy, et al. 2018. "Single-Cell Transcriptomic Analysis of Cardiac Differentiation from Human PSCs Reveals HOPX-Dependent Cardiomyocyte Maturation." *Cell Stem Cell* 23 (4): 586–598.e8. <https://doi.org/10.1016/j.stem.2018.09.009>.
- Fu, Ji Dong, Stephanie N. Rushing, Deborah K. Lieu, Camie W. Chan, Chi Wing Kong, Lin Geng, Kitchener D. Wilson, et al. 2011. "Distinct Roles of MicroRNA-1 and -499 in Ventricular Specification and Functional Maturation of Human Embryonic Stem Cell-Derived Cardiomyocytes." *PLoS ONE* 6 (11). <https://doi.org/10.1371/journal.pone.0027417>.
- Fujiwara, Masataka, Peishi Yan, Tomomi G. Otsuji, Genta Narazaki, Hideki Uosaki, Hiroyuki Fukushima, Koichiro Kuwahara, et al. 2011. "Induction and Enhancement of Cardiac Cell Differentiation from Mouse and Human Induced Pluripotent Stem Cells with Cyclosporin-A." *PLoS ONE* 6 (2). <https://doi.org/10.1371/journal.pone.0016734>.
- Fukuda, Ryuichi, Felix Gunawan, Radhan Ramadass, Arica Beisaw, Anne Konzer, Sri Teja Mullapudi, Alessandra Gentile, Hans Martin Maischein, Johannes Graumann, and Didier Y.R. Stainier. 2019. "Mechanical Forces Regulate Cardiomyocyte Myofilament Maturation via the VCL-SSH1-CFL Axis." *Developmental Cell* 51 (1): 62–77.e5. <https://doi.org/10.1016/j.devcel.2019.08.006>.
- G. Lumsden, Natalie, Rayomand S. Khambata, and Adrian J. Hobbs. 2011. "C-Type Natriuretic Peptide (CNP): Cardiovascular Roles and Potential as a Therapeutic Target." *Current Pharmaceutical Design* 16 (37): 4080–88. <https://doi.org/10.2174/138161210794519237>.
- Gautel, Mathias, and Kristina Djinović-Carugo. 2016. "The Sarcomeric Cytoskeleton: From Molecules to Motion." *Journal of Experimental Biology*. Company of Biologists Ltd. <https://doi.org/10.1242/jeb.124941>.
- Gauthier, Chantal, Dominique Langin, and Jean Luc Balligand. 2000. "B3-Adrenoceptors in the Cardiovascular System." *Trends in Pharmacological Sciences*. Trends Pharmacol Sci. [https://doi.org/10.1016/S0165-6147\(00\)01562-5](https://doi.org/10.1016/S0165-6147(00)01562-5).
- Gauthier, Chantal, Véronique Leblais, Lester Kobzik, Jean Noël Trochu, Nassirah Khandoudi, Antoine Bril, Jean Luc Balligand, and Hervé Le Marec. 1998. "The Negative Inotropic Effect of B3-Adrenoceptor Stimulation Is Mediated by Activation of a Nitric Oxide Synthase Pathway in Human Ventricle." *Journal of Clinical Investigation* 102 (7): 1377–84. <https://doi.org/10.1172/JCI2191>.
- Geoffroy, Valérie, Françoise Fouque, Valérie Nivet, Jean Pierre Clot, Claire Lugnier, Bernard Desbuquois, and Chantal Benelli. 1999. "Activation of a CGMP-Stimulated CAMP Phosphodiesterase by Protein Kinase C in a Liver Golgi-Endosomal Fraction." *European Journal of Biochemistry* 259 (3): 892–900. <https://doi.org/10.1046/j.1432-1327.1999.00123.x>.
- Gerdes, A. Martin, Scott E. Kellerman, Jo Ann Moore, Karl E. Muffly, Linda C. Clark, Phyllis Y. Reaves, Krystyna B. Malec, Peter P. McKeown, and Douglas D. Schocken. 1992. "Structural Remodeling of Cardiac Myocytes in Patients with Ischemic Cardiomyopathy." *Circulation* 86 (2): 426–30. <https://doi.org/10.1161/01.CIR.86.2.426>.

- Germanguz, Igal, Oshra Sedan, Naama Zeevi-Levin, Ronit Shtrichman, Efrat Barak, Anna Ziskind, Sivan Eliyahu, et al. 2011. "Molecular Characterization and Functional Properties of Cardiomyocytes Derived from Human Inducible Pluripotent Stem Cells." *Journal of Cellular and Molecular Medicine* 15 (1): 38–51. <https://doi.org/10.1111/j.1582-4934.2009.00996.x>.
- Gerzer, Rupert, Eycke Böhme, Franz Hofmann, and Günter Schultz. 1981. "Soluble Guanylate Cyclase Purified from Bovine Lung Contains Heme and Copper." *FEBS Letters* 132 (1): 71–74. [https://doi.org/10.1016/0014-5793\(81\)80429-2](https://doi.org/10.1016/0014-5793(81)80429-2).
- Gherghiceanu, Mihaela, Lili Barad, Atara Novak, Irina Reiter, Joseph Itskovitz-Eldor, Ofer Binah, and L. M. Popescu. 2011. "Cardiomyocytes Derived from Human Embryonic and Induced Pluripotent Stem Cells: Comparative Ultrastructure." *Journal of Cellular and Molecular Medicine* 15 (11): 2539–51. <https://doi.org/10.1111/j.1582-4934.2011.01417.x>.
- Ghigo, Alessandra, and Delphine Mika. 2019. "CAMP/PKA Signaling Compartmentalization in Cardiomyocytes: Lessons from FRET-Based Biosensors." *Journal of Molecular and Cellular Cardiology*. Academic Press. <https://doi.org/10.1016/j.yjmcc.2019.04.020>.
- Giacomelli, Elisa, Viviana Meraviglia, Giulia Campostrini, Amy Cochrane, Xu Cao, Ruben W.J. van Helden, Ana Krotenberg Garcia, et al. 2020. "Human-IPSC-Derived Cardiac Stromal Cells Enhance Maturation in 3D Cardiac Microtissues and Reveal Non-Cardiomyocyte Contributions to Heart Disease." *Cell Stem Cell* 26 (6): 862–879.e11. <https://doi.org/10.1016/j.stem.2020.05.004>.
- Giacomelli, Elisa, Viviana Meraviglia, Giulia Campostrini, Ana Krotenberg Garcia, Ruben W J Van Helden, Martin Giera, Carolina R Jost, et al. 2019. "Cardiac-but Not Dermal Fibroblasts Induce Structural and Functional Maturation of hiPSC-Derived Cardiomyocytes in 3D Microtissues."
- Gilotra, Nisha A., Adam D. Devore, Thomas J. Povsic, Allison G. Hays, Virginia S. Hahn, Tolu A. Agunbiade, Allison Delong, et al. 2021. "Acute Hemodynamic Effects and Tolerability of Phosphodiesterase-1 Inhibition with ITI-214 in Human Systolic Heart Failure." *Circulation: Heart Failure*, 941–50. <https://doi.org/10.1161/CIRCHEARTFAILURE.120.008236>.
- Götz, Konrad R., and Viacheslav O. Nikolaev. 2013. "Advances and Techniques to Measure CGMP in Intact Cardiomyocytes." In *Methods in Molecular Biology*, 1020:121–29. Humana Press, Totowa, NJ. https://doi.org/10.1007/978-1-62703-459-3_7.
- Götz, Konrad R., Julia U. Sprenger, Ruwan K. Perera, Julia H. Steinbrecher, Stephan E. Lehnart, Michaela Kuhn, Julia Gorelik, Jean Luc Balligand, and Viacheslav O. Nikolaev. 2014. "Transgenic Mice for Real-Time Visualization of CGMP in Intact Adult Cardiomyocytes." *Circulation Research* 114 (8): 1235–45. <https://doi.org/10.1161/CIRCRESAHA.114.302437>.
- Grancharova, Tanya, Kaytlyn A. Gerbin, Alexander B. Rosenberg, Charles M. Roco, Joy E. Arakaki, Colette M. DeLizo, Stephanie Q. Dinh, et al. 2021. "A Comprehensive Analysis of Gene Expression Changes in a High Replicate and Open-Source Dataset of Differentiating hiPSC-Derived Cardiomyocytes." *Scientific Reports* 11 (1): 1–21. <https://doi.org/10.1038/s41598-021-94732-1>.
- Guazzi, Marco, Marco Vicenzi, and Ross Arena. 2012. "Phosphodiesterase 5 Inhibition with Sildenafil Reverses Exercise Oscillatory Breathing in Chronic Heart Failure: A Long-Term Cardiopulmonary Exercise Testing Placebo-Controlled Study." *European Journal of Heart Failure* 14 (1): 82–90. <https://doi.org/10.1093/eurjhf/hfr147>.
- Guazzi, Marco, Marco Vicenzi, Ross Arena, and Maurizio D. Guazzi. 2011. "PDE5 Inhibition with Sildenafil Improves Left Ventricular Diastolic Function, Cardiac Geometry, and Clinical Status in Patients with Stable Systolic Heart Failure: Result of a 1-Year, Prospective, Randomized,

- Placebo-Controlled Study." *Circulation: Heart Failure* 4 (1): 8–17.
<https://doi.org/10.1161/CIRCHEARTFAILURE.110.944694>.
- Guo, Yuxuan, Yangpo Cao, Blake D. Jardin, Isha Sethi, Qing Ma, Behzad Moghadaszadeh, Emily C. Troiano, et al. 2021. "Sarcomeres Regulate Murine Cardiomyocyte Maturation through MRTF-SRF Signaling." *Proceedings of the National Academy of Sciences of the United States of America* 118 (2). <https://doi.org/10.1073/pnas.2008861118>.
- Guo, Yuxuan, Blake D. Jardin, Pingzhu Zhou, Isha Sethi, Brynn N. Akerberg, Christopher N. Toepfer, Yulan Ai, et al. 2018. "Hierarchical and Stage-Specific Regulation of Murine Cardiomyocyte Maturation by Serum Response Factor." *Nature Communications* 9 (1).
<https://doi.org/10.1038/s41467-018-06347-2>.
- Guo, Yuxuan, and William T. Pu. 2020. "Cardiomyocyte Maturation: New Phase in Development." *Circulation Research* 126 (8): 1086–1106. <https://doi.org/10.1161/CIRCRESAHA.119.315862>.
- Guustein, David E., Gregory E. Morley, Houman Tamaddon, Dhananjay Vaidya, Michael D. Schneider, Ju Chen, Kenneth R. Chien, Heidi Stuhlmann, and Glenn I. Fishman. 2001. "Conduction Slowing and Sudden Arrhythmic Death in Mice with Cardiac-Restricted Inactivation of Connexin43." *Circulation Research* 88 (3): 333–39. <https://doi.org/10.1161/01.RES.88.3.333>.
- Haase, Alexandra, Ruth Olmer, Kristin Schwanke, Stephanie Wunderlich, Sylvia Merkert, Christian Hess, Robert Zweigerdt, et al. 2009. "Generation of Induced Pluripotent Stem Cells from Human Cord Blood." *Cell Stem Cell* 5 (4): 434–41. <https://doi.org/10.1016/j.stem.2009.08.021>.
- Halbach, Marcel, Kurt Pfannkuche, Frank Pillekamp, Agnieszka Ziomka, Tobias Hannes, Michael Reppel, Juergen Hescheler, and Jochen Müller-Ehmsen. 2007. "Electrophysiological Maturation and Integration of Murine Fetal Cardiomyocytes after Transplantation." *Circulation Research* 101 (5): 484–92. <https://doi.org/10.1161/CIRCRESAHA.107.153643>.
- Hammond, J., and J.-L. Balligand. 2017. "Signalling Microdomains: The Beta-3 Adrenergic Receptor/NOS Signalosome." In , 215–44. Springer, Cham. https://doi.org/10.1007/978-3-319-54579-0_11.
- Hammond, Joanna, and Jean Luc Balligand. 2012. "Nitric Oxide Synthase and Cyclic GMP Signaling in Cardiac Myocytes: From Contractility to Remodeling." *Journal of Molecular and Cellular Cardiology*. Academic Press. <https://doi.org/10.1016/j.yjmcc.2011.07.029>.
- Han, Jingjia, Qingling Wu, Younan Xia, Mary B. Wagner, and Chunhui Xu. 2016. "Cell Alignment Induced by Anisotropic Electrospun Fibrous Scaffolds Alone Has Limited Effect on Cardiomyocyte Maturation." *Stem Cell Research* 16 (3): 740–50.
<https://doi.org/10.1016/j.scr.2016.04.014>.
- Harada, Kazuki, Motoki Ito, Xiaowen Wang, Mika Tanaka, Devina Wongso, Ayumu Konno, Hirokazu Hirai, Hajime Hirase, Takashi Tsuboi, and Tetsuya Kitaguchi. 2017. "Red Fluorescent Protein-Based CAMP Indicator Applicable to Optogenetics and in Vivo Imaging." *Scientific Reports* 7 (1).
<https://doi.org/10.1038/s41598-017-07820-6>.
- Hasan, Alveera. 2020. "Investigation of Bar-Dependent Camp Signalling in Induced Pluripotent Stem Cell-Derived Cardiomyocytes."
- Hasan, Alveera, Neda Mohammadi, Aisha Nawaz, Thusharika Kodagoda, Ivan Diakonov, Sian E. Harding, and Julia Gorelik. 2020. "Age-Dependent Maturation of iPSC-CMs Leads to the Enhanced Compartmentation of B2AR-CAMP Signalling." *Cells* 9 (10): 2275.
<https://doi.org/10.3390/cells9102275>.
- Hashmi, Satwat, and H. R. Ahmad. 2019. "Molecular Switch Model for Cardiomyocyte Proliferation."

Cell Regeneration 8 (1): 12–20. <https://doi.org/10.1016/j.cr.2018.11.002>.

- Haufe, Volker, Juan A. Camacho, Robert Dumaine, Bernd Günther, Christian Bollensdorff, Gisela Segond von Banchet, Klaus Benndorf, and Thomas Zimmer. 2005. "Expression Pattern of Neuronal and Skeletal Muscle Voltage-Gated Na⁺ Channels in the Developing Mouse Heart." *Journal of Physiology* 564 (3): 683–96. <https://doi.org/10.1113/jphysiol.2004.079681>.
- Hazeltine, Laurie B., Chelsey S. Simmons, Max R. Salick, Xiaojun Lian, Mehmet G. Badur, Wenqing Han, Stephanie M. Delgado, et al. 2012. "Effects of Substrate Mechanics on Contractility of Cardiomyocytes Generated from Human Pluripotent Stem Cells." *International Journal of Cell Biology*. <https://doi.org/10.1155/2012/508294>.
- Heidi Au, Hoi Ting, Bo Cui, Zane E. Chu, Teodor Veres, and Milica Radisic. 2009. "Cell Culture Chips for Simultaneous Application of Topographical and Electrical Cues Enhance Phenotype of Cardiomyocytes." *Lab on a Chip* 9 (4): 564–75. <https://doi.org/10.1039/b810034a>.
- Henderson, Christine A., Christopher G. Gomez, Stefanie M. Novak, Lei Mi-Mi, and Carol C. Gregorio. 2017. "Overview of the Muscle Cytoskeleton." In *Comprehensive Physiology*, 7:891–944. Hoboken, NJ, USA: John Wiley & Sons, Inc. <https://doi.org/10.1002/cphy.c160033>.
- Hendriks, William T., Xin Jiang, Laurence Daheron, and Chad A. Cowan. 2015. "TALEN- and CRISPR/Cas9-Mediated Gene Editing in Human Pluripotent Stem Cells Using Lipid-Based Transfection." *Current Protocols in Stem Cell Biology* 2015: 5B.3.1-5B.3.25. <https://doi.org/10.1002/9780470151808.sc05b03s34>.
- Hoendermis, Elke S., Licette C.Y. Liu, Yoran M. Hummel, Peter Van Der Meer, Rudolf A. De Boer, Rolf M.F. Berger, Dirk J. Van Veldhuisen, and Adriaan A. Voors. 2015. "Effects of Sildenafil on Invasive Haemodynamics and Exercise Capacity in Heart Failure Patients with Preserved Ejection Fraction and Pulmonary Hypertension: A Randomized Controlled Trial." *European Heart Journal* 36 (38): 2565–73. <https://doi.org/10.1093/eurheartj/ehv336>.
- Hoit, Brian D., Saeb F. Khoury, Yanfu Shao, Marjorie Gabel, Stephen B. Liggett, and Richard A. Walsh. 1997. "Effects of Thyroid Hormone on Cardiac β -Adrenergic Responsiveness in Conscious Baboons." *Circulation* 96 (2): 592–98. <https://doi.org/10.1161/01.CIR.96.2.592>.
- Hom, Jennifer R., Rodrigo A. Quintanilla, David L. Hoffman, Karen L. de Mesy Bentley, Jeffery D. Molkentin, Shey Shing Sheu, and George A. Porter. 2011. "The Permeability Transition Pore Controls Cardiac Mitochondrial Maturation and Myocyte Differentiation." *Developmental Cell* 21 (3): 469–78. <https://doi.org/10.1016/j.devcel.2011.08.008>.
- Honda, Akira, Stephen R. Adams, Carolyn L. Sawyer, Varda Lev-Ram, Roger Y. Tsien, and Wolfgang R.G. Dostmann. 2001. "Spatiotemporal Dynamics of Guanosine 3',5'-Cyclic Monophosphate Revealed by a Genetically Encoded, Fluorescent Indicator." *Proceedings of the National Academy of Sciences of the United States of America* 98 (5): 2437–42. <https://doi.org/10.1073/pnas.051631298>.
- Hu, Dongjian, Annet Linders, Abir Yamak, Cláudia Correia, Jan David Kijlstra, Arman Garakani, Ling Xiao, et al. 2018. "Metabolic Maturation of Human Pluripotent Stem Cell-derived Cardiomyocytes by Inhibition of HIF1 α and LDHA." *Circulation Research* 123 (9): 1066–79. <https://doi.org/10.1161/CIRCRESAHA.118.313249>.
- Huang, Chen Yu, Rebeca Peres Moreno Maia-Joca, Chin Siang Ong, Ijala Wilson, Deborah DiSilvestre, Gordon F. Tomaselli, and Daniel H. Reich. 2020. "Enhancement of Human iPSC-Derived Cardiomyocyte Maturation by Chemical Conditioning in a 3D Environment." *Journal of Molecular and Cellular Cardiology* 138 (January): 1–11. <https://doi.org/10.1016/j.yjmcc.2019.10.001>.

- Huang, Jianhe, Min Min Lu, Lan Cheng, Li Jun Yuan, Xiaoqing Zhu, Andrea L. Stout, Mary Chen, Jian Li, and Michael S. Parmacek. 2009. "Myocardin Is Required for Cardiomyocyte Survival and Maintenance of Heart Function." *Proceedings of the National Academy of Sciences of the United States of America* 106 (44): 18734–39. <https://doi.org/10.1073/pnas.0910749106>.
- Huethorst, E., M. Hortigon, V. Zamora-Rodriguez, P. M. Reynolds, F. Burton, G. Smith, and N. Gadegaard. 2016. "Enhanced Human-Induced Pluripotent Stem Cell Derived Cardiomyocyte Maturation Using a Dual Microgradient Substrate." *ACS Biomaterials Science and Engineering* 2 (12): 2231–39. <https://doi.org/10.1021/acsbiomaterials.6b00426>.
- Ibrahim, Michael, Julia Gorelik, Magdi H. Yacoub, and Cesare M. Terracciano. 2011. "The Structure and Function of Cardiac T-Tubules in Health and Disease." *Proceedings of the Royal Society B: Biological Sciences* 278 (1719): 2714–23. <https://doi.org/10.1098/rspb.2011.0624>.
- Isidori, Andrea M., Marisa Cornacchione, Federica Barbagallo, Antonio Di Grazia, Florencia Barrios, Lorenzo Fassina, Lucia Monaco, et al. 2015. "Inhibition of Type 5 Phosphodiesterase Counteracts B2-Adrenergic Signalling in Beating Cardiomyocytes." *Cardiovascular Research* 106 (3): 408–20. <https://doi.org/10.1093/cvr/cvv123>.
- Itzhaki, Ilanit, Sophia Rapoport, Irit Huber, Itzhak Mizrahi, Limor Zwi-Dantsis, Gil Arbel, Jackie Schiller, and Lior Gepstein. 2011. "Calcium Handling in Human Induced Pluripotent Stem Cell Derived Cardiomyocytes." *PLoS ONE* 6 (4). <https://doi.org/10.1371/journal.pone.0018037>.
- Iwase, Mitsunori, Sanford P. Bishop, Masami Uechi, Dorothy E. Vatner, Richard P. Shannon, Raymond K. Kudej, David C. Wight, et al. 1996. "Adverse Effects of Chronic Endogenous Sympathetic Drive Induced by Cardiac Gs α Overexpression." *Circulation Research* 78 (4): 517–24. <https://doi.org/10.1161/01.RES.78.4.517>.
- Jackman, Christopher P., Aaron L. Carlson, and Nenad Bursac. 2016. "Dynamic Culture Yields Engineered Myocardium with Near-Adult Functional Output." *Biomaterials* 111 (December): 66–79. <https://doi.org/10.1016/j.biomaterials.2016.09.024>.
- Jacot, Jeffrey G., Hiroko Kita-Matsuo, Karen A. Wei, H. S. Vincent Chen, Jeffrey H. Omens, Mark Mercola, and Andrew D. McCulloch. 2010. "Cardiac Myocyte Force Development during Differentiation and Maturation." In *Annals of the New York Academy of Sciences*, 1188:121–27. Ann N Y Acad Sci. <https://doi.org/10.1111/j.1749-6632.2009.05091.x>.
- Jacot, Jeffrey G., Jody C. Martin, and Darlene L. Hunt. 2010. "Mechanobiology of Cardiomyocyte Development." *Journal of Biomechanics* 43 (1): 93–98. <https://doi.org/10.1016/j.jbiomech.2009.09.014>.
- Jacot, Jeffrey G., Andrew D. McCulloch, and Jeffrey H. Omens. 2008. "Substrate Stiffness Affects the Functional Maturation of Neonatal Rat Ventricular Myocytes." *Biophysical Journal* 95 (7): 3479–87. <https://doi.org/10.1529/biophysj.107.124545>.
- Jalink, Kees. 2006. "Spying on CGMP with FRET." *Nature Methods* 3 (1): 11–12. <https://doi.org/10.1038/nmeth0106-11>.
- Johnson, W. B., S. Katugampola, S. Able, C. Napier, and S. E. Harding. 2012. "Profiling of CAMP and CGMP Phosphodiesterases in Isolated Ventricular Cardiomyocytes from Human Hearts: Comparison with Rat and Guinea Pig." *Life Sciences* 90 (9–10): 328–36. <https://doi.org/10.1016/j.lfs.2011.11.016>.
- Jorde, Rolf, Henrik Schirmer, Tom Wilsgaard, Ragnar Martin Joakimsen, Ellisiv Bøgeberg Mathiesen, Inger Njølstad, Maja Lisa Løchen, et al. 2014. "The Phosphodiesterase 8B Gene Rs4704397 Is Associated with Thyroid Function, Risk of Myocardial Infarction, and Body Height: The Tromsø

- Study." *Thyroid* 24 (2): 215–22. <https://doi.org/10.1089/thy.2013.0177>.
- Jørgensen, Carina, Saiqa Yasmeen, Helle K. Iversen, and Christina Kruuse. 2015. "Phosphodiesterase4D (PDE4D) - A Risk Factor for Atrial Fibrillation and Stroke?" *Journal of the Neurological Sciences*. *J Neurol Sci*. <https://doi.org/10.1016/j.jns.2015.11.010>.
- Jung, Gwanghyun, Giovanni Fajardo, Alexandre J.S. Ribeiro, Kristina Bezold Kooiker, Michael Coronado, Mingming Zhao, Dong Qing Hu, et al. 2016. "Time-Dependent Evolution of Functional vs. Remodeling Signaling in Induced Pluripotent Stem Cell-Derived Cardiomyocytes and Induced Maturation with Biomechanical Stimulation." *FASEB Journal* 30 (4): 1464–79. <https://doi.org/10.1096/fj.15-280982>.
- Kadota, Shin, Itsunari Minami, Nobuhiro Morone, John E. Heuser, Konstantin Agladze, and Norio Nakatsuji. 2013. "Development of a Reentrant Arrhythmia Model in Human Pluripotent Stem Cell-Derived Cardiac Cell Sheets." *European Heart Journal* 34 (15): 1147–56. <https://doi.org/10.1093/eurheartj/ehs418>.
- Kadota, Shin, Lil Pabon, Hans Reinecke, and Charles E. Murry. 2017. "In Vivo Maturation of Human Induced Pluripotent Stem Cell-Derived Cardiomyocytes in Neonatal and Adult Rat Hearts." *Stem Cell Reports* 8 (2): 278–89. <https://doi.org/10.1016/j.stemcr.2016.10.009>.
- Kamakura, Tsukasa, Takeru Makiyama, Kenichi Sasaki, Yoshinori Yoshida, Yimin Wuriyanghai, Jiarong Chen, Tetsuhisa Hattori, et al. 2013. "Ultrastructural Maturation of Human-Induced Pluripotent Stem Cell-Derived Cardiomyocytes in a Long-Term Culture." *Circulation Journal* 77 (5): 1307–14. <https://doi.org/10.1253/circj.CJ-12-0987>.
- Kamgoué, A., J. Ohayon, Y. Usson, L. Riou, and P. Tracqui. 2009. "Quantification of Cardiomyocyte Contraction Based on Image Correlation Analysis." *Cytometry Part A* 75 (4): 298–308. <https://doi.org/10.1002/cyto.a.20700>.
- Kangawa, Kenji, and Hisayuki Matsuo. 1984. "Purification and Complete Amino Acid Sequence of α -Human Atrial Natriuretic Polypeptide (α -HANP)." *Biochemical and Biophysical Research Communications* 118 (1): 131–39. [https://doi.org/10.1016/0006-291X\(84\)91077-5](https://doi.org/10.1016/0006-291X(84)91077-5).
- Karbach, Susanne, Philip Wenzel, Ari Waisman, Thomas Munzel, and Andreas Daiber. 2014. "eNOS Uncoupling in Cardiovascular Diseases - the Role of Oxidative Stress and Inflammation." *Current Pharmaceutical Design* 20 (22): 3579–94. <https://doi.org/10.2174/13816128113196660748>.
- Karbassi, Elaheh, Aidan Fenix, Silvia Marchiano, Naoto Muraoka, Kenta Nakamura, Xiulan Yang, and Charles E. Murry. 2020. "Cardiomyocyte Maturation: Advances in Knowledge and Implications for Regenerative Medicine." *Nature Reviews Cardiology* 17 (6): 341–59. <https://doi.org/10.1038/s41569-019-0331-x>.
- Kass, David A. 2012. "Cardiac Role of Cyclic-Gmp Hydrolyzing Phosphodiesterase Type 5: From Experimental Models to Clinical Trials." *Current Heart Failure Reports* 9 (3): 192–99. <https://doi.org/10.1007/s11897-012-0101-0>.
- Kass, David A., Hunter C. Champion, and Joseph A. Beavo. 2007. "Phosphodiesterase Type 5: Expanding Roles in Cardiovascular Regulation." *Circulation Research*. *Circ Res*. <https://doi.org/10.1161/CIRCRESAHA.107.162511>.
- Kehat, Izhak, Dorit Kenyagin-Karsenti, Mirit Snir, Hana Segev, Michal Amit, Amira Gepstein, Erella Livne, Ofer Binah, Joseph Itskovitz-Eldor, and Lior Gepstein. 2001. "Human Embryonic Stem Cells Can Differentiate into Myocytes with Structural and Functional Properties of Cardiomyocytes." *Journal of Clinical Investigation* 108 (3): 407–14.

<https://doi.org/10.1172/jci12131>.

- KEILBACH, Alexandra, Peter RUTH, and Franz HOFMANN. 1992. "Detection of CGMP Dependent Protein Kinase Isozymes by Specific Antibodies." *European Journal of Biochemistry* 208 (2): 467–73. <https://doi.org/10.1111/j.1432-1033.1992.tb17209.x>.
- Kim, Changsung, Maryam Majdi, Peng Xia, Karen A. Wei, Maria Talantova, Sean Spiering, Brandon Nelson, Mark Mercola, and Huei Sheng Vincent Chen. 2010. "Non-Cardiomyocytes Influence the Electrophysiological Maturation of Human Embryonic Stem Cell-Derived Cardiomyocytes during Differentiation." *Stem Cells and Development* 19 (6): 783–95. <https://doi.org/10.1089/scd.2009.0349>.
- Kim, Changsung, Johnson Wong, Jianyan Wen, Shirong Wang, Cheng Wang, Sean Spiering, Natalia G. Kan, et al. 2013. "Studying Arrhythmogenic Right Ventricular Dysplasia with Patient-Specific iPSCs." *Nature* 494 (7435): 105–10. <https://doi.org/10.1038/nature11799>.
- Kita-Matsuo, Hiroko, Maria Barcova, Natalie Prigozhina, Nathan Salomonis, Karen Wei, Jeffrey G. Jacot, Brandon Nelson, et al. 2009. "Lentiviral Vectors and Protocols for Creation of Stable HESC Lines for Fluorescent Tracking and Drug Resistance Selection of Cardiomyocytes." Edited by Mikhail V. Blagosklonny. *PLoS ONE* 4 (4): e5046. <https://doi.org/10.1371/journal.pone.0005046>.
- Klarenbeek, Jeffrey B., Joachim Goedhart, Mark A. Hink, Theodorus W.J. Gadella, and Kees Jalink. 2011. "A MTurquoise-Based CAMP Sensor for Both FLIM and Ratiometric Read-out Has Improved Dynamic Range." Edited by Neil A. Hotchin. *PLoS ONE* 6 (4): e19170. <https://doi.org/10.1371/journal.pone.0019170>.
- Kléber, André G., and Yoram Rudy. 2004. "Basic Mechanisms of Cardiac Impulse Propagation and Associated Arrhythmias." *Physiological Reviews*. *Physiol Rev*. <https://doi.org/10.1152/physrev.00025.2003>.
- Kodama, Masami, Kazuharu Furutani, Reiko Kimura, Tomoko Ando, Kazuho Sakamoto, Shushi Nagamori, Takashi Ashihara, et al. 2019. "Systematic Expression Analysis of Genes Related to Generation of Action Potentials in Human IPS Cell-Derived Cardiomyocytes." *Journal of Pharmacological Sciences* 140 (4): 325–30. <https://doi.org/10.1016/j.jphs.2019.06.006>.
- Kokkonen, Kristen, and David A. Kass. 2017. "Nanodomain Regulation of Cardiac Cyclic Nucleotide Signaling by Phosphodiesterases." *Annual Review of Pharmacology and Toxicology*. Annual Reviews Inc. <https://doi.org/10.1146/annurev-pharmtox-010716-104756>.
- Koller, Kerry J., David G. Lowe, Gregory L. Bennett, Naoto Minamino, Kenji Kangawa, Hisayuki Matsuo, and David V. Goeddel. 1991. "Selective Activation of the B Natriuretic Peptide Receptor by C-Type Natriuretic Peptide (CNP)." *Science* 252 (5002): 120–23. <https://doi.org/10.1126/science.1672777>.
- Kozlovskis, P. L., A. M. Gerdes, M. Smets, J. A. Moore, A. L. Bassett, and R. J. Myerburg. 1991. "Regional Increase in Isolated Myocyte Volume in Chronic Myocardial Infarction in Cats." *Journal of Molecular and Cellular Cardiology* 23 (12): 1459–66. [https://doi.org/10.1016/0022-2828\(91\)90191-N](https://doi.org/10.1016/0022-2828(91)90191-N).
- Kuhn, Michaela. 2003. "Structure, Regulation, and Function of Mammalian Membrane Guanylyl Cyclase Receptors, With a Focus on Guanylyl Cyclase-A." *Circulation Research*. Lippincott Williams & Wilkins. <https://doi.org/10.1161/01.RES.0000094745.28948.4D>.
- Kuo, Po Ling, Hyungsuk Lee, Mark Anthony Bray, Nicholas A. Geisse, Yen Tsung Huang, William J. Adams, Sean P. Sheehy, and Kevin K. Parker. 2012. "Myocyte Shape Regulates Lateral Registry

- of Sarcomeres and Contractility." *American Journal of Pathology* 181 (6): 2030–37. <https://doi.org/10.1016/j.ajpath.2012.08.045>.
- Lab, Max J., Anamika Bhargava, Peter T. Wright, and Julia Gorelik. 2013. "The Scanning Ion Conductance Microscope for Cellular Physiology." *American Journal of Physiology - Heart and Circulatory Physiology*. *Am J Physiol Heart Circ Physiol*. <https://doi.org/10.1152/ajpheart.00499.2012>.
- Laflamme, Michael A., Kent Y. Chen, Anna V. Naumova, Veronica Muskheli, James A. Fugate, Sarah K. Dupras, Hans Reinecke, et al. 2007. "Cardiomyocytes Derived from Human Embryonic Stem Cells in Pro-Survival Factors Enhance Function of Infarcted Rat Hearts." *Nature Biotechnology* 25 (9): 1015–24. <https://doi.org/10.1038/nbt1327>.
- Laflamme, Michael A., and Charles E. Murry. 2011. "Heart Regeneration." *Nature*. Nature Publishing Group. <https://doi.org/10.1038/nature10147>.
- Lange, Willem J. de, Emily T. Farrell, Caroline R. Kreitzer, Derek R. Jacobs, Di Lang, Alexey V. Glukhov, and J. Carter Ralphe. 2021. "Human iPSC-Engineered Cardiac Tissue Platform Faithfully Models Important Cardiac Physiology." *American Journal of Physiology - Heart and Circulatory Physiology* 320 (4): H1670–86. <https://doi.org/10.1152/AJPHEART.00941.2020>.
- Langenickel, Thomas H., Jens Buttgerit, Ines Pagel-Langenickel, Maren Lindner, Jan Monti, Knut Beuerlein, Widai Al-Saadi, et al. 2006. "Cardiac Hypertrophy in Transgenic Rats Expressing a Dominant-Negative Mutant of the Natriuretic Peptide Receptor B." *Proceedings of the National Academy of Sciences of the United States of America* 103 (12): 4735–40. <https://doi.org/10.1073/pnas.0510019103>.
- Lee, Desy S., Jyh Hong Chen, David J. Lundy, Chung Hung Liu, Shiaw Min Hwang, Lil Pabon, Ru Chi Shieh, et al. 2015. "Defined MicroRNAs Induce Aspects of Maturation in Mouse and Human Embryonic-Stem-Cell-Derived Cardiomyocytes." *Cell Reports* 12 (12): 1960–67. <https://doi.org/10.1016/j.celrep.2015.08.042>.
- Lee, Dong I., Guangshuo Zhu, Takashi Sasaki, Gun Sik Cho, Nazha Hamdani, Ronald Holewinski, Su Hyun Jo, et al. 2015. "Phosphodiesterase 9A Controls Nitric-Oxide-Independent cGMP and Hypertrophic Heart Disease." *Nature* 519 (7544): 472–76. <https://doi.org/10.1038/nature14332>.
- Lee, Yee Ki, Kwong Man Ng, Yau Chi Chan, Wing Hon Lai, Ka Wing Au, Chung Yee Jenny Ho, Lai Yung Wong, Chu Pak Lau, Hung Fat Tse, and Chung Wah Siu. 2010. "Triiodothyronine Promotes Cardiac Differentiation and Maturation of Embryonic Stem Cells via the Classical Genomic Pathway." *Molecular Endocrinology* 24 (9): 1728–36. <https://doi.org/10.1210/me.2010-0032>.
- Leor, Jonathan, Michael Patterson, Manuel J. Quinones, Laurence H. Kedes, and Robert A. Kloner. 1996. "Transplantation of Fetal Myocardial Tissue into the Infarcted Myocardium of Rat: A Potential Method for Repair of Infarcted Myocardium?" *Circulation* 94 (9 SUPPL.): II332-6.
- Li, Peng, Dajun Wang, Jason Lucas, Suzanne Oparil, Dongqi Xing, Xu Cao, Lea Novak, Matthew B. Renfrow, and Yiu Fai Chen. 2008. "Atrial Natriuretic Peptide Inhibits Transforming Growth Factor β -Induced Smad Signaling and Myofibroblast Transformation in Mouse Cardiac Fibroblasts." *Circulation Research* 102 (2): 185–92. <https://doi.org/10.1161/CIRCRESAHA.107.157677>.
- Li, Shenglan, Anqi Zhang, Haipeng Xue, Dali Li, and Ying Liu. 2017. "One-Step PiggyBac Transposon-Based CRISPR/Cas9 Activation of Multiple Genes." *Molecular Therapy - Nucleic Acids* 8 (September): 64–76. <https://doi.org/10.1016/j.omtn.2017.06.007>.

- Lian, Xiaojun, Jianhua Zhang, Samira M. Azarin, Kexian Zhu, Laurie B. Hazeltine, Xiaoping Bao, Cheston Hsiao, Timothy J. Kamp, and Sean P. Palecek. 2013. "Directed Cardiomyocyte Differentiation from Human Pluripotent Stem Cells by Modulating Wnt/ β -Catenin Signaling under Fully Defined Conditions." *Nature Protocols* 8 (1): 162–75. <https://doi.org/10.1038/nprot.2012.150>.
- Liau, Brian, Nicolas Christoforou, Kam W. Leong, and Nenad Bursac. 2011. "Pluripotent Stem Cell-Derived Cardiac Tissue Patch with Advanced Structure and Function." *Biomaterials* 32 (35): 9180–87. <https://doi.org/10.1016/j.biomaterials.2011.08.050>.
- Lieu, Deborah K., Jing Liu, Chung Wah Siu, Gregory P. Mc Nerney, Hung Fat Tse, Amir Abu-Khalil, Thomas Huser, and Ronald A. Li. 2009. "Absence of Transverse Tubules Contributes to Non-Uniform Ca²⁺ Wavefronts in Mouse and Human Embryonic Stem Cell-Derived Cardiomyocytes." *Stem Cells and Development* 18 (10): 1493–1500. <https://doi.org/10.1089/scd.2009.0052>.
- Lin, Brian Leei, David A. Kass, and Dong I. Lee. 2017. "Cyclic GMP/Protein Kinase Localized Signaling and Disease Implications." In , 273–90. Springer, Cham. https://doi.org/10.1007/978-3-319-54579-0_13.
- Lin, Ching Shwun, Angie Lau, Richard Tu, and Tom F. Lue. 2000. "Expression of Three Isoforms of CGMP-Binding CGMP-Specific Phosphodiesterase (PDE5) in Human Penile Cavernosum." *Biochemical and Biophysical Research Communications* 268 (2): 628–35. <https://doi.org/10.1006/bbrc.2000.2187>.
- Liu, H., and D. H. Maurice. 1998. "Expression of Cyclic GMP-Inhibited Phosphodiesterases 3A and 3B (PDE3A and PDE3B) in Rat Tissues: Differential Subcellular Localization and Regulated Expression by Cyclic AMP." *British Journal of Pharmacology* 125 (7): 1501–10. <https://doi.org/10.1038/sj.bjp.0702227>.
- Liu, Jing, Ji Dong Fu, Chung Wah Siu, and Ronald A. Li. 2007. "Functional Sarcoplasmic Reticulum for Calcium Handling of Human Embryonic Stem Cell-Derived Cardiomyocytes: Insights for Driven Maturation." *Stem Cells* 25 (12): 3038–44. <https://doi.org/10.1634/stemcells.2007-0549>.
- Lopaschuk, Gary D., and Jagdip S. Jaswal. 2010. "Energy Metabolic Phenotype of the Cardiomyocyte during Development, Differentiation, and Postnatal Maturation." In *Journal of Cardiovascular Pharmacology*, 56:130–40. *J Cardiovasc Pharmacol*. <https://doi.org/10.1097/FJC.0b013e3181e74a14>.
- Louch, William E., Katherine A. Sheehan, and Beata M. Wolska. 2011. "Methods in Cardiomyocyte Isolation, Culture, and Gene Transfer." *Journal of Molecular and Cellular Cardiology*. NIH Public Access. <https://doi.org/10.1016/j.yjmcc.2011.06.012>.
- Loucks, Alexandra D., Thomas O'Hara, and Natalia A. Trayanova. 2018. "Degradation of T-Tubular Microdomains and Altered CAMP Compartmentation Lead to Emergence of Arrhythmogenic Triggers in Heart Failure Myocytes: An in Silico Study." *Frontiers in Physiology* 9 (December): 1737. <https://doi.org/10.3389/fphys.2018.01737>.
- Lowe, D. G., M. S. Chang, R. Hellmiss, E. Chen, S. Singh, D. L. Garbers, and D. V. Goeddel. 1989. "Human Atrial Natriuretic Peptide Receptor Defines a New Paradigm for Second Messenger Signal Transduction." *EMBO Journal* 8 (5): 1377–84. <https://doi.org/10.1002/j.1460-2075.1989.tb03518.x>.
- Lu, David, Nakon Aroonsakool, Utako Yokoyama, Hemal H. Patel, and Paul A. Insel. 2013. "Increase in Cellular Cyclic AMP Concentrations Reverses the Profibrogenic Phenotype of Cardiac Myofibroblasts: A Novel Therapeutic Approach for Cardiac Fibrosis." *Molecular Pharmacology*

84 (6): 787–93. <https://doi.org/10.1124/mol.113.087742>.

- Lueder, Thomas G. Von, S. Jeson Sangaralingham, Bing H. Wang, Andrew R. Kompa, Dan Atar, John C. Burnett, and Henry Krum. 2013. “Renin-Angiotensin Blockade Combined with Natriuretic Peptide System Augmentation Novel Therapeutic Concepts to Combat Heart Failure.” *Circulation: Heart Failure* 6 (3): 594–605. <https://doi.org/10.1161/CIRCHEARTFAILURE.112.000289>.
- Lugnier, Claire, Thérèse Keravis, Alain Le Bec, Olivier Pauvert, Sonia Proteau, and Eric Rousseau. 1999. “Characterization of Cyclic Nucleotide Phosphodiesterase Isoforms Associated to Isolated Cardiac Nuclei.” *Biochimica et Biophysica Acta - General Subjects* 1472 (3): 431–46. [https://doi.org/10.1016/S0304-4165\(99\)00145-2](https://doi.org/10.1016/S0304-4165(99)00145-2).
- Lundy, Scott D., Wei Zhong Zhu, Michael Regnier, and Michael A. Laflamme. 2013. “Structural and Functional Maturation of Cardiomyocytes Derived from Human Pluripotent Stem Cells.” *Stem Cells and Development* 22 (14): 1991–2002. <https://doi.org/10.1089/scd.2012.0490>.
- Lyon, Alexander R., Ken T. MacLeod, Yanjun Zhang, Edwin Garcia, Gaelle Kikonda Kanda, Max J. Lab, Yuri E. Korchev, Sian E. Harding, and Julia Gorelik. 2009. “Loss of T-Tubules and Other Changes to Surface Topography in Ventricular Myocytes from Failing Human and Rat Heart.” *Proceedings of the National Academy of Sciences of the United States of America* 106 (16): 6854–59. <https://doi.org/10.1073/pnas.0809777106>.
- Lyon, Alexander R., Viacheslav O. Nikolaev, Michele Miragoli, Markus B. Sikkell, Helen Paur, Ludovic Benard, Jean Sebastien Hulot, et al. 2012. “Plasticity of Surface Structures and 2-Adrenergic Receptor Localization in Failing Ventricular Cardiomyocytes during Recovery from Heart Failure.” *Circulation: Heart Failure* 5 (3): 357–65. <https://doi.org/10.1161/CIRCHEARTFAILURE.111.964692>.
- Ma, Junyi, Liang Guo, Steve J. Fiene, Blake D. Anson, James A. Thomson, Timothy J. Kamp, Kyle L. Kolaja, Bradley J. Swanson, and Craig T. January. 2011. “High Purity Human-Induced Pluripotent Stem Cell-Derived Cardiomyocytes: Electrophysiological Properties of Action Potentials and Ionic Currents.” *American Journal of Physiology - Heart and Circulatory Physiology* 301 (5). <https://doi.org/10.1152/ajpheart.00694.2011>.
- Mahdavi, V., A. M. Lompre, A. P. Chambers, and B. Nadal-Ginard. 1984. “Cardiac Myosin Heavy Chain Isozymic Transitions during Development and under Pathological Conditions Are Regulated at the Level of mRNA Availability.” *European Heart Journal* 5 (SUPPL. F): 181–91. https://doi.org/10.1093/eurheartj/5.suppl_f.181.
- Mali, Prashant, John Aach, P. Benjamin Stranges, Kevin M. Esvelt, Mark Moosburner, Sriram Kosuri, Luhan Yang, and George M. Church. 2013. “CAS9 Transcriptional Activators for Target Specificity Screening and Paired Nickases for Cooperative Genome Engineering.” *Nature Biotechnology* 31 (9): 833–38. <https://doi.org/10.1038/nbt.2675>.
- Mali, Prashant, Luhan Yang, Kevin M. Esvelt, John Aach, Marc Guell, James E. DiCarlo, Julie E. Norville, and George M. Church. 2013. “RNA-Guided Human Genome Engineering via Cas9.” *Science* 339 (6121): 823–26. <https://doi.org/10.1126/science.1232033>.
- Mannhardt, Ingra, Alexandra Eder, Berengere Dumotier, Maksymilian Prondzynski, Elisabeth Kramer, Martin Traebert, Frederik Flenner, et al. 2017. “Blinded Contractility Analysis in Hpsc-Cardiomyocytes in Engineered Heart Tissue Format: Comparison with Human Atrial Trabeculae.” *Toxicological Sciences* 158 (1): 164–75. <https://doi.org/10.1093/toxsci/kfx081>.
- Martherus, Ruben S.R.M., Sabina J.V. Vanherle, Erika D.J. Timmer, Volkert A. Zeijlemaker, Jos L. Broers, Hubert J. Smeets, Joep P. Geraedts, and Torik A.Y. Ayoubi. 2010. “Electrical Signals

- Affect the Cardiomyocyte Transcriptome Independently of Contraction." *Physiological Genomics* 42 A (4): 283–89. <https://doi.org/10.1152/physiolgenomics.00182.2009>.
- Martinez, Sergio E., Albert Y. Wu, Natalie A. Glavas, Xiao Bo Tang, Stewart Turley, Wim G.J. Hol, and Joseph A. Beavo. 2002. "The Two GAF Domains in Phosphodiesterase 2A Have Distinct Roles in Dimerization and in CGMP Binding." *Proceedings of the National Academy of Sciences of the United States of America* 99 (20): 13260–65. <https://doi.org/10.1073/pnas.192374899>.
- Massion, P. B., O. Feron, C. Dessy, and J. L. Balligand. 2003. "Nitric Oxide and Cardiac Function: Ten Years after, and Continuing." *Circulation Research*. Circ Res. <https://doi.org/10.1161/01.RES.0000088351.58510.21>.
- Matsuda, Takahisa, Kyoko Takahashi, Tetsuro Nariai, Takashi Ito, Tomoka Takatani, Yasushi Fujio, and Junichi Azuma. 2004. "N-Cadherin-Mediated Cell Adhesion Determines the Plasticity for Cell Alignment in Response to Mechanical Stretch in Cultured Cardiomyocytes." *Biochemical and Biophysical Research Communications* 326 (1): 228–32. <https://doi.org/10.1016/j.bbrc.2004.11.019>.
- Maurice, Donald H., Hengming Ke, Faiyaz Ahmad, Yousheng Wang, Jay Chung, and Vincent C. Manganiello. 2014. "Advances in Targeting Cyclic Nucleotide Phosphodiesterases." *Nature Reviews Drug Discovery*. Nat Rev Drug Discov. <https://doi.org/10.1038/nrd4228>.
- Maurice, Donald H., Daniel Palmer, Douglas G. Tilley, Heather A. Dunkerley, Stuart J. Netherton, Daniel R. Raymond, Hisham S. Elbatarny, and Sandra L. Jimmo. 2003. "Cyclic Nucleotide Phosphodiesterase Activity, Expression, and Targeting in Cells of the Cardiovascular System." *Molecular Pharmacology* 64 (3): 533–46. <https://doi.org/10.1124/mol.64.3.533>.
- McDevitt, Todd C., John C. Angello, Marsha L. Whitney, H. Reinecke, Stephen D. Hauschka, Charles E. Murry, and Patrick S. Stayton. 2002. "In Vitro Generation of Differentiated Cardiac Myofibers on Micropatterned Laminin Surfaces." *Journal of Biomedical Materials Research* 60 (3): 472–79. <https://doi.org/10.1002/jbm.1292>.
- McDevitt, Todd C., Michael A. Laflamme, and Charles E. Murry. 2005. "Proliferation of Cardiomyocytes Derived from Human Embryonic Stem Cells Is Mediated via the IGF/PI 3-Kinase/Akt Signaling Pathway." *Journal of Molecular and Cellular Cardiology* 39 (6): 865–73. <https://doi.org/10.1016/j.yjmcc.2005.09.007>.
- Medley, Tanya L., Milena Furtado, Nicholas T. Lam, Rejhan Idrizi, David Williams, Paul J. Verma, Mauro Costa, and David M. Kaye. 2013. "Effect of Oxygen on Cardiac Differentiation in Mouse IPS Cells: Role of Hypoxia Inducible Factor-1 and Wnt/Beta-Catenin Signaling." *PLoS ONE* 8 (11). <https://doi.org/10.1371/journal.pone.0080280>.
- Mehats, Celine, Carsten B. Andersen, Marcello Filopanti, S. L. Catherine Jin, and Marco Conti. 2002. "Cyclic Nucleotide Phosphodiesterases and Their Role in Endocrine Cell Signaling." *Trends in Endocrinology and Metabolism*. Elsevier. [https://doi.org/10.1016/S1043-2760\(01\)00523-9](https://doi.org/10.1016/S1043-2760(01)00523-9).
- Mehel, Hind, Julius Emons, Christiane Vettel, Katrin Wittköpper, Danilo Seppelt, Matthias Dewenter, Susanne Lutz, et al. 2013. "Phosphodiesterase-2 Is up-Regulated in Human Failing Hearts and Blunts β -Adrenergic Responses in Cardiomyocytes." *Journal of the American College of Cardiology* 62 (17): 1596–1606. <https://doi.org/10.1016/j.jacc.2013.05.057>.
- Melkounian, Zara, Jennifer L. Weber, David M. Weber, Andrei G. Fadeev, Yue Zhou, Paula Dolley-Sonneville, Jiwei Yang, et al. 2010. "Synthetic Peptide-Acrylate Surfaces for Long-Term Self-Renewal and Cardiomyocyte Differentiation of Human Embryonic Stem Cells." *Nature Biotechnology* 28 (6): 606–10. <https://doi.org/10.1038/nbt.1629>.

- Mendez, Melissa G., and Paul A. Janmey. 2012. "Transcription Factor Regulation by Mechanical Stress." *International Journal of Biochemistry and Cell Biology*. Int J Biochem Cell Biol. <https://doi.org/10.1016/j.biocel.2012.02.003>.
- Menendez-Montes, Ivan, Beatriz Escobar, Beatriz Palacios, Manuel Jose Gómez, Jose Luis Izquierdo-Garcia, Lorena Flores, Luis Jesus Jiménez-Borreguero, et al. 2016. "Myocardial VHL-HIF Signaling Controls an Embryonic Metabolic Switch Essential for Cardiac Maturation." *Developmental Cell* 39 (6): 724–39. <https://doi.org/10.1016/j.devcel.2016.11.012>.
- Méry, Pierre François, Catherine Pavoine, Laurent Belhassen, Françoise Pecker, and Rodolphe Fischmeister. 1993. "Nitric Oxide Regulates Cardiac Ca²⁺ Current: Involvement of CGMP-Inhibited and CGMP-Stimulated Phosphodiesterases through Guanylyl Cyclase Activation." *Journal of Biological Chemistry* 268 (35): 26286–95. [https://doi.org/10.1016/s0021-9258\(19\)74313-0](https://doi.org/10.1016/s0021-9258(19)74313-0).
- Mika, Delphine, Pierre Bobin, Martine Pomérance, Patrick Lechêne, Ruth E. Westenbroek, William A. Catterall, Grégoire Vandecasteele, Jérôme Leroy, and Rodolphe Fischmeister. 2013. "Differential Regulation of Cardiac Excitation-Contraction Coupling by CAMP Phosphodiesterase Subtypes." *Cardiovascular Research* 100 (2): 336–46. <https://doi.org/10.1093/cvr/cvt193>.
- Miller, Clint L., Yujun Cai, Masayoshi Oikawa, Tamlyn Thomas, Wolfgang R. Dostmann, Manuela Zaccolo, Keigi Fujiwara, and Chen Yan. 2011. "Cyclic Nucleotide Phosphodiesterase 1A: A Key Regulator of Cardiac Fibroblast Activation and Extracellular Matrix Remodeling in the Heart." *Basic Research in Cardiology* 106 (6): 1023–39. <https://doi.org/10.1007/s00395-011-0228-2>.
- Miller, Clint L., Masayoshi Oikawa, Yujun Cai, Andrew P. Wojtovich, David J. Nagel, Xiangbin Xu, Haodong Xu, et al. 2009. "Role of Ca²⁺/Calmodulin-Stimulated Cyclic Nucleotide Phosphodiesterase 1 in Mediating Cardiomyocyte Hypertrophy." *Circulation Research* 105 (10): 956–64. <https://doi.org/10.1161/CIRCRESAHA.109.198515>.
- Mills, Richard J., Drew M. Titmarsh, Xaver Koenig, Benjamin L. Parker, James G. Ryall, Gregory A. Quaife-Ryan, Holly K. Voges, et al. 2017. "Functional Screening in Human Cardiac Organoids Reveals a Metabolic Mechanism for Cardiomyocyte Cell Cycle Arrest." *Proceedings of the National Academy of Sciences of the United States of America* 114 (40): E8372–81. <https://doi.org/10.1073/pnas.1707316114>.
- Mishima, Yuichiro, Carlos Stahlhut, and Antonio J. Giraldez. 2007. "MiR-1-2 Gets to the Heart of the Matter." *Cell*. Elsevier. <https://doi.org/10.1016/j.cell.2007.04.008>.
- Moens, An L., Eiki Takimoto, Carlo G. Tocchetti, Khalid Chakir, Djahida Bedja, Gianfranco Cormaci, Elizabeth A. Ketner, et al. 2008. "Reversal of Cardiac Hypertrophy and Fibrosis from Pressure Overload by Tetrahydrobiopterin Efficacy of Recoupling Nitric Oxide Synthase as a Therapeutic Strategy." *Circulation* 117 (20): 2626–36. <https://doi.org/10.1161/CIRCULATIONAHA.107.737031>.
- Moltzau, Lise Román, Silja Meier, Kjetil Wessel Andressen, and Finn Olav Levy. 2017. "Compartmentation of Natriuretic Peptide Signalling in Cardiac Myocytes: Effects on Cardiac Contractility and Hypertrophy." In , 245–71. Springer, Cham. https://doi.org/10.1007/978-3-319-54579-0_12.
- Mongillo, Marco, Carlo G. Tocchetti, Anna Terrin, Valentina Lissandron, York Fong Cheung, Wolfgang R. Dostmann, Tullio Pozzan, et al. 2006. "Compartmentalized Phosphodiesterase-2 Activity Blunts β -Adrenergic Cardiac Inotropy via an NO/CGMP-Dependent Pathway." *Circulation Research* 98 (2): 226–34. <https://doi.org/10.1161/01.RES.0000200178.34179.93>.

- Montessuit, Christophe, Tatiana Palma, Christelle Viglino, Corinne Pellioux, and René Lerch. 2006. "Effects of Insulin-like Growth Factor-I on the Maturation of Metabolism in Neonatal Rat Cardiomyocytes." *Pflugers Archiv European Journal of Physiology* 452 (4): 380–86. <https://doi.org/10.1007/s00424-006-0059-4>.
- Movsesian, Matthew A., and Rakesh C. Kukreja. 2011. "Phosphodiesterase Inhibition in Heart Failure." *Handbook of Experimental Pharmacology* 204 (204): 237–49. https://doi.org/10.1007/978-3-642-17969-3_10.
- Muller, Bernard, Jean Claude Stoclet, and Claire Lugnier. 1992. "Cytosolic and Membrane-Bound Cyclic Nucleotide Phosphodiesterases from Guinea Pig Cardiac Ventricles." *European Journal of Pharmacology: Molecular Pharmacology* 225 (3): 263–72. [https://doi.org/10.1016/0922-4106\(92\)90028-T](https://doi.org/10.1016/0922-4106(92)90028-T).
- Mummery, Christine L., Jianhua Zhang, Elizabeth S. Ng, David A. Elliott, Andrew G. Elefanty, and Timothy J. Kamp. 2012. "Differentiation of Human Embryonic Stem Cells and Induced Pluripotent Stem Cells to Cardiomyocytes: A Methods Overview." *Circulation Research* 111 (3): 344–58. <https://doi.org/10.1161/CIRCRESAHA.110.227512>.
- Mummery, Christine, Dorien Ward-van Oostwaard, Pieter Doevendans, Rene Spijker, Stieneke Van den Brink, Rutger Hassink, Marcel Van der Heyden, et al. 2003. "Differentiation of Human Embryonic Stem Cells to Cardiomyocytes: Role of Coculture with Visceral Endoderm-like Cells." *Circulation* 107 (21): 2733–40. <https://doi.org/10.1161/01.cir.0000068356.38592.68>.
- Nagayama, Takahiro, Manling Zhang, Steven Hsu, Eiki Takimoto, and David A. Kass. 2008. "Sustained Soluble Guanylate Cyclase Stimulation Offsets Nitric-Oxide Synthase Inhibition to Restore Acute Cardiac Modulation by Sildenafil." *Journal of Pharmacology and Experimental Therapeutics* 326 (2): 380–87. <https://doi.org/10.1124/jpet.108.137422>.
- Nakano, Haruko, Itsunari Minami, Daniel Braas, Herman Pappoe, Xiuju Wu, Addelynn Sagadevan, Laurent Vergnes, et al. 2017. "Glucose Inhibits Cardiac Muscle Maturation through Nucleotide Biosynthesis." *ELife* 6 (December). <https://doi.org/10.7554/eLife.29330>.
- Narsinh, Kazim H., Jordan Plews, and Joseph C. Wu. 2011. "Comparison of Human Induced Pluripotent and Embryonic Stem Cells: Fraternal or Identical Twins?" *Molecular Therapy*. American Society of Gene & Cell Therapy. <https://doi.org/10.1038/mt.2011.41>.
- Neo, Boon Hwa, Sharath Kandhi, and Michael S. Wolin. 2011. "Roles for Redox Mechanisms Controlling Protein Kinase G in Pulmonary and Coronary Artery Responses to Hypoxia." *American Journal of Physiology - Heart and Circulatory Physiology* 301 (6): 2295–2304. <https://doi.org/10.1152/ajpheart.00624.2011>.
- Newman, Robert H., Matthew D. Fosbrink, and Jin Zhang. 2011. "Genetically Encodable Fluorescent Biosensors for Tracking Signaling Dynamics in Living Cells." *Chemical Reviews* 111 (5): 3614–66. <https://doi.org/10.1021/cr100002u>.
- Niino, Yusuke, Kohji Hotta, and Kotaro Oka. 2009. "Simultaneous Live Cell Imaging Using Dual FRET Sensors with a Single Excitation Light." Edited by Karl-Wilhelm Koch. *PLoS ONE* 4 (6): e6036. <https://doi.org/10.1371/journal.pone.0006036>.
- Nikolaev, Viacheslav O., Moritz Bünemann, Lutz Hein, Annette Hannawacker, and Martin J. Lohse. 2004. "Novel Single Chain CAMP Sensors for Receptor-Induced Signal Propagation." *Journal of Biological Chemistry* 279 (36): 37215–18. <https://doi.org/10.1074/jbc.C400302200>.
- Nikolaev, Viacheslav O., Stepan Gambaryan, and Martin J. Lohse. 2006. "Fluorescent Sensors for Rapid Monitoring of Intracellular CGMP." *Nature Methods* 3 (1): 23–25.

<https://doi.org/10.1038/nmeth816>.

- Nikolaev, Viacheslav O., Alexey Moshkov, Alexander R. Lyon, Michele Miragoli, Pavel Novak, Helen Paur, Martin J. Lohse, Yuri E. Korchev, Sian E. Harding, and Julia Gorelik. 2010. "B2-Adrenergic Receptor Redistribution in Heart Failure Changes CAMP Compartmentation." *Science* 327 (5973): 1653–57. <https://doi.org/10.1126/science.1185988>.
- Nunes, Sara S., Jason W. Miklas, Jie Liu, Roozbeh Aschar-Sobbi, Yun Xiao, Boyang Zhang, Jiahua Jiang, et al. 2013. "Biowire: A Platform for Maturation of Human Pluripotent Stem Cell-Derived Cardiomyocytes." *Nature Methods* 10 (8): 781–87. <https://doi.org/10.1038/nmeth.2524>.
- Oceguera-Yanez, Fabian, Shin Il Kim, Tomoko Matsumoto, Ghee Wan Tan, Long Xiang, Takeshi Hatani, Takayuki Kondo, et al. 2016. "Engineering the AAVS1 Locus for Consistent and Scalable Transgene Expression in Human iPSCs and Their Differentiated Derivatives." *Methods* 101 (May): 43–55. <https://doi.org/10.1016/j.ymeth.2015.12.012>.
- Ockaili, Ramzi, Fadi Salloum, John Hawkins, and Rakesh C. Kukreja. 2002. "Sildenafil (Viagra) Induces Powerful Cardioprotective Effect via Opening of Mitochondrial KATP Channels in Rabbits." *American Journal of Physiology - Heart and Circulatory Physiology* 283 (3 52-3). <https://doi.org/10.1152/ajpheart.00324.2002>.
- Ogawa, K., and K. Imura. 1982. "Cyclic Nucleotides and the Cardiac Function." *Nippon Rinsho. Japanese Journal of Clinical Medicine* 40 (11): 2350–55. <https://doi.org/10.1161/RES.44.2.216502>.
- Okamoto, Sachiko, Yasunori Amaishi, Izumi Maki, Tatsuji Enoki, and Junichi Mineno. 2019. "Highly Efficient Genome Editing for Single-Base Substitutions Using Optimized SsODNs with Cas9-RNPs." *Scientific Reports* 9 (1): 1–11. <https://doi.org/10.1038/s41598-019-41121-4>.
- Olivetti, Giorgio, Elena Cigola, Roberta Maestri, Domenico Corradi, Costanza Lagrasta, Steven R. Gambert, and Piero Anversa. 1996. "Aging, Cardiac Hypertrophy and Ischemic Cardiomyopathy Do Not Affect the Proportion of Mononucleated and Multinucleated Myocytes in the Human Heart." *Journal of Molecular and Cellular Cardiology* 28 (7): 1463–77. <https://doi.org/10.1006/jmcc.1996.0137>.
- Packer, Milton, Joseph R. Carver, Richard J. Rodeheffer, Russell J. Ivanhoe, Robert DiBianco, Steven M. Zeldis, Grady H. Hendrix, et al. 1991. "Effect of Oral Milrinone on Mortality in Severe Chronic Heart Failure." *New England Journal of Medicine* 325 (21): 1468–75. <https://doi.org/10.1056/nejm199111213252103>.
- Park, Min, Peter Sandner, and Thomas Krieg. 2018. "CGMP at the Centre of Attention: Emerging Strategies for Activating the Cardioprotective PKG Pathway." *Basic Research in Cardiology*. Dr. Dietrich Steinkopff Verlag GmbH and Co. KG. <https://doi.org/10.1007/s00395-018-0679-9>.
- Parton, Robert G., Kerrie Ann McMahon, and Yeping Wu. 2020. "Caveolae: Formation, Dynamics, and Function." *Current Opinion in Cell Biology*. Elsevier Current Trends. <https://doi.org/10.1016/j.ceb.2020.02.001>.
- Parton, Robert G., Michael Way, Natasha Zorzi, and Espen Stang. 1997. "Caveolin-3 Associates with Developing T-Tubules during Muscle Differentiation." *Journal of Cell Biology* 136 (1): 137–54. <https://doi.org/10.1083/jcb.136.1.137>.
- Patrucco, Enrico, Masami Shimizu Albergine, Luis F. Santana, and Joseph A. Beavo. 2010. "Phosphodiesterase 8A (PDE8A) Regulates Excitation-Contraction Coupling in Ventricular Myocytes." *Journal of Molecular and Cellular Cardiology* 49 (2): 330–33. <https://doi.org/10.1016/j.yjmcc.2010.03.016>.

- Paulus, Walter J. 2020. "Nitric Oxide and Cardiac Contraction: Clinical Studies." In *Endothelial Modulation of Cardiac Function*, 35–51. CRC Press. <https://doi.org/10.1201/9780367810559-3>.
- Pavlaki, Nikoleta, and Viacheslav O. Nikolaev. 2018. "Imaging of PDE2- and PDE3-Mediated CGMP-to-CAMP Cross-Talk in Cardiomyocytes." *Journal of Cardiovascular Development and Disease* 5 (1): 4. <https://doi.org/10.3390/jcdd5010004>.
- Perera, Ruwan K., Julia U. Sprenger, Julia H. Steinbrecher, Daniela Hübscher, Stephan E. Lehnart, Marco Abesser, Kai Schuh, Ali El-Armouche, and Viacheslav O. Nikolaev. 2015. "Microdomain Switch of CGMP-Regulated Phosphodiesterases Leads to ANP-Induced Augmentation of β -Adrenoceptor-Stimulated Contractility in Early Cardiac Hypertrophy." *Circulation Research* 116 (8): 1304–11. <https://doi.org/10.1161/CIRCRESAHA.116.306082>.
- Peters, Nicholas S., Nicholas J. Severs, Stephen M. Rothery, Christopher Lincoln, Magdi H. Yacoub, and Colin R. Green. 1994. "Spatiotemporal Relation between Gap Junctions and Fascia Adherens Junctions during Postnatal Development of Human Ventricular Myocardium." *Circulation* 90 (2): 713–25. <https://doi.org/10.1161/01.CIR.90.2.713>.
- Pijnappels, Daniël A., Martin J. Schalij, Arti A. Ramkisoensing, John Van Tuyn, Antoine A.F. De Vries, Arnoud Van Der Laarse, Dirk L. Ypey, and Douwe E. Atsma. 2008. "Forced Alignment of Mesenchymal Stem Cells Undergoing Cardiomyogenic Differentiation Affects Functional Integration with Cardiomyocyte Cultures." *Circulation Research* 103 (2): 167–76. <https://doi.org/10.1161/CIRCRESAHA.108.176131>.
- Pillekamp, Frank, Moritz Hausteil, Markus Khalil, Markus Emmelheinz, Rewa Nazzal, Roland Adelman, Filomain Nguemo, et al. 2012. "Contractile Properties of Early Human Embryonic Stem Cell-Derived Cardiomyocytes: Beta-Adrenergic Stimulation Induces Positive Chronotropy and Lusitropy but Not Inotropy." *Stem Cells and Development* 21 (12): 2111–21. <https://doi.org/10.1089/scd.2011.0312>.
- Pinto, Alexander R., Alexei Ilinykh, Malina J. Ivey, Jill T. Kuwabara, Michelle L. D'antoni, Ryan Debuque, Anjana Chandran, et al. 2016. "Revisiting Cardiac Cellular Composition." *Circulation Research* 118 (3): 400–409. <https://doi.org/10.1161/CIRCRESAHA.115.307778>.
- Posern, Guido, and Richard Treisman. 2006. "Actin' Together: Serum Response Factor, Its Cofactors and the Link to Signal Transduction." *Trends in Cell Biology*. Trends Cell Biol. <https://doi.org/10.1016/j.tcb.2006.09.008>.
- Potter, Lincoln R., Sarah Abbey-Hosch, and Deborah M. Dickey. 2006. "Natriuretic Peptides, Their Receptors, and Cyclic Guanosine Monophosphate-Dependent Signaling Functions." *Endocrine Reviews*. Oxford Academic. <https://doi.org/10.1210/er.2005-0014>.
- Prakash, Y. S., Mark J. Cody, Philippe R. Housmans, James D. Hannon, and Gary C. Sieck. 1999. "Comparison of Cross-Bridge Cycling Kinetics in Neonatal vs. Adult Rat Ventricular Muscle." *Journal of Muscle Research and Cell Motility* 20 (7): 717–23. <https://doi.org/10.1023/A:1005585807179>.
- Puppala, Dinesh, Leon P. Collis, Sunny Z. Sun, Vinicius Bonato, Xian Chen, Blake Anson, Mathew Pletcher, Bernard Fermini, and Sandra J. Engle. 2013. "Comparative Gene Expression Profiling in Human-Induced Pluripotent Stem Cell-Derived Cardiocytes and Human and Cynomolgus Heart Tissue." *Toxicological Sciences* 131 (1): 292–301. <https://doi.org/10.1093/toxsci/kfs282>.
- Qu, Yongxia, and Mohamed Boutjdir. 2001. "Gene Expression of SERCA2a and L- and T-Type Ca Channels during Human Heart Development." *Pediatric Research* 50 (5): 569–74. <https://doi.org/10.1203/00006450-200111000-00006>.

- Radisic, Milica, Hyoungshin Park, Helen Shing, Thomas Consi, Frederick J. Schoen, Robert Langer, Lisa E. Freed, and Gordana Vunjak-Novakovic. 2004. "Functional Assembly of Engineered Myocardium by Electrical Stimulation of Cardiac Myocytes Cultured on Scaffolds." *Proceedings of the National Academy of Sciences of the United States of America* 101 (52): 18129–34. <https://doi.org/10.1073/pnas.0407817101>.
- Ramuz, Masoud, Alveera Hasan, Lena Gruscheski, Ivan Diakonov, Nikoleta Pavlaki, Viacheslav O. Nikolaev, Sian Harding, Chris Dunsby, and Julia Gorelik. 2019. "A Software Tool for High-Throughput Real-Time Measurement of Intensity-Based Ratio-Metric FRET." *Cells* 8 (12): 1541. <https://doi.org/10.3390/cells8121541>.
- Ran, F. Ann, Patrick D. Hsu, Jason Wright, Vineeta Agarwala, David A. Scott, and Feng Zhang. 2013. "Genome Engineering Using the CRISPR-Cas9 System." *Nature Protocols* 8 (11): 2281–2308. <https://doi.org/10.1038/nprot.2013.143>.
- Redfield, Margaret M., Horng H. Chen, Barry A. Borlaug, Marc J. Semigran, Kerry L. Lee, Gregory Lewis, Martin M. LeWinter, et al. 2013. "Effect of Phosphodiesterase-5 Inhibition on Exercise Capacity and Clinical Status in Heart Failure with Preserved Ejection Fraction: A Randomized Clinical Trial." *JAMA - Journal of the American Medical Association* 309 (12): 1268–77. <https://doi.org/10.1001/jama.2013.2024>.
- Rich, T. C., K. A. Fagan, H. Nakata, J. Schaack, D. M.F. Cooper, and J. W. Karpen. 2000. "Cyclic Nucleotide-Gated Channels Colocalize with Adenylyl Cyclase in Regions of Restricted CAMP Diffusion." *Journal of General Physiology* 116 (2): 147–61. <https://doi.org/10.1085/jgp.116.2.147>.
- Richter, Wito, Moses Xie, Colleen Scheitrum, Judith Krall, Matthew A. Movsesian, and Marco Conti. 2011. "Conserved Expression and Functions of PDE4 in Rodent and Human Heart." *Basic Research in Cardiology* 106 (2): 249–62. <https://doi.org/10.1007/s00395-010-0138-8>.
- Robertson, Claire, David D. Tran, and Steven C. George. 2013. "Concise Review: Maturation Phases of Human Pluripotent Stem Cell-Derived Cardiomyocytes." *Stem Cells*. Stem Cells. <https://doi.org/10.1002/stem.1331>.
- Rodriguez, Anthony G., Sangyoon J. Han, Michael Regnier, and Nathan J. Sniadecki. 2011. "Substrate Stiffness Increases Twitch Power of Neonatal Cardiomyocytes in Correlation with Changes in Myofibril Structure and Intracellular Calcium." *Biophysical Journal* 101 (10): 2455–64. <https://doi.org/10.1016/j.bpj.2011.09.057>.
- Rooij, Eva Van, Lillian B. Sutherland, Xiaoxia Qi, James A. Richardson, Joseph Hill, and Eric N. Olson. 2007. "Control of Stress-Dependent Cardiac Growth and Gene Expression by a MicroRNA." *Science* 316 (5824): 575–79. <https://doi.org/10.1126/science.1139089>.
- Rosman, Guy J., Timothy J. Martins, William K. Sonnenburg, Joseph A. Beavo, Ken Ferguson, and Kate Loughney. 1997. "Isolation and Characterization of Human cDNAs Encoding a cGMP-Stimulated 3',5'-Cyclic Nucleotide Phosphodiesterase." *Gene* 191 (1): 89–95. [https://doi.org/10.1016/S0378-1119\(97\)00046-2](https://doi.org/10.1016/S0378-1119(97)00046-2).
- Ruan, Jia Ling, Nathaniel L. Tulloch, Maria V. Razumova, Mark Saiget, Veronica Muskheli, Lil Pabon, Hans Reinecke, Michael Regnier, and Charles E. Murry. 2016. "Mechanical Stress Conditioning and Electrical Stimulation Promote Contractility and Force Maturation of Induced Pluripotent Stem Cell-Derived Human Cardiac Tissue." *Circulation* 134 (20): 1557–67. <https://doi.org/10.1161/CIRCULATIONAHA.114.014998>.
- Ruan, Jia Ling, Nathaniel L. Tulloch, Mark Saiget, Sharon L. Paige, Maria V. Razumova, Michael Regnier, Kelvin Chan Tung, et al. 2015. "Mechanical Stress Promotes Maturation of Human

- Myocardium from Pluripotent Stem Cell-Derived Progenitors." *Stem Cells* 33 (7): 2148–57. <https://doi.org/10.1002/stem.2036>.
- Russwurm, Michael, Florian Mullershausen, Andreas Friebe, Ronald Jäger, Corina Russwurm, and Doris Koesling. 2007. "Design of Fluorescence Resonance Energy Transfer (FRET)-Based CGMP Indicators: A Systematic Approach." *Biochemical Journal* 407 (1): 69–77. <https://doi.org/10.1042/BJ20070348>.
- Ruwhof, Cindy, Annemieke E.T. Van Wamel, Janneke M. Egas, and Arnoud Van Der Laarse. 2000. "Cyclic Stretch Induces the Release of Growth Promoting Factors from Cultured Neonatal Cardiomyocytes and Cardiac Fibroblasts." *Molecular and Cellular Biochemistry* 208 (1–2): 89–98. <https://doi.org/10.1023/a:1007046105745>.
- Ry, Silvia Del, Manuela Cabiati, Vincenzo Lionetti, Chiara Colotti, Maristella Maltinti, Michele Emdin, Fabio A. Recchia, and Daniela Giannessi. 2007. "Sequencing and Cardiac Expression of Natriuretic Peptide Receptor 2 (NPR-B) in Sus Scrofa." *Peptides* 28 (7): 1390–96. <https://doi.org/10.1016/j.peptides.2007.05.003>.
- Ry, Silvia Del, Manuela Cabiati, Vincenzo Lionetti, Michele Emdin, Fabio A. Recchia, and Daniela Giannessi. 2008. "Expression of C-Type Natriuretic Peptide and of Its Receptor NPR-B in Normal and Failing Heart." *Peptides* 29 (12): 2208–15. <https://doi.org/10.1016/j.peptides.2008.09.005>.
- Ry, Silvia Del, Manuela Cabiati, Vincenzo Lionetti, Anca Simioniu, Chiara Caselli, Tommaso Prescimone, Michele Emdin, and Daniela Giannessi. 2009. "Asymmetrical Myocardial Expression of Natriuretic Peptides in Pacing-Induced Heart Failure." *Peptides* 30 (9): 1710–13. <https://doi.org/10.1016/j.peptides.2009.06.013>.
- Saggin, L., L. Gorza, S. Ausoni, and S. Schiaffino. 1989. "Troponin I Switching in the Developing Heart." *Journal of Biological Chemistry* 264 (27): 16299–302. [https://doi.org/10.1016/s0021-9258\(18\)71621-9](https://doi.org/10.1016/s0021-9258(18)71621-9).
- Sakmann, B., and E. Neher. 1984. "Patch Clamp Techniques for Studying Ionic Channels in Excitable Membranes." *Annual Review of Physiology* VOL. 46 (November): 455–72. <https://doi.org/10.1146/annurev.ph.46.030184.002323>.
- Salameh, Aida, Anne Wustmann, Sebastian Karl, Katja Blanke, Daniel Apel, Diana Rojas-Gomez, Heike Franke, Friedrich W. Mohr, Jan Janousek, and Stefan Dhein. 2010. "Cyclic Mechanical Stretch Induces Cardiomyocyte Orientation and Polarization of the Gap Junction Protein Connexin43." *Circulation Research* 106 (10): 1592–1602. <https://doi.org/10.1161/CIRCRESAHA.109.214429>.
- Saleem, Umber, Djemail Ismaili, Ingra Mannhardt, Hans Pinnschmidt, Thomas Schulze, Torsten Christ, Thomas Eschenhagen, and Arne Hansen. 2020. "Regulation of I_{Ca,L} and Force by PDEs in Human-Induced Pluripotent Stem Cell-Derived Cardiomyocytes." *British Journal of Pharmacology* 177 (13): 3036–45. <https://doi.org/10.1111/bph.15032>.
- Salloum, Fadi N., Antonio Abbate, Anindita Das, Jon Erik Houser, Colin A. Mudrick, Ian Z. Qureshi, Nicholas N. Hoke, et al. 2008. "Sildenafil (Viagra) Attenuates Ischemic Cardiomyopathy and Improves Left Ventricular Function in Mice." *American Journal of Physiology - Heart and Circulatory Physiology* 294 (3). <https://doi.org/10.1152/ajpheart.91438.2007>.
- Sanchez-Alonso, Jose L., Anamika Bhargava, Thomas O'Hara, Alexey V. Glukhov, Sophie Schobesberger, Navneet Bhogal, Markus B. Sikkell, et al. 2016. "Microdomain-Specific Modulation of L-Type Calcium Channels Leads to Triggered Ventricular Arrhythmia in Heart Failure." *Circulation Research* 119 (8): 944–45. <https://doi.org/10.1161/CIRCRESAHA.116.308698>.

- Sartiani, Laura, Esther Bettioli, Francesca Stillitano, Alessandro Mugelli, Elisabetta Cerbai, and Marisa E. Jaconi. 2007. "Developmental Changes in Cardiomyocytes Differentiated from Human Embryonic Stem Cells: A Molecular and Electrophysiological Approach." *Stem Cells* 25 (5): 1136–44. <https://doi.org/10.1634/stemcells.2006-0466>.
- Sasaki, Hideyuki, Takahiro Nagayama, Robert M. Blanton, Kinya Seo, Manling Zhang, Guangshuo Zhu, Dong I. Lee, et al. 2014. "PDE5 Inhibitor Efficacy Is Estrogen Dependent in Female Heart Disease." *Journal of Clinical Investigation* 124 (6): 2464–71. <https://doi.org/10.1172/JCI70731>.
- Sassi, Yassine, Andrea Ahles, Dong Jiunn Jeffery Truong, Younis Baqi, Sang Yong Lee, Britta Husse, Jean Sébastien Hulot, et al. 2014. "Cardiac Myocyte-Secreted CAMP Exerts Paracrine Action via Adenosine Receptor Activation." *Journal of Clinical Investigation* 124 (12): 5385–97. <https://doi.org/10.1172/JCI74349>.
- Sathaye, Alok, Nenad Bursac, Sean Sheehy, and Leslie Tung. 2006. "Electrical Pacing Counteracts Intrinsic Shortening of Action Potential Duration of Neonatal Rat Ventricular Cells in Culture." *Journal of Molecular and Cellular Cardiology* 41 (4): 633–41. <https://doi.org/10.1016/j.yjmcc.2006.06.076>.
- Satin, Jonathan, Ilanit Itzhaki, Sophia Rapoport, Elizabeth A. Schroder, Leighton Izu, Gil Arbel, Rafael Beyar, C. William Balke, Jackie Schiller, and Lior Gepstein. 2008. "Calcium Handling in Human Embryonic Stem Cell-Derived Cardiomyocytes." *Stem Cells* 26 (8): 1961–72. <https://doi.org/10.1634/stemcells.2007-0591>.
- Sato, M., N. Hida, T. Ozawa, and Y. Umezawa. 2000. "Fluorescent Indicators for Cyclic GMP Based on Cyclic GMP-Dependent Protein Kinase α and Green Fluorescent Proteins." *Analytical Chemistry* 72 (24): 5918–24. <https://doi.org/10.1021/ac0006167>.
- Schaper, J., E. Meiser, and Stammler. 1985. "Ultrastructural Morphometric Analysis of Myocardium from Dogs, Rats, Hamsters, Mice, and from Human Hearts." *Circulation Research* 56 (3): 377–91. <https://doi.org/10.1161/01.RES.56.3.377>.
- Schobesberger, Sophie, Peter T. Wright, Claire Poulet, Jose L. Sanchez-Alonso, Catherine Mansfield, Andreas Friebe, Sian E. Harding, Jean Luc Balligand, Viacheslav O. Nikolaev, and Julia Gorelik. 2020. " β -Adrenoceptor Redistribution Impairs NO/CGMP/PDE2 Signalling in 4 Failing Cardiomyocytes." *ELife* 9 (March). <https://doi.org/10.7554/eLife.52221>.
- Schulz, Stephanie, Sujay Singh, Rae Ann Bellet, Gita Singh, D. Janette Tubb, Hemin Chin, and David L. Garbers. 1989. "The Primary Structure of a Plasma Membrane Guanylate Cyclase Demonstrates Diversity within This New Receptor Family." *Cell* 58 (6): 1155–62. [https://doi.org/10.1016/0092-8674\(89\)90513-8](https://doi.org/10.1016/0092-8674(89)90513-8).
- SENZAKI, HIDEAKI, CAROLYN J. SMITH, GEORGE J. JUANG, TAKAYOSHI ISODA, SHARON P. MAYER, ANDREAS OHLER, NAZARENO PAOLOCCI, GORDON F. TOMASELLI, JOSHUA M. HARE, and DAVID A. KASS. 2001. "Cardiac Phosphodiesterase 5 (CGMP-specific) Modulates B-adrenergic Signaling in Vivo and Is Down-regulated in Heart Failure." *The FASEB Journal* 15 (10): 1718–26. <https://doi.org/10.1096/fj.00-0538com>.
- Shakur, Yasmin, Lena Stenson Holst, Tova Rahn Landstrom, Matthew Movsesian, Eva Degerman, and Vincent Manganiello. 2000. "Regulation and Function of the Cyclic Nucleotide Phosphodiesterase (PDE3) Gene Family." *Progress in Nucleic Acid Research and Molecular Biology*. Academic Press. [https://doi.org/10.1016/s0079-6603\(00\)66031-2](https://doi.org/10.1016/s0079-6603(00)66031-2).
- Shen, Bin, Wensheng Zhang, Jun Zhang, Jiankui Zhou, Jianying Wang, Li Chen, Lu Wang, et al. 2014. "Efficient Genome Modification by CRISPR-Cas9 Nickase with Minimal off-Target Effects." *Nature Methods* 11 (4): 399–402. <https://doi.org/10.1038/nmeth.2857>.

- Shepard, Thomas Hill, Lara Elaine Muffley, and Lynne Thayer Smith. 1998. "Ultrastructural Study of Mitochondria and Their Cristae in Embryonic Rats and Primate (N. Nemestrina)." *Anatomical Record* 252 (3): 383–92. [https://doi.org/10.1002/\(SICI\)1097-0185\(199811\)252:3<383::AID-AR6>3.0.CO;2-Z](https://doi.org/10.1002/(SICI)1097-0185(199811)252:3<383::AID-AR6>3.0.CO;2-Z).
- Shimko, Valerie F., and William C. Claycomb. 2008. "Effect of Mechanical Loading on Three-Dimensional Cultures of Embryonic Stem Cell-Derived Cardiomyocytes." *Tissue Engineering - Part A*. 14 (1): 49–58. <https://doi.org/10.1089/ten.a.2007.0092>.
- Shin, Chong Hyun, Zhi Ping Liu, Robert Passier, Chun Li Zhang, Da Zhi Wang, Thomas M. Harris, Hiroyuki Yamagishi, James A. Richardson, Geoffrey Childs, and Eric N. Olson. 2002. "Modulation of Cardiac Growth and Development by HOP, an Unusual Homeodomain Protein." *Cell* 110 (6): 725–35. [https://doi.org/10.1016/S0092-8674\(02\)00933-9](https://doi.org/10.1016/S0092-8674(02)00933-9).
- Shyu, Kou Gi, Wei Hsu Ko, Wei Shiung Yang, Bao Wei Wang, and Peiliang Kuan. 2005. "Insulin-like Growth Factor-1 Mediates Stretch-Induced Upregulation of Myostatin Expression in Neonatal Rat Cardiomyocytes." *Cardiovascular Research* 68 (3): 405–14. <https://doi.org/10.1016/j.cardiores.2005.06.028>.
- Siedner, Sharon, Martina Krüger, Mechthild Schroeter, Doris Metzler, Wilhelm Roell, Bernd K. Fleischmann, Juergen Hescheler, Gabriele Pfitzer, and Robert Stehle. 2003. "Developmental Changes in Contractility and Sarcomeric Proteins from the Early Embryonic to the Adult Stage in the Mouse Heart." *Journal of Physiology* 548 (2): 493–505. <https://doi.org/10.1113/jphysiol.2002.036509>.
- Silvestri, Pasquale, Cristian Di Russo, Stefano Rigattieri, Silvio Fedele, Daniel Todaro, Giuseppe Ferraiuolo, Giuliano Altamura, and Paolo Loschiavo. 2009. "MicroRNAs and Ischemic Heart Disease: Towards a Better Comprehension of Pathogenesis, New Diagnostic Tools and New Therapeutic Targets." *Recent Patents on Cardiovascular Drug Discovery*. Recent Pat Cardiovasc Drug Discov. <https://doi.org/10.2174/157489009788452977>.
- Smith, Carolyn J., Raymond Huang, Dong Sun, Sidonie Ricketts, Carl Hoegler, Jia Zhen Ding, Richard A. Moggio, and Thomas H. Hintze. 1997. "Development of Decompensated Dilated Cardiomyopathy Is Associated with Decreased Gene Expression and Activity of the Milrinone-Sensitive CAMP Phosphodiesterase PDE3A." *Circulation* 96 (9): 3116–23. <https://doi.org/10.1161/01.CIR.96.9.3116>.
- Smith, Shirley H., and Sanford P. Bishop. 1985. "Regional Myocyte Size in Compensated Right Ventricular Hypertrophy in the Ferret." *Journal of Molecular and Cellular Cardiology* 17 (10): 1005–11. [https://doi.org/10.1016/S0022-2828\(85\)80081-X](https://doi.org/10.1016/S0022-2828(85)80081-X).
- Snir, Mirit, Izhak Kehat, Amira Gepstein, Raymond Coleman, Joseph Itskovitz-Eldor, Erella Livne, and Lior Gepstein. 2003. "Assessment of the Ultrastructural and Proliferative Properties of Human Embryonic Stem Cell-Derived Cardiomyocytes." *American Journal of Physiology - Heart and Circulatory Physiology* 285 (6 54-6): 2355–63. <https://doi.org/10.1152/ajpheart.00020.2003>.
- Soderling, S. H., S. J. Bayuga, and J. A. Beavo. 1998. "Cloning and Characterization of a CAMP-Specific Cyclic Nucleotide Phosphodiesterase." *Proceedings of the National Academy of Sciences of the United States of America* 95 (15): 8991–96. <https://doi.org/10.1073/pnas.95.15.8991>.
- Soderling, Scott H., Sharon J. Bayuga, and Joseph A. Beavo. 1998. "Identification and Characterization of a Novel Family of Cyclic Nucleotide Phosphodiesterases." *Journal of Biological Chemistry* 273 (25): 15553–58. <https://doi.org/10.1074/jbc.273.25.15553>.
- Soonpaa, Mark H., Gou Young Koh, Michael G. Klug, and Loren J. Field. 1994. "Formation of Nascent Intercalated Disks between Grafted Fetal Cardiomyocytes and Host Myocardium." *Science* 264

(5155): 98–101. <https://doi.org/10.1126/science.8140423>.

- Spach, Madison S., J. Francis Heidlage, Roger C. Barr, and Paul C. Dolber. 2004. "Cell Size and Communication: Role in Structural and Electrical Development and Remodeling of the Heart." *Heart Rhythm* 1 (4): 500–515. <https://doi.org/10.1016/j.hrthm.2004.06.010>.
- Sprenger, Julia U., and Viacheslav O. Nikolaev. 2013. "Biophysical Techniques for Detection of CAMP and CGMP in Living Cells." *International Journal of Molecular Sciences* 14 (4): 8025–46. <https://doi.org/10.3390/ijms14048025>.
- Sprenger, Julia U., Ruwan K. Perera, Konrad R. Götz, and Viacheslav O. Nikolaev. 2012. "FRET Microscopy for Real-Time Monitoring of Signaling Events in Live Cells Using Unimolecular Biosensors." *Journal of Visualized Experiments*, no. 66 (August). <https://doi.org/10.3791/4081>.
- Sprenger, Julia U., Ruwan K. Perera, Julia H. Steinbrecher, Stephan E. Lehnart, Lars S. Maier, Gerd Hasenfuss, and Viacheslav O. Nikolaev. 2015. "In Vivo Model with Targeted CAMP Biosensor Reveals Changes in Receptor-Microdomain Communication in Cardiac Disease." *Nature Communications* 6 (April). <https://doi.org/10.1038/ncomms7965>.
- Stangherlin, Alessandra, Frank Gesellchen, Anna Zoccarato, Anna Terrin, Laura Ashley Fields, Marco Berrera, Nicoletta Concetta Surdo, et al. 2011. "CGMP Signals Modulate Camp Levels in a Compartment-Specific Manner to Regulate Catecholamine-Dependent Signaling in Cardiac Myocytes." *Circulation Research* 108 (8): 929–39. <https://doi.org/10.1161/CIRCRESAHA.110.230698>.
- Steinhelper, Mark E., Karen L. Cochrane, and Loren J. Field. 1990. "Hypotension in Transgenic Mice Expressing Atrial Natriuretic Factor Fusion Genes." *Hypertension* 16 (3): 301–7. <https://doi.org/10.1161/01.HYP.16.3.301>.
- Subramanian, Hariharan, Alexander Froese, Peter Jönsson, Hannes Schmidt, Julia Gorelik, and Viacheslav O. Nikolaev. 2018. "Distinct Submembrane Localisation Compartmentalises Cardiac NPR1 and NPR2 Signalling to CGMP." *Nature Communications* 9 (1): 2446. <https://doi.org/10.1038/s41467-018-04891-5>.
- Sudoh, Tetsuji, Kenji Kangawa, Naoto Minamino, and Hisayuki Matsuo. 1988. "A New Natriuretic Peptide in Porcine Brain." *Nature* 332 (6159): 78–81. <https://doi.org/10.1038/332078a0>.
- Sudoh, Tetsuji, Naoto Minamino, Kenji Kangawa, and Hisayuki Matsuo. 1990. "C-Type Natriuretic Peptide (CNP): A New Member of Natriuretic Peptide Family Identified in Porcine Brain." *Biochemical and Biophysical Research Communications* 168 (2): 863–70. [https://doi.org/10.1016/0006-291X\(90\)92401-K](https://doi.org/10.1016/0006-291X(90)92401-K).
- Sugioka, Masaki, Masaaki Ito, Hiroshi Masuoka, Kazuhito Ichikawa, Tokuji Konishi, Toshio Tanaka, and Takeshi Nakano. 1994. "Identification and Characterization of Isoenzymes of Cyclic Nucleotide Phosphodiesterase in Human Kidney and Heart, and the Effects of New Cardiotonic Agents on These Isoenzymes." *Naunyn-Schmiedeberg's Archives of Pharmacology* 350 (3): 284–93. <https://doi.org/10.1007/BF00175034>.
- Surdo, Nicoletta C., Marco Berrera, Andreas Koschinski, Marcella Brescia, Matias R. MacHado, Carolyn Carr, Peter Wright, et al. 2017. "FRET Biosensor Uncovers CAMP Nano-Domains at β -Adrenergic Targets That Dictate Precise Tuning of Cardiac Contractility." *Nature Communications* 8. <https://doi.org/10.1038/ncomms15031>.
- Takahashi, Kazutoshi, Koji Tanabe, Mari Ohnuki, Megumi Narita, Tomoko Ichisaka, Kiichiro Tomoda, and Shinya Yamanaka. 2007. "Induction of Pluripotent Stem Cells from Adult Human Fibroblasts by Defined Factors." *Cell* 131 (5): 861–72.

<https://doi.org/10.1016/j.cell.2007.11.019>.

- Takasu, Nobuyuki. 2006. "Thyroid Hormone and the Cardiovascular System." *Nippon Rinsho. Japanese Journal of Clinical Medicine*. N Engl J Med. <https://doi.org/10.1056/nejm200102153440707>.
- Takimoto, Eiki, Diego Belardi, Carlo G. Tocchetti, Susan Vahebi, Gianfrancesco Cormaci, Elizabeth A. Ketner, An L. Moens, Hunter C. Champion, and David A. Kass. 2007. "Compartmentalization of Cardiac β -Adrenergic Inotropy Modulation by Phosphodiesterase Type 5." *Circulation* 115 (16): 2159–67. <https://doi.org/10.1161/CIRCULATIONAHA.106.643536>.
- Takimoto, Eiki, Hunter C. Champion, Diego Belardi, Javid Moslehi, Marco Mongillo, Evanthia Mergia, David C. Montrose, et al. 2005. "cGMP Catabolism by Phosphodiesterase 5A Regulates Cardiac Adrenergic Stimulation by NOS3-Dependent Mechanism." *Circulation Research* 96 (1): 100–109. <https://doi.org/10.1161/01.RES.0000152262.22968.72>.
- Takimoto, Eiki, Hunter C. Champion, Manxiang Li, Diego Belardi, Shuxun Ren, E. Rene Rodriguez, Djahida Bedja, Kathleen L. Gabrielson, Yibin Wang, and David A. Kass. 2005. "Chronic Inhibition of Cyclic GMP Phosphodiesterase 5A Prevents and Reverses Cardiac Hypertrophy." *Nature Medicine* 11 (2): 214–22. <https://doi.org/10.1038/nm1175>.
- Takimoto, Eiki, Hunter C. Champion, Manxiang Li, Shuxun Ren, E. Rene Rodriguez, Barbara Tavazzi, Giuseppe Lazzarino, et al. 2005. "Oxidant Stress from Nitric Oxide Synthase-3 Uncoupling Stimulates Cardiac Pathologic Remodeling from Chronic Pressure Load." *Journal of Clinical Investigation* 115 (5): 1221–31. <https://doi.org/10.1172/JCI21968>.
- Tamura, Naohisa, Yoshihiro Ogawa, Hideki Chusho, Kenji Nakamura, Kazuki Nakao, Michio Suda, Masato Kasahara, et al. 2000. "Cardiac Fibrosis in Mice Lacking Brain Natriuretic Peptide." *Proceedings of the National Academy of Sciences of the United States of America* 97 (8): 4239–44. <https://doi.org/10.1073/pnas.070371497>.
- Thomas, M. K., S. H. Francis, and J. D. Corbin. 1990. "Characterization of a Purified Bovine Lung cGMP-Binding cGMP Phosphodiesterase." *Journal of Biological Chemistry* 265 (25): 14964–70. [https://doi.org/10.1016/s0021-9258\(18\)77210-4](https://doi.org/10.1016/s0021-9258(18)77210-4).
- Troncoso, Rodrigo, Cristián Ibarra, Jose Miguel Vicencio, Enrique Jaimovich, and Sergio Lavandero. 2014. "New Insights into IGF-1 Signaling in the Heart." *Trends in Endocrinology and Metabolism*. Elsevier. <https://doi.org/10.1016/j.tem.2013.12.002>.
- Tulloch, Nathaniel L., Veronica Muskheli, Maria V. Razumova, F. Steven Korte, Michael Regnier, Kip D. Hauch, Lil Pabon, Hans Reinecke, and Charles E. Murry. 2011. "Growth of Engineered Human Myocardium with Mechanical Loading and Vascular Coculture." *Circulation Research* 109 (1): 47–59. <https://doi.org/10.1161/CIRCRESAHA.110.237206>.
- Vaidya, Dhananjay, Houman S. Tamaddon, Cecilia W. Lo, Steven M. Taffet, Mario Delmar, Gregory E. Morley, and José Jalife. 2001. "Null Mutation of Connexin43 Causes Slow Propagation of Ventricular Activation in the Late Stages of Mouse Embryonic Development." *Circulation Research* 88 (11): 1196–1202. <https://doi.org/10.1161/hh1101.091107>.
- Vandeput, Fabrice, Nicolas Szabo-Fresnais, Faiyaz Ahmad, Changwon Kho, Ahyoung Lee, Judith Krall, Allan Dunlop, et al. 2013. "Selective Regulation of Cyclic Nucleotide Phosphodiesterase PDE3A Isoforms." *Proceedings of the National Academy of Sciences of the United States of America* 110 (49): 19778–83. <https://doi.org/10.1073/pnas.1305427110>.
- Vettel, C., S. Lämmle, S. Ewens, C. Cervirgen, J. Emons, A. Ongherth, M. Dewenter, et al. 2014. "PDE2-Mediated cAMP Hydrolysis Accelerates Cardiac Fibroblast to Myofibroblast Conversion

- and Is Antagonized by Exogenous Activation of CGMP Signaling Pathways." *American Journal of Physiology - Heart and Circulatory Physiology* 306 (8).
<https://doi.org/10.1152/ajpheart.00852.2013>.
- Villardaga, Jean Pierre, Moritz Bünemann, Cornelius Krasell, Mariàn Castro, and Martin J. Lohse. 2003. "Measurement of the Millisecond Activation Switch of G Protein-Coupled Receptors in Living Cells." *Nature Biotechnology* 21 (7): 807–12. <https://doi.org/10.1038/nbt838>.
- Wang, Peng Yuan, Jiashing Yu, Jia Hua Lin, and Wei Bor Tsai. 2011. "Modulation of Alignment, Elongation and Contraction of Cardiomyocytes through a Combination of Nanotopography and Rigidity of Substrates." *Acta Biomaterialia* 7 (9): 3285–93.
<https://doi.org/10.1016/j.actbio.2011.05.021>.
- Wang, Ruixin, Dongni Wang, Dekai Kang, Xusen Guo, Chong Guo, Meimei Dongye, Yi Zhu, et al. 2020. "An Artificial Intelligent Platform for Live Cell Identification and the Detection of Cross-Contamination." *Annals of Translational Medicine* 8 (11): 697–697.
<https://doi.org/10.21037/atm.2019.07.105>.
- Warren, Chad M., Paul R. Krzesinski, Kenneth S. Campbell, Richard L. Moss, and Marion L. Greaser. 2004. "Titin Isoform Changes in Rat Myocardium during Development." *Mechanisms of Development* 121 (11): 1301–12. <https://doi.org/10.1016/j.mod.2004.07.003>.
- Wei, Chi Ming, Denise M. Heublein, Mark A. Perrella, Amir Lerman, Richard J. Rodeheffer, Christopher G.A. McGregor, William D. Edwards, Hartzell V. Schaff, and John C. Burnett. 1993. "Natriuretic Peptide System in Human Heart Failure." *Circulation* 88 (3): 1004–9.
<https://doi.org/10.1161/01.CIR.88.3.1004>.
- Weisstein, Eric W. 2011. "Affine Transformation." In *SpringerReference*. Wolfram Research, Inc.
https://doi.org/10.1007/springerreference_5221.
- Wells, Linda, Kevin A. Edwards, and Sanford I. Bernstein. 1996. "Myosin Heavy Chain Isoforms Regulate Muscle Function but Not Myofibril Assembly." *EMBO Journal* 15 (17): 4454–59.
<https://doi.org/10.1002/j.1460-2075.1996.tb00822.x>.
- Wright, Peter Thomas. 2013. "The Regionality of Cardiac B Eta-2- Adrenoceptor Signalling National Heart and Lung Institute , Imperial College London," no. December.
<https://spiral.imperial.ac.uk:8443/handle/10044/1/15514>.
- Wu, Haodi, Jaecheol Lee, Ludovic G. Vincent, Qingtong Wang, Mingxia Gu, Feng Lan, Jared M. Churko, et al. 2015. "Epigenetic Regulation of Phosphodiesterases 2A and 3A Underlies Compromised β -Adrenergic Signaling in an iPSC Model of Dilated Cardiomyopathy." *Cell Stem Cell* 17 (1): 89–100. <https://doi.org/10.1016/j.stem.2015.04.020>.
- Xia, Yang, L. Maximilian Buja, Richard C. Scarpulla, and Jeanie B. Mcmillin. 1997. "Electrical Stimulation of Neonatal Cardiomyocytes Results in the Sequential Activation of Nuclear Genes Governing Mitochondrial Proliferation and Differentiation." *Proceedings of the National Academy of Sciences of the United States of America* 94 (21): 11399–404.
<https://doi.org/10.1073/pnas.94.21.11399>.
- Xiu, Qin Xu, Yen Soo Set, William Sun, and Robert Zweigerdt. 2009. "Global Expression Profile of Highly Enriched Cardiomyocytes Derived from Human Embryonic Stem Cells." *Stem Cells* 27 (9): 2163–74. <https://doi.org/10.1002/stem.166>.
- Yamakage, Michiaki, and Akiyoshi Namiki. 2002. "Calcium Channels - Basic Aspects of Their Structure, Function and Gene Encoding; Anesthetic Action on the Channels - A Review." *Canadian Journal of Anesthesia* 49 (2): 151–64. <https://doi.org/10.1007/BF03020488>.

- Yang, Hui, Haoyi Wang, and Rudolf Jaenisch. 2014. "Generating Genetically Modified Mice Using CRISPR/Cas-Mediated Genome Engineering." *Nature Protocols* 9 (8): 1956–68. <https://doi.org/10.1038/nprot.2014.134>.
- Yang, Luhan, Marc Guell, Susan Byrne, Joyce L. Yang, Alejandro De Los Angeles, Prashant Mali, John Aach, et al. 2013. "Optimization of Scarless Human Stem Cell Genome Editing." *Nucleic Acids Research*. 2013. <https://doi.org/10.1093/nar/gkt555>.
- Yang, Xiulan, Lil Pabon, and Charles E. Murry. 2014. "Engineering Adolescence: Maturation of Human Pluripotent Stem Cell-Derived Cardiomyocytes." *Circulation Research* 114 (3): 511–23. <https://doi.org/10.1161/CIRCRESAHA.114.300558>.
- Yang, Xiulan, Marita L. Rodriguez, Andrea Leonard, Lihua Sun, Karin A. Fischer, Yuliang Wang, Julia Ritterhoff, et al. 2019. "Fatty Acids Enhance the Maturation of Cardiomyocytes Derived from Human Pluripotent Stem Cells." *Stem Cell Reports* 13 (4): 657–68. <https://doi.org/10.1016/j.stemcr.2019.08.013>.
- Yoshida, Shohei, Shigeru Miyagawa, Satsuki Fukushima, Takuji Kawamura, Noriyuki Kashiyama, Fumiya Ohashi, Toshihiko Toyofuku, Koichi Toda, and Yoshiki Sawa. 2018. "Maturation of Human Induced Pluripotent Stem Cell-Derived Cardiomyocytes by Soluble Factors from Human Mesenchymal Stem Cells." *Molecular Therapy* 26 (11): 2681–95. <https://doi.org/10.1016/j.ymthe.2018.08.012>.
- Young, Jennifer L., and Adam J. Engler. 2011. "Hydrogels with Time-Dependent Material Properties Enhance Cardiomyocyte Differentiation in Vitro." *Biomaterials* 32 (4): 1002–9. <https://doi.org/10.1016/j.biomaterials.2010.10.020>.
- Yu, Junying, Maxim A. Vodyanik, Kim Smuga-Otto, Jessica Antosiewicz-Bourget, Jennifer L. Frane, Shulan Tian, Jeff Nie, et al. 2007. "Induced Pluripotent Stem Cell Lines Derived from Human Somatic Cells." *Science* 318 (5858): 1917–20. <https://doi.org/10.1126/science.1151526>.
- Yu, Liangzhu, Shijun Gao, Li Nie, Ming Tang, Weifeng Huang, Hongyan Luo, Xinwu Hu, et al. 2011. "Molecular and Functional Changes in Voltage-Gated Na⁺ Channels in Cardiomyocytes during Mouse Embryogenesis." *Circulation Journal* 75 (9): 2071–79. <https://doi.org/10.1253/circj.CJ-10-1212>.
- Zaccolo, Manuela, and Matthew A. Movsesian. 2007. "cAMP and cGMP Signaling Cross-Talk: Role of Phosphodiesterases and Implications for Cardiac Pathophysiology." *Circulation Research* 100 (11): 1569–78. <https://doi.org/10.1161/CIRCRESAHA.106.144501>.
- Zagotta, William N., Nelson B. Olivier, Kevin D. Black, Edgar C. Young, Rich Olson, and Eric Gouaux. 2003. "Structural Basis for Modulation and Agonist Specificity of HCN Pacemaker Channels." *Nature* 425 (6954): 200–205. <https://doi.org/10.1038/nature01922>.
- Zhang, Donghui, Ilya Y. Shadrin, Jason Lam, Hai Qian Xian, H. Ralph Snodgrass, and Nenad Bursac. 2013. "Tissue-Engineered Cardiac Patch for Advanced Functional Maturation of Human ESC-Derived Cardiomyocytes." *Biomaterials* 34 (23): 5813–20. <https://doi.org/10.1016/j.biomaterials.2013.04.026>.
- Zhang, Jianhua, Gisela F. Wilson, Andrew G. Soerens, Chad H. Koonce, Junying Yu, Sean P. Palecek, James A. Thomson, and Timothy J. Kamp. 2009. "Functional Cardiomyocytes Derived from Human Induced Pluripotent Stem Cells." *Circulation Research* 104 (4): e30. <https://doi.org/10.1161/CIRCRESAHA.108.192237>.
- Zhang, Manling, and David A. Kass. 2011. "Phosphodiesterases and Cardiac cGMP: Evolving Roles and Controversies." *Trends in Pharmacological Sciences*. NIH Public Access.

<https://doi.org/10.1016/j.tips.2011.02.019>.

- Zhang, Manling, Norimichi Koitabashi, Takahiro Nagayama, Ryan Rambaran, Ning Feng, Eiki Takimoto, Trisha Koenke, et al. 2008. "Expression, Activity, and pro-Hypertrophic Effects of PDE5A in Cardiac Myocytes." *Cellular Signalling* 20 (12): 2231–36. <https://doi.org/10.1016/j.cellsig.2008.08.012>.
- Zhang, Manling, Eiki Takimoto, Dong Ik Lee, Celio X.C. Santos, Taishi Nakamura, Steven Hsu, Aiyang Jiang, et al. 2012. "Pathological Cardiac Hypertrophy Alters Intracellular Targeting of Phosphodiesterase Type 5 from Nitric Oxide Synthase-3 to Natriuretic Peptide Signaling." *Circulation* 126 (8): 942–51. <https://doi.org/10.1161/CIRCULATIONAHA.112.090977>.
- Zhang, W., C. W. Kong, M. H. Tong, W. H. Chooi, N. Huang, R. A. Li, and B. P. Chan. 2017. "Maturation of Human Embryonic Stem Cell-Derived Cardiomyocytes (HESC-CMs) in 3D Collagen Matrix: Effects of Niche Cell Supplementation and Mechanical Stimulation." *Acta Biomaterialia* 49 (February): 204–17. <https://doi.org/10.1016/j.actbio.2016.11.058>.
- Zhang, Xiao hua, and Martin Morad. 2020. "Ca²⁺ Signaling of Human Pluripotent Stem Cells-Derived Cardiomyocytes as Compared to Adult Mammalian Cardiomyocytes." *Cell Calcium* 90 (September): 102244. <https://doi.org/10.1016/j.ceca.2020.102244>.
- Zhang, Yin Hua. 2017. "Nitric Oxide Signalling and Neuronal Nitric Oxide Synthase in the Heart under Stress." *F1000Research*. Faculty of 1000 Ltd. <https://doi.org/10.12688/f1000research.10128.1>.
- Zhang, Yin Hua, Chun Zi Jin, Ji Hyun Jang, and Yue Wang. 2014. "Molecular Mechanisms of Neuronal Nitric Oxide Synthase in Cardiac Function and Pathophysiology." *Journal of Physiology* 592 (15): 3189–3200. <https://doi.org/10.1113/jphysiol.2013.270306>.
- Zhao, Yong, Joshua F. Ransom, Ankang Li, Vasanth Vedantham, Morgan von Drehle, Alecia N. Muth, Takatoshi Tsuchihashi, Michael T. McManus, Robert J. Schwartz, and Deepak Srivastava. 2007. "Dysregulation of Cardiogenesis, Cardiac Conduction, and Cell Cycle in Mice Lacking MiRNA-1-2." *Cell* 129 (2): 303–17. <https://doi.org/10.1016/j.cell.2007.03.030>.
- Zhou, Pingzhu, and William T. Pu. 2016. "Recounting Cardiac Cellular Composition." *Circulation Research*. Lippincott Williams & Wilkins Hagerstown, MD. <https://doi.org/10.1161/CIRCRESAHA.116.308139>.
- Zhu, Wei Zhong, Luis F. Santana, and Michael A. Laflamme. 2009. "Local Control of Excitation-Contraction Coupling in Human Embryonic Stem Cell-Derived Cardiomyocytes." *PLoS ONE* 4 (4). <https://doi.org/10.1371/journal.pone.0005407>.
- Zhu, Wei Zhong, Yiheng Xie, Kara White Moyes, Joseph D. Gold, Bardia Askari, and Michael A. Laflamme. 2010. "Neuregulin/ErbB Signaling Regulates Cardiac Subtype Specification in Differentiating Human Embryonic Stem Cells." *Circulation Research* 107 (6): 776–86. <https://doi.org/10.1161/CIRCRESAHA.110.223917>.
- Zhu, Xiaoming, Afu Fu, and Kathy Qian Luo. 2012. "A High-Throughput Fluorescence Resonance Energy Transfer (FRET)-Based Endothelial Cell Apoptosis Assay and Its Application for Screening Vascular Disrupting Agents." *Biochemical and Biophysical Research Communications* 418 (4): 641–46. <https://doi.org/10.1016/j.bbrc.2012.01.066>.
- Ziman, Andrew P., Norma Leticia Gómez-Viquez, Robert J. Bloch, and W. J. Lederer. 2010. "Excitation-Contraction Coupling Changes during Postnatal Cardiac Development." *Journal of Molecular and Cellular Cardiology* 48 (2): 379–86. <https://doi.org/10.1016/j.yjmcc.2009.09.016>.
- Zimmermann, W. H., K. Schneiderbanger, P. Schubert, M. Didié, F. Münzel, J. F. Heubach, S. Kostin, W. L. Neuhuber, and T. Eschenhagen. 2002. "Tissue Engineering of a Differentiated Cardiac

Muscle Construct.” *Circulation Research* 90 (2): 223–30.
<https://doi.org/10.1161/hh0202.103644>.

Zoccarato, Anna, Nicoletta C. Surdo, Jan M. Aronsen, Laura A. Fields, Luisa Mancuso, Giuliano Dodoni, Alessandra Stangherlin, et al. 2015. “Cardiac Hypertrophy Is Inhibited by a Local Pool of CAMP Regulated by Phosphodiesterase 2.” *Circulation Research* 117 (8): 707–19.
<https://doi.org/10.1161/CIRCRESAHA.114.305892>.

Zorio, E., P. Medina, J. Rueda, J. Millan, M. Arnau, M. Beneyto, F. Marin, et al. 2009. “Insights Into the Role of MicroRNAs in Cardiac Diseases: From Biological Signalling to Therapeutic Targets.” *Cardiovascular & Hematological Agents in Medicinal Chemistry* 7 (1): 82–90.
<https://doi.org/10.2174/187152509787047676>.